Design of Powder Core Motors

Avo Reinap

LUND UNIVERSITY

Doctoral Dissertation in Industrial Electrical Engineering

Department of Industrial Electrical Engineering and Automation

Department of Industrial Electrical Engineering and Automation
Lund University
Box 118
SE-221 00 LUND
SWEDEN

ISBN 91-88934-36-5
CODEN:LUTEDX/(TEIE-1044)/1-220/(2004)

Printed in Sweden by Media-Tryck, Lund University
Lund 2004

Abstract

The goal of the study presented in this thesis is to evaluate the advantages and drawbacks of using powder technology in the design of the iron core of small claw-pole electric motors. The use of soft magnetic composites (SMC) and compaction technology allows the creation of complex 3D iron cores. The additional dimension opens for new solutions of the electromechanical energy conversion. A claw-pole motor among the transversal flux machines that has particularly high specific torque is in the focus of research interest. Generally, as the iron core can be more complicated, the winding is chosen to be simpler in the powder core motors. The thesis focuses on the machine design of a single-phase and a two-phase low-power claw-pole motor. The predicted results compare well with measurements of the prototype motors.

The motor design process in this thesis uses a magnetic equivalent circuit (MEC) model of the outer-rotor claw-pole motors that is accurate enough to describe the physics of the electromagnetic conversion. Additional equivalent circuits are made to evaluate the mechanic and thermal loading of the machines. The outcome of the equivalent circuit models is enough to estimate roughly the optimal size of the motor and the motor output according to the materials selected.

After the rough design process, which is based on equivalent circuits, is finished, a series of FE magnetostatic analyses are made in order to evaluate the static characteristics of the motors, to specify the magnetization losses and to carry out a sensitivity study for the proposed size of the motors. Finally, the magnetic, mechanic and thermal design is analyzed dynamically and statically by the use of coupled multiphysics. The task of the coupled multiphysics is to find out the cooling capability and the thermal limit of the motor as well as the mechanic stress in the motor parts due to magneto-mechanic loading. It is discussed how the discrepancy between the calculated and measured cogging torque depends on the fineness of the 3D FE air gap mesh.

Iron loss estimation based on the results of the FE-analysis is made taking the local rotation, and not only pulsation, of the magnetic flux into consideration. It is shown that the loss coefficients in the material model must be adapted to account for flux rotation.

A part from the output of the machine as an electromechanical energy converter is their controllability in the electric drive system. Based on the static characteristics, which are calculated in the FE-analysis and verified in prototype measurements, a tailor made control method is developed for the machines designed. Results are presented of extensive simulations and experimental verifications of the proposed control strategy and power electronic circuitry. The high-speed four-pole single-phase motor shows satisfactory results. The other motor, which has 20 poles and two phases, has a main weakness in its complex assembling and a large cogging torque.

Acknowledgement

Everything that is good in this thesis is thanks for the inspiration and knowledge of the following people. Without following any order of importance they are my roommate David Martínez Muñoz, my supervisor Prof. Mats Alaküla, the prefect of the Department of Industrial Electrical Engineering and Automation Prof. Gustaf Olsson and the rest of the people at this department. My sincere gratitude goes to people who were involved in the VAMP-25 project: Tomas Johansson at Viktor Hasselblad AB, Jan-Olov Krona at Callo Sintermetall AB, Nils Pahlbäck at Sura Magnets AB, Thomas Rundqvist at ProEngCo AB, Tord Cedell, at, the Division of Production and Materials Engineering (LTH), and the other people who were involved to this project. Special thanks to Göran Nord, Lars Hultman and Lars-Olov Pennander at Höganäs AB. Invaluable FEM support was provided from Vector Fields Ltd. by John Simkin, Alex Michaelides, Klaus Hoeffer, and Chris Riley; from Comsol AB by Johan Linde, Ola Lindgren; and from The Japan Research Institute, Ltd. by Akinori Shiga and Takashi Yamada. Thanks to my family for their support.

Contents

CHAPTER 1 INTRODUCTION 1

1.1 BACKGROUND 5
1.2 OBJECTIVES 8
1.3 CONTRIBUTIONS 8
1.4 OUTLINES 9
1.5 PUBLICATIONS 10

CHAPTER 2 CONSTRUCTION OF A CLAW-POLE MOTOR 11

2.1 MOTOR DESIGN 11
2.2 PHASE RING MADE OF CLAW-POLE RINGS 17
2.3 SOFT MAGNETIC COMPOSITE 23
2.4 PERMANENT MAGNET RING 26

CHAPTER 3 DESIGN MODEL 39

3.1 MAGNETIC CIRCUIT 40
3.2 CORE LOSS IN THE SMC CORE 48
3.3 MECHANICAL CALCULATION AND ANALYSIS 53
3.4 THERMAL DESIGN 56
3.5 OPTIMIZATION 59
3.6 OPTIMAL SIZE OF A SMALL CLAW-POLE MOTOR 61

CHAPTER 4 NUMERIC FIELD COMPUTATION 67

4.1 MAGNETOSTATICS 68
4.2 CORE LOSS PREDICTION 80
4.3 STRUCTURAL MECHANICS 84
4.4 HEAT TRANSFER 87
4.5 INCORPORATING 3D FEA IN AN OPTIMIZATION ROUTINE 92

CHAPTER 5 SENSITIVITY STUDY AND PROTOTYPING 105

5.1 VARIATION OF STATOR DIMENSIONS 106
5.2 VARIATION OF MATERIAL PROPERTIES 120
5.3 VARIATION OF MAGNETIZATION PATTERN 122
5.4 THE PROTOTYPES 132
5.5 STATIC CHARACTERISTICS 135
5.6 CORE LOSS MEASUREMENT 141
5.7 CONCLUSIONS 145

CHAPTER 6 CONTROL OF A CLAW-POLE MOTOR 147

6.1 CONTROL STRATEGIES 147
6.2 MODEL OF DRIVE SYSTEM 151
6.3 SIMULATIONS 155
6.4 EXPERIMENTAL RESULTS 166
6.5 CONCLUSIONS AND REMARKS 170

CHAPTER 7 CONCLUSIONS 173

7.1 SUMMARY OF RESULTS 173
7.2 FUTURE WORK 177

REFERENCES 179

APPENDIX A MATERIAL DATA 197

APPENDIX B MOTOR CONSTRUCTION 201

B.1 FORMULATION OF A CLAW-POLE CORE 201
B.2 CORE FORMULATION IN 3D FE CONSTRUCTION 204

APPENDIX C CAD INCORPORATED WITH 3D FEA 207

C.1 CONTROLLED CAD AND 3D FEA 207
C.2 ACCURACY OF 3D FE MODELLING 210
C.3 ANALYSIS AT POST-PROCESSING LEVEL 214

APPENDIX D POWER ELECTRONIC CONTROL 217

D.1 DRIVER CIRCUIT 217
D.2 FEEDBACK 218

Chapter 1

Introduction

The potential in design and development of electromechanical devices seems today higher than ever before. Even though the principles of machine design are more than 100 years old and remain unchanged, there is more to be done than just some small improvements. There are at least three reasons for this. First, the possibilities with new materials and manufacturing methods open an opportunity towards integration and improved manufacturability. Second, tailor made design is required more often for specific applications. Third, the use of an integrationability of control electronics increases the involved functionality.

In the conventional electrical machine the electromechanical energy conversion is governed by magnetic fields. Generally, in order to get mechanical movement in any electrical machine, either the electric circuit or the magnetic circuit needs to be complex. The source of mechanic force is the shear stress, appearing due the principle of electromagnetic interaction or attraction between the magnetic sources, or between magnetic source and magnetic conductor. An air-gap separates the stationary and the moving body mechanically, and couples them magnetically. In order to get a continuous movement the magnetic coupling has to be on a plane that is orthogonal to the direction of the movement. In rotating electrical machine, there are a number of constructional combinations between the direction of a winding producing the magnetizing field and a plane of motion that is perpendicular to the magnetic coupling (Figure 1.1).

Magnetic cores are used to guide and to enlarge the magnetic flux. In order to keep the volume of the machine as small as possible the flux density has to be maximized. This is essential for the energy conversion process. Often, the torque or thrust magnification via a geared magnetic coupling and flux

concentration is required from an electromechanical device. Torque magnification is obtained by the ratio of the magnetic poles to the stator excitation poles. The latter is the ability of the electric current to produce magnetic field and poles in a coil, while the magnetic poles designate the magnetic coupling between the stationary part and the moving part. The magnetic poles take part in torque production over the air-gap. Principally, either a stronger magnetic coupling or a higher electric loading improves torque production. Typically and constructionally, the magnetic circuit has been relatively simple as it is conventionally made of a stack of 2D electromechanical sheets, which conducts magnetic flux in two dimensions and restrains eddy currents perpendicular to the flux flow. As the electric circuit competes with the magnetic circuit for the same volume, the specific torque of the radial flux machine (RFM) (figure 1.1 A), the axial flux machine (AFM) (figure 1.1 B) and the circumferential flux (torus) machine (CFM) (figure 1.1 C) [46] remain unchanged from the change of number of poles. Hereby the same magnetic coupling and shear stress over an air-gap is assumed. The magnetic flux of a single pole that links with a single coil in a winding would not increase the mechanic torque by doubling the number of poles of a machine that operates at the same mechanic speed. As both the number of turns and the linking flux have to decrease to half, while the number of coils is doubled, the total peak flux linkage of the winding decreases to one half (Eq. 1.1)[39]. On the contrary, the specific output of the transverse flux machines (TFM) (figure 1.1 D), where the source flux is transverse to the rotation plane, is dependent on the number of poles. As the slot area remains the same, i.e. the number of turns is unchanged; the total peak flux linkage is ideally independent of the number of poles, while the coupling flux has to decrease to half by doubling the number of poles. In TFM, the shape of the coil(s) is kept relatively simple while the complexity of the iron core requires a magnetic conductor that can carry the magnetic flux in three dimensions. As the number of poles increases, the frequency of the magnetic flux increases too. For the same mechanic speed low core loss will be another important design criterion. A magnetic core that is pressed from insulated iron powder particles enables to create an isotropic magnetic medium that has inherently low dynamic magnetic losses.

A better torque magnification can be reached in two ways: by changing the shape of the core structure or/and by choosing a better medium to carry the magnetic flux [38]. The use of soft magnetic composites (SMC) and compaction technology allows creation of a complex 3D ferrous core. A high winding filling factor can be reached with a simple hoop coil. The more circular the coil cross-section is the bigger the reduction of copper and copper losses are. Typically, concentrated windings, assembled with narrow

geometrical tolerance to the iron core, are used in SMC machines [80]. As an outcome, the powder technology improves not only the material utilization but also the possibility to reduce the production cost of the motor. The replacement of the core material does not necessarily lead to improvements in the machine design, even though the motor is well designed [45].

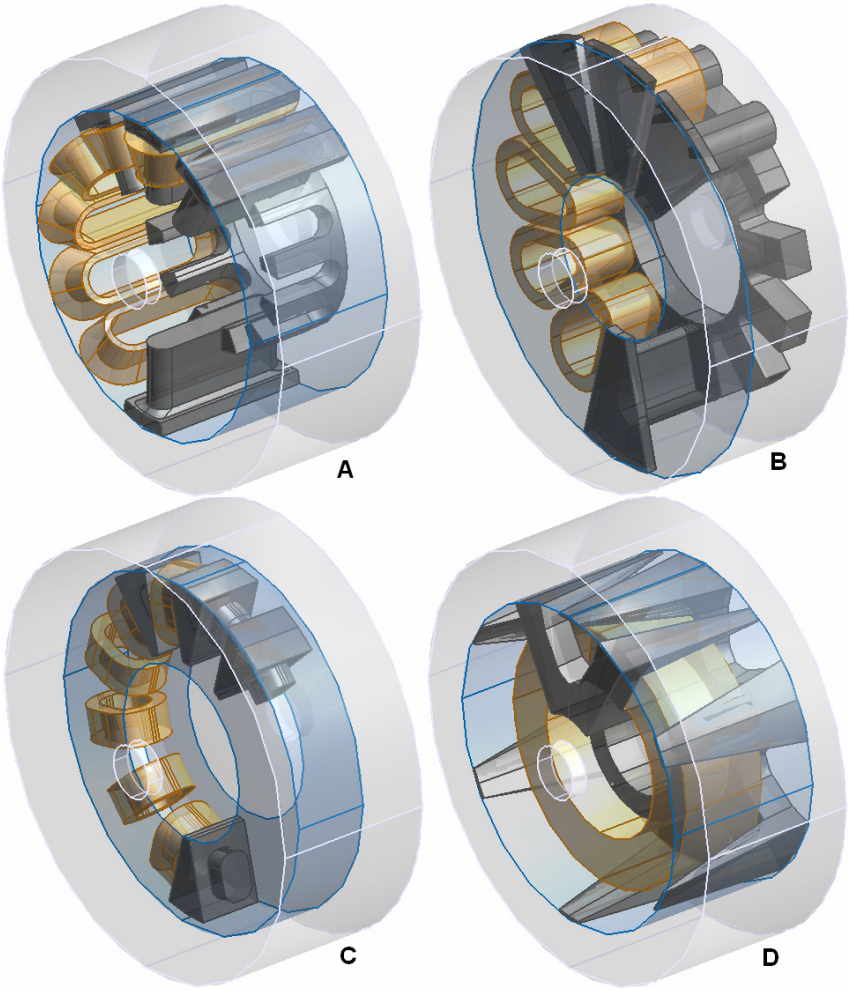

Figure 1.1: Structural choice of the plane of air-gap surface in the radial/circumferential or the axial/circumferential plane and the direction of the coil field lead to four types of construction: (A) radial flux, (B) axial flux, (C) circumferential flux and (D) transversal flux machines. The classical shapes of the SMC core parts are shown.

The main reason is that the SMC material has lower ability to conduct the magnetic flux. Generally, the lower permeability of magnetic material leads to a weaker magnetic coupling between the stator and the rotor. The low permeability has less influence on the electric machines with large effective air-gap e.g. permanent magnet machines.

Without considering the leakage flux, the idealized electromechanical output of an electrical machine can be expressed as

$$T_{em} = \frac{1}{2} \cdot \frac{\hat{E} \cdot \hat{I}}{\Omega} = \frac{N_P}{4} \cdot N \cdot \hat{\Phi} \cdot \hat{I}\,, \tag{1.1}$$

where the electromechanical device of N_P poles has a phase winding of N turns that carry electric current I (peak of fundamental). The coupling magnetic flux Φ induces of voltage E at a mechanic speed of Ω.

Independent of the low permeability, the SMC material becomes attractive at high magnetization frequencies because the dynamic loss of the core material is lower than in the conventional electromagnetic sheets. The constructional limitation of the electromagnetic sheets and the relatively high possible magnetization frequency is in favor of 3D SMC machines. A claw-pole construction among the transversal flux machines, which has particularly high specific torque, is a good option for SMC material. A simple structure, high energy-volume ratio, high reliability and relatively low price are making claw-pole motors attractive. The advantageous features are the way of achieving adjacent poles, a simple structure of press-formed magnetic poles and wound coil, and a high specific torque. Less favorable peculiarities are: a high reactance i.e. low power factor, a large magnetic leakage flux, detent torque and a tendency to magnetic saturation.

Another advantageous feature of a SMC core is a smooth surface that allows the use of simple concentrated windings. Flux concentration together with the compressed winding, and a good thermal contact between the coil and the core assembly leads to more efficient electromagnetic coupling with increased thermal limit. Even though the compressed SMC core is poorer thermal conductor the final shape of the core, reduction of slot wall insulation and the compact assembling improves the overall thermal loading of an electromechanical device [68].

1.1 Background

The wide variety of previous work on electrical machines with a complex 3D magnetic core is a relevant input to this thesis. First of all it is important to identify where the iron powder application is beneficial in electrical machines. The complexity of the multi-physic problem of electromechanics requires efficient methods in order to carry out fast and correct analysis that can consider the most significant phenomena. The following survey of previous work that inspires the design of powder core machines is arranged under the following guiding topics.

Electrical machines with complex 3D cores

There are two types of commonly used and well investigated electric machines where magnet core is subject to 3D magnetic flux – the Lundell alternator [66] and the stepper motor with a TFM claw-pole structure [53]. The latter takes an advantage of electromagnetic sheet while in the claw-pole structure of the Lundell alternator a solid iron is used. With solid iron, the eddy-current distribution in the claws, which depends on material purity and operation speed, and mechanic stress due to centrifugal forces are especially important in order to determine the possible use for SMC. The most common type of Lundell alternator includes slip rings but these can be avoided by using the an additional magnetic coupling and stationary coils [22][27]. In design of a claw-pole rotor synchronous generator geometry optimization is used for improved electromagnetic output [37] or reduced noise level [13]. The goals of the structural-dynamic analysis are to study the electromagnetic stress distribution [85], the acoustic behavior and possibilities to reduce noise level [84]. Similarly, electro-dynamic analysis is mainly focused on eddy current problems and loss generation [52].

The claw-pole structure holds the excitation coil and is subject to a stationary field in the Lundell alternator [25]. On the contrary, the structure with the armature coil is subject to alternating excitation fields in claw-pole motors. The claw-pole structure is introduced in some miniature permanent magnet synchronous motors as a low-cost and competitive solution [24] [41] [92]. The design issues of the claw-pole motors are mainly related to the improvements on manufacturability [54], magnetic coupling and reduction of leakage [92], the cogging [43] and torque ripple, acoustic analysis and noise reduction [92], and integrated design [23] [24]. The rate of change of the exciting magnetic flux that enters into the claw-pole, which is a bended electromagnetic sheet perpendicular to the field, induces eddy currents, damps the field and generates

heat losses. The additional cuts [1] can be used in a claw poles in order to restrain the induced currents and to improve motor characteristics at the high frequency operation [92].

Iron powder application in electrical machines

From a motor construction concept point of view, the TFM, including claw-pole structure, is distinguishable from the other types of machines by a leading figure of specific torque [6] [44] [70]. TFM is a reasonable solution for electromagnetic conversion in the high-torque low-speed domain. As the machine torque is proportional to the pole number, the number of poles can be increased until it is magnetically and mechanically feasible for a certain radius [16]. Soft magnetic composites (SMC) are showing attractive features for such kind of machines. Most of the transverse flux machines have permanent magnet excitation, which is mainly in the rotor. It can be argued whether electrically magnetized SMC core is a reasonable solution together with permanent magnet excitation. The lower permeability of an SMC core asks for the higher current loading for the same gap induction. Furthermore, the increased reluctance of the core magnifies the influence of leakage flux paths. On the contrary, SMC core becomes attractive in the motors that operate in deep saturation such as universal motors. Due to the ability to create more compact motor the torque per volume can be improved [14][48].

Iron powder application in electrical machines leads to two approaches. The SMC can supplement the conventional electromagnetic sheets in order to improve manufacturability [54] or/and electromechanical characteristics. The other approach focuses on the compression molded powder core motors that fully utilize the advantageous and less attractive features of an iron powder core [15][45][82]. Generally, the low ability to conduct flux of a SMC core, the high static magnetization losses and the weak structural strength should be compensated with a high winding fill factor and a compact assembling, which leads to the good thermal contact and cooling capability. A higher operating frequency can be used as dynamic losses are considered to be small [40]. An advantage should be taken of the freedom while forming 3D iron cores that improves magnetic coupling, utilizes the concept of force/torque magnification and gives a good constructional integration [15] [49]. With the intention of reduce the production cost of the motor, it is advisable to use as few parts and as identical parts in the motor core as possible in order to increase assembly simplicity [48] [80]. Manufacturability is an important factor of machine design and for a low cost device the electromechanical performance have lower importance. Injection molded composite powder with

thermoplastic synthetic resin can be used to form an iron core and to increase integration of a stepper motor [41]. Basically, if the magnetic material can give the magnetic guidance so that the electromechanical conversion will be improved then it is reasonable to consider the use of the material in the machine design.

Analysis of complex 3D magnetic core

Complex electromagnetic devices need 3D field analysis that can be made analytically on the basis of magnetic equivalent circuit (MEC) [35][75][78] or 3D finite element (FE) analysis [28][30][32]. The combination of rough design model with MEC combined with 2D or/and 3D FE calculations can give good results and gives an opportunity to reduce the computation time [1] [36]. The magnetostatic field calculation is often used for obtaining the static characteristics and for geometry optimization. The correct field representation, the right force computation methods [29] and accuracy [42] of the obtained results have high importance while the computation time is to be minimized, especially, when the 3D core optimization and detent torque minimization is based on 3D FE analysis [43]. The analytical approaches and experimental work [20] are part of the optimization process that aims to find an optimal shape of the claw-pole structure. Flux density variation in an isotropic SMC core, generally, causes field rotation and higher magnetization losses. The losses that are generated by the field alternation are smaller than the ones caused by the magnetic field rotation. Therefore, it is important to consider the origin of the losses when determining the loss coefficients [97] and evaluating the results [47]. For the sake of simplicity the dynamics of the complex 3D motor can be evaluated on the basis of static characteristics, which are obtained in 3D FE analysis [11].

Design of electrical machines

Design of electrical machines is an optimization process. The exhaustiveness of calculations and optimization methods is still to be improved in order to handle a complex multiphysical process of electromechanical energy conversion. It can be considered that the material development and manufacturability have the biggest influence on the machine design. At the same time the tools of efficient machine analysis and the correctness of calculation methods have a vital importance to the success of the machine design. Injection molded magnets with sophisticated shape and magnetization increases flexibility and integrity in the design of an electromechanical device [79]. An integrated drive design is increasingly one of the main design goals [23]. Integration leads to the need to consider several disciplines in physics

simultaneously. The design of electrical machines or the optimization process does not give a unique solution. Nevertheless, the objective of the process is mainly the improvements or savings that appears from the better material utilization, smaller consumption of energy, simpler low-cost production or/and a longer life span of an electromechanical device.

1.2 Objectives

The objective of this work is to study the feasibility with small-size SMC core claw-pole motors, the design, the analysis and some production constrains related to the motor. The armature coils are designed to be as simple as possible and the ferrous core accordingly complicated. Furthermore, the motor design aims for a construction, which allows good manufacturability and high utilization factors.

1.3 Contributions

The contributions of this work are given in Chapter 2 to 6 and concluded in Chapter 7. The main contributions are

- Claw Pole motor design methods for soft magnetic composite (SMC) and hard magnetic composite (HMC) materials with three different levels of accuracy and calculation speed:
  - EC. Equivalent networks are used for rough magnetic and thermal design. In addition, a 2D mechanical stress analysis tool is developed.
  - "Broadsearch". A broad parameter space is scanned systematically with low resolution FEA for improved design.
  - "Sensitivity". A narrow parameter space is scanned systematically with high resolution FEA for refined design.
- A Software environment for automatic design. In this thesis a software environment is developed that provides a high degree of automation to the design process involving Matlab, Vector Fields /Opera, FEMLAB and to some extent JMAG Studio.
- FEA calculation accuracy estimation that is focused on 3D FE mesh quality.

- Analysis on the influence of various magnetization patterns in the permanent magnet rotor on the coupling torque and cogging torque.
- Two prototypes produced and evaluated. A four pole one phase and a 20 pole two phase claw pole motor, both with outer rotors are designed, built and evaluated.
- Claw pole drive control, with and without position sensor. A complete dSpace based control system for both machines is developed. In addition, the control system for the two pole one phase machine is designed to start and run without position sensor.

1.4 Outlines

The first part of this work presents the topology of the magnetic circuit and the mechanical construction of a claw-pole machine concept. Motor parameters are evaluated and design preferences are discussed in Chapter 2. The next chapter focuses on the analytic design model of the selected claw-pole motors. Simple magnetic and thermal equivalent circuits have been derived and a design optimization is presented in Chapter 3. A rough size of the motor is a subject to the extensive numeric field analysis. The model formulation for the different disciplines in physics is worked out in Chapter 4. A series of 3D FE calculations has been made and some static characteristics of the machine are presented in order to validate the analytical models. The importance of numeric field computation is to provide more accurate field representation and to study the influence on the change of material properties and structure dimensions. The sensitivity study, the motor characteristics and their influence on small constructional changes are presented in Chapter 5. The main results of prototyping and the comparison between the static characteristics are presented in this chapter. The objectives of Chapter 6 are to specify the control strategy for the claw pole motors, to implement control circuitry and to carry out simulations and experiments. Motor dynamics is simulated on the basis of the static characteristics and proposed control circuits. For this purpose is used Matlab Simulink, and the same control circuits are implemented in dSpace. The work is concluded in Chapter 7.

1.5 Publications

The previous work on design of powder core motors is published in a number of conferences and workshop.

Reinap, A., Alaküla, M., "Design of a Claw-Pole Motor", International Conference on Electrical Machines IEMC'02, 25-28 August, 2002, Brugge, Belgium, 5 pp.

Reinap, A., Alaküla, M., "Study of a three-phase claw-to-claw pole machine", IEEE International Electric Machines and Drives Conference, IEMDC'03, June 1-4, 2003, Madison, Wisconsin, USA, 5 pp.

Reinap, A., Martínez-Muñoz, D., Alaküla, M., "Iron loss calculation in a claw-pole structure", Nordic Workshop on Power and Industrial Electronics, NORPIE'04, Trondheim, Norway, 5 pp.

Reinap, A., Alaküla, M., "Simulation and experimentation of a single-phase claw-pole motor", International Conference on Electrical Machines IEMC'04, 6-8 September, 2004, Cracow, Poland, 5 pp.

Reinap, A., Alaküla, M., "Simulation and experimentation of a two-phase claw-pole motor", International Conference on Electrical Machines IEMC'04, 6-8 September, 2004, Cracow, Poland, 5 pp.

Martínez-Muñoz, D., Reinap, A., Alaküla, M., "Comparison between three iron-powder topologies of electrically magnetized synchronous machines", International Conference on Electrical Machines IEMC'04, 6-8 September, 2004, Cracow, Poland, 6 pp.

Martínez-Muñoz, D., Reinap, A., Alaküla, M., "Comparison between four topologies of synchronous machines using SMC", invited paper, The UK Magnetics Society, Seminar on soft magnetic composites and their use in electrical machines, 16 November, 2004, University of Newcastle-upon-Tyne, UK, 7 pp.

Chapter 2

Construction of a claw-pole motor

Transversal flux machines that incorporate the claw-pole structure is considered as one of the most suitable machine constructions for iron powder application. The advantageous feature is that the transversal flux claw-pole machines allow high specific output. The high specific output is proportional to the number of poles and this leads to higher magnetization frequency. The core losses will be tremendous for the solid iron core due to induced currents. The core construction with claw-poles is not an easy target for electromagnetic sheets to restrain the eddy current loss. A compressed molded core of electrically insulated iron powder allows getting an isotropic magnetic circuit with very low eddy current losses than laminated steel. Even though the powder core is a poorer magnetic conductor and causes higher static magnetization loss, the minimized complexity and the higher packing factor of the winding compensates the less favorable features. The importance of this chapter is to highlight the main consideration for the machine design, to select and to specify the constructions of the claw-pole motors for the further study. The main motor dimensions, the sizing principles, the choice of materials and manufacturing methods are described below.

2.1 Motor Design

The important part of the design procedure is to present a reliable relation between the motor dimensions, the choice of materials and the electromechanical outcome. A most suitable (optimized) ratio between the dimensions and the output has to be found where the desired performance of

the proposed motor construction fulfils the electric, magnetic, mechanic and thermal loading conditions.

Claw-pole structure involved in electromechanical conversion

From a motor operation point of view, the current carrying solenoid in a claw-pole structure causes magnetic flux around the coil, which due to bended claws causes radial flux in the air-gap, influences magnetic field and applies force to the secondary part. From a power generation point of view, as there is magnetic flux that links with the coil, induces electromotive force and generates electric power, the current carrying coil counteracts with the excitation field and applies opposite force to the moving body. As a result of magnetic interaction, the magnetic forces between the permanent magnet excitation on the rotor and the alternating current in the armature cause rotational motion. The applied magnetomotive force (mmf) appears across every pole. The magnetic flux passing claw-poles and the magnetic core is the result of current carrying coils and permanent magnets. Consequently, the size of these sources is determined by an allowable flux density and power loss density in the magnetic and electric circuit. The compromise between electric and magnetic loading is determined by the demagnetization risk of permanent magnet, temperature constraints of materials and cooling capability. The dissipation of losses is preferred to occur at natural cooling conditions.

Design goals and criteria

Previous research and experimentation of claw-pole motors has shown that these kinds of motors can be successful in miniature scale. The design goal is to construct a small-scale claw-pole motor that combines the advantages of the SMC and TFM concepts. Even though an ability to produce higher torque due to larger gap radius and a capability of excitation field concentration can be seen towards inner radii, the main purpose of using an outer-rotor concept is related to the mechanic coupling with application. A plastic bounded magnet-ring with lateral polar magnetization along its inner periphery is selected for a TFM with claw-pole structure. The single-piece magnet with a sophisticated magnetization pattern simplifies the construction of the rotor. The additional design goals are manufacturability and cost-effectiveness.

Two different claw-pole motors are designed. A single-phase claw-pole motor is designed for a medium speed drive while another two-phase claw-pole motor is designed for low-speed high torque drive. Both motors should be able to give a certain mechanic output inside a well defined volume. The preliminary sizing of the motor can be done according to the torque density

and the used type of magnet excitation. Alternatively, the size of the motor can be calculated according to the shear stress of the claw-pole motors, which is around *200 kN/m²*. Apart from the specified electromechanical output, it is important that the electromechanical conversion is as efficient as possible. The main requirementss show (Table 2.1) that the two-phase claw-pole motor suppose to give five times more torque from three times smaller volume than the single-phase claw-pole motor. On the contrary, the single-phase claw-pole motor is supposed to deliver torque at high speed.

Table 2.1: The main requirements to the TFM with claw-pole structure.

Claw-pole motor	Inner radius, mm	Outer radius, mm	Height, mm	Torque, Nmm	Speed, rpm	Torque density, Nm/dm^3
Single-phase	-	24	25	10	4000	0.22
Two-phase	21	32	8	50	-	3.41

A single-phase claw-pole motor

Single-phase permanent magnet (brushless dc) motors are likely to be adopted for many low cost applications. An application that requires constant speed at the speed range of a few thousand revolutions per minute gives preference to an exterior-rotor motor. The outer-rotor gives higher inertia and smoothes torque pulsation. A low-cost single-piece magnet is chosen that has the same

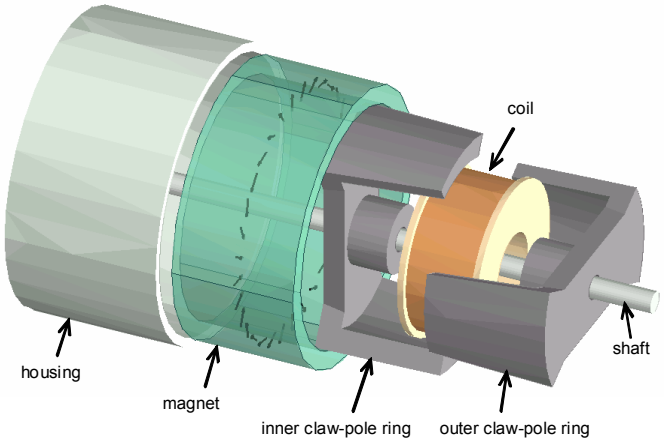

Figure 2.1: Structural view of a single-phase claw-pole motor.

number of poles as a claw-pole stator. The construction of the outer-rotor claw-pole motor is shown in Figure 2.1. The leading edge of the claw-pole has a narrower gap than the lagging edge so that the progressive radius of the single claw-pole creates a difference between the resting positions of the non-excited and excited motor, and thus causes a starting torque. This leads to the drawback that the opposite claw-pole rings are not identical and they have to be manufactured separately. The single-phase claw-pole motor is designed for a high-speed application, where the load is a function of rotating speed and has a large inertia. The single-phase claw-pole stator counteracts with the outer four-pole rotor and has to build enough torque in order to accelerate the system. At the same time, it has to overcome friction losses and to give the output torque needed.

A two-phase claw-pole motor

A two-phase claw-pole motor is designed for a low-speed high-torque servo drive. The same TFM claw-pole construction is used in the stepper motors as a simple and inexpensive solution. As the machine torque is proportional to the pole number, and the eddy current losses have to be considered at the operation speed chosen, then the use of SMC becomes relevant for this motor.

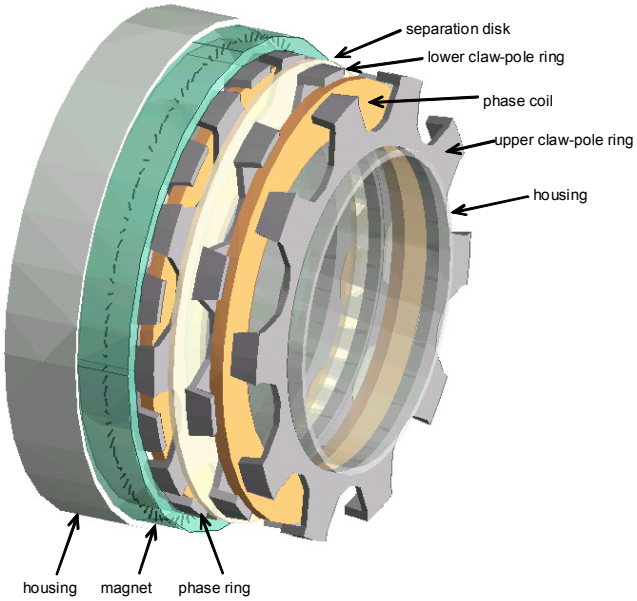

Figure 2.2: Structural view of a two-phase claw-pole motor.

The claw-pole motor consists of four identical claw-pole rings and an outer-rotor permanent magnet excitation ring. A single-piece plastic bounded compression molded magnet with two different magnetization patterns is studied. One magnet-ring has lateral multi-polar magnetization pattern without back yoke and the other magnet-ring is radially magnetized magnets inside a ferrous ring. The phase ring offers high pole numbers with a very simple axially directed hoop coil and pole system. The pole system contains two claw-pole rings made from a compression molded SMC that interlock the hoop coil. The claw-pole ring has U-shaped cross-section in the rz-plane and one claw per angular width of a single pole-pair on the outer diameter. Claw-pole motors have poles of opposite polarity close to each other, so they tend to have a large stator leakage inductance. This puts a limitation to high number of poles in certain radius, though high number of poles enables higher torque. The two-phase machine has two phases each made of two claw-pole rings. The angular shift between phases is $\pi/2$ electrical degree. Between the claw-pole rings a material has been used, which separates the claw-pole rings and gives an axial shift. It is necessary to add an axial air-gap between each single-phase stator in order to avoid magnetic short circuits and to reduce the magnetic coupling between the phase windings. A cross-section of the motor is shown in Figure 2.2. Due to relatively low speed and low duty cycle, the use of stator and rotor sliding surfaces is one of the possible methods in order to achieve the mechanical support system or bearings.

Parameterized model

In order to describe the size and the layout of the outer-rotor claw-pole motor, the construction and the corresponding parameterized dimension are shown (Figure 2.3). The symmetric part of the claw-pole motor with N_p poles is shown, where the outer magnet ring and its' magnetization pattern is visualized in the radial/circumferential (r-θ) plane. Three distinctive ferrous parts in the claw-pole ring are distinguished: the tapered claw-pole(s), the flank of claw-pole ring and the bottom of claw-pole ring. The claw-pole sharper top than the bottom, which is connected to a flank, is determined by an axial and circumferential tapering, respectively γ_2 and γ_1. The latter forms the trapezoidal shape of the claw-pole. The radial thickness of the pole is thinner in the top and thicker bottom, where the pole joins to the flank. The difference is determined by the height of the pole h_p and the axial tapering angle γ_2. The pole length and the space between the adjacent poles are defined by an angle γ_0. This angle is calculated from the pole pitch $2\pi/N_p$ and the relative space K_p between the adjacent poles. The claw-pole in a certain gap radius of r_i+l_p has flux concentrator effect. Ideally, the flank and the base core operate in the

maximum magnetic loading conditions. The angle γ_3 defines a constant cross-section area of the flank until radius r_{s2}. At the lower radius the flank is expanding gradually in circumferential direction and joins with the base core and the neighboring flank with the same magnetic polarity. The axial thickness of the flank is h_f and this defines the slot opening for the axial winding. The radial thickness of the base core is l_b. The size of the single claw-pole ring is determined by the inner radius r_i, the axial height h_p and the radial length l_p of the claw pole structure. The air-gap width and the size of the rotor are defined by the thickness of the magnet-ring l_{pm} and the thickness of the housing cylinder l_y.

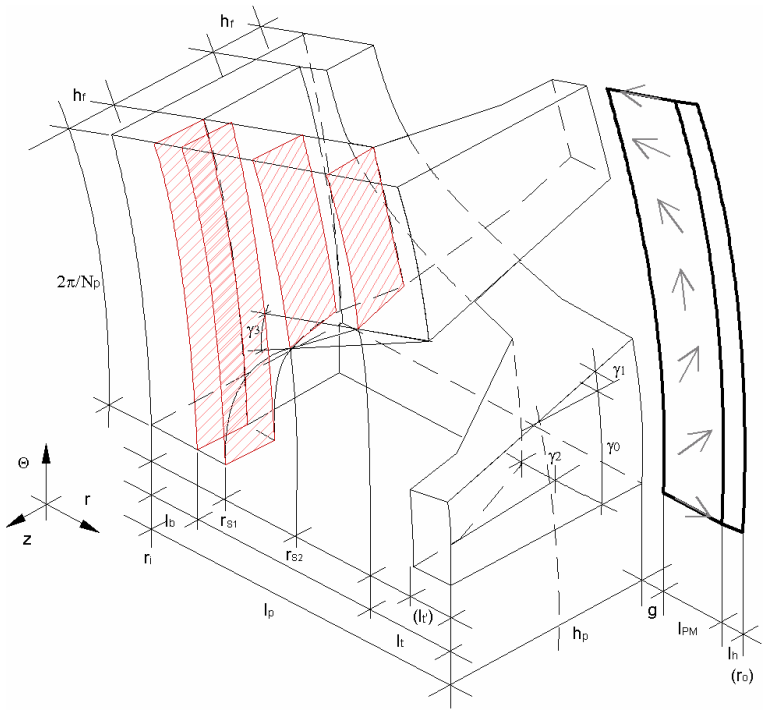

Figure 2.3: Parameterized model of a claw-pole motor.

The following parameterized dimensions are necessary in order to describe fully the structure of a half of pole-pair of the single phase claw-pole core. In order to describe the claw-pole structure it is reasonable to divide the 3D geometry into sectors (θ=const), levels (r=const) and layers (z=const) (Appendix B).

2.2 Phase ring made of claw-pole rings

This section describes the geometry formulation that is implemented later in 3D FE preprocessing (Appendix B). Additionally, some sizing considerations and selection criteria are discussed.

Axial tapering vs. circumferential tapering

The purpose of the claw-poles is to lead the magnetic flux from the radial/circumferential plane in the air-gap to the axial/circumferential plane that is perpendicular to the axis of the coil. For the evenly loaded claw-pole the increment of claw-pole surface in axial direction supposed to be equal to the cross section area that increases in radial direction (Eq. 2.1).

$$\int_0^z r_g(\theta + d\theta)dz = \frac{1}{2}\int_{r_g - r}^{r_g}\left[r_g^2 \cdot (\theta + 2d\theta) - (r_g - r)^2 \cdot (\theta + 2d\theta)\right]dr \qquad (2.1)$$

The axial sharpening that reduces the thickness of the claw-poles along the axial direction is defined as an axial tapering. The peripheral angle, which forms the trapezoidal sharpening of the claw-pole, is called circumferential tapering. From a magnetic loading point of view, the best material utilization will be achieved if the claw-pole has the same magnitude of the flux density everywhere in the iron core. On the contrary, from easy manufacturability that considers simple processing and safety it is advisable not to introduce axial tapering unless it gives significant improvement.

Pole width

The space between the adjacent claw-poles has been determined by the ratio *(1-K_p)* of pole width to pole pitch. A smaller space between the poles (pole clearance factor K_p) leads to the higher leakage between the adjacent poles. At the same time a larger claw-pole area allows higher torque.

The construction of the motor is formulated as a three dimensional matrix where the first dimensions divides a symmetric part of the motor to four sectors. The angles of the sectors or the radial/axial (r-z) planes that define the claw-pole formulation is as follow,

$$\theta(j,k) = \left[0 \quad \frac{1 - K_P(j)}{2} - \theta_P(j,k) \quad \frac{1 + K_P(j)}{2} - \theta_P(j,k) \quad 1\right] \cdot \frac{2 \cdot \pi}{N_P} \qquad (2.2)$$

Five levels will be defined in order to distinguish the specific parts of the claw-pole structure along different radii. The sixth level or the axial/circumferential (z-θ) plane is the air-gap of the motor. For the sake of clarity no levels from the rotor side has been shown in the vector of the second dimension (Eq. 2.3).

$$r(i,k)=\begin{bmatrix}0 & l_B & l_B+l_F(i) & l_P-l_T(k) & l_P & l_P+g\end{bmatrix}+r_i \tag{2.3}$$

The third dimension (Eq. 2.4) separates the different media along z-axis. Four layers or the radial/circumferential planes (r-θ) are necessary to complete the shape and to specify the media of the claw-pole structure.

$$z(i,j)=\begin{bmatrix}0 & h_F & h_P-h_F & h_P\end{bmatrix}-\frac{h_P}{2} \tag{2.4}$$

A circumferential and an axial tapering determine the shape of the claw-pole. The shape of claw-pole in the axial/circumferential (z-θ) plane where the top of the pole is narrower than the bottom and forms the shape of trapeze in the direction of z-axis is defined as a tangential (circumferential) tapering (Eq. 2.5). The symmetric trapezoidal pole face is formulated by changing the coordinate of the sector while the coordinate of the layer remains the same.

$$\theta_P(j,k)=2\cdot\arcsin\left(\frac{z(k)\cdot\tan(\gamma_1(j))}{2\cdot r(j)}\right) \tag{2.5}$$

The width of the flank along the circumferential direction (Eq. 2.6) is defined to have a constant cross-section area or even progressive area towards the base of the core and the axis of rotation.

$$\theta_P(2,4,1)=\arcsin\left(\frac{r(5)}{r(4)}\sin(\theta(2,5,1))\right) \tag{2.6}$$

The claw-pole structure is formulated so that the dominating magnetic leakage appears between the claw-poles.

Air-gap asymmetry

A single-phase armature core in a rotating electric motor is not able to produce electromagnetic torque at two positions over a magnetization cycle. The nonexistent electromagnetic torque occurs at the positions of electro-mechanic equilibrium. In order to get the single-phase motor started, the electromagnetic torque has to be different from zero at all stable resting positions of the rotor. This is possible either ways where the stable equilibrium point of the

electrically non-excited motor occurs at an unalignment position [87] or when it is shifted by a dissymmetry angle from an alignment position [5]. In the first case the stable position of a cogging torque component is at the same position as the maximum of the electromagnetic torque component. The cogging (detent) torque is a no load reluctance torque due to a presence of rotor magnet(s). In principle, a smaller magnetic reluctance causes the rotor to turn to a position where the flux linkage of the armature coil becomes the smallest. If the first case is applicable for a symmetrical structure $(R_{transversal}>R_{circumferential})$, then the other case bases on a magnetic or mechanic dissymmetry $(R_x>R_y)$. A dissymmetry angle, which is an angle between resting positions for the electrically excited and non-excited machine, can be achieved in different ways introducing an asymmetry in the air-gap. A progressive radius of a pole causes an air-gap tapering along circumferential direction and a different gap width at the pole edges. Alternatively, a stepped or a slotted pole, an incomplete pole or any other mechanical dissymmetry reasons the different stable equilibrium points of the magneto-mechanic system [5]. Whether the dissymmetry is introduced or not, the single-phase motor with the starting torque capability is able to accelerate at the desired direction of rotation [87][5].

In a single-phase permanent magnet motor the cogging torque is an essential characteristic. Nevertheless, the cogging or detent torque has to be small but at the same time as a torque needs to be present, which leads the rotor to the stable resting position. A large magnetic or mechanic dissymmetry leads to higher cogging torque. Usually, it causes higher air-gap reluctance and reduces the electromagnetic coupling torque. In the case of high pole numbers the dissymmetry and the cogging torque are increased. For sake of minimum cogging torque, the poles with progressive radius that causes tapered air-gap in the circumferential direction are preferred [5]. Furthermore, carefully selected pole dimensions and permanent magnet excitation lead to cogging torque reduction or/and improved starting conditions with symmetric air-gap [87].

It is practical to use a finite element (FE) method in order to predict air-gap permeance as a function of angular position for some complicated asymmetric air-gaps [35][36]. The air-gap permeance evaluation bases on an idealized flux penetration through the gap where the complexity of the geometry is reduced to a minimum. The difference in magnetic vector potential is introduced on the periodicity edges of a single pole pitch length of gap region (Figure 2.4). Neumann boundary condition is introduced on all the other boundaries. These boundary conditions let to describe the flux penetration and the magnetic coupling through the gap. The shape of the flux tube determines the air-gap permeance per unit of length that is perpendicular to the plane (Figure 2.4).

The permeance *P(θ)* is calculated according to the magnetic flux *Φ(θ)* passing the cross-section area *A(θ)* of the flux tube, the average length *l(θ)* of the flux tube and the field intensity *H(θ)* in the tube.

$$P(\theta)=\frac{\mu_0 \cdot A(\theta)}{l(\theta)}=\frac{\Phi(\theta)}{H(\theta)\cdot l(\theta)} \tag{2.7}$$

This assumption is true when the soft ferromagnetic materials that surround the gap region are infinitely permeable. If the magnetic potential is defined to the whole side then only the coupling permeance is defined (dark equipotential lines). On the contrary, if a magnetic potential is given to the corner nodes, which is in the cross section of the gap outer radius and the periodicity line, then the leakage component is taken into consideration (light equipotential lines) (Figure 2.4).

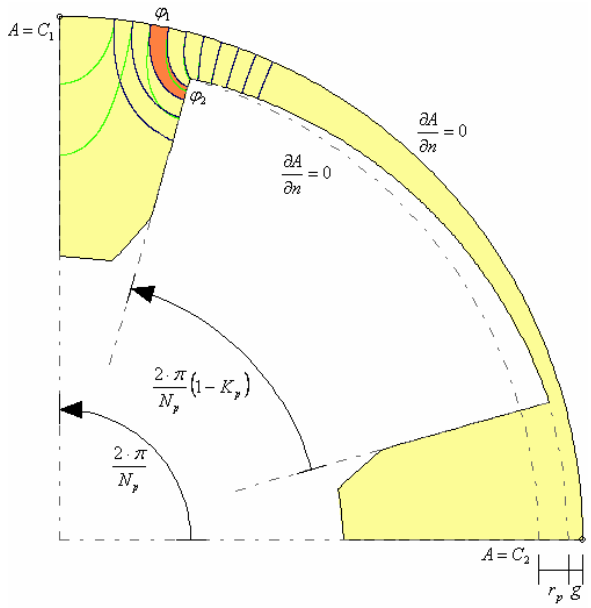

Figure 2.4: Air-gap permeance calculation and model formulation for 2D FE analysis.

As the reluctance torque is the outcome from this magnetic flux that couples with a magnetic conductor, then only the coupling air-gap permeance is considered [74]. This may give slightly wrong answers due to the permeance overestimation at the pole sides. An inner stator pole of a four-pole motor is considered as an example. The pole length is 0.65 of the pole pitch, the outer gap radius is 17.925 mm and the gap width *g* is 0.5 mm. The ultimate

subtraction r_p of the gradually reduced pole radius is selected from the range of 0.0, 0.2, 0.5, 1.0, 2.0 and 5.0 mm. The gap permeance is normalized according to the maximum value of 7.91 ·10-7 Vs/A (Figure 2.5).

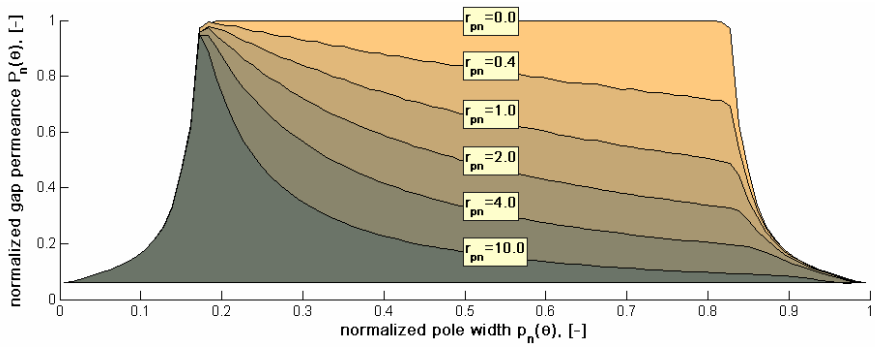

Figure 2.5: Air-gap permeance as a function of progressive radius. The ultimate subtraction distance r_p is normalized in respect to the air-gap length g.

The cogging torque can be calculated from the rate of change of mechanical work. The supplied mechanical work, which is negative, into the closed linear system equals to the change of stored magnetic energy (Eq. 2.8). In the ideal magnetic core there is no magnetomotive force drop considered and the magnetic energy in the air-gap can be calculated according to the magnetic scalar potential $\varphi_1(\theta)$ specified by a magnetic excitation [74].

$$T = \frac{\partial W_m(\theta)}{\partial \theta} = \frac{1}{2} \cdot N_p \cdot \sum_{gap} (\varphi_1(\theta))^2 \cdot \frac{\partial P(\theta)}{\partial \theta} \tag{2.8}$$

The corresponding magnetic equivalent circuit is drawn (Figure 2.6) on the left side and the reflection in the right side represents the closing path of the magnetic flux. A symmetric part of core, which is a single pole-pitch, is selected for the torque computation. The symmetry line φ_0 represents the excitation position relative to the stator geometry and gap permeance. In order to calculate the cogging torque, the angular width of the magnet and the type of magnetization pattern have to be represented in the excitation function $\varphi_1(\theta)$.

$$\varphi_1(\theta) = \frac{B_n(\theta)}{B_R} \cdot H_C \cdot l_{pm}(\theta) \tag{2.9}$$

The excitation function (Eq. 2.9) is derived according to the normal component of the flux density $B_n(\theta)$ and flux path length in the magnet $l_{pm}(\theta)$.

In addition, the working point of the (linear) permanent magnet is defined according to internal leakage permeance [74] of the magnet and the gap permeance.

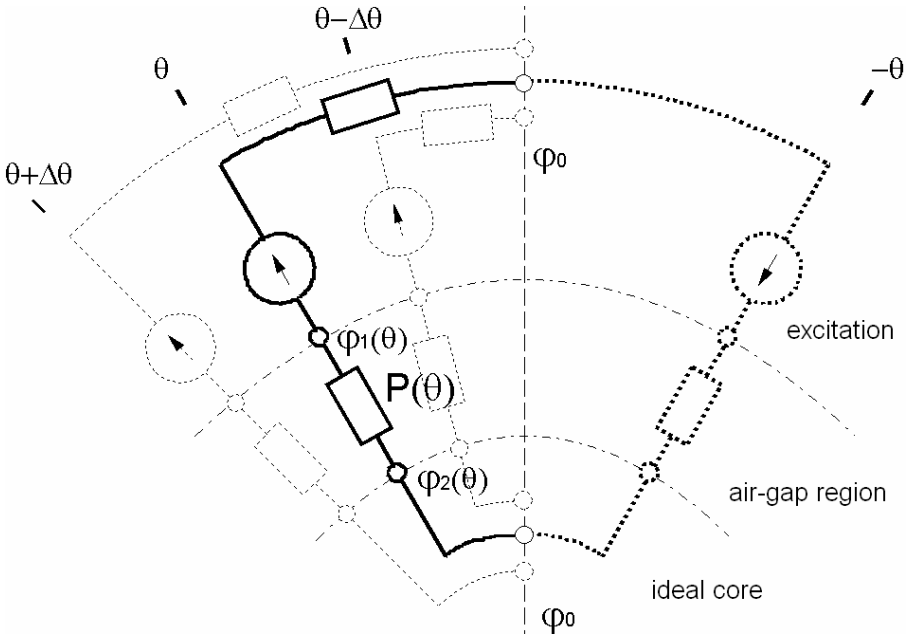

Figure 2.6: A simple permeance network for a complex shape air-gap and permanent magnet excitation. No mmf drop is considered in the core and the excitation function $\varphi_1(\theta)$ is defined by the internal leakage permeance and mmf source.

Multi-phase configuration

In order to get a continuous electromagnetic torque from a TFM, a multi-phase configuration with an appropriate angular phase shift is required. Apart from the angular shift, the phases and an axial displacement must be considered too. The small axial distance between the phases is essential for the autonomous operation of the adjacent phases and the prevention of a magnet short-circuits. The proximity of the neighboring claw-pole rings in different phases causes additional flux path and results in an asymmetric reluctance torque waveform [3].

A proper winding arrangement increases material utilization and/or reduces the amount of electronic switches needed to control the armature current and

field. Concentrated coils, which are conventionally used in powder core motors, give good constructional and functional advantages. Simplified coils allow higher filling factor, better cooling capability and higher thermal loading. It is important to consider the type of winding and the position of the start-strand and the end-strand in order to get the best assembling and packing factor of the winding. Thermal adhesive wire is used to wound a compact coils for the two-phase claw-pole motor. No other insulation than the strand coating is introduced. A bobbin with a wound coil is used in the armature of the single-phase claw-pole motor. The importance of the bobbin is to hold the wound strands in the place and to center the claw-pole halves.

The cost of power electronics is important factor for the low-cost device when the armature circuit is designed. The monofilar winding that is subject to bipolar excitation needs the highest number of electronically commutated switches. The bifiliar winding, which can be effectively used in single-phase motors [23], needs two switches to produce bipolar field with improved commutation characteristics. Only a single switch is needed to create monopolar field with a monofilar winding. A reduced number of switches lead either to limited controllability or to lower utilization.

2.3 Soft magnetic composite

The quality of magnetic conductive medium can be measured with its permeability and the specific loss. The quantitative parameter is the limit of magnetic loading – saturation. Lower permeability leads to a weaker ability of the magnetic material to conduct and shape the flux. This causes proportionally a higher leakage at the same value of field intensity and saturation compared to a high permeable iron core. Due to the core complexity in TFM, the flux path that supposes to couple with the ac-coil is relatively longer compared to RFM, AFM or CFM. Low qualitative parameters lead to low efficiency core and low quantitative parameter leads to a bigger core.

Physical properties of a powder core

The most advantageous features of SMC are that the magnetically and thermally isotropic material allows flux flow all in 3 dimensions and the electrically insulated particles restrain the eddy current flow in the material. The main important factors to consider are:

1. A compressed core of magnetic powder materials forms a distributed air gap system. The relatively low permeability of the powder core, which depends on binder, lubrication and compression techniques, makes the use of the core most appropriate for permanent magnet machines that are insensible of the small variation of permeability due to inhomogeneity, impurity or anisotropy [59]. Another type of machine where the maximum permeability is of less importance is a high magnetic field (saturated) driven motors such like the universal motor. The lower magnetic permeance of the core can be compensated with a larger cross-section area of the core.

2. The static core losses are twice as much as they are in conventional electromagnetic laminated steel. Static hysteresis loss is affected by impurity, grain orientation and internal strains. Heat treatment helps to reduce the mechanic strains and hysteresis losses up to 25% under the thermal limit for insulating coating [68]. The heat treatment of SMC+LB1 compacted core improves only material strength of the material and does not reduce losses in the core.

3. Selection of grain size influences the wall sizes and the domain where the eddy current takes place. Basically, smaller grains lead to smaller excess losses and to its poorer texture leads to higher hysteresis losses. Even though the eddy current losses in the electrically insulated particles are considered to be negligible small, the compression and the binder determines the bulk resistivity of the material and 'global' eddy current losses.

4. The weaker structural strength of the powder core limits the application of the SMC core at extensive mechanic loading conditions. The shape of the core part has to be designed according to the mechanic loading and maximum allowable stresses in the material. The practical limits are set to the aspect ratio (1:6) of a core part which is possible for successful compaction [68][90].

5. The uniaxial compaction allows using a number of levels along the compaction direction. For a more complex shape the compressed core needs to be machined with care [68] in order to get the final shape. The manufacturability of the compression molded powder depends on the binders used and compaction technique. From mechanic loading and post-processing point of view, the soft magnetic composite material is rigid and brittle and this limits the mechanic work with the compressed detail.

6. The constrained thermal loading is to be followed during the heat treatment of a SMC core and later during the exploitation time in the machine applications. It is important to keep the good electric insulation properties between the particles, which is essential for low eddy current losses and slow ageing [50].
7. The powder core motor will be most profitable for the high volume low cost applications, for the motor structures that is unpractical to make of conventional laminated steel or/and the core that operates at high frequency and otherwise suffers under extensive eddy current losses.

Choice of soft magnetic powders and manufacturing methods

There are a number of combinations (Table 2.2) between the soft magnetic powders for electromagnetic application, the binders and the possible compression-molding techniques. Different grades of iron powders with different particle size, shape, compounds and thickness of coating are suitable for different frequencies and magnetic loading [50][90]. The variety of resin additives and lubricants influences the particle insulation, compressibility and the mechanic and magnetic properties of the core. They are chosen according to the complexity of the core, the need for post-processing in order to get the final shape, the application orientation in magnetic loading vs frequency domain and according to the other properties emphasized. High compressibility and warm compaction increases the permeability and saturation induction. The addition of a binder attains higher strength. The heat treatment and purity reduces the strains and static core losses in the SMC core. It is important that the compaction process and the heat treatment allow getting a good homogeneous core with the low eddy current loss coefficient.

Table 2.2: Soft magnetic powders, binders, lubricants and production methods.

Magnetic powder	Lubricant/Binder	Production method
• Somaloy500 • Somaloy550 • ABM100.32	• Kenolube • LB1 • Resin additives	• Cold compaction • Warm compaction

The soft magnetic composite powder Somaloy 500 is selected for the motor construction. The press ready mix, which contains lubricating binder (0.6%LB1) (Appendix A), is selected to be treated under warm compaction process at 800 MPa+130°C and heat treatment at 275°C. This combination

gives higher strength [50][80][90] and improves post-processing, when the final shape of the claw-pole structure is formed. Using Kenolube gives a more brittle composite material, which is more difficult to tool. Generally, the SMC premix with 0.5% Kenolube is better adapted for the use in electromagnetic design purposes. It has a higher permeability and lower static core losses. The bulk resistivity is lower due to the higher filling rate [89][90].

2.4 Permanent magnet ring

Like the magnet cores are used to guide and to shape the magnetic flux, the permanent magnets are used to produce the magnetic flux. Therefore, one of the most important magnetic parameters of a permanent magnet is the ability to produce the magnetic flux – remanence [94]. The stability of the magnetic orientation in the permanent magnet material is determined by coercive force. The larger the coercive force, the greater the stability of the magnet and the less the magnetization is changed by a large external magnetic field. Apart from the external field, the factors affecting magnet stability is mainly temperature and reluctance changes. The shape of the magnet, magnetization pattern and assembling are the other important factors that designer should consider. Similar to the soft magnetic composites (SMC), the hard magnetic composite (HMC) has a great geometric flexibility. Similarly, the magnetic properties are reduced comparing to the full dense hard magnetic materials. The HMC is mixed into compound and then molded to give final shape and magnetization. There are a number of combinations (Table 2.3) between hard magnetic powder, a binder and a manufacturing process [77][94].

Table 2.3: Hard magnetic powders, binders and production methods.

Magnetic powder	Binder	Production method
• Hard ferrite • Isotropic NdFeB (quenching process) • Anisotropic NdFeB (HDDR)	• Flexible binder: rubber or elastomer • Rigid binder: thermoplastic resin	• Extrusion and calandering • Injection molding • Compression molding • Compacting and rolling

The magnetic properties depend on HMC powder, the grain size, and the filling rate. The latter depends on the type of binder and the production method. Typically the filling rate for injection molding is about 45-65% of total

volume and for compression molding about 75-85%. Usually, ferrite or NdFeB magnetic powder is used in bonded permanent magnet electrical machines [77]. The attractive feature of the ferrite magnet is low cost while the NdFeB magnet becomes preferred when the high magnetic performance is needed. From stability factors point of view, the ferrite magnets are less dependent on the change of temperature.

Plastic bounded magnetic materials allow magnets in complex shapes with a multipole magnetization. The single piece magnet-ring, which has circular polar magnetization (Figure 2.7), enables significant simplification in rotor construction and improves the static characteristics of the motors [96]. Even though the permanent magnet material is considered as the most expensive part in the electrical machines, the relative price reduction is introduced due to simpler production and assembling. As the magnetization distribution forms semi-closed paths inside the material, the use of back iron for return paths is unnecessary.

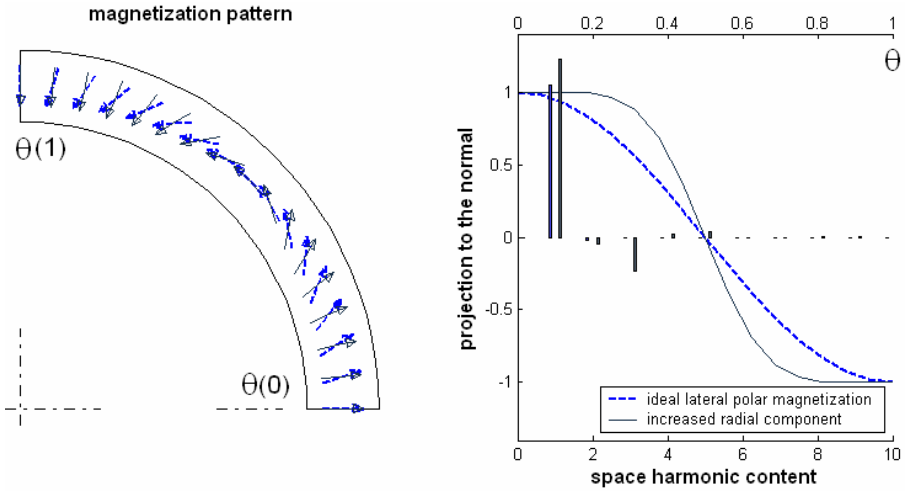

Figure 2.7: Magnetization pattern of a ring permanent magnet.

The magnetization vector describes how the material is magnetized. It can be interpreted as the volume density of magnetic dipole moments. The orientation of the magnetization vector inside a magnet-ring with an ideal lateral polar magnetization pattern can be expressed as

$$\beta(\theta)=\left(1+\frac{N_p}{2}\right)\cdot\theta \tag{2.10}$$

The orientation depends on the number of poles N_p and the lateral polar magnetization with increased radial component (Figure 2.7) is

$$\beta(\theta)=\left(1+\frac{N_p}{2}\right)\cdot\theta-\frac{\pi}{6}\cdot\sin\left(N_p\cdot\theta\right) \tag{2.11}$$

Basic problems of permanent magnet design revolve around estimating the distribution of magnetic flux in a magnetic circuit. This estimation should lead to the optimal amount of magnet material and to the optimal shape of the magnetization pattern. The optimal amount of magnet material is determined by the operating condition. The optimal shape of magnetization improves the waveform of induced voltage and reduces cogging torque, which is useful for designing high-performance motors with low torque ripple or to design good starting conditions for a single-phase motor [5]. Therefore, it is necessary to analyze magnetic fields taking into account the magnetization process of the multi-pole magnet-rings. The static magnetization method is modeled for the plastic bonded ferrite magnet.

Choice of hard magnetic materials

The choice of permanent magnet material considers the operation point of the magnet and the magnetic flux production capability B_R. The choice of magnetic material depends not only on the physical properties of material, the application conditions and the price but also on a required shape, magnetization and dimensions. While selecting a bonded permanent magnet for an electrical machine two main choices can be distinguished – compression molded isotropic quenched NdFeB or injection molded anisotropic ferrite. The best magnetic performance of ferrite material is achieved with lateral multi-pole anisotrophy where magnetization process takes place in the tool during molding. Compression molded magnets are isotropic, and therefore they are magnetized after molding. The compression molded magnets are normally restricted in applications to temperatures below 125 degrees, while the injection molded are used for the temperatures above.

The selection criteria are the magnet capability to magnetize an iron core for a selected number of poles and the price set by manufacturing and magnetization cost. As the higher remanence of the permanent magnet material is preferred, the types MQ1B and MQ1D are selected among MQ1 NdFeB bonded magnets. The lower coercivity makes these two magnets

attractive from magnetization characteristics point of view. Better saturation behavior is important in small magnets due to the space limitation for the magnetizer. The lower coercitivity is problematic with respect to magnetization stability. As the MQ1D magnet material has improved knee value and smaller dependence of the temperature changes, the material is finally selected [77]. Anisotropic ferrite with nylon 12 binder has been selected for the single-phase claw-pole motor (Appendix A). The design constraint is set by the size of an existing mold and an easy prototyping that in turn defines the inner and the outer radius of the magnet-ring and influences the size of the motor.

Magnetization pattern

When studying motor torque etc. in detail, it is necessary to analyze magnetic fields taking into account the magnetization process of the magnets magnetized with multiple poles. This section introduces an example of magnetic field analysis in which first the magnetization process of a bounded ferrite magnet-ring is simulated, then the magnetic field distribution from the permanent magnet is studied and compared to measurements. This study is necessary for characterizing the realistic magnetization distribution of a bonded magnet-ring.

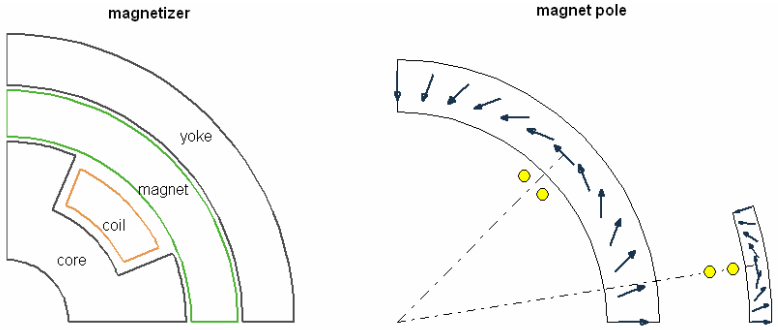

Figure 2.8: Layout of a magnetizer that is used in the study of the possible shape of the magnetization pattern in a magnet ring. Figure on the right shows a single pole of the 4-pole and the 20-pole magnet ring. A sensor coil is shown in proportions with the magnet-rings. The coil has 25 turns around a plastic holder that thickness is 1mm and length 20mm.

The model of the molding die of the magnetizer consists of a dc-coil inserted into a slot of a magnetic core [94]. The magnetic core forms the shape of magnetizing field. The influence of the slot width is studied with and without back yoke. The circumferential magnetizing field component compared to the

radial component is different depending on whether the yoke is absent or present. A single pole is considered. The FE model supposes to have enough air volume around the magnetizer in order to model properly the field distribution and not to suppress it with Neumann boundary condition or to expand it due to Dirichlet boundary condition.

The objective of magnetization is initially to magnetize a magnet to saturation [94], even if it will later be slightly demagnetized for stabilization purposes. Saturating the magnet and then demagnetizing it in a controlled manner ensures that the domains with the least commitment to orientation will be the first to lose their orientation, thereby leading to a more stable magnet. Unsaturated material, on the other hand, leads to orientation of only the most weakly committed domains that in turn leads to a less stable magnet. Anisotropic magnets must be magnetized parallel to the direction of orientation in order to achieve optimum magnetic properties. Isotropic magnets can be magnetized through any direction with small or no loss of magnetic properties. Slightly higher magnetic properties are obtained in the pressing direction. The magnetizing field strength about 800 kA/m is required in order to saturate ferrite magnet. In the magnetizer model the magnetizing current is 20 kA that gives current density in the conductor as high as 337 A/mm^2.

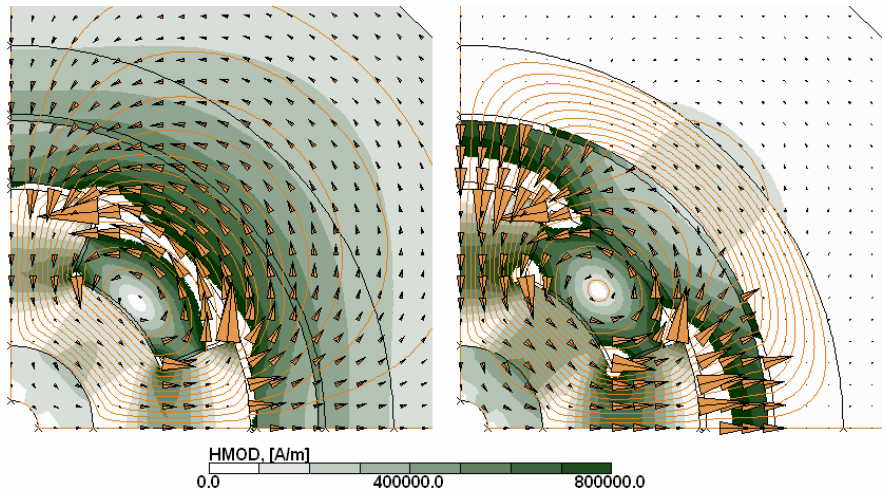

Figure 2.9: Magnetizing field of the magnetizer. The magnetizer consists of a slotted core where angular width is changed. The magnet-ring is placed on top of magnetizer and can be with solid iron yoke (right) or without it (left).

As a result from the magnetization analysis, the flux density vectors of each element *B(e)* in bonded magnet region are obtained. The anisotropic directions of the ferrite material are arranged to the same direction as external flux. Therefore the magnetization direction *θ(e)* is determined directly in each element (Eq. 2.12). The magnetostatic analysis does not consider the effect of the transient field, the field distribution due to induced voltages and eddy currents. For the sake of simplicity, according to the virgin curve the residual magnetization direction is assumed to remain the same as the peak of magnetization of the saturated magnet [51].

$$\begin{aligned} \theta^{(e)} &= \tan^{-1}\frac{B_y^{(e)}}{B_x^{(e)}} \\ M_x^{(e)} &= M_R^{(e)}\cos\left(\theta^{(e)}\right) \\ M_y^{(e)} &= M_R^{(e)}\sin\left(\theta^{(e)}\right) \end{aligned} \tag{2.12}$$

Depending on the structure of the magnetic core in the magnetizer, the preferred magnetization orientation can be achieved (Figure 2.10).

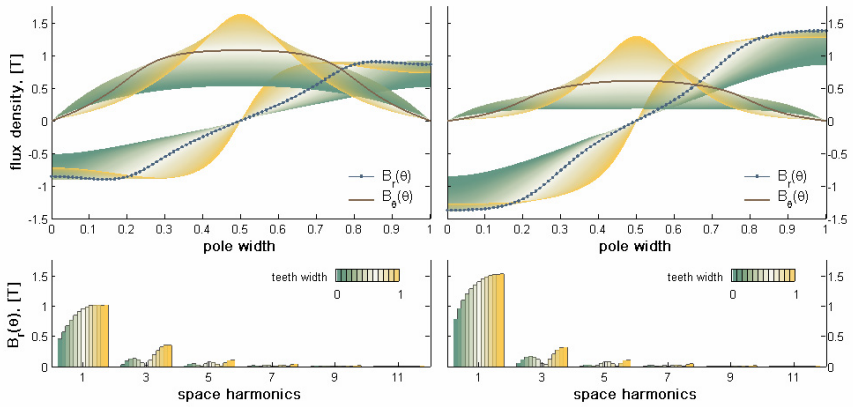

Figure 2.10: The flux density components inside the magnet-ring for the saturated magnet. By changing the angular width of the tooth in magnetizer the flux density distribution varies and it depends on whether the solid iron yoke is present (figures on the right) or not (figures on the left). The radial and the circumferential components of the flux density are collected along the circumference in the middle of magnet ring starting from vertical axis. The spatial spectrum of the radial component is shown depending on the angular width of the teeth that varies from 0 to 0.95 of pole pitch.

In reality, during the demagnetization process the magnetization direction in the material changes according to the easy direction. The magnetization direction, which is determined by the flux density distribution of the saturated magnets, is the initial condition for the study of the magnet ring. Alternatively the demagnetization curve is defined for the virgin curve and the magnetostatic analysis is started from the point of saturated magnet-ring.

The magnetic field distribution inside the magnetized magnet-ring is simulated and compared via the induced voltage in the measurement coil close to the magnet-ring. Depending on the structure of the magnetizer (Figure 2.9) and the magnetic field (Figure 2.10) of the saturated magnet, the field distribution of the magnetically unloaded magnet (Figure 2.10) and the field distribution near to the magnet (Figure 2.12) are calculated. The darker lines in the field position diagrams correspond to the construction of magnetizer shown. The right side of the figures belongs to the magnet with a dominating radial component, the left side with dominating circumferential component.

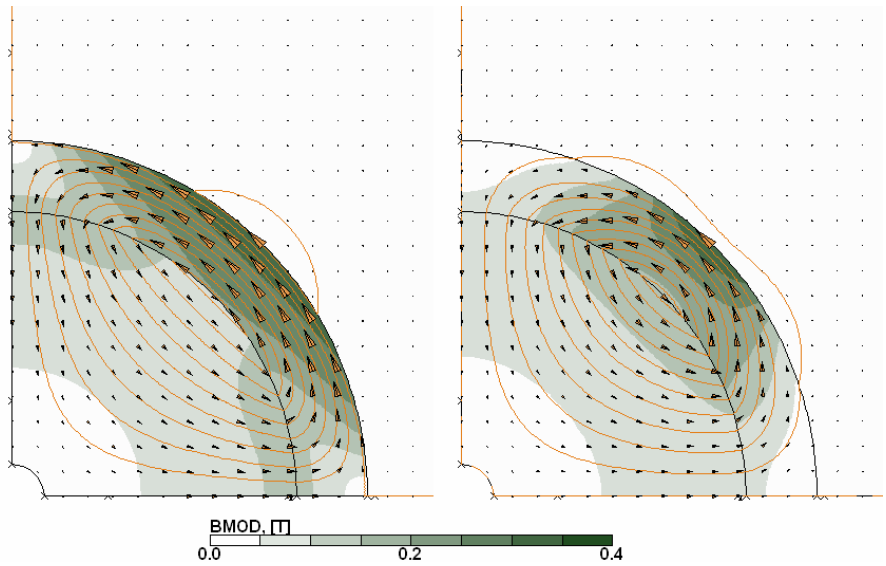

Figure 2.11: Magnetic flux density distribution of the magnet-ring. The magnet-ring on the left is magnetized without back-iron. The back iron is used to magnetize the magnet ring that is show in the right.

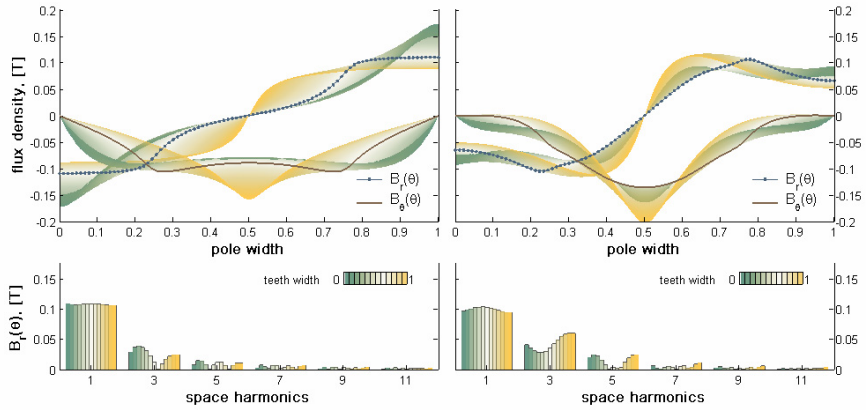

Figure 2.12: Magnetic flux density components inside the magnet-ring.

The evaluation of the realistic magnetization pattern is based on the estimation of the flux density distribution along the inner circumference of the magnet-ring. The spectrum of the integral of the measured voltage waveform is compared to the results from the FE calculations. The results show that the circumferential field component is more dominating compared to the ideal lateral polar magnetization pattern. The FE result that shows the same harmonic content in the gap specifies also the magnetization distribution in the magnet material.

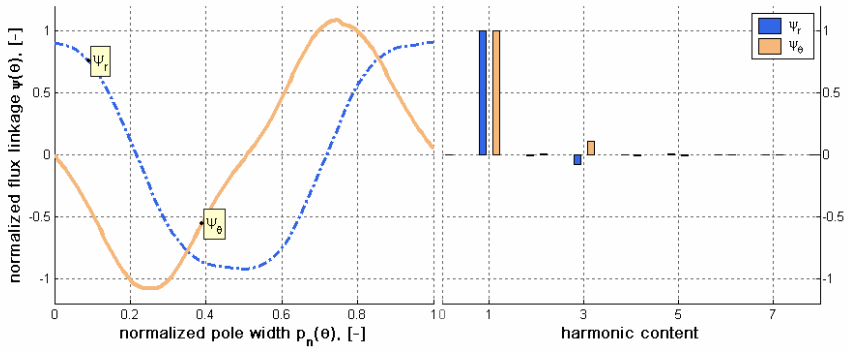

Figure 2.13: The flux linkage waveform is integrated over the averaged induced voltage waveforms (61.0Hz). The measurements are done for the plastic bounded ferrite magnet ring with circular polar magnetization. The measurements are normalized in respect to the magnitude of the fundamental radial ($6.07 \cdot 10^{-4} Vs$) and angular ($4.82 \cdot 10^{-4} Vs$) flux linkage components.

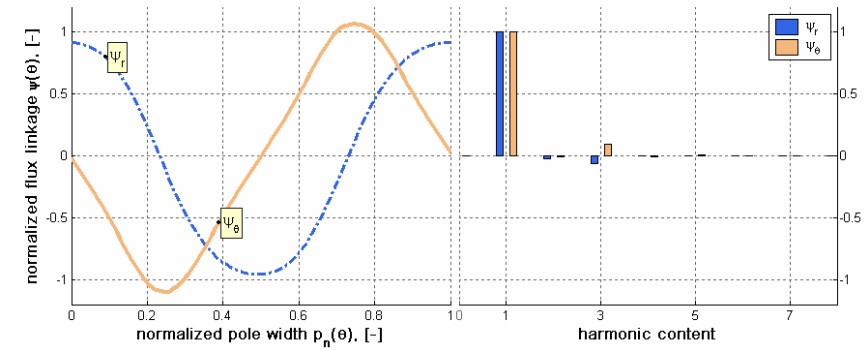

Figure 2.14: The flux linkage waveform is integrated over the averaged induced voltage waveforms (227.2Hz). The measurements are done for the plastic bounded NdFeB magnet ring with circular polar magnetization. The measurements are normalized in respect to the magnitude of the fundamental radial ($6.33 \cdot 10^{-4} Vs$) and angular ($8.35 \cdot 10^{-4} Vs$) flux linkage components.

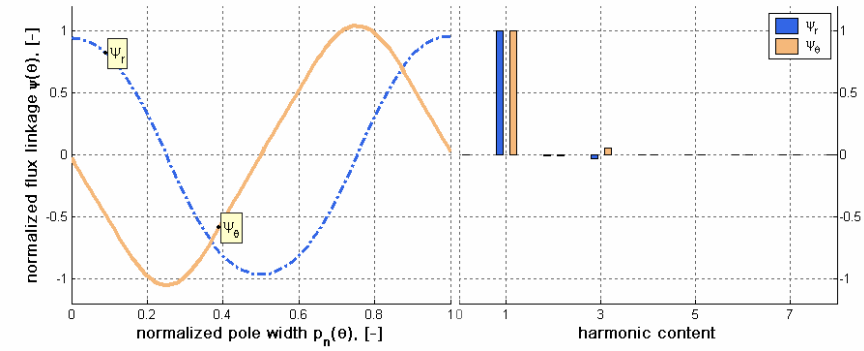

Figure 2.15: The flux linkage waveform is integrated over the averaged induced voltage waveforms (287.4Hz). The measurements are done for the plastic bounded NdFeB magnet ring with radial magnetization. The measurements are normalized in respect to the magnitude of the fundamental radial ($5.46 \cdot 10^{-4} Vs$) and angular ($7.45 \cdot 10^{-4} Vs$) flux linkage components.

The estimation of the gap flux from the induced voltage waveforms indicate that the circular polar magnetized and radially magnetized magnet-rings give rather similar field distribution in the surface of permanent magnet. The discrepancy between the analytical results and the experimental results complicates to estimate the real magnetization pattern present in the magnet-ring.

The size of magnet-ring

The size of the magnet affects not only the magnetic loading and motor characteristics but also the cost of magnet material. The radial thickness is determined by the number of poles and the angular length of poles [94]. The number of pole-pairs of the magnet-ring with lateral polar magnetization pattern depends on the inner radius of a ring magnet, the feasible magnetization and the length of air-gap. Small air-gap permits a larger number of poles. If the pole pitch is too small the flux will pass between the poles rather than through the air-gap. It can be expected that the magnetization vector form semi-circular rings inside the material (Figure 2.16).

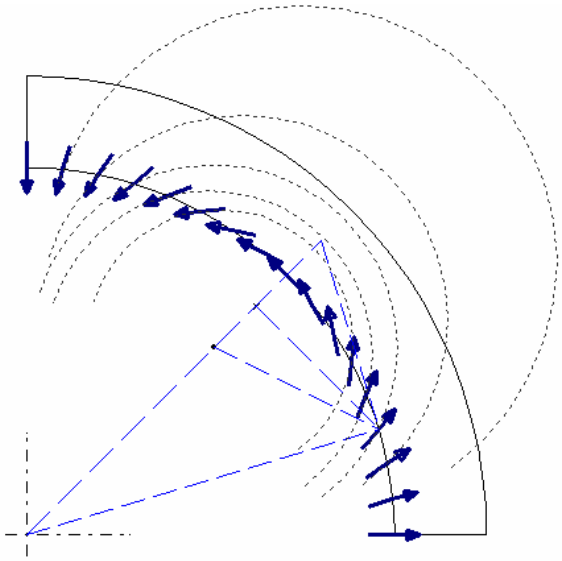

Figure 2.16: Graphical determination of the optimal radial thickness of a magnet-ring. The optimal thickness of the magnet ring, which carries circular polar magnetization, is a function of inner radius of the ring, number of poles, and a magnetic loading. The graphical determination of the semicircular flux paths is based on the assumption of the field distribution on the surface of the magnet-ring and the corresponding slope that forms a circle.

In reality the flux path inside the material can be different and it depends on magnetization process. In some cases (lateral anisotropy) the modeling is rather difficult since some of the flux exists on the backside of the pole. The advantage of using an axially higher magnet than the motor core is due to flux concentration. This is used in some small motors with ferrite magnet excitation [34].

Magnetization pattern influence on the motor characteristics

It is important to investigate the influence of the magnetization pattern to the motor characteristics according to the selected size of the claw-pole and the asymmetric gap region chosen. The reduction of the cogging torque is a critical design issue at high pole numbers. The preliminary study of the cogging torque waveforms is based on the air-gap permeance network and magnetization pattern introduced before (Figure 2.5, Figure 2.7). Instead of the magnet as a source of magnetomotive force, the linear magnetic characteristics are defined by the increment cross section area A, which is selected per unit of axial length, and the remanence B_R. It is assumed that the magnet-ring consist of a number of radially magnetized magnets along the periphery. Each magnet gives magnetic flux $\Phi_{pm}(\theta)$ (Eq. 2.13), which is the normal component of the magnetization pattern.

$$\phi_{pm}(\theta) = B_R \cdot A(\theta) \cdot \cos(\beta(\theta) - \theta) = B_R \cdot \Delta\theta \cdot r_{pm} \cdot \cos(\beta(\theta) - \theta) \tag{2.13}$$

The branch of the magnetic equivalent circuit includes a source of a magnetomotive force NI that belongs to a coil (Eq. 2.14), the coupling gap permeance $P_g(\theta)$ and the magnetic flux $\Phi_{pm}(\theta)$ source together with magnet inherent permeance P_{pm}. No leakage branches or magnetic flux flow in circumferential direction is considered.

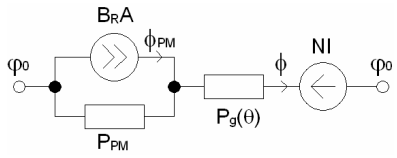

Figure 2.17: A branch of the permeance network for asymmetric gap and permanent magnet analysis.

The circuit can be described by the following formulation,

$$N \cdot I = \frac{1}{P_{pm}} \cdot (\phi_{pm} - \phi) - \frac{1}{P_g(\theta)} \cdot \phi, \tag{2.14}$$

where the inherent permeance of magnet P_{pm} is evaluated according to coercive force H_C, remanence B_R, the increment cross-section area A_{pm} of the (radial) magnet and the thickness l_{pm} of the magnet on the radial magnetization direction

$$P_{pm} = \frac{B_R \cdot A_{pm}}{H_C \cdot l_{pm}} \cdot \tag{2.15}$$

The cogging waveforms are calculated for a four-pole motor that has an axial length of about *20 mm*. Two different magnetization patterns (Figure 2.7) are compared to five asymmetric pole shapes (Figure 2.5). The ratio *r* shows the rela *Permanent magnet ring*) width. The torque waveform with *r=0* belongs to the symmetric poles and the characteristics starts and ends with stable equilibrium points $T_{cog}=0$ and $dT_{cog}/d\theta<0$. The rotation of magnetization pattern starts from unalignment position, where the pole of the magnet situates between the claw-poles.

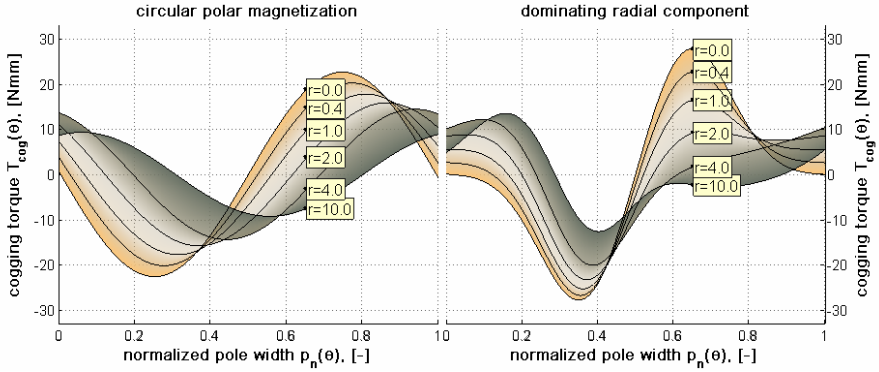

Figure 2.18: Reluctance torque in respect of the dissymmetry of the pole and the magnetization pattern of the magnet-ring.

Demagnetization

The magnetization of the magnet itself causes a magnetic field in the opposite direction to it. How far down along the demagnetization curve the magnetic flux moves will depend upon the air-gap size and the geometry of the magnet. A permeance coefficient, which is the ratio of the internal flux density to the internal demagnetizing force, is a slope that describes the demagnetization risk. The smaller the number the higher is the risk that the operation point under a static condition is shifted lower than a knee point and a flux loss occurs. Another important issue to consider is the irreversible flux loss due to the applied external field. The temperature and the permeance coefficient change when the operating point goes below the knee point. Below the knee point the irreversible demagnetization starts.

The internal flux Φ_D of the permanent magnet considering the external field and the magnetic circuit is expressed as

$$\phi_D = \phi_{pm} - \phi = \phi_{pm} \cdot \left(1 - \frac{P_g(\theta)}{P_{pm} + P_g(\theta)}\right) + \frac{N \cdot I}{P_{pm} + P_g(\theta)} \cdot \tag{2.16}$$

It is assumed that the magnetic flux Φ_{pm} of each increment of radially magnetized magnet is influenced of the armature mmf NI via coupling permeance $P_g(\theta)$ in the gap. The internal demagnetizing field H_D is evaluated from the internal flux and magnet linear characteristics (Eq. 2.16).

$$H_D = \frac{\phi_D}{P_{pm}} \cdot \frac{1}{l_{pm}} \tag{2.17}$$

The worst case during the magnetization cycle i.e. the rotation of magnet-ring occurs at the positions of low external permeance and the high opposing external field. The calculation results show the ratio of demagnetizing field intensity to coercive force for two different magnet rings at four different level of armature reaction. Instead of a permeance coefficient (B/H) of a magnet the depth of the demagnetizing field compared to the coercive force is shown (Figure 2.19). The calculation show "almost" the open circuit condition when the core is considerable far away and the shortest leakage path, which is fringing around the magnet sides, is about the same size as the flux linkage to the core.

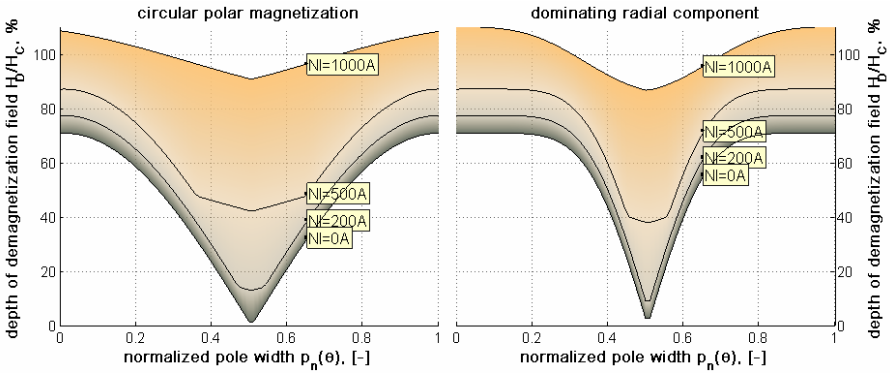

Figure 2.19: Depth of demagnetizing field for two different magnetization patterns at four different levels of demagnetizing field from an armature coil.

In reality, the influence of the external field is smaller due to different leakage paths. The opposite magnetic field caused by the demagnetizing current closes between the opposite claw-poles, and between the claw-pole and the adjacent flanks. The effect of the demagnetization of the outer magnet-ring is relatively small due to long flux paths through the magnets.

Chapter 3

Design model

Design model incorporates the main goals of motor design and formulates the motor performance according to the dimensions, sources and materials. The formulation bases on a set of simple equivalent circuits (EC), which describe the magnetic, mechanic and thermal behavior. The output from the equivalent circuit is considered as a rough estimation. Nevertheless, it is necessary that the equivalent circuits are able correctly to account for changes in the motor construction, and to give realistic results in a wide range of input variables. The purpose of the equivalent circuit is to give a rough estimate of the optimal relations in motor construction and sources according to the design criteria.

The equivalent circuit method is essentially a finite (FE) method. A set of 1D-elements describes the main flux flows, which appears under the set of sources and the boundary conditions. Basically, the EC of 1D-elements that describes the field distribution in a 3D-object differs from 3D FE of the element shaping functions and 'mesh' continuity. It is not practical to divide the 3D region into too many 1D elements. There are two practical reasons: firstly the 'meshing' time and secondly the inaccuracy to define flux paths, which remain the same when the change in the core structure or materials is introduced. Regardless of the low preciseness of field representation the important aspect of EC method is to evaluate the correctness of FE analysis and to improve the understanding of mathematic modeling in physics. The skilled user of FE analysis program is not necessarily a good analyst of results from FE analysis [56]. The EC method is considered as a simple FE analysis with a low number of 1D-elements, and which implements the same calculation principles and helps to understand the problem formulation in FE model.

One-dimensional heat flow, magnetic flux flow and elasticity problems are formulated according to conservation equation and constitutive relation at stationary conditions.

$$\frac{d}{dx}\left(A\lambda \frac{d\vartheta}{dx} \right) + Q = 0 \tag{3.1}$$

$$\frac{d}{dx}\left(A\mu \frac{dV_m}{dx} \right) + \Psi = 0 \tag{3.2}$$

$$\frac{d}{dx}\left(AE \frac{du}{dx} \right) + b = 0 \tag{3.3}$$

If the heat transfer problem describes the temperature ϑ distribution between a source Q and coolant (Eq. 3.1), then the magnetostatic problem specifies the magnetic potential V_m according to the flow of magnetic flux sources Ψ (Eq. 3.2). The displacement u is the unknown for elasticity problem (Eq. 3.3) with body forces b. The thermal and the elasticity problem are defined over an open chain that is defined by boundary conditions, while a closed loop according to a magnetic flux path specifies the chain for the magnetostatic problem. The ability to conduct flow in different media and physical problem are defied with thermal conductivity λ, magnetic permeability μ or elasticity E and the corresponding cross section A.

Magnetic (MEC), structural mechanic (SEC) and thermal (TEC) equivalent circuits are the main tools for the 3D iron core design. The rough optimization result is the input to more precise 3D-FE analysis. The 3D FE model enables to specify the field distribution more accurately and at the same time it gives accuracy verification to the analytical EC models.

3.1 Magnetic circuit

Often the magnetic equivalent circuit (MEC) has been introduced as a fast design model that is able to estimate the magnetic loading, force characteristics [74] and the optimal size of the core [16] [95]. Even though the model of 1D elements describing the 3D object is far from precise, the approximate sizing is enough to initialize the geometry for the further 3D finite element (FE) sensitivity study. In this thesis, the MEC method enables to model any claw-pole machine with an extremely low number of elements, and at the same time retains high computational accuracy [36][75].

Magnetic equivalent circuit

First of all, the MEC gives a solution to a magnetostatic problem. The problem is formulated over a symmetric part of a claw-pole motor. The motor construction is described as a set of magnetic conductive elements. These permeances are determined according to geometrical consideration that is based on knowledge of the direction of flux tubes. There are three types of elements: nonlinear core elements, which permeance depends on the magnetic loading, parametric gap elements, which depends on the position of the rotor respect to the rotor and leakage permeances. The latter can be also parametric. This is in case when the permeance of the flux leakage path depends on the rotor position. The importance of selecting flux paths and defining magnetic permeances is to determine geometrically the transversal coupling permeance and the direct circumferential leakage permeance. The latter includes all the parallel leakage elements that are coupled between the poles. Maximizing the ratio of the coupling permeance to the leakage permeance is of the crucial importance to the development of a claw-pole motor with high specific output.

There is a tradeoff between the accurate description of the core and the number of 1D-elements to be introduced. The influence of tapered claws and the geometric and magnetic formulation of the rotor can be correctly taken into account only in a three-dimensional magnetic circuit representation. Ideally, each flux path in the motor has to be represented by a permeance and source in the magnetic circuit considering geometry of the path and magnetic properties of the medium [74]. In order to obtain a proper permeance network in the claw-pole structure, the claws has to be divided into different zones along the axis of rotation, the number of which varies between two [35] and five [75]. Basically, the gap permeance has to be described along the circumference (Figure 2.5) and along the axial direction. The latter is the gap permeance along the circumference for a different pole length that describes the circumferential tapering. If the rotor structure is a concentric cylinder without saliencies then, when the rotor rotates, the shape of gap permeance that describes the magnetic coupling remains the same. The rotation of the permanent magnet excitation function defines the amount of flux that penetrates through the core and links with the coil. The main permeances over the symmetric part of the outer-rotor claw-pole motor are introduced (Figure 3.1). These permeances represent the flux linkage G_M through the core and the main leakage G_{ML} paths between the surfaces with difference in magnetic scalar potential.

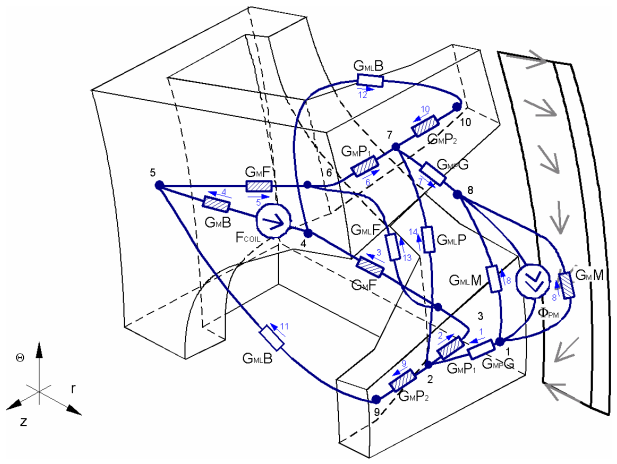

Figure 3.1: The simplified magnetic equivalent circuit.

The MEC is formulated according to the main flux path at no-load conditions [19]. The magnetic equivalent circuit has 18 elements (referred to *'e'* in Eq. 3.4) describing the main flux paths for the 3D core at the alignment position. The topology matrix (Eq. 3.4) is used to assemble the permeance matrix $\boldsymbol{G}$ [10].

$$M^{e}_{mec} = \begin{bmatrix} e & node_1 & node_2 & G^{e}_{m} \end{bmatrix} \tag{3.4}$$

Homogeneous bidirectional flux flow is assumed in a single permeance element G_{me}. These, as most permeance calculations, are based upon simplified equations of geometry and approximations of the effective length of the material. The results are, therefore, only approximate. An averaged formulation for the complete value of circuit reluctance is used (Eq. 3.5). The element is assumed to have the same base area A_{ie}, where the total length of the element considers the thickness L_{ie} of different material, its' permeability μ_{ie}, and the area variation c_{ie}.

$$G^{e}_{m} = A^{e} \cdot \frac{1}{\sum_{i=1}^{l} \frac{L^{e}_{i}}{c^{e}_{i} \cdot \mu^{e}_{1}}} \tag{3.5}$$

The node potential method is used to calculate the scalar magnetic potential, branch fluxes and magnetic loading for each element. The core elements (filled) are nonlinear and three leakage paths are considered in the core: the leakage between claw-poles *(P)*, between the flanks *(F)* and between the claw-pole and the bottom of the core *(B)* (Figure 3.1). The permeance model in the

air gap consists only of the sum of radial coupling permeances between the opposite stator and rotor poles. Alternatively, the permeance element can have a circumferential and a radial subdivision inside its sector without any response from neighboring regions. The flux transfer between the regions crosses at the borders of the regions [81].

The node potential method (Eq. 3.6) [74][95]states the relation between the permeance (stiffness) matrix $\boldsymbol{G}$, magnetic scalar potential (unknowns) vector $\boldsymbol{V_m}$ and magnetic flux input (load) vector $\boldsymbol{\Psi}$.

$$\mathbf{G}\mathbf{V}_\mathbf{m} = \boldsymbol{\Psi} \tag{3.6}$$

The value of the magnetic potential (Eq. 3.7) in each node point,

$$\mathbf{V}_\mathbf{m} = \begin{bmatrix} V_{m1} & \cdots & V_{mn} & \cdots & V_{m10} \end{bmatrix}^T, \tag{3.7}$$

depends on the magnetic source flux flow (Eq. 3.8) in to the node points,

$$\boldsymbol{\Psi} = \begin{bmatrix} \Psi_1 & \cdots & \Psi_n & \cdots & \Psi_{10} \end{bmatrix}^T. \tag{3.8}$$

The magnetic flux source Ψ, which is analogous to a current source in electric circuits, represents a permanent magnet [74]. The source flux inflow of a permanent magnet is connected to the same node point of the internal leakage reluctance of the magnet. An outflow or zero potential needs to be specified in the other node point of the internal leakage reluctance. The remanence B_R of the permanent magnet, the averaged radial magnetization per half a pole of the magnet and the cross-section area A_{pm} of the half magnet pole determine the value of the source magnetic flux (Eq. 3.9).

$$\Psi_1 = \int_0^{\pi/N_p} \Phi_{pm}(\theta) = \frac{2}{\pi} \cdot B_R \cdot \frac{\pi}{N_p} \cdot r_{pm} \cdot h_{pm} \tag{3.9}$$

The cross-section area is specified according to the axial height h_{pm} and inner radius r_{pm} of the magnet-ring. The averaged radial magnet has inherent permeability P_{pm}, which is defined according to the coercive force H_C and the radial thickness of the magnet-ring l_{pm} (Eq. 2.15). The leakage element G_{ML} between the magnet poles determines the magnet flux that passes the air-gap and the one which does not enter to the core. In order to consider the non-zero current in the armature coil the mmf source (Eq. 3.10) has to be added to the algebraic equations for the node points.

$$(V_{m5} - V_{m4}) \cdot G_{45} + \phi_{45} = -NI \cdot G_{45} \tag{3.10}$$

The magnetic saturation is taken into account (Figure 3.2) in nonlinear elements G_{ML}, where the new value of permeability is updated gradually. The permeability update bases on recent permeability value from the last iteration and on the new estimated value of permeability according to magnetization curve respect to the magnetic loading B [65].

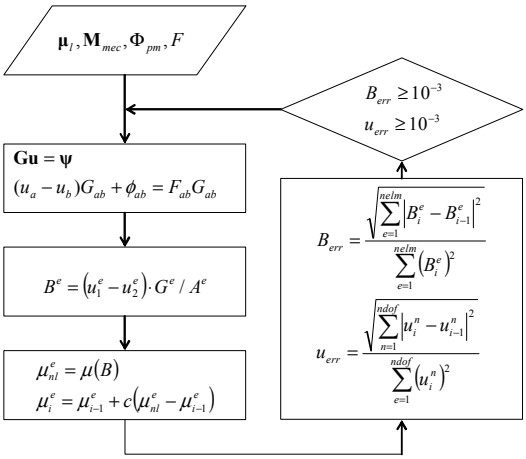

Figure 3.2: Iterative process flowchart for non-linear magnetic calculation.

If the sinusoidal flux variation is assumed at the bottom of the core

$$\phi = \Phi_B \cdot \sin(\omega t), \tag{3.11}$$

then the electromotive force can be derived

$$e(t) = -N \frac{d\phi}{dt} = -\omega \cdot N \cdot \Phi_B \cdot \cos(\omega t) \cdot \tag{3.12}$$

In order to get mechanic power, the electric loading is applied to the coil

$$i(t) = \hat{I} \cdot \cos(\omega t) = \frac{J_C \cdot A_S \cdot K_f}{N} \cdot \cos(\omega t) \cdot \tag{3.13}$$

The electromagnetic torque of the motor can be derived as

$$T_{em} = \frac{1}{2} \cdot \frac{\hat{E} \cdot \hat{I}}{\Omega} = \frac{1}{4} \cdot \Phi_B \cdot N_P \cdot J_C \cdot A_S \cdot K_f \cdot \tag{3.14}$$

The drawback of using MEC is that the EC analysis depends on motor configuration and the EC model reliability needs to be observed with a 3D FE model [95]. If the sources are modeled well then the simple MEC is able to predict magnetic flux accurately. Usually, the values of flux and flux density become overestimated, which is mainly due to the overestimation in the permeance formulation according to the shortest flux path through the average cross-section area. By changing the geometry of the claw-pole structure, some new unspecified flux path might appear or some element become more dominant. As a consequence, the accuracy diminishes and the whole EC model turns to be unreliable.

Forming static characteristics

The static characteristics of a claw-pole motor can be formulated according to the gap permeance and the magnetization pattern of a magnet-ring. This preliminary shaping of claw-pole relies on a number of assumptions and simplifications. If the radial magnetization component of a magnet-ring couples with an infinitely permeable core then the cogging torque waveforms can be evaluated for a claw-pole motor.

The dependence of the circumferential tapering on the cogging torque has been studied (Figure 3.3). The core of the single-phase four-pole motor has an outer diameter of l_p*=17.425mm*, the height of h_p*=20mm* and gap width of g*=0.5mm*. The pole clearance factor K_p, which is the ratio of the angular space between the poles to the pole pitch, is set to *0.3*. The circumferential tapering of the claw-pole shows small influence on the cogging torque. The difference becomes more distinguishable if the pole facet in the circumferential/axial plane shapes up as a triangle.

Mechanical energy is supplied to the magnetomechanical system in order to overcome the change of the stored magnetic energy in the air-gap (Eq. 2.8). The motor torque is against to the supplied work and this can be calculated approximately from the variation of magnetic co-energy against the angular displacement of the rotor. The calculated torque waveforms represent an ideal magnetic coupling, which corresponds to no load reluctance torque that a generator needs to provide.

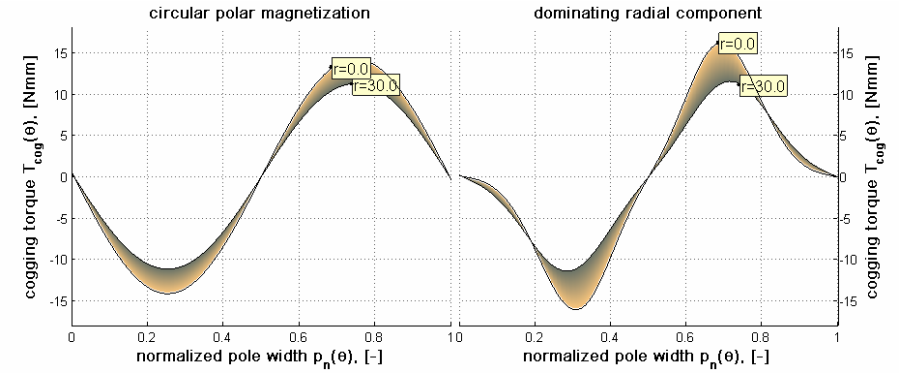

Figure 3.3: Cogging torque waveform of a single-phase core where the circumferential tapering γ_1 has been changed between 0 and 30 degrees.

The pole clearance factor K_p has a bigger influence on the static torque characteristics. The pole clearance factor has been changed between *0.3* and *0.7* (Figure 3.4).

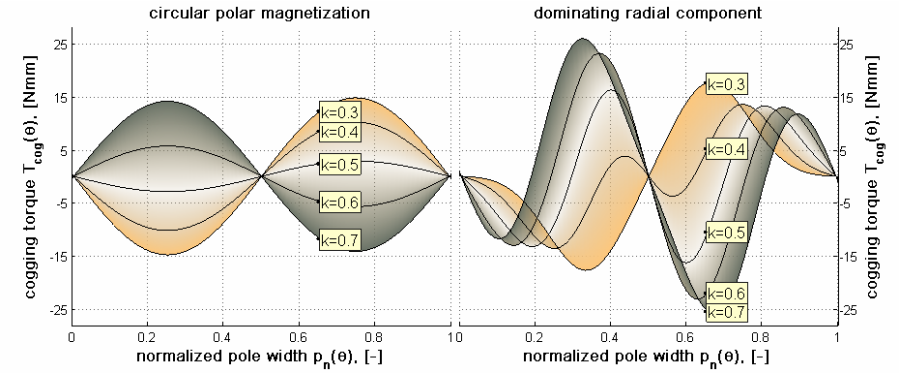

Figure 3.4: Cogging torque waveform of a single-phase core where the ratios of angular pole clearance to the pole pitch K_p are changed between 0.3 and 0.7 for two different magnet-rings.

When the angular width of pole becomes narrower i.e. the pole clearance factor is higher, the stabile equilibrium position co-aligns with zero electrodynamic torque at the angular position of *0.5* pole pitch where the magnet pole is in alignment with the core pole. If the angular width of claw-pole is half of the pole pitch or more then the stable resting position of the motor occurs at the position of maximum electrodynamic torque.

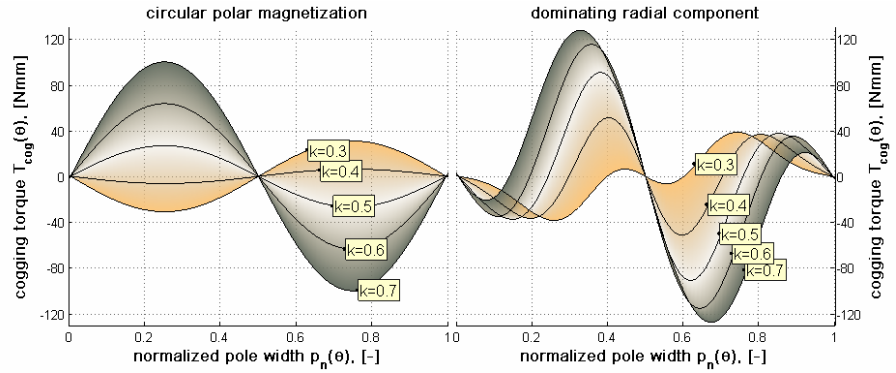

Figure 3.5: Cogging torque waveforms of a single 20 pole phase with claw-poles where the ratio angular space between poles to pole pitch k has been varied for two different magnet-rings.

Another claw-pole ring with the size l_p=*30.0 mm*, h_p=*3.6 mm* and gap width g=*0.25 mm*, is used in the two-phase claw-pole motor. As the claw-pole ring has a relatively high number of poles, it is important to reduce cogging torque. The pole clearance factor is varied between *0.3* and *0.7*. When the pole clearance is *0.4* or less, then the resting position of a single phase occurs at position of zero electrodynamic torque.

The axial height of the claw-pole is relatively small and that is why the circumferential tapering has insignificant impact on the static torque characteristics. If an additional claw pole ring is added with a phase shift with a half pole length then the cogging torque of the two phase machine peaks at *0.2 Nmm* with pole clearance of 0.6. The mutual flux between the neighboring phase rings is considered to be negligible here.

In order to consider the effect of the claw-pole core and magnetic saturation of the core structure, or the structures for multiphase construction, the existing MEC (Figure 3.1) needs to be extended to a more general case. Basically, a parametric non-linear permeance is added into a simple MEC (Figure 2.17). The value of this permeance changes together with position and magnetic loading. A new position of the rotor that is different from the pole alignment, causes the magnetic flux to the flow in the circumferential direction (Eq. 3.15) through the symmetric surfaces

$$\phi_\theta(r,\theta,z_0+z) = -\phi_\theta(r,\theta+2\pi/N_P,z_0+z), \tag{3.15}$$

where N_p is number of poles and z_0 is the coordinate of reflection surface.

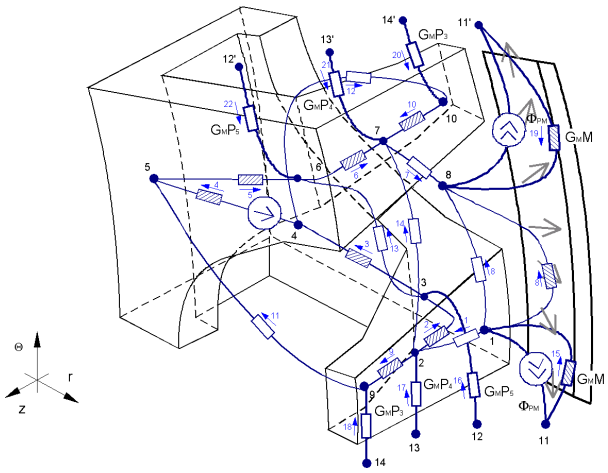

Figure 3.6: Permenance network at the unalignment position. The additional elements connect the corresponding symmetric surfaces.

The additional formulation that considers the periodic boundaries in the MEC model can be continued from the connection between nodes *14* and *14'*

$$G_{MP3}\cdot\begin{bmatrix}1 & -1\\ -1 & 1\end{bmatrix}\cdot\left(\begin{bmatrix}u_9\\ u_{14}\end{bmatrix}+\begin{bmatrix}u_{10}\\ u_{14'}\end{bmatrix}\right)=\begin{bmatrix}0\\ 0\end{bmatrix}. \tag{3.16}$$

For the sake of simplicity the equivalent position dependent gap permeance can be considered only in pairs of elements $G_{MP}G$ or, alternatively, it can be distributed along the axial length of the pole. The latter will be important if the axial increment in the core has higher influence on the linking flux. In the current claw-pole motors the axial length of the claw pole is relatively short and a low magnetic loading is considered in the poles. This allows to reduce the complexity of pole modeling and to use a simpler MEC (Figure 3.6).

The MEC model predicts the magnetic loading in four different parts of the core: base core, flank and two parts in the claw-pole. If the flux variation is considered only for the fundamental excitation frequency, then the core loss per pole can be calculated according to a loss model in the main core parts.

3.2 Core loss in the SMC core

A method that allows estimating core loss correctly and quickly is crucial for a design of a magnet core. There are always errors present on any kind of core

loss models. The exhaustiveness of considering all the main loss mechanisms in the loss calculation of a magnetic core may increase the accuracy, but it definitely increases the processing time [9]. The magnetic core that carries 3D magnetic flux is a subject to magnetic field rotation and a rotational core loss. The magnetization cycle may cause asymmetric magnetic loading or include high frequency effects. An ideal core loss model deals with the effect of field alternation, rotation and asymmetry. The loss model should be able to consider the real shape of magnetizing field and its' influence on the losses at different temperature and mechanic loading [8][61][91][98].

Core loss formulation

According to simplistic macro-physic concept of core losses in ferrous materials the losses can be divided into hysteresis, classical eddy current and anomlaous or excess losses. The specific core loss energy over a magnetization cycle can be expressed as a sum of the loss components

$$w_{core}^{locus} = k_h \hat{B}^n + k_e \int_0^T \left(\frac{d\vec{B}}{dt} \right)^2 dt + k_a \int_0^T \left| \frac{d\vec{B}}{dt} \right|^{3/2} dt \cdot \tag{3.17}$$

This expression is applicable either to the alternating field or to the rotating field [97]. The loss energy or the work to re-magnetize the core depends on the material, the magnetic loading and the rate of the change of the flux density. The loss coefficients k_h, n, k_e, and k_a (Eq. 3.17), respectively, loss coefficients for hysteresis, classical eddy current and anomalous loss, consider the different loss mechanisms and have to be chosen according to the modulus and locus of flux density vector $\boldsymbol{B}$ [31]. The magnetic friction loss energy i.e. hysteresis, is the mechanical work to orient the magnetic domains according to the external field and to overcome the friction between the domains. It is considered that the hysteresis loss energy is independent of the re-magnetization speed. Apart from the static loss energy the dynamic loss energy depends on the rate of the change of the flux density. For fixed sinusoidal frequency the core loss energy expression can be reduced to

$$w_{core}^{locus} = k_h \cdot \hat{B}^n + 2 \cdot k_e \cdot \pi^2 \cdot f \cdot \vec{B}^2 + 8.76 \cdot k_a \cdot f^{1/2} \cdot \vec{B}^{3/2} . \tag{3.18}$$

This formulation (Eq. 3.18) is applicable when the magnetizing field waveform over the magnetization cycle is assumed to be sinusoidal. The core loss that is obtained from the sum of harmonic losses gives misleading results when the core becomes saturated and the principle of superposition is invalid [91]. For a proper core loss evaluation it is necessary to consider the instantaneous flux

density 3D waveform at different parts of the core. In the general case, the flux density locus forms an ellipse, and this is a combination of alternation and circular rotation. The trajectory of flux density alternation is a line, while flux density rotation with a constant magnitude forms a circle.

$$w_{core}^{ellipse} = \frac{B_{\text{minor}}}{B_{\text{major}}} \cdot w_{core}^{circle} + \left(1 - \frac{B_{\text{minor}}}{B_{\text{major}}}\right)^2 \cdot w_{core}^{line} \,. \tag{3.19}$$

The minor and major axes of the elliptical locus are determined (Eq. 3.19) as B_{minor} and B_{major}. The Flux density variation in different parts of a claw-pole structure can be evaluated from a MEC and/or a FE model. It is assumed that, the minor and the major axis of the elliptical flux density locus are determined by the magnetic loading at the alignment and unalignment position. At the alignment the claw-poles are aligned with the magnet poles and the core carries the maximum flux in the radial or axial direction. The unalignment position causes flux flow in circumferential direction through the claw poles.

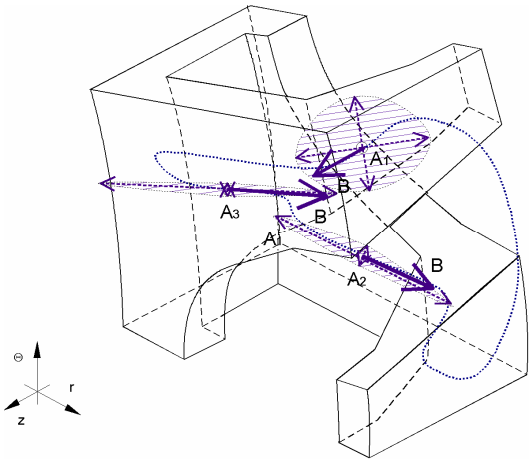

Figure 3.7: The magnetic flux penetration at the alignment position. Field rotation is assumed to occur in the claw-poles while in the bottom of the core the field alternation takes place.

The accurate field variation does not give reliable loss estimation unless the loss coefficients are correct. The loss coefficients are very difficult to determine analytically and in this reason empirical values or test data is used instead. It is important that the test measurements cover the range of the magnetic loading and the frequencies where iron core operates [89].

Furthermore, the complete loss prediction requires a priori knowledge of loss coefficients for the different flux density loci [31].

The core loss coefficients, which are used in the core loss computation models, are evaluated from measurements of alternating magnetic field [89] and rotating magnetic field [31].

Static core loss

The easy magnetic domain reorientation and contribution to the external field that insure low coercitivity is relevant for magnetic medium in alternating field. The macro physical concept states that the static hysteresis loss is due to the irreversible processes in the magnetization mechanism. The static loss energy is the work required to magnetize the core during the magnetization period and this equals to the area of the major hysteresis loop [64]. If no local minima (minor hysteresis loops) or bias (asymmetric hysteresis loop) in the magnetizing waveform are considered, then the specific hysteresis core loss (Eq. 3.20) energy for alternating field depends on the peak value of B_{mod}.

$$w_{hyst}^{line} = k_h \hat{B}_{\mathrm{mod}}^{n} \tag{3.20}$$

The hysteresis core loss energy (Eq. 3.21 and 3.22) for the magnetic field rotation [97] has been formulated as

$$w_{hyst}^{circle} = a_1 \left[\frac{1/s}{(a_2 + 1/s)^2 + a_3^2} - \frac{1/(2-s)}{(a_2 + 1/(2-s))^2 + a_3^2} \right] \tag{3.21}$$

The rotational core loss depends on the saturation B_S.

$$s = 1 - \frac{\max(B_{\mathrm{mod}})}{B_S} \sqrt{1 - \frac{1}{a_2^2 + a_3^2}} \tag{3.22}$$

Usually, the effect of magnetic hysteresis is considered in post-processing level after the field values are calculated. If the hysteresis model is coupled into field computation method then the magnetic hysteresis can be considered directly. This causes burdensome field computation with a small improvement of obtained accuracy [9].

For a proper core design it is important to consider the effect of field rotation for an iron core material that has high coercive field. Otherwise, the differences between the measurement and computation are mainly due to rotating fields inside the stator core [67]. Additionally, the exclusion of high

frequency effects such as minor hysteresis loops due to magnetization or influence of the pulse width modulated (PWM) armature field [7][86] leads to an underestimated value of the static core loss in the real motor operation.

Dynamic core loss

The dynamic loss is the dissipated energy per magnetization cycle, where the dissipated energy depends on the frequency of the cycle. The dynamic core loss is caused by induced currents. Dynamic core loss is a sum of classical eddy current loss and anomalous loss in the magnetic material. The specific dynamic power loss is computed (Eq. 3.23) according to the average of the position rate of change of the flux density vector over the magnetization cycle T for a constant rotational frequency ω during the re-magnetization cycle

$$\begin{aligned} p_{core}^{locus} &= k_e \frac{1}{T}\int_0^T \left(\frac{d\vec{B}}{dt}\right)^2 dt + k_a \frac{1}{T}\int_0^T \left|\frac{d\vec{B}}{dt}\right|^{3/2} dt = \\ &= k_e \frac{1}{2\pi}\int_0^{2\pi} \left(\omega\frac{d\vec{B}}{d\theta}\right)^2 d\theta + k_a \frac{1}{2\pi}\int_0^{2\pi} \left|\omega\frac{d\vec{B}}{d\theta}\right|^{3/2} d\theta \end{aligned} . \tag{3.23}$$

If the core loss coefficients are defined according to the measurements with the sinusoidal magnetic field then the total average dynamic core loss over one cycle per unit of volume at any arbitrary flux density waveform is expressed as

$$\begin{aligned} p_{core}^{locus} &= \frac{k_e'}{2\pi^2}\frac{1}{T}\int_0^T \left(\frac{d\vec{B}}{dt}\right)^2 dt + \frac{k_a'}{\left(2\pi^2\right)^{3/2}}\frac{1}{T}\int_0^T \left|\frac{d\vec{B}}{dt}\right|^{3/2} dt = \\ &= \frac{k_e'}{2\pi^2}\frac{1}{2\pi}\int_0^{2\pi} \left(\omega\frac{d\vec{B}}{d\theta}\right)^2 d\theta + \frac{k_a'}{\left(2\pi^2\right)^{3/2}}\frac{1}{2\pi}\int_0^{2\pi} \left|\omega\frac{d\vec{B}}{d\theta}\right|^{3/2} d\theta \end{aligned} . \tag{3.24}$$

The magnetostatic field computation assumes a full field penetration. Instead of considering the loss generation separately for each space flux density component [9][63][71] the variation of flux density space vector is calculated beforehand. The dynamic loss is calculated from a cycle of N discrete steps over the magnetization cycle can be expressed as follows

$$p_{core}^{locus} = \frac{k_e'}{2\pi^2}\cdot f^2 \sum_{i=1}^{N}\left(\Delta\vec{B}_i^{\,2}\right) + \frac{k_a'}{\left(2\pi^2\right)^{3/2}}\cdot f^{3/2}\sum_{i=1}^{N}\left(\Delta\vec{B}_i^{\,3/2}\right)\cdot \tag{3.25}$$

The discrete variation of the flux density space vector is formulated as the incremental change of the modulus of the space vector (Eq. 3.26).

$$\Delta\vec{B}_i^2 = \left(B_{x,i} - B_{x,i-1}\right)^2 + \left(B_{y,i} - B_{y,i-1}\right)^2 + \left(B_{z,i} - B_{z,i-1}\right)^2 \tag{3.26}$$

The anomalous or excess loss is calculated according to the arbitrary flux density waveform and not according to the minor and the major value ellipsoidal flux variation [9]. Similarly to the hysteresis loss, the anomalous loss due to field rotation reduces to zero when the iron core gets saturated The advantage of using only one formulation with combined eddy current losses introduces a simplification that originates in the dynamic and static loss coefficient deduction of the loss measurements [31][89].

The iron loss model that considers the time and space dependent flux density variation is applicable to a model that is able to provide such data. A MEC model has a low resolution to interpret the variation of flux density vector in different parts of the core. Therefore, a sinusoidal flux density variation is assumed in the main core parts when the core losses are calculated according to MEC model.

3.3 Mechanical calculation and analysis

Magnetic coupling between permanent magnet and iron parts causes magnetic attraction and tensile forces between the bodies. Hereby, it is assumed that the normal field component is dominating compared to the tangential component. The magneto-mechanic load to the bodies becomes the biggest when the poles are aligned, the gap flux is the largest and the magnetic potential surfaces are perpendicular to the pole surfaces. The normal stress t_n (Eq. 3.27) and the shear stress t_s (Eq. 3.28) relate to the gap flux density normal component B_n and tangential component B_s in respect of the pole surfaces.

$$t_n = \frac{1}{2 \cdot \mu_0} \cdot \left(B_n^2 - B_s^2\right) \tag{3.27}$$

$$t_s = \frac{B_n \cdot B_s}{\mu_0} \tag{3.28}$$

The main interest in the structural mechanic calculation is to evaluate stresses in the core material and to find the maximum load-carrying capacity of a geometrical core configuration. Even though the magnetic pressure is considered to be negligible in the conventional machines, the reason for elasticity and structural mechanic calculation is a complicated magnetic core, which is made of a weaker material with a lower constructional strength.

Structural mechanics

A problem formulation in structural mechanics has to determine the compression and tensile stresses in the different part of the motor core. The easiest formulation is to consider stresses in a thin sheet of a core. This sheet is loaded only its own plane without any restraint that is normal to the plane. Therefore, the constructional support is neglected (axi-symmetry) and the stresses normal to the plane is considered to be very small (plane stress). The mechanic stresses due to the magnetic attraction are investigated over a cross-section area of a claw-pole on radial/axial plane.

The mechanic stresses in the material depend on the structure of the claw pole and on the magnetic stress applied to the claw-pole surface. The elasticity problem in solid mechanics is expressed as the mechanical equilibrium of stresses σ and body forces b where the strains ε is taken into consideration on the basis of linear elasticity (Eq. 3.29) [55][76]. Due to relatively low operating temperature, the effect of thermo-elasticity and thermal strains ε_0 are neglected. The kinematical relation and boundary conditions, i.e. displacement or traction vector, specify the whole problem to an entire 2D area that is independent of the circumferential-coordinate. A matrix differential operator $\tilde{\nabla}$ facilitates writing the differential equations for elasticity in compact form [76].

$$\tilde{\nabla}^T D\left(\tilde{\nabla} u - \varepsilon_0\right) + b = 0 \tag{3.29}$$

The forms of the constitutive matrix $\boldsymbol{D}$ and strain vector depend on whether plane stress or strain is emphasized. The calculation of the plane stress over the cross-section area is made according to the following three conditions. Firstly, the attraction tensile forces are applied on the claw-pole surface. The gap flux density value is obtained from MEC. Secondly, the inner surface, which is determined by radius r_i, is considered to be fixed and the displacement vector for the corresponding node points is set zero. Thirdly, the actual shape of the claw-pole ring that is orthogonal to the cross-section area is neglected. It is considered that the reduced complexity gives fast and still valuable stress distribution over the cross-section area with respect to different geometrical configuration and applied load.

A number of triangular first order elements are used to calculate the stresses in the material [10]. In order to reduce the meshing error and to get a proper stress distribution it is necessary to use a few layers of properly shaped elements [58]. The higher number of elements distinguishes the compression and tension between the parallel surfaces and specifies the most stressed regions. The results are obtained from a claw-pole motor with a ferrite magnet

that gives as high as *0.2T* flux density in the air-gap. The pole height in axial direction is h_p*=10mm* and the length in radial direction is l_p*=15.4mm*. The thickness of the core is $l_t=l_b=h_f$*=3.5mm*.

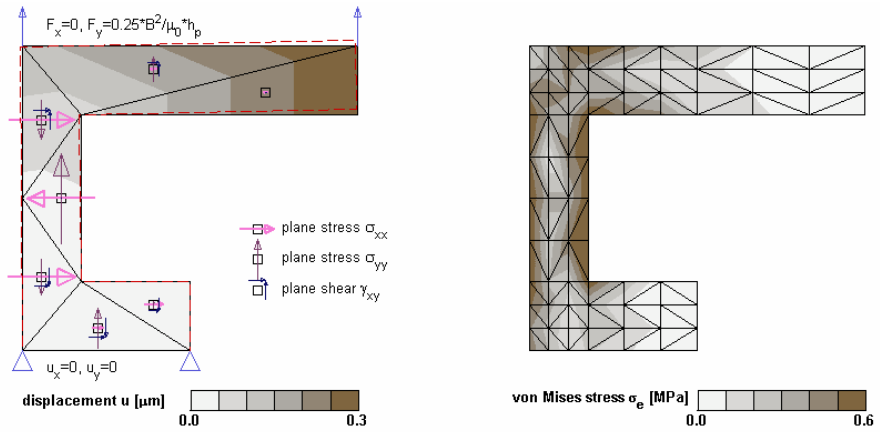

Figure 3.8: The subdivision of triangular elements and the stress distribution accuracy. The cross section area on the left has 7 elements and on the right 114 elements. The latter increases stress distribution accuracy.

If a few low order triangular elements are applied over the cross-section area (Figure 3.8 on the left) then the influence of tensile force to the total displacement is inadequately represented. The stresses and strains that are computed in elements according to the node displacements give a constant value in a single element and this is insufficient [57]. The increased number of element order or elements improves the representation of displacement in the node points and stress distribution in the material (Figure 3.8 on the right). The existence of the singular values in the sharp corners of the cross section area causes stress concentration and leads to unrealistically high values of stresses [57]. The maximum stresses in the core, which base on a relatively low number of linear elements, are likely to be underestimated [56].

Safety margin

The fundamental problem of structural analysis is the estimation of the reliable mechanic functionality of the motor parts [55]. The reduced size of the core increases not only the magnetic loading but also the mechanic loading. The mechanic loading is considered as mechanic stresses in the core material. The safety margin is evaluated for the powder core with a specific size. The obtained value of the mechanic loading in the material leads to an overestimated safety margin as the thermal effect is not taken into

consideration. The allowable values of the stress in the core are determined by the material limitation such as rupture stress and safety margin in respect of the rupture.

The mechanic strength of soft magnetic composite is described by two values: green strength and transverse rupture strength (TRS). The green strength is a manufacturing figure that shows the ability of an incompletely cured material to undergo removal from the mold and handling without distortion. The strength limitations of a compacted green powder present fabricators with processing problems. The value depends on powder characteristics, such as particle size distribution and morphology, compressibility and common lubricant systems. All these characteristics pose limitations on the compact green strength. The other value, transverse rupture strength, like the green strength, is a calculated value, which is required to break a specimen. In an electromechanical device the construction has to be loaded within material elastic or reversible range. Basically, the elastic limit specifies the region of linear deformation and the maximum stress recommended in the structure [55]. As the elastic limit is not specified for the SMC material then the maximum recommended stress is chosen in respect of TRS and a safety margin. An equivalent stress is defined in terms of stress components to represent the total stress applied to a specimen. In the case of plane stress formulation the effective stress is calculated

$$\sigma_e = \left(\sigma_{xx}^2 + \sigma_{yy}^2 + 3 \cdot \gamma_{xy}^2 - \sigma_{xx}\sigma_{yy}\right). \tag{3.30}$$

A generalized stress distribution i.e. von Mises stress (Eq. 3.30), which does not carry directional stress information, is used to identify the hot-spots where material failure may occur.

3.4 Thermal design

Electromechanical conversion through the electromagnetic field generates loss power in the windings and in the iron core. In order to guarantee the expected lifespan of the motor, the hottest point in the motor, which is usually in the winding, must be lower from a certain limit. The purpose of thermal calculation is to determine the temperature distribution in the motor and to investigate the better heat dissipation in order to get a higher thermal limit of the motor and a good utilization factor of materials. The maximum temperature in the motor parts must be lower than the limits that pose an

insulation system, permanent magnet and some other parts, which are strongly temperature dependent and cause failure of motor functionality.

Thermal equivalent circuit

The thermal analysis and calculation can be easily built up on thermal equivalent circuit (TEC), which corresponds to magnetic equivalent circuit [12][69]. In this case the sources are the loss power in the coil and ferrous core, and the elements are the thermal conductance to the heat flow. The temperature drops on the elements cause the difference between the maximum inside temperature and the outside temperature. The weakest part in this circuit is the prediction of heat dissipation from the motor surface to the surrounding. For the sake of simplicity, the thermal equivalent circuit can consist of only a single heat loss power source and a conductance that specifies the cooling capability over the cooling area [83]. Typically, electrical motors allow self-cooling in normal circumstances up to $1.5\text{-}2.0\ kW/m^2$, which is loss power per cooling surface. This simple computation would not be able to specify the temperature rise or its' dependence on material properties or construction.

A stationary heat transfer problem is formulated according to heat balance and heat flow in material over an entire area specified by boundary conditions such as known heat flow q_n (including convection) or known temperature ϑ. Similarly, the MEC the heat conductivity matrix $\boldsymbol{G}$ is assembled according to a topology matrix of a TEC (17) nodes and (24) elements G_{TH}. The heat flow and temperature distribution $\boldsymbol{\vartheta}$ in the motor is calculated by using the node potential method (Eq. 3.31).

$$\mathbf{G}\vartheta = \mathbf{Q} \tag{3.31}$$

The heat sources $\boldsymbol{Q}$, which is the loss power, is inserted into the corresponding node points. The resistive heat losses in the coil that is loaded with direct current density is

$$P_{Cu} = \rho J_C^2 l_{av} A_S k_f \,. \tag{3.32}$$

Equivalent heat conductivity [21] is used in the slot volume of a wrapped coil with a certain fill factor k_f. The slot volume is described as the slot area A_S times the average length l_{av} of conductor strand.

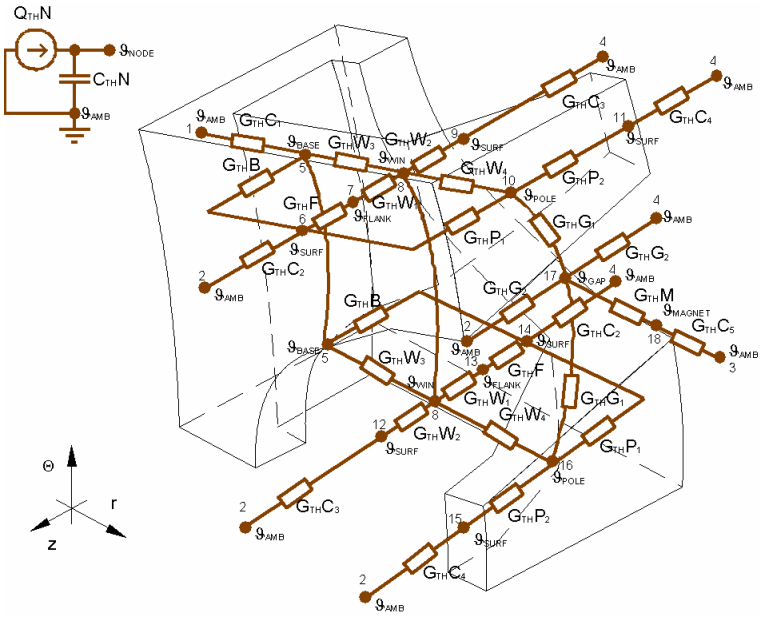

Figure 3.9: Thermal equivalent circuit.

The heat dissipation from the winding is assumed to be in both radial and axial direction through the heat conductance $G_{TH}W$. Uniform heat distribution is assumed along the circumference in the middle of the coil where the coil resistive heat source is attached. The iron core is divided into three distinguishable regions, which are a base *(B)*, a flank *(F)* and a pole *(P)*, similar to MEC, so that the core loss can be easily attached to the TEC. Heat dissipation or on the contrary thermal insulation can be defined on four different surfaces. The heat dissipation is defined through the convection heat conductance $G_{TH}C$.

The TEC can be used to study the transient heat flow by adding heat capacitances C_{TH} into the circuit. The importance of the TEC is to investigate the thermal limit according to the conditions at the steady-state. The steady-state operation can be distinguished between the case where the rotor rotates at a certain speed and the rotor stands still. In the first case intensive heat dissipation occurs in the gap region. On the contrary, when the rotor is not able to rotate and the heat is generated in the coil(s) and in the core then, from thermal loading point of view, this is considered as the heaviest thermal loading condition. This means that motor operation does not support cooling, and the generated heat is mainly dissipated by normal convection or

transferred by heat conduction through the housing elements. An air forced cooling and radiation are neglected.

3.5 Optimization

In order to optimize any electromagnetic device it is necessary to find an appropriate geometric distribution of materials and sources. The optimal design of an electric machine is to choose a set of dimensions for the machine (design variables), so that the designed machine will satisfy the design criteria (constraints) and minimize (or maximize) some additional criterion. The objective functions, which are efficiency and a high force/volume ratio, are optimized [16][37].

The importance in the design process is to reduce the cost of materials and energy. The objective in the optimization is to find the biggest torque of a claw-pole motor with a constant motor volume. Furthermore, by choosing a stronger magnet and reducing the motor volume, it is expected that the motor can deliver the same torque.

Design variables

The main variables, which are gradually changed in the optimization loop, are the inner radius of the motor r_i, the size of the cross section area of motor and the number of poles N_p. The cross-section area of the motor is defined as the axial height h_{mot} to the radial length $l_{mot}=l_p+g+l_{pm}$. Consequently, the optimization is concentrated only to the size of the unit of the electromechanical converter excluding the additional mechanic support system. By changing the proportions K_{mot} of the cross-section area and the inner radius of the motor, the size of the motor is determined by the constant volume.

$$V_{mot} = \pi\left(r_o^2 - r_i^2\right)h_{mot} = \pi\left(\left(l_{mot} + r_i\right)^2 - r_i^2\right)h_{mot} = \pi\left(l_{mot}^2 + 2r_i l_{mot}\right)h_{mot} \tag{3.33}$$

$$K_{mot} = \frac{l_{mot}}{h_{mot}} \tag{3.34}$$

The objective is to find a size of the claw-pole motor that is able to deliver the largest torque according to the gap-radius and the selected number of poles N_p. On the basis of the EC models, the domain is scanned through in order to find the optimal combination of the size of the claw-pole motor for a constant motor volume. The ratio of the radial length to the axial height K_{mot} considers the different cross-sections for the claw-pole structure and the winding.

Additionally, the proportions of the cross-section area affect an optimal thickness of the core parts versus the cross-section area of the coil. In turn this influences the maximum output of the electromechanical conversion.

Constraints

Different criteria that satisfy the motor pattern can be distinguished. From physics point of view, electric, thermal, magnetic and mechanic constraints are considered.

Electric

The source of the power supply, the selected voltage level and switching conditions specifies the demands to motor inductance and the number of turns. According to the supply voltage U and physical coupling flux Φ_B that induces back electromotive force due to the rotation of the magnet-ring at the nominal speed Ω the number of turns is chosen (Eq. 3.35).

$$N = \frac{U}{0.5 \cdot N_P \cdot \Omega \cdot \Phi_B} \tag{3.35}$$

Large inductance causes electric inertia, which decrease response time. The inductance is calculated (Eq. 3.36) from the MEC on the basis of the field change that considers the non-linear properties of material at normal operating conditions.

$$L = \frac{N^2}{A_S \cdot k_f} \cdot \frac{\Delta \Phi_B}{\Delta J_C} \tag{3.36}$$

In the case of the multiple coils the corresponding field change of n-coil due to the change of the current in it determines the self inductance of the coil. Mutual inductance is calculated from the field change that causes current change from another coil.

Magnetic

The proper value of magnetic loading is a message of properly used magnetic soft and hard materials as well as the applied maximum magnetomotive force. Another indicator to the proper magnetic loading is the reasonable magnitude of ferrous losses at an operating frequency.

A well designed magnetic circuit has low magnetic flux leakage and limited magnetic saturation. As a matter of a saturated core, it does not guide the

magnetic flux as intended. The same happens if the leakage path becomes relatively shorter than the long coupling path through the powder core.

Hard magnet material demagnetization risk, which increases due to applied field and high temperature, is the other factors that pose constrains to the design.

Mechanic

Manufacturability and functional durability of the powder core and magnet determine the mechanic conditions. The way of processing the claw pole rings and magnet-rings can be different. Nevertheless, the thickness and the mechanical proportions of the motor parts suppose to be selected that the stator parts are reasonable to produce, to assemble into the motor and to keep their functionality during lifespan. As a matter of fact the electric and magnetic constrains of the stator core become important after the motor is assembled, while the mechanic and thermal constraint are important already in manufacturing process.

Thermal

Cooling capability and the maximum allowable temperature for coil insulation and magnets determine thermal constraints. Therefore, the losses that have to be dissipated should be small or cooling conditions good that the maximum temperature would not exceed the thermal limit.

3.6 Optimal size of a small claw-pole motor

The volume of the small claw-pole motors are well specified (Table 2.1). The purpose of searching an optimal size is not only to determine the optimal size of the miniature claw pole motor but also to verify the reliability of the EC models and to look for the improvements. The optimal output of the electromechanical energy conversion is looked for. The number of poles, the inner radius of the outer rotor motor and the proportions of the cross-section area of the motor is to be changed in order to find the most suitable domain for small volume TFM with SMC core, with respect to losses and torque. At the same time the temperature rise in the coil, in respect of a natural cooling condition of $a=20\ W/(m^2 \cdot K)$ and the mechanic stress in the core is specified.

The inner radius determines the size of the stator, which have constant volume about $V_{mot}=18.8\ m^3$ (Figure 3.10). The cooling surface and the cross-section

area of the claw-pole stator change according to the inner radius, the axial height and the radial length of the stator core (Figure 3.11).

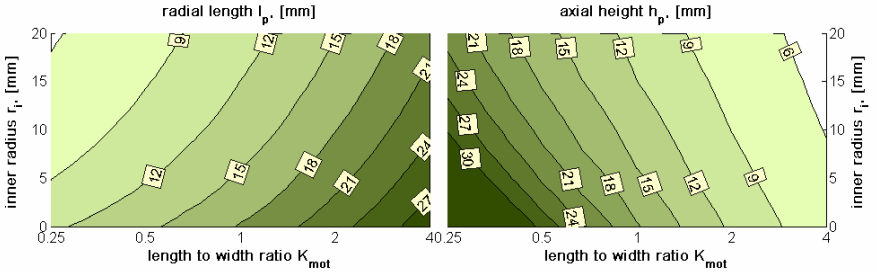

Figure 3.10 The axial height and the radial length of the claw-pole stator as a function of the inner radius of the stator core and the proportions of the core cross-section area.

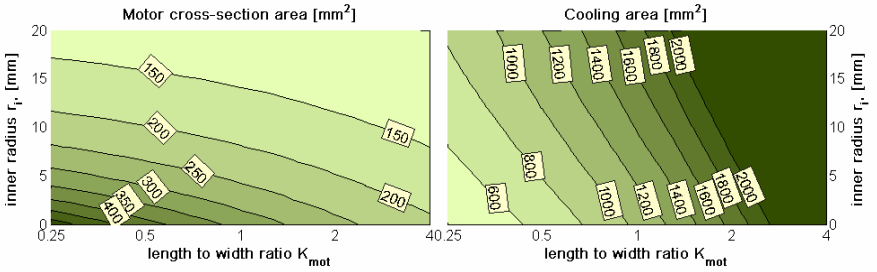

Figure 3.11 The stator cross-section area and a cooling area of the claw-pole stator as a function of inner radius of the stator core and the proportions of the core cross-section area.

The radial length of the air-gap and the electric loading of the coil have been kept constant. The magnetic loading decreases as the number of poles increases. This causes lower core loss energy per excitation cycle. On the contrary, the claw-pole motor is expected to operate at higher frequency, at the higher pole numbers. The high magnetic gearing ratio, which corresponds to the number of poles, increases the angular velocity of the stator excitation at the constant angular velocity of rotor. As the dynamic frequency dependent losses are expected to be lower for SMC, than for the solid iron, the material has advantage over the solid iron. As the machine torque is proportional to the pole number, the number of poles can be increased until it is magnetically and mechanically feasible for a certain radius [19][44].

The magnetic loading of the claw-pole structure is determined by the pole surface area of the magnet-ring. Basically, the source of the magnetic flux decreases to the minimum at the high number of poles. The model of

permanent magnet is rather simple than accurate. According to the magnet model the strongest magnetic loading is determined for axially wide magnet at low number of poles (Figure 3.12).

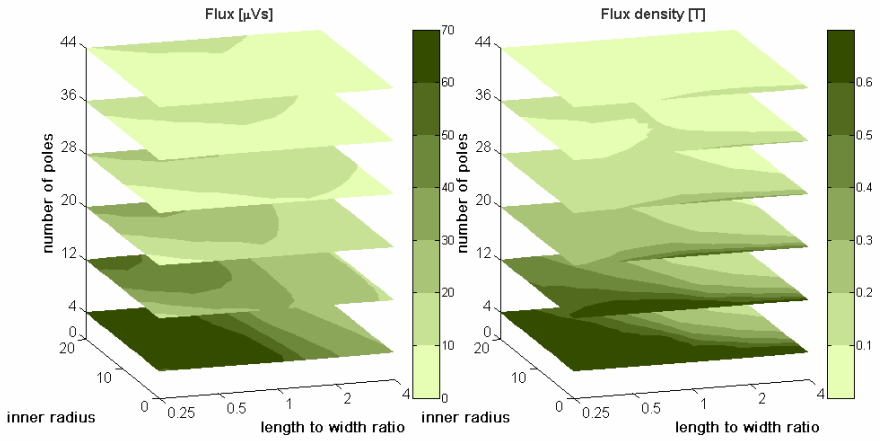

Figure 3.12: A coupling flux (left) and magnetic loading (right) as a function of number of poles, inner radius and the cross-section of the claw-pole stator.

According to the coupling flux and the number of poles, the average value of the coupling torque is determined. The temperature in the motor corresponds to the current loading of $4\ A/mm^2$.

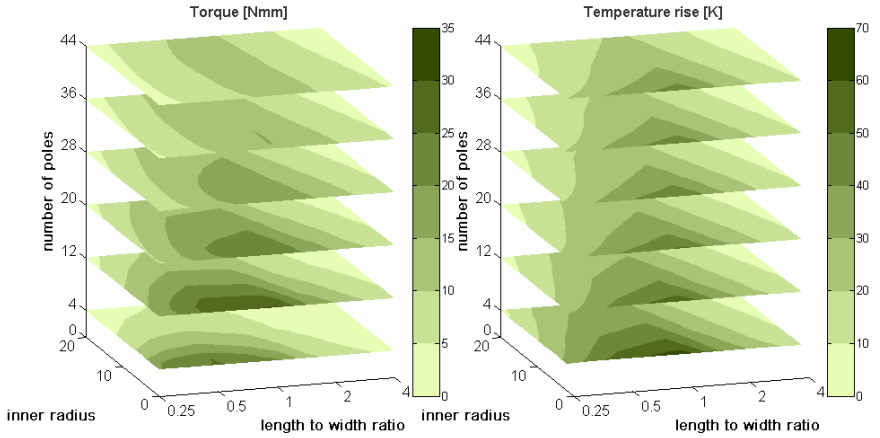

Figure 3.13: The best output of torque and thermal loading as a function of number of poles, inner radius and the cross-section of the claw-pole stator.

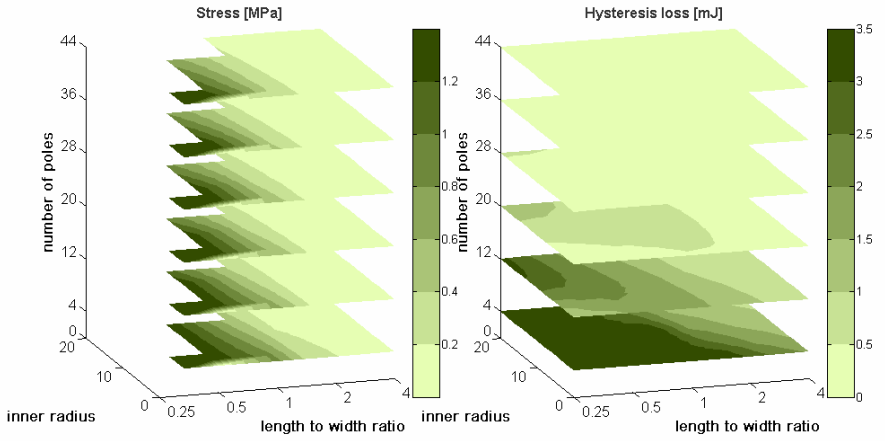

Figure 3.14: Best choise of number of poles, inner radius and the cross-section of the claw-pole stator. The graph on the left shows von Mises stress in the claw-pole structure and the figure on the right indicates the hysteresis loss energy per magnetization cycle.

The axially wider magnet causes stronger mechanic loading to the radially thin claw-pole. The formulation is 2D elasticity problem fails in the region of wide magnet. The core losses are determined at the magnetization speed of *1 rad/sec*. The core losses dominate at low number of poles and an axially wide magnet-ring. The EC analysis depends on how accurately a magnet-ring is modeled. The paper presented in NORPIE considers the cross-section area of the magnet-ring instead of the pole surface area.

The drawback of the magnetic equivalent circuit is that the accuracy of the circuit needs to be evaluated with a series of 3D FE analysis. The MEC is able to correctly estimate the values of the magnetic loading and the coupling torque at initial conditions. The drawback is that the model works fine in certain domain while the results become distrusted at the larger domain. The systematic scan, which is done in order to validate the MEC model, leads to a new flexible method that is a broad-search of the best motor construction based to the 3D FEA.

The specification of the motor dimensions is summarized in Table 3.1. The stator core is specified according to the maximized coupling flux and minimized leakage flux.

Table 3.1: Initial measures for the claw-pole motors.

Quantity	symbol	unit	A single-phase claw-pole motor	A two-phase claw-pole motor
Number of poles	N_P	-	4	20
Number of phases	N_{PH}	-	1	2
Pole clearance factor	K_P	-	0.38	0.40
Copper fill factor	K_F	-	0.50	0.60
Magnet width factor	K_M	-	0.60	0.58
Height of the claw-pole ring	h_P	mm	20.00	3.60
Thickness of the flank	h_F	mm	3.50	0.90
Height of the magnet ring	h_{PM}	mm	20.00	10.80
Thickness of the bobbin	h_{cl}	mm	1.00	0.00
Length of the claw-pole ring	l_P	mm	15.425	8.85
Thickness of the base	l_B	mm	3.50	0.90
Thickness of the pole	l_T	mm	3.50	1.20
Width of the air-gap	g	mm	0.50	0.25
Thickness of the magnet ring	l_{PM}	mm	4.475	1.90
Thickness of the housing	l_H	mm	1.50	1.50
Tangential tapering angle	γ_1	deg	8.0	20.0
Axial tapering angle	γ_2	deg	0.0	0.0
Flank forming angle	γ_3	deg	5.0	4.0
Progressive radius	d_r	mm	1.00	0.00
Distance between phases	h_d	mm	-	0.80

The designs of Table 3.1 are the basis for the further FEM analysis in Chapter 4. The nominal conditions of the claw-pole motors are summarized in Table 3.2.

Table 3.2: Nominal conditions for the claw-pole motors.

Quantity	symbol	unit	A single-phase claw-pole motor	A two-phase claw-pole motor
Current density	J_C	A/mm²	4.0	7.0
Nominal speed	Ω	rpm	4000	600
Nominal voltage	U	V	12	3

The motor parameters are summarized in Table 3.3.

Table 3.3: Parameter specifications for the claw-pole motors.

Quantity	symbol	unit	The single-phase claw-pole motor	The two-phase claw-pole motor
Number of turns	N	-	180	54
Winding resistance	R	Ω	0.75	1.2
Winding inductance	L	mH	5.5	0.1
Rotor inertia	J	$kg \cdot m^2$	6.66	5.1e-7
Mass of SMC core	m_S	g	54.0	58.70
Mass of copper	m_C	g	21.5	12.05
Mass of magnet	m_M	g	68.0	17.79

Chapter 4

Numeric field computation

If the real model, which is a prototype, contains infinite number of degrees of freedom (d.o.f.) then the EC model incorporates too low d.o.f. Similar to the EC, the FE gives an approximate solution to a physic problem described by differential or integral equations in a number of small regions – finite number of d.o.f. Finite element analysis is an approximation numeric calculation method, which based on the principle of differentiation that distributes in such a way as to minimize the potential energy for general functions expressing the field state. It is used in a wide range of fields, such as calculation of the strength of structures, and thermal conduction, electromagnetic field analysis, and fluid analysis. In this chapter the heat transfer, magnetostatic and structural mechanic problems are formulated and calculated in FE software namely VectorFields, FEMLAB and Jmag-Studio.

The success of finite element analysis (FEA) bases on an adequate FE model. The accurate geometric representation is often less important in a FE model than high quality meshing with certain types of elements, the correct representation of sources and boundaries [56]. Similarly, the result of FEA is often less valuable than the error estimate of the obtained result. In this case, the importance of FEA is to study electromechanical conversion of TFM with claw-pole structure in great detail. The magnetostatic analysis is sufficient in order to obtain static characteristics and to optimize the core according to improved specific torque and/or minimized cogging torque. Static implies that the time rate of change is slow, full field penetration takes place and no damping effects due to induced currents occur. By neglecting the influence of the electrodynamic effects such as induced currents, the transient and steady-state magnetodynamic FEA can be ignored. A series of the position dependent

magnetostatic computations are the basis of the magnetization loss evaluation in the core. Structural mechanic and thermal analysis follow to the FEA in magnetics as the problems of multiphysics.

4.1 Magnetostatics

The problem in electromagnetic analysis on a macroscopic level is the problem of solving Maxwell's equations subject to certain boundary conditions. The problem formulation on 3D magnetic field analysis may take advantage either on total scalar potential or on vector potential as the unknown in the node points. Total scalar potential method is least computation dense formulation. This divides the total magnetic field intensity (Eq. 4.1) in the magnetic materials as the superposition of the field contribution from current conducting coils H_J and the field due to magnetized materials H_M.

$$H = H_J + H_M \tag{4.1}$$

In the non-current region the gradient of total scalar potential V_M is used to represent the magnetic field

$$H = -\nabla V_M , \tag{4.2}$$

and according to the divergence of the flux density

$$\nabla \cdot (\mu \nabla V_M) = 0 . \tag{4.3}$$

In the current conducting region the reduced scalar potential V_{MR} represents the field of magnetized materials

$$H_M = -\nabla V_{MR} , \tag{4.4}$$

and the contribution of coil field H_J according to Biot-Savart law is the relation between current density and its' caused field

$$H_J(r) = \frac{1}{4\pi} \times \int_V \frac{J_C(r)}{r} dV , \tag{4.5}$$

which describes the magnetic scalar distribution over the conductor volume

$$\nabla \cdot (\mu \nabla V_{MR}) = \nabla \cdot \mu_0 H_C . \tag{4.6}$$

The inter-regional boundary condition between the total and the reduced volumes must ensure the uniqueness of the solution. Alternatively, the flux density distribution B can be computed according to the magnetic vector potential A

$$B = \nabla \times A, \tag{4.7}$$

where three unknowns is solved at each node point

$$\nabla \times \left(\frac{1}{\mu} \nabla \times A - M \right) = J_C \cdot \tag{4.8}$$

As a number of equations increases to represent a single node in the 3D space then that in turn limits the number of elements that is reasonable to use for a set of computation power.

In a domain the magnetic potential satisfies the field distribution equation and the boundary conditions. The energy of the field has to have a minimum value for the approximated solution to be exact [62].

3D finite element model

The 3D FE model is defined over a pole-pair of the claw-pole motor. VectorFields 3D FE software, Opera-3d Pre-processor (versions from 8.0 to 10.0) is used to construct a 3D FE mesh of hexahedral elements for representing the geometry of a claw-pole motor. Alternatively, the motor model is imported into or created in the Modeller that uses the tetrahedral elements to mesh the symmetric part of the model.

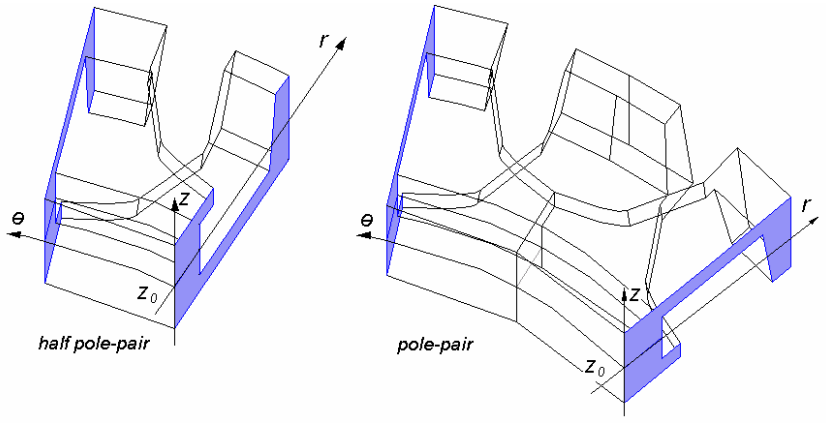

Figure 4.1: Periodicity surfaces of a claw-pole structure.

The boundary conditions are used to reduce the size of the FE model and to constrain the field that surrounds the machine. Basically, there are three types of boundary conditions that are used to reduce the size of the FE model.

1. Dirichlet (essential) condition is introduced when the magnetic flux through the surface is zero. This boundary condition is used when the flux lines are parallel to the boundary, and it is used to 'contain' the flux lines within a certain region (TANG MAGN – VectorFields notation, the magnetic field is tangential to the boundary);
2. Neumann's (natural) condition ($\partial V_M/\partial n$ known) determines the surfaces that the magnetic flux crosses orthogonally (NORM MAGN – VectorFields notation, the magnetic field is perpendicular (i.e. normal) to the boundary);
3. Periodicity condition is set to reduce the size of the model according to the periodic structure. Magnetic fields are periodic over the length of one pole pitch of the machine. The periodic nature over the length of one pole pitch is anti-symmetric and a 3D machine has to be symmetric along the axis of rotation.

Concerning the size reduction of a motor model, it is not possible to define a symmetric part of a TFM with claw-pole structure over a pole pitch in Opera-3d Pre-processor. The anti-symmetric connection between an identical source and destination causes inaccurate potential representation. (*THETA=180 PSI=180-360/Np PSI=0*). The destination symmetry plane is rotated around the centre axis, which is perpendicular to the source symmetry plane and passes the origin. Furthermore, it is turned around the axis of motion until it touches the surface of the claw-pole structure. This coupling causes a wrong orientation and, visually, there is no normal flux component present [16]. Therefore, the two pole pitch (Eq. 4.9) model is in FE model.

$$V_m(r,\theta,z) = V_m\left(r,\theta+\frac{4\pi}{N_p},z\right) \tag{4.9}$$

The 3D FE-model needs certain concern at the edges of the magnet-ring and the ferrous core so that the fringing field and its contribution to the force production are modeled well. The outer boundary of the model supposes to be placed far enough, so that the boundary conditions do not force the field distribution and the overall field values are simulated correctly.

One of the strengths of the VectorFields (TOSCA) magnetostatics solver is the formulation of two scalar potentials, which allows the primary coils not to be

part of the mesh. The reduced scalar potential volumes are introduced there, where the conductor is to be placed and the coil field has to be calculated. It is important that the coil fields are represented well by the finite element mesh on the interface between the reduced and total potentials. Ideally, the best choice of reduced potential region is a simple shaped region that contains the coils and has a surface as far as possible from the coil surface. Practically, the coil is wrapped on an iron surface of a total potential volume, and in this case, the interface between different potential regions must have enough elements in order to maintain the coil field representation accuracy. The total scalar potential volumes, which surround the conductor, can rise to the problems of multiply connected regions. This means that the magnetic scalar potential becomes multi-valued at some of the total potential volumes and a sudden jump in potential across the element occurs. In order to ensure that a total potential volume is not multiply connected, the reduced potential volumes should cut through the encircling total potential volumes. The reduced potential volume within magnetic material supposes to be as small as possible and away from regions where accuracy is critical. The cancellation error appears in this volume due to the space variation of the material field H_M that is represented as the derivation of FE shape functions, and the conductor field H_J, which is evaluated directly from integral equation. Potential cut is placed between the slot reduced potential volume and the boundary at the inner radius of the FE model. This is necessary in order to avoid multiply connected regions in the TFM of claw-pole structure and to model properly the contribution of the conductor field in the iron core.

3D finite element mesh

The choice of element type, the element quality and density, i.e. mesh, determine the accuracy of the FE-analysis and the force computation. The Maxwell Stress Tensor method enables calculating of the torque directly from the field solution for a given position. The field solution is obtained from an approximate potential distribution by means of numerical differentiation. The numerical differentiation magnifies the inaccurate potential representation in the node points. It is important to investigate the 3D FE mesh quality and its' influence on the accuracy of torque computation [2][34].

If a volume element has to be selected, then, from the point of view of computational efficiency, for the same number of degrees of freedom, hexahedral elements can give higher accuracy than tetrahedral elements. The higher accuracy is achieved due to a higher expression capability of the hexahedral elements. The approximation function for the 4-node tetrahedral

and 8-node prism element, where the parameters a_n depend on geometry and the magnetic potential, is written:

$$V_M = \alpha_1 + \alpha_2 x + \alpha_3 y + \alpha_4 z \tag{4.10}$$

$$V_M = \alpha_1 + \alpha_2 x + \alpha_3 y + \alpha_4 z + \alpha_5 xy + \alpha_6 xz + \alpha_7 yz + \alpha_8 xyz \tag{4.11}$$

In general for highest accuracy, it is necessary to align the element edges with the equipotential lines. This can be achieved with hexahedra, but automatically generated tetrahedra edges are unlikely to align ever correctly, and that leads to errors [73]. A region, where nearly balanced forces are to be computed, has to have very regular mesh. It is necessary that these mesh elements have a regular shape and distribution, in order to avoid as much of the "discretisation error" as possible. Due to complexity, the narrow gap of 3D electrical machine can hardly be the region of regular and continuous 3D mesh. The hexahedral elements are preferred, even though the filling space of a complex geometry with high quality is easier using tetrahedral elements or combine different types of elements. The hexahedral elements are reasonable from computation efficiency, the speed of numeric convergence, the regular shape and the element orientation point of view [62]. However, the circumferential distortion along the axial direction, which takes place in a transversal flux machine of a claw-pole structure, is the reason why the hexahedral elements become irregular.

Distortion of hexahedral element may reduce numerical accuracy because numerical approximation is no more centered (or symmetric) in the centroid of the volume element. This drawback may be balanced by the increase in local grid resolution, which can be afforded by the distortion. Due to distortion the numeric approximation becomes more complex. The lower mesh quality may lead to a bigger error in potential solution and, thus, in numeric differentiation.

Another source of errors in the field solution is the energy minimization which produces a solution that is optimal for a given discretisation. The field solution is globally optimal, even though it may possess considerable local errors.

Calculation of accuracy and errors

Different types of errors may occur in FE-analysis [34]. The way of creating the computational model causes the modeling errors in pre-processing. The finite element model is often simplified, but still adequate, in order to simplify the meshing of the FE model. Discretisation errors and calculation errors appear due to improper mesh. The calculation errors will be amplified in

numerical differentiation process. Errors may occur due to wrong or improper settings such as multiply connected regions and forcing functions introduced in FEA [88]. At post-processing a large rotational displacement makes it difficult to represent properly the variation of torque against position. Improper number of steps per length of pole-pair causes inaccuracies at cogging torque evaluation and minimization.

The accuracy of the FE solution is related to the size of the discrete elements. The local error at a point within a finite element model is strongly linked to the size of the elements that are surrounding the point and weakly linked to the average element size over the whole space. A local error associated to each finite element of a mesh depends on the ability of the finite element approximation function to represent the local spatial variation of the vector or scalar potential. The low order finite element approximation function is not able to handle correctly the problem of singularity at the edges and corners of the geometric representation of the physical model. The error of the field is one order less than the error for the solved node potential. It is due to differentiation of the FE shape functions. The field precision or the smoothness can be improved by nodal weighted averaging and a volume integration technique, respectively. The local error in the derived fields is evaluated with a posteriori method, which bases on comparison between field values obtained from differentiation of the element approximation functions and the nodally averaged fields computed in the analysis. The high value of the error estimate indicates the regions where FE discretization needs refinement. The sensitivity of the meshing error is evaluated with a number of trial analyses that have different element order or/and size. Nevertheless, this evaluation does not show the modeling errors.

Finite element analysis

The calculation results are obtained from 3D FE magneto-static analysis of the claw-pole motor. A magnetic two-scalar potential method together with Galerkin weighted residual method is used to obtain a solution to partial differential equation over the whole domain. Newton-Raphson is used to model the non-linearities in the ferromagnetic material.

The magnetic loading is calculated for a single-phase and a two-phase claw pole motor. Two different rotor constructions are specified: a magnet ring with lateral polar magnetization along inner periphery (Figure 4.2) and a surface mounted radial magnets inside the solid iron cylinder (Figure 4.3). Even though the pole pitch FE model is shown, the complete FE model is formulated over two poles with positive periodicity condition (Eq. 4.9).

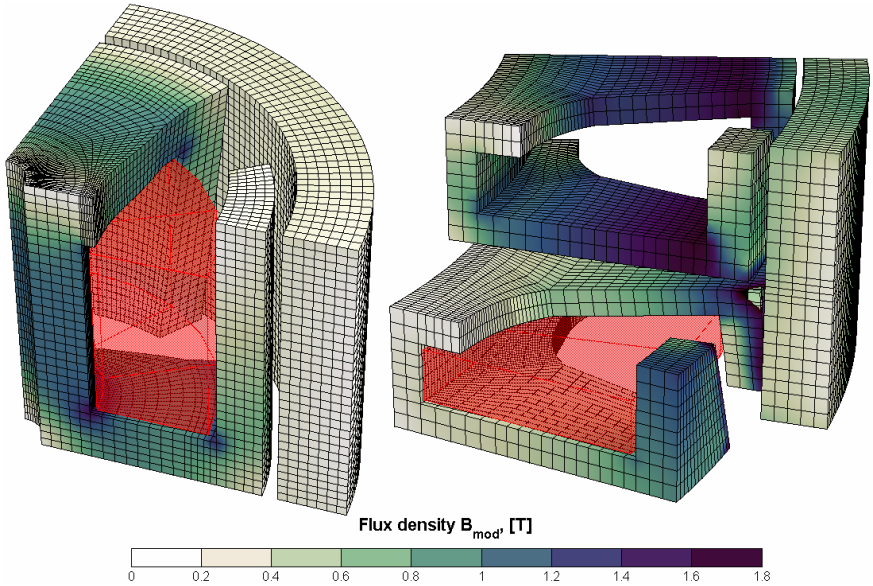

Figure 4.2: Magnetic loading of polar magnet motors.

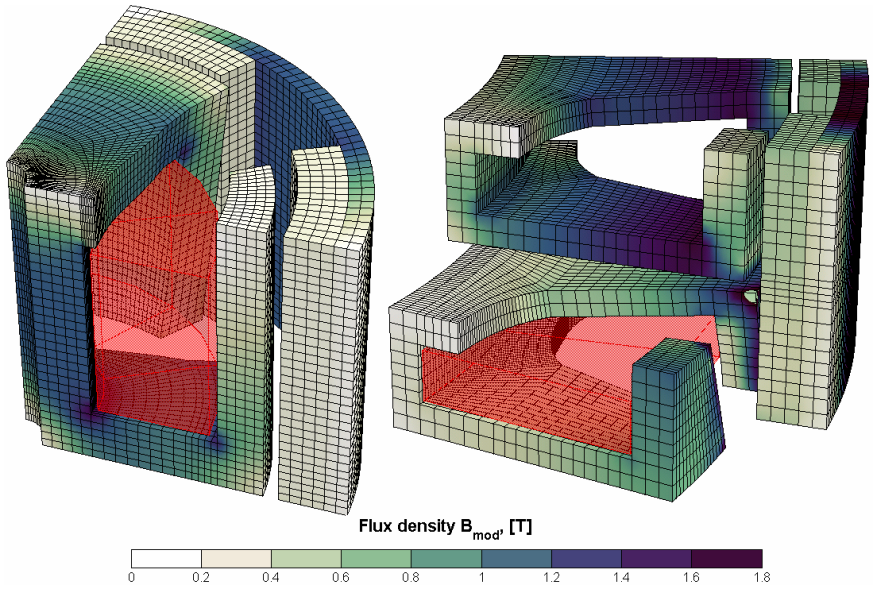

Figure 4.3: Magnetic loading of the radial magnets claw-pole motors.

The FE model of the single-phase claw-pole motor has around 250000 hexahedral elements, while the two-phase motor has around 150000 elements. The size of element is defined in the axial and the radial plane, 1.5 elements per mm and 2.5 elements per mm for the single-phase and for the two-phase claw-pole motor, respectively. The number of elements in the circumferential directions is selected to be 4 elements per sector. This formulation gives evenly sized elements in the circumferential/axial plane and an allowed aspect ratio in radial direction in the air-gap. A number of element levels are defined in the air-gap and rotor mesh. The stator mesh is sometimes defined separately in order to improve the whole FE model assembling at different positions. Similar to the 3D core construction, the element distribution in space, in circumferential, radial and axial directions are described as sectors, levels and layers, respectively.

The largest relative discretization error appears in the section of the outer side of the flank and the plane that passes the origin and is orthogonal to the outer side of the flank. The error in the low field core region has the maximum of 0.79. The relative discretization error (*ERRBMOD*/*BMOD*) shows the difference between the field values obtained from differentiation of the element approximation functions and the nodally averaged fields (*ERRBMOD*) to the differentiated field (*BMOD*). The relative discretization error of 10% takes place at the corners of the claw-pole, at the inner corner of the pole and the flank, and the outer radius of the magnet-ring where the radial component of the magnetization is dominating. The two-phase claw-pole motor has additional discretization errors in the volumes, which introduce the axial and the circumferential shift between the phases. This is the region of distorted elements.

The narrow air-gap is the region of high field intensity and highly distorted elements. The relative discretization error is high at the pole edges, where the effect of the singular field derivation together with the element skewing in the circumferential/axial plane introduces errors about 50% and more. This number becomes smaller at the radial gap levels which are in the middle of the air-gap. In order to improve the field differentiation, higher order elements are introduced in the pole regions and in the air-gap. Additional levels of gap elements reduce the field differentiation error due to the pole edges. If instead of four levels of air-gap elements are used six and the element size in circumferential/axial plane is reduced correspondingly, then the field error can be reduced to 10-30%. The field differentiation error depends on the radius of the integration patch and on the position of the rotor. The price of reduced error is governed by the increased number of elements and computation time.

It has been found that in 3D FE model the reasonable number of elements should not exceed more than 500000.

Torque computation

Static torque is calculated using Maxwell's stress tensor and from the rate of change of co-energy. These two methods are the most common methods for torque computations in electrical machines [29][34]. As both methods are dependent on the mesh quality, they help to evaluate the accuracy of FE model discretization and analysis. The torque can be directly obtained from the field values by using Maxwell's stress tensor while at least two different positions have to be modeled in order to find the torque by the co-energy method.

The Maxwell's stress tensor method is influenced by the gap mesh and only with a very fine and regular mesh it is possible to obtain reliable results. The 'one-step' torque computation technique needs significant efforts in order to model the air-gap region well. Coarse modeling of the air-gap can produce meshes, which predict the air-gap flux within a few percent. However, the forces in the gap depend on the multiple of the flux density *B* components and a modest error in *B* can lead a large error in force. The air-gap region requires very careful meshing by using several levels of elements, recommendable at least 4 levels, along the radial direction and so many subdivisions in axial and circumferential direction that the proportions of elements would be within an allowed aspect ratio. The Maxwell stress is computed over the rotor volume, an arbitrarily placed patch in the air-gap and over a predefined surface in the middle of the gap. Two layers of elements are added around the rotor volume so that the entire integration surface is in the air, like it is in two other cases for surface integration.

$$T = \oint_A t_s r dA = \oint_A \frac{1}{\mu_0} B_n B_s r dA \tag{4.12}$$

In case of a selected rotor volume or a gap surface the integration surface is passing the node points. Alternatively, a patch surface can be placed arbitrarily in the gap or/and around the rotor volume. The accuracy of the torque integration depends on where the integration surface is situated [29]. The experimentations have shown that arbitrary placement of a patch within an element level in the gap has negligible dependence on torque computation. A larger influence is noticed between the patches within different gap element levels. The difference between the torque computations within the element levels, excluding the first one closest to the claw-pole and the last one closest

to the magnet, is less than 3%. The reduction of this value is insignificant when instead of 4 levels 6 levels of gap elements are used.

The torque computation, according to the virtual work method, considers the rate of the change of the total co-energy against the virtual displacement. Typically, the values of the volume integral of the co-energy are close in two adjacent rotor positions and round-off error can reduce the torque estimate. Round-off error becomes more significant at small angular steps when the values of co-energy are very close. On the contrary, a large angular increment leads to a low informative torque estimate that can be considered as an average over the region [29][33].

$$T = \frac{\partial W_C}{\partial \theta} = \frac{\partial}{\partial \theta} \int_{V_M} \int_0^H B dH dV \tag{4.13}$$

Experimentations are shown that the cogging torque, which is calculated from the rate of total co-energy of the motor, has about ten times higher magnitude for the torque than the results from the Maxwell stress computation. The shape of the cogging waveform is near to sinusoidal shape. The method has been repeated in the Modeller-3D with tetrahedral elements and in Pre-Processor by using the solver for rotating machines. The latter facilitates to achieve smaller positional increment. Due to the large discrepancy between the two methods, the Maxwell Stress method is preferred. Moreover, the fact that the energy method needs two simulations in order to obtain torque in one position makes it less attractive. The large difference between the torque computation methods does not smooth the progress of the analysis on mesh quality.

Static characteristics

A series of 3D FE computations is made where, in order model the rotor angular displacement, either the magnetization pattern is shifted or the mesh is shifted. The single-piece magnet, wherein the distribution of the magnetization vector can be described as a function, simplifies the FE modeling of the rotation. Otherwise, the angular displacement of the 3D FE mesh needs to be modeled so that the symmetry conditions couples the periodicity surfaces. The smallest surface, where a boundary condition can be specified, is a facet in the Opera-3d Pre-processor. The pole pitch of the motor is divided into 12 sectors and this determines the smallest discrete angular displacement of the mesh rotation. Alternatively, a solver for rotating machines is used in order to compute the torque and flux as a function of the rotor position. The smallest

angular increment is specified according to the angular width of element sector on a sliding surface. The drawback of using Vector Fields solver for rotating machines (CARMEN) is that the whole motor needs to be present. The advantageous model size reduction, by the help of the periodicity condition, enables to model motors with high pole numbers in Jmag-Studio. By using the FE solver for rotating machines, it is useful to keep the rotation speed low so that the dynamic field effects are reduced [18]. The undefined functionality of nonlinear characteristics of magnetic materials and torque computation with Maxwell Stress method excludes FEMLAB's powerful FEA tool from this study [17].

The polar anisotropy along the inner radius can be described as a mathematic function of material or magnetization vector orientation. More advantageous is to use the data obtained from a magnetizer as an initial condition for a FE model. This feature is not available in Opera-3D where the real magnetization distribution needs to be written as a mathematic function in the magnet volumes. The advantageous feature of importing the magnetization patterns is actually the only way to introduce the idealized circular polar magnetization along the inner periphery of the magnet-ring in Jmag-Studio (v8.1.0).

The FE model with the lateral polar magnet-ring (Figure 4.2) according to the specified measures (Table 3.1), is built and the static characteristics of the single-phase (Figure 4.4) and two-phase (Figure 4.5) claw-pole motors are calculated.

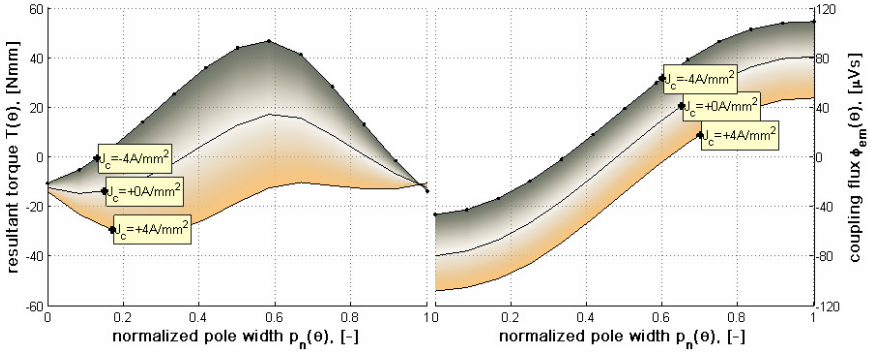

Figure 4.4: Static characteristics of the single-phase claw-pole motor. A stator core of the initial design has a larger cross-section area of the base-core, which is due to smaller hole (1.5 mm) for the axis.

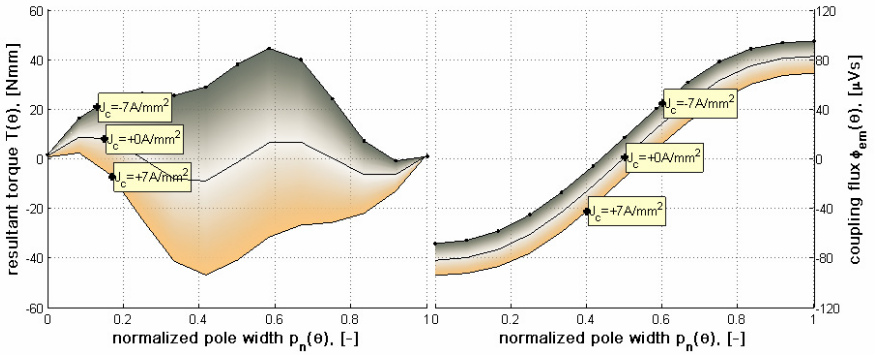

Figure 4.5: Static characteristics of the two-phase claw-pole motor. The outer rotor has solid magnet cylinder with circular polar magnetization pattern. The magnet utilizes all the rotor excitation volume available.

If instead an outer rotor with surface mounted radially magnetized magnets are used then the magnet volume is reduced, the coupling flux decreases due to that, and the cogging increases because of the unsmooth magnet mmf (Figure 4.6).

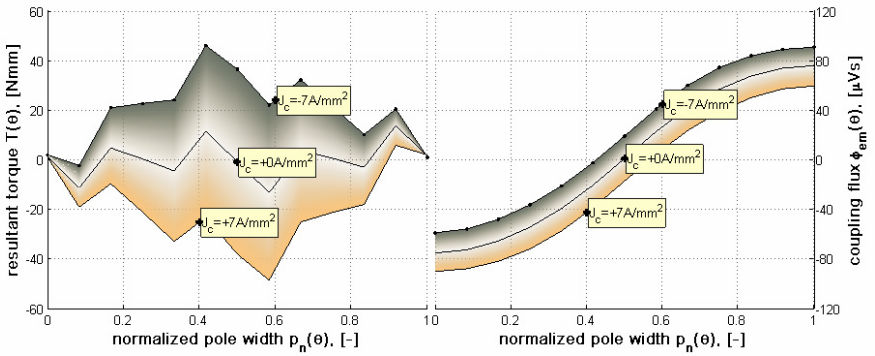

Figure 4.6: Static characteristics of the two-phase claw-pole motor. The outer rotor motor has surface mounted radially magnetized magnets. The optimal angular width of magnets K_m=0.58 is selected.

Apart from the torque and flux as a function of position, the core losses are calculated from the series of static 3D FE computations.

4.2 Core loss prediction

A core loss model (Eq. 3.17) is attached to the FEA in the post-processing level. A series of FE models, which have been created to compute the static characteristics of the motor, are used to follow the behavior of the magnetic loading and to describe the spatial and temporal variation of a field. The change of the flux density vector is recorded at each angular step and in each finite element. The identical mesh and the same element numeration facilitate the data processing. The mesh rotation changes the element numeration and the space coordinates. Moreover, the calculation can be carried out from the same motor with completely different meshes. The field values are read according to a reference FE model, which is used later to upload the loss calculation results (Appendix C). The field values are read from and the results written into the centre coordinates of the 3D finite elements.

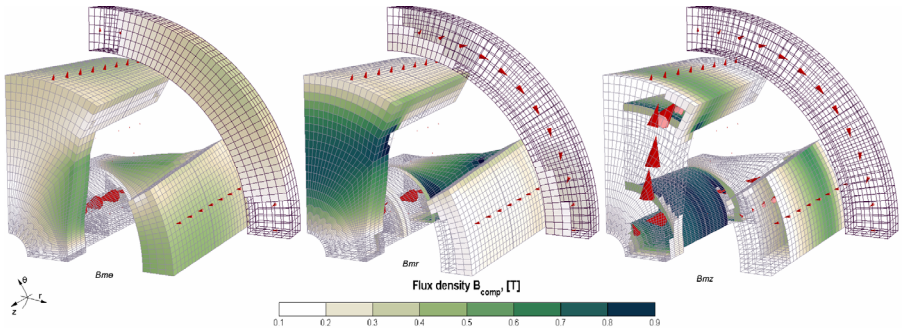

Figure 4.7: The magnitude of flux density components at the fundamental magnetization waveform in the claw-pole structure. The dc component of the permanent magnet excitation is shown in a slice of the magnet-ring. Circumferential flux density component B_θ is shown in the left, radial flux density B_r in the middle and the axial flux density B_z is shown in the right. The color mapping of the flux density magnitude is between 0.1T and 0.9T. The increment is 0.1T. If the flux density value is below or exceeds the scale of color mapping then the transparency is defined.

The magnitudes of the fundamental flux components are shown in finite elements (Figure 4.7). At the alignment position the radial and the axial components are present, while the rotation gives a rise to the circumferential component. It can be seen from FEM that the flux alternation occurs in the base core, while the flux density loci are close to a circle in the claw-poles and it forms an ellipse in the flanks (Figure 4.7).

The specific hysteresis loss energy over the stator core is calculated for the alternating and for the rotating flux density vector that forms different loci. The ratio of the minor to the major ellipse axis (Figure 4.8) is defined as

$$\frac{B_{\text{minor}}}{B_{\text{major}}} = \frac{\min(B_{\text{mod}})}{\max(B_{\text{mod}})}, \tag{4.14}$$

where B_{mod} is the modulus of the varying flux density vector as a function of the rotor angular position. The formulation becomes erroneous if a dc flux density component is present.

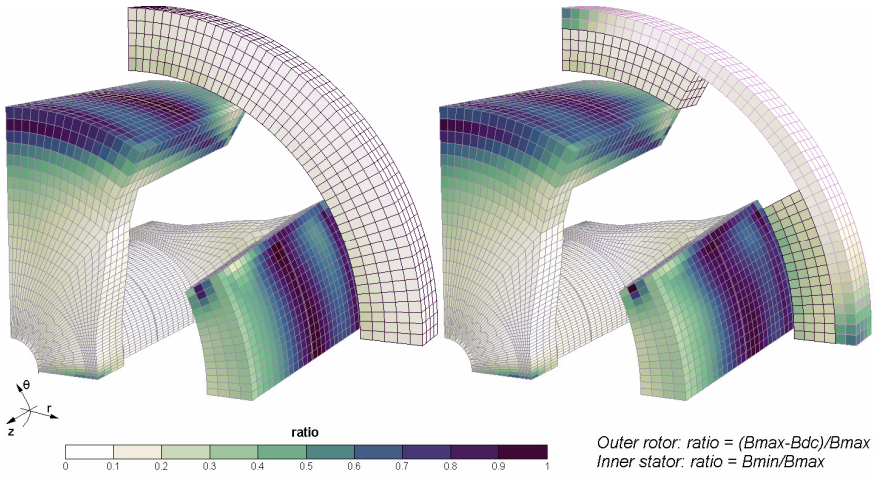

Figure 4.8: The ratios of flux density component show the rotation of flux density vector in different parts of claw-pole structure, and flux variation in the outer rotor. The flux density vector circular rotation occurs in the claw-poles (ratio=1), the ellipsoidal rotation is partly presented in the flanks (ratio=0.5). The field is alternating in the centre of the core (ratio=0). The field variation in the rotor is indicated with a color tone different than white.

Discrete Fourier transform is made over each FE element over a magnetization cycle, where the weighted sum of higher harmonics is calculated (Figure 4.9). The total harmonic distortion in the stator core has a maximum of 2.5% for the circular polar magnetized magnet ring. If the outer rotor has surface mounted magnets (57% of permanent magnet material reduction), then the total harmonic distortion is as high as 15%, while the average torque is the same.

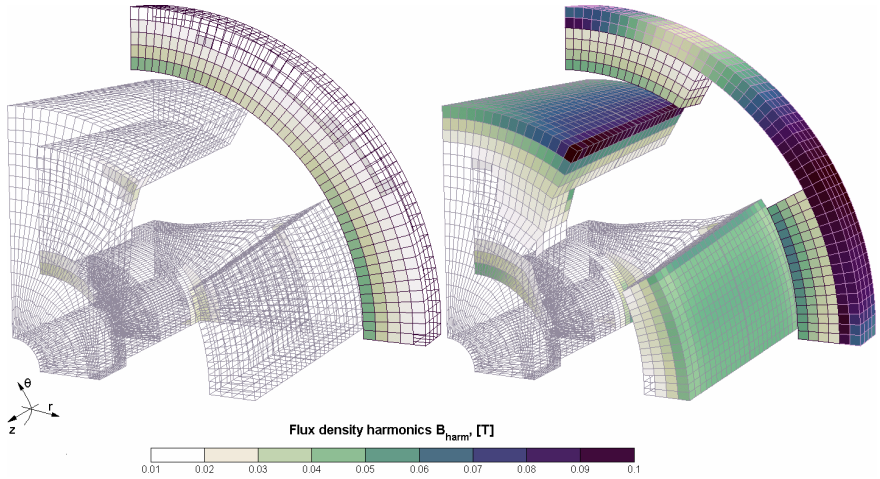

Figure 4.9: Flux density higher harmonics in the stationary claw-pole core and in the rotor.

A high field derivative in the claw-poles is expected due to the rapid change of magnetization, when the radial magnets are present. The flux pulsation in the rotor is due to the change of the gap permeance when the rotor rotates. The rotation direction determines the asymmetry in the high harmonic flux density distribution. The additional core loss, apart from the hysteresis that is caused by the flux density alternation, appears in the core due to rotational loci of $\boldsymbol{B}$ (Figure 4.10).

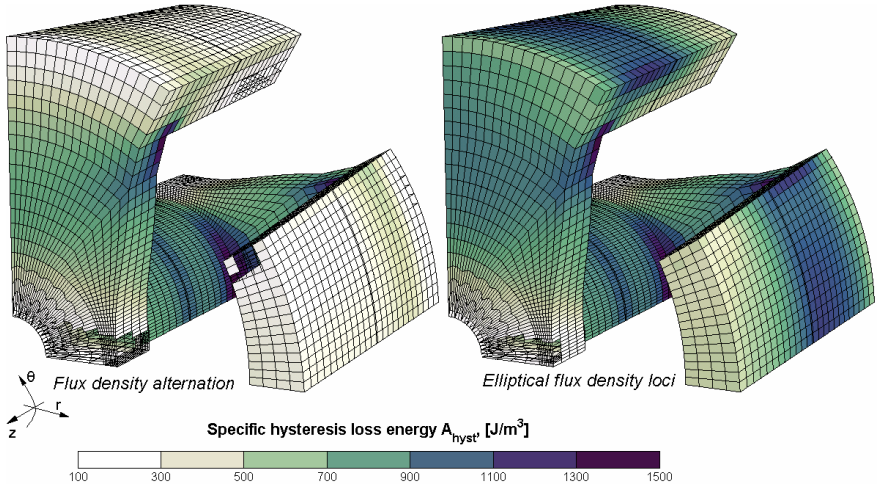

Figure 4.10: Specific hysteresis loss energy at different flux density loci. The specific loss energy due to the field alternation (left) and the ellipsoidal rotation (right) are shown.

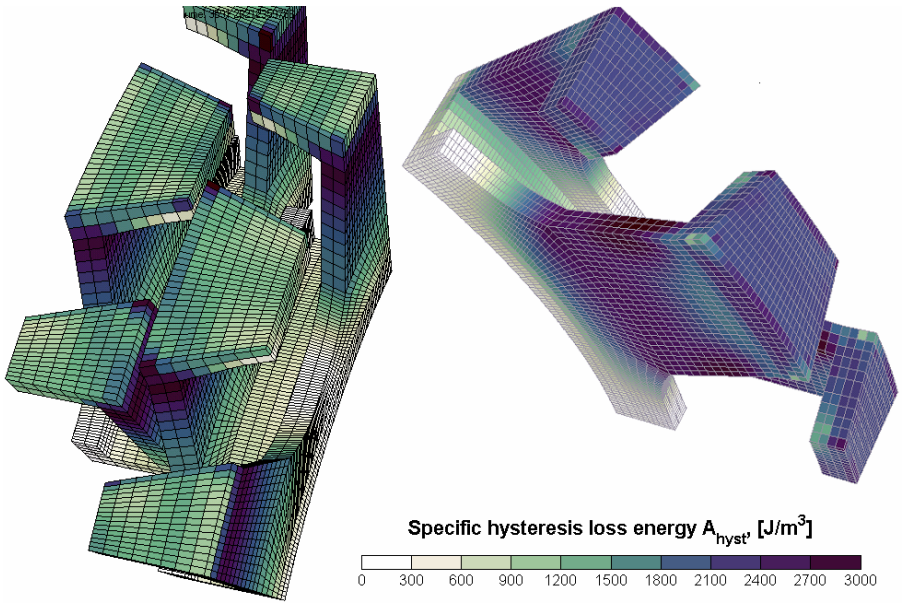

Figure 4.11: Specific hysteresis loss energy of the two-phase claw-pole motor according to the field alteration and the resultant field ellipsoidal rotation. The specific loss energy due to the field alternation (left) is calculated for a complete motor, which has an axial height of magnet equal to the height of complete stator. The ellipsoidal rotation (right) is shown for a single-phase placed in centre of a wide magnet-ring.

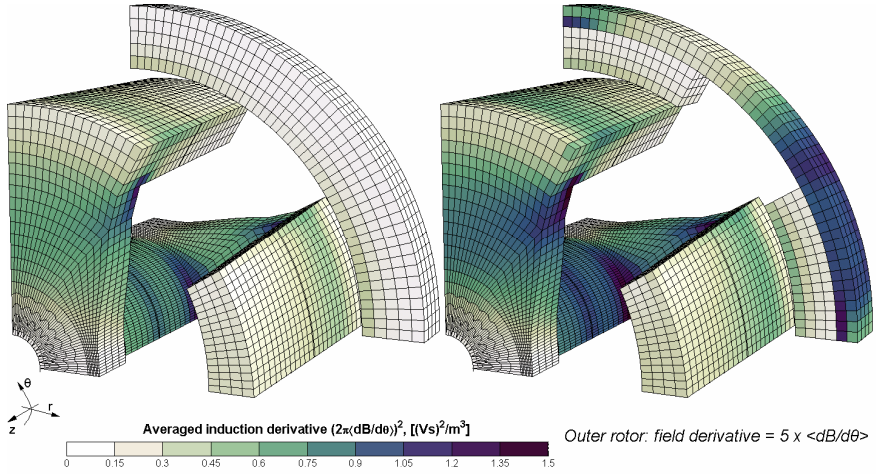

Figure 4.12: Quasi-static source of the classical eddy current loss. For the sake of visualization, the average induction change in the rotor is increased 5 times.

Table 4.1: Core loss components according to different permanent magnet excitation.

Quantity	symbol	unit	The single-phase claw-pole motor		The two-phase claw-pole motor	
Type of outer rotor magnetization			polar	radial	polar	radial
Hysteresis loss energy at alternating **B**	W_h^{line}	mJ	3.2	4.1	6.0	7.6
Hysteresis loss energy at rotating **B**	$W_h^{ellipse}$	mJ	5.2	6.1	6.9	8.0
Anomalous loss at alternating **B**	W_a^{line}	$mJ \cdot s^{-0.5}$	0.11	0.14	0.21	0.30
Dynamic loss at alternating **B**	W_d^{line}	$mJ \cdot s^{-0.4}$	0.15	0.19	0.24	0.35

The core losses are calculated at no load. If the same formulation is used to calculate the loaded motor then the core losses are increasing between 13-20% in respect with the motor configuration. This formulation is expected to be erroneous in case the motor is fed from a voltage source converter.

4.3 Structural mechanics

The structural mechanic problem focuses on the calculation of the electromagnetic forces in an elastic solid that is surrounded by air and constrained with mechanical support. The total force applied to the body is calculated by integrating the Maxwell stress tensor in the air outside of the pole. This is the only way to determine the forces applied to the body, where the exact distribution of the volume forces is not known. In order to retrieve the exact distribution of volume forces the interaction between the magnetization and strains (magnetostriction) has to be known [17].

3D FE formulation for structural mechanics

The physical coupling of the magneto-elastic problem is considered as weak. In order to study the influence of the tensile stress to the claw-pole structure, Navier's equation for structural mechanics is considered. The normal stress is applied locally to the claw-poles, while the inner radius of the claw-pole ring is constrained. The stress is applied only to the outer surface of the claw-pole ring. Even though the magnetic field is present all around the structure, it is considered to be small that the affect of the other stressed surfaces would be

neglected. Furthermore, the weak coupling formulation does not consider the mechanic strain influence on the magnetic permeability.

The normal stress component is evaluated from the magnetostatic analysis with no currents (FEMLAB). This physic formulation is necessary in order to couple successfully the periodicity surfaces of a single pole-pitch of the claw-pole structure. If there is no magnetic flux flow expected through the periodicity planes, then Dirichle't condition of magnetic insulation can be specified. Therefore the single-phase motor that has an asymmetric air-gap has to be analyzed in magnetostatic solver with no stator currents present [17]. Otherwise, the whole motor needs to be modeled where the magnetic vector potential have to be calculated (FEMLAB v.3.0). The size of the FE model is reduced considerably if the single magnetic total scalar potential is calculated at every node point in one quarter of the motor instead of vector potential at every node in the whole motor. Consequently, the mechanic stresses can be underestimated as the affect of the coil field component. The influence of the rotor position is not accounted. On the other hand, the magnetizing influence of the coil field on the gap-flux density is relatively small (variation of the maximum flux density in the gap is less than 3%). The increase of the tensile forces over claw-pole is the highest of 15%, considering the contribution of the coil field at rated current and the position with the maximum gap induction.

In the case of the two-phase claw-pole motor, the smallest unit that is to be analyzed is a single pole pitch of the single phase. The symmetric part of the motor can be analyzed either with magnetic scalar potential or magnetic vector potential formulation, because there is no flux flow in the normal to the periodicity surfaces. The tensile stress applied to the claw-pole surface has the highest of 4.4% difference between the minimum and the maximum stress. This is due to the position and the contribution of the coil field at the rated current.

The symmetric boundary conditions in the structural mechanic analysis are the locked displacements along the normal of the periodicity surfaces. In the case of asymmetric gap over the pole pitch of claw-pole structure the displacement vectors need to be coupled on the corresponding periodicity surfaces (Eq. 4.15).

$$\mathbf{u}(r,\theta,z_0+z)=\mathbf{u}\left(r,\theta+\frac{2\pi}{N_p},z_0-z\right) \tag{4.15}$$

Mechanic stresses of the assembled motors

The magnetic attraction for the assembled motors at alignment position is computed. The lateral polar magnetized magnet-ring is the source that causes tensile stress to the core of the single-phase claw-pole motor (Figure 4.13 on the left) and the core of two-phase claw-pole motor (Figure 4.13 on the right).

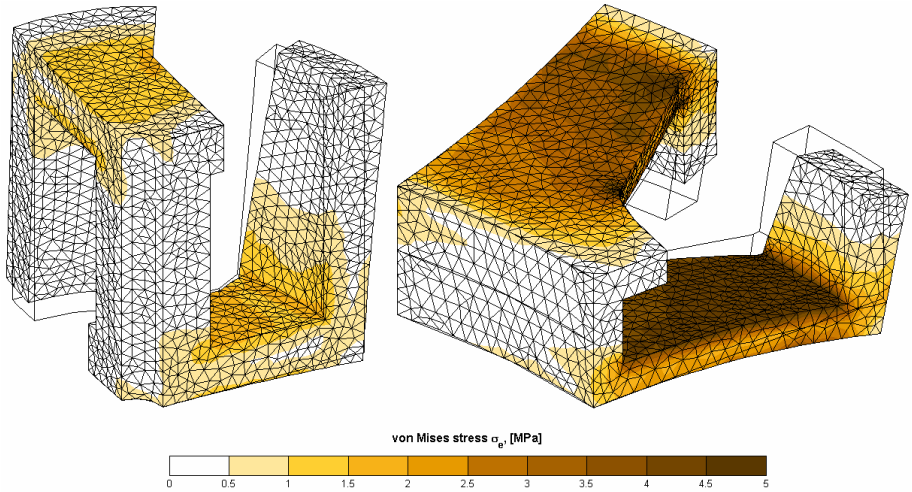

Figure 4.13: Mechanical stress due to magnetic attraction in the air-gap.

The maximum value of the effective stress is almost five times larger for the two-phase claw-pole motor than for the single-phase claw-pole motor, while the surface force is more than double for the single-phase motor pole. The thin stator structure of the two-phase claw-pole motor suffers under an obvious mechanic loading compared to the single-phase motor. However, from the safety margin point of view, the estimated effective stress is just 5% of the transverse rupture strength of a compressed core SMC core with 0.6% of LB1, for the two-phase claw-pole motor.

The tensile stress displaces the tip of the pole as much as *3 μm* and *4 μm* for the single-phase claw-pole and the two-phase claw-pole motor, respectively.

Mechanic stresses in motor assembling

The two-phase claw-pole motor needs a special concern while assembling. The narrow gap combined with large gap diameter requires high precision in motor assembling in order that the mechanic contact between the rotor and the stator could be avoided. The shorter axial height of the motor does not give an advantage compared to the longer motor as the limited space for mechanical

support and the accuracy of centering are equally complex. Furthermore, the magnet-ring attracts and stresses the stator core already in the process of assembling. When the centered motor parts have a space between of *1 mm* then the same order of effective stresses can be noticed in the stator core (Figure 4.14) as the assembled machine (Figure 4.13).

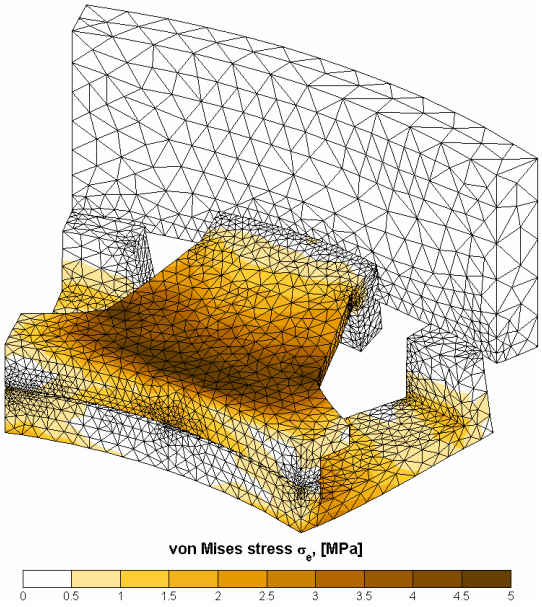

Figure 4.14: Mechanical stresses in a claw-pole ring of the two-phase claw-pole motor due to the rotor assembling.

Similar to the plane stress analysis, the 3D elasticity analysis does not couple the problem of heat flow analysis in order to consider the effect of the thermo-elasticity.

4.4 Heat transfer

If the FEA of structural mechanics can be focused only on a single body from the whole FE model then in the thermal analysis the presence of all the heat carrying media need to be considered. Similar to the thermal equivalent circuit, the biggest influence on the temperature distribution has the determination of heat dissipation. The heat dissipation can be defined as a heat transfer coefficient for a certain cooling area, where the coefficient describes the heat dissipation under natural convection. The heat transfer coefficient for natural

convection h=5-25 $W/(m^2 \cdot K)$ depends on 'natural' cooling conditions. Alternatively, the fluid dynamic formulation can be coupled to the heat transfer problem that the temperature dissipation on the solid motor bodies depends on the condition of how the surrounding air 'dissipates' the heat.

3D FE formulation for heat transfer

The stationary (i.e. time-independent) heat problem is described as a balance (Eq. 4.16) between heat supply to the body per unit of time and the amount of heat leaving the body per unit of time [83].

$$\nabla \cdot (k \nabla \vartheta) + Q = 0 \tag{4.16}$$

The thermal conductivity, is denoted by k, and describes the relation between the heat flux vector q, and the temperature gradient. This relation is also known as Fourier's law of heat conduction. This differential equation of the heat balance is solved for a finite size of volume which boundaries specify the heat flow through them. The boundary conditions can be of Dirichlet type, where the temperature ϑ on the boundary is specified. This boundary is used to describe, approximately, a boundary with very high heat transfer coefficient. A Neumann type of boundary condition specifies the heat flux flow q_n through a boundary. Anyway, it is not possible to prescribe the heat flux and the temperature at the same region. The unknowns are described in terms of a linear combination of the flux and the temperature. Newton's convection boundary condition is

$$q_n = n \cdot (k \nabla \vartheta) = h(\vartheta - \vartheta_{amb}) . \tag{4.17}$$

The heat flux flow through the boundaries to the surrounding is described with the heat transfer coefficient h and the external temperature ϑ_{amb}. The convective heat transfer to the surroundings is dependent on the geometry and the cooling conditions. The radiative heat transfer is considerably small for a small temperature difference. The convective heat transportation, which is fluid motion around a body, is a very effective means of transporting heat between the body and the fluid. The type of fluid, the velocity of the fluid, etc. determine the value of convection coefficient. The heat transfer, more specifically the convection coefficient, determines a positive heat flow which can be seen as a negative heat source in the heat balance equation.

The stationary heat balance can be formulated for a number of cases such like a loaded motor with a constant speed, a locked rotor motor with extensive current loading or some other circumstances. The different cases introduce a

number of heat sources and heat dissipation sinks. The case of the locked rotor motor with extensive current loading at starting condition specifies the problem, which determines the limit of resistive heating in the coil. In this case the heat source is only considered to be the resistive heating in the coil due to presence of dc current. Thus, the effect of ac current and core losses are neglected, even if they can be present in the starting conditions. The heat dissipation is only considered by the natural convection.

The calculation of the thermal limit for the electric loading is a problem of multiphysics that involves resistive heating, heat transfer and fluid dynamics. The heat sources and sinks can be considered directly in the differential equation of the stationary heat balance. The source is the copper loss dissipated in the coil volume, where the equivalent thermal conductivity $\lambda_{coil}=0.11\ W/(m \cdot K)$ considers how the coils are wounded [21]. Convective heat transportation is introduced in the inner boundaries, when the whole problem is surrounded by air, and bounded with the value of the ambient temperature ϑ_{amb} in the boundaries. The boundaries of the motor constructional periodicity are considered as heat insulations that restricts flux flow normal to the surfaces. A resistive heat source is considered at the rated current. The distribution of the temperature rise in the motor volume is computed for the single- phase and for the two-phase claw-pole motor (Figure 4.15).

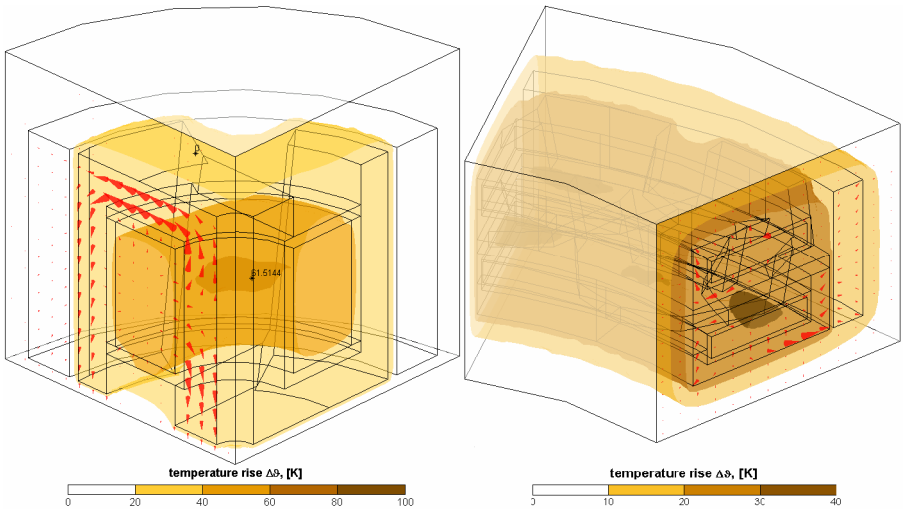

Figure 4.15: Distribution of the temperature rise in the claw-pole motors according to predefined heat convection at the inner boundaries: The hot spot for the single-phase claw-pole motor (left) exceeds 60K, while for the two-phase motor (right) the temperature rise exceeds 30K.

The convective heat transfer is specified on the outer surfaces of the rotor, on the one side of stator and on the surface of the inner radius of the stator. It is observed that the size of the surrounding air influences the temperature distribution inside the motor bodies. This phenomenon is due to the large difference between the thermal conductivity of different media. If there is no internal heat dissipation, considered from the motor surface, then the distance of the external boundary from the motor bodies determines the overall heat dissipation.

Fluid mechanics coupled to heat transfer problem

For a complete heat transfer and dissipation formulation, two types of equations are joined in order to calculate the complete problem [17]. A heat transfer convection-diffusion equation

$$\rho c_p \frac{\partial \vartheta}{\partial t} + \nabla \cdot \left(-k \nabla \vartheta + \rho c_p \vartheta \mathbf{u} \right) = Q, \tag{4.18}$$

together with incompressible Navier-Stokes equations for fluid dynamics

$$\begin{aligned} &\rho \frac{\partial \mathbf{u}}{\partial t} + \rho \cdot (\mathbf{u} \cdot \nabla) \cdot \mathbf{u} = -\nabla p + \eta \nabla^2 \mathbf{u} + \mathbf{F}, \\ &\nabla \cdot \mathbf{u} = 0 \end{aligned} \tag{4.19}$$

are solved for a 3D finite element model. The pure Incompressible Navier-Stokes equations consist of a momentum balance, a mass conservation and incompressibility condition. There are three unknown field variables: the velocity field components $\boldsymbol{u}$, the pressure p and the temperature ϑ. They are all interrelated through bidirectional multiphysics couplings. The additional variables are: $\boldsymbol{F}$ is a volume force, ϱ is the fluid density and η is the dynamic viscosity. The heat equation interprets an energy conservation principle, where the change in energy equals to the heat source Q minus the divergence of the diffusive heat flux. The heat flux vector (the expression in the brackets) contains a diffusive and a convective term, where the latter is proportional to the velocity field $\boldsymbol{u}$. The properties of the heat carrier medium that is air, which surrounds the motor, are described by the heat capacity of the fluid c_p, the thermal conductivity λ and fluid density ϱ. The heat capacity or specific heat is denoted by c_p, and describes the amount of heat energy required to produce a unit temperature change in unit mass, that is the capacity of a material to store thermal energy.

The heat transfer and fluid dynamics equations are coupled through the $\boldsymbol{F}$ and Q terms. Free convection is accounted to the momentum balance according to the Boussinesq approximation

$$F_z = \alpha \cdot g \cdot \rho \cdot (\vartheta - \vartheta_{amb}). \tag{4.20}$$

where α is volume expansion coefficient of the fluid. Thereby, variations in density with temperature are ignored, except insofar as they give rise to a buoyancy force that lifts the fluid (Marangoni Convection). The effect of temperature on the density of the fluid is entered only as a buoyancy force in the z direction. Hereby, the motor is in horizontal xy-plane and the air circulation occurs according to vertical axis z (Figure 4.16).

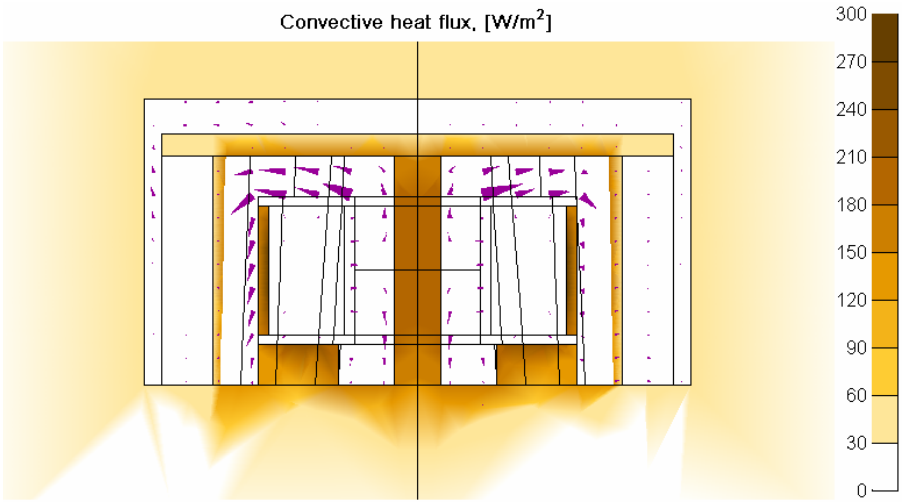

Figure 4.16: Simulation results of heat convection in surrounding air (filled zones) and heat transfer from the motor body. The temperature rise in the coil of 56 K is due to the resistive heat loss about 2 W. The speed of air circulation is 0.005 m/s along the vertical axis. A shaft is not included in the model.

Heat transfer of a distributed heat source

So far it has been considered that there is uniform distribution of the resistive heat loss in the coil and no loss present in the motor core. In reality, the current density displacement in the parallel strands and inhomogeneous distribution of core losses affects the thermal loading in different parts of motor.

4.5 Incorporating 3D FEA in an optimization routine

Similarly an optimization routine that bases on the EC models, the FE model reliability is important, in particular, when the geometrical or material changes are introduced. The geometrical changes are rather made according to visibility study than to an objective function driven 'search'. In this study the gap radius and the number of poles are changed gradually. As a result, the magnetic loading, electromechanical coupling and loss production is studied. The reason why the broadsearch method is called as visibility study, is the advantageous feature of the method to scan systematically through a number of motor designs and to visualize the result a solution of a specific problem. Relatively coarse 3D FE mesh is used in order to maintain short simulation time for a single model. Around 100000 elements are used to represent the symmetric part of the single-phase claw-pole motor.

Apart from the correct FE model formulation, the other important factor is reliable meshing routine. The 3D mesh of hexahedral elements is constructed by extrusions of layering of a 2D geometry formulation on a base plane. The extrusions form a number of macro volumes, which fill the whole model volume layer by layer from the base to the top. These macro volumes represent different materials and potential types in the FE model. The automatic meshing fills the macro volumes with elements according to the specified subdivision on the edges. One particular problem in the Pre-processor is in the node transformation routine, wherein the hexahedral macro volumes are formed to give a shape to a claw-pole structure. When the corner points of these hexahedral volumes are close to each other then there is a risk that the displaced point coincides with an un-shifted node point. The next displacement subroutine task selects and displaces incorrect nodes and destroys the continuity of the macro volumes.

In order to make the hexahedral meshing successful, basically, the 3D FE mesh is constructed first and motor parts are defined later. Alternatively, the motor parts can be defined first and later the volumes can be filled with elements. Usually, only the 3D FE mesh with tetrahedral elements can be created for the 'uncontrolled' volumes. The changes in the geometry are harmful to the successful meshing of the tetrahedral elements as much as of the hexahedral elements. The reason is that the conditions for the automatic mesh generator, like the shape of the motor body, proximity of the other bodies etc., are changing and new condition might not be successful to complete the meshing task.

Visibility study of a single-phase claw-pole core

The number of poles and the inner radius of the stator have been changed. This change is made to visualize the quantitative values such as magnetic loading, losses and the output of the electromechanical coupling in a claw-pole structure. The volume of the phase ring is constant and the proportions of the cross-section area are kept unchanged. The gap length as well the radial length of the bonded ferrite magnet-ring is the same. The stator core of N_p*=4 poles* and the inner radius of r_i*=2 mm* corresponds to the single-phase claw-pole motor. The magnetic loading of the N_p*=4 pole* and N_p*=20 pole* motors at three different inner radii are presented. There is no asymmetric air-gap present and the circumferential tapering has been changed between γ_1*=0°* (Figure 4.17) and γ_1*=5°* (Figure 4.18). The mechanic contact between the claw-pole rings is considered to be ideal without any axial air-gap present.

A number of problems are formulated:

- Magnetic loading of the claw-pole core,
- Field coupling and field weakening ratio,
- Core losses for an alternating and for a rotating field,
- Cogging torque waveform,
- Core loading, evaluation of coupling torque and core losses,
- Calculation for different permanent magnet excitation.

From the results, which are obtained for the single-phase claw-pole motor, the output of the electromechanical energy conversion for the two-phase claw-pole motor can be predicted.

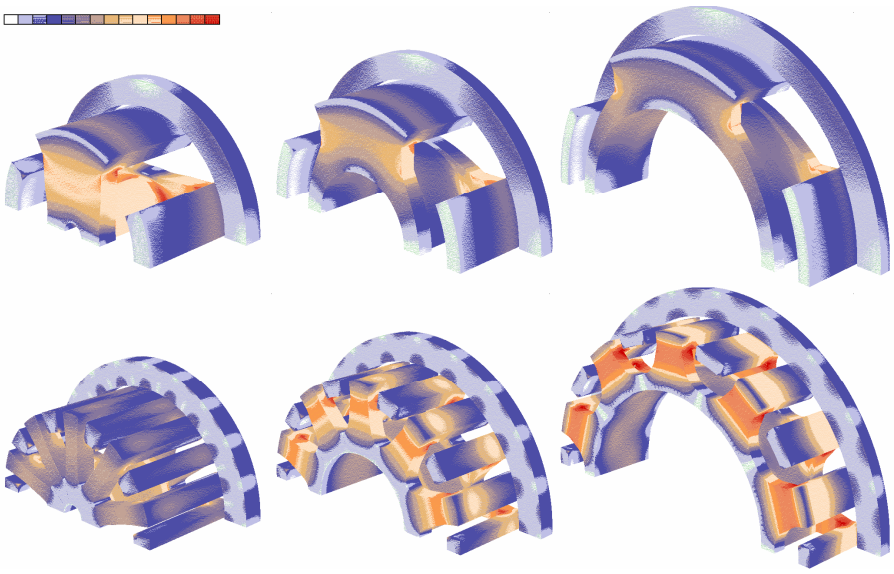

Figure 4.17: Magnetic loading between 0 and 1.5T of a single-phase claw pole structure with circumferential tapering of γ_1=0°. A geometric change is introduced in the number of poles N_p of 4 and 20, and inner radii r_i of 2, 10 and 20 mm.

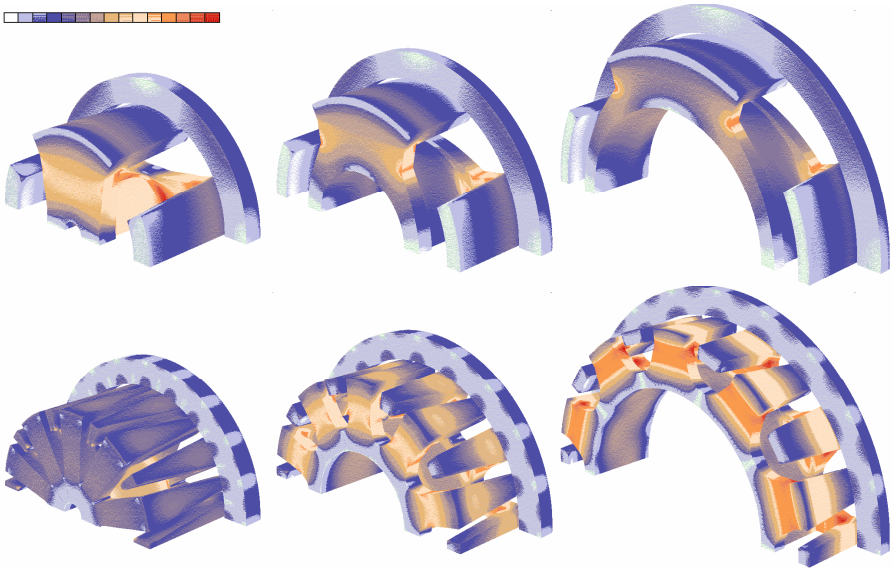

Figure 4.18: Magnetic loading between 0 and 1.5T of a single-phase claw pole structure with circumferential tapering of γ_1=0°.

The volume of the stator is the same as the stator of the single-phase claw-pole motor. It can be argued whether the variable rotor volume makes the visibility study impractical or not. The thickness of the magnet-ring is considered to be constant. The change in the gap radius increases the volume of the magnet and this variation is as big as 60% in this study. As the volume of the magnet is changing, the magnet source gets stronger when the inner radius of the stator core is increased. On the other hand this helps to understand the optimal shape of the magnet-ring that carries lateral polar magnetization pattern along the inner periphery. Basically, the magnet gets 'stronger' when the semi circular path of magnetization is formed inside the magnet-ring. On the other way around, the magnet ring with few poles and large inner radius forms 'unsupported' radial magnets on the poles.

The magnetic loading and the coupling flux show (Figure 4.19) the resulting outcome of the changes in geometry in the magnet-ring and the phase with claw poles. The figure shows the magnetic quantities for the core that has a rectangular shape of poles. Due to the increase in the inner radius of the stator core, the cross-section area of centre core becomes larger and the magnetic loading smaller. The increase in the number of poles causes the distance between the adjacent poles to be reduced. The leakage becomes correspondingly stronger and the magnetic coupling weaker. Larger surface area of magnet and 'embedded' semi-circular magnetization path at higher number of poles make the magnet-ring and the magnetic coupling visually stronger.

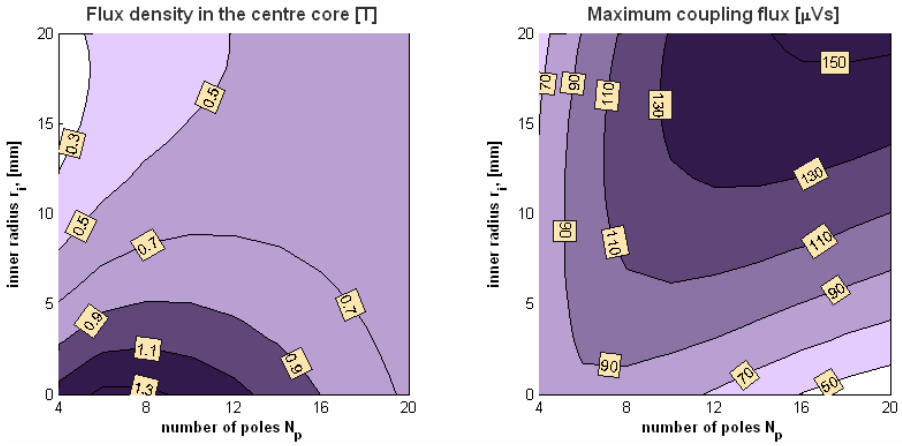

Figure 4.19: Flux density in the centre core and the coupling flux as a function of inner radius of the core and the number of poles.

The coupling flux increases proportionally with the number of poles when the circumferential tapering is introduced. The increase is the highest of 5% compared to the initial stator core of 4 poles and inner radius of 2 mm. The highest increase of the magnetic loading appears in the domain of high poles and small inner radius.

The other quantitative/qualitative values of the magnetic coupling between the magnet-ring and the core are the field coupling ratio (Figure 4.20 on the left) and field weakening ratio (Figure 4.20 on the right).

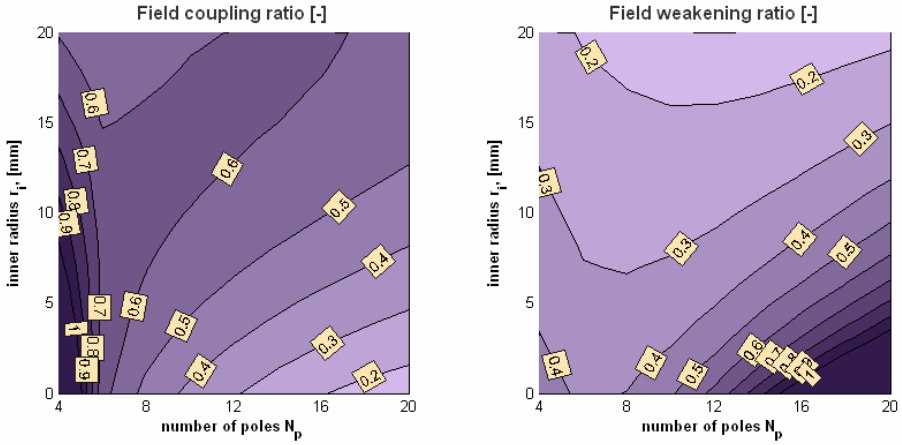

Figure 4.20: The amount of magnet flux seen in the centre core is defined as coupling ratio. The coil field ability to change the excitation field from magnets is noted as field weakening ratio.

A cross-section area of the magnet-ring in the radial/axial plane is taken as a reference area in order to compute the maximum circumferential flux through it. Alternatively, the magnetic flux passing a pole surface of the magnet-ring can represent the total flux from magnet. Inaccuracies of the total flux computation from the magnet can be present if the flux is calculated over the cross section area, especially, when the magnet-ring is thin and the pole pitch is large. The ratio of magnetic flux through the centre of the claw pole core to the total flux from magnet, as it is seen from the magnet cross-section area, is calculated (Figure 4.20 on the left). The field coupling ratio is largest at small number of poles and at small gap radius. The ratio is more uniform at large gap radii.

The coil field ability to magnetize or demagnetize the centre part of claw-pole core is visualized by the help of field weakening ratio. When the magnetic field coupling becomes weaker then the field weakening ratio is proportionally

stronger (Figure 4.20 on the right), if the coil field is constant. The electric loading of the coil is as high as *4 A/mm²*. That introduces a constant heat supply to the body of *280 kJ/(s m³)*. As the slot cross-section area changes and the wall thickness of a bobbin is kept constant then the total winding fill-factor of coil in respect of the slot opening area is reduced. Even though a full dense coil of 100% winding fill-factor is selected in conductor cross-section area, the total winding fill-factor decreases to *49.5%*, *38.2%* and *27.8%*, with the inner radii *2 mm*, *10 mm*, and *20 mm*, where the axial and the radial wall thickness of the bobbin is *1.5 mm*. The reduced copper volume reduces the copper losses, which are *2.40 W*, *1.25 W* and *0.71 W* according to the selected radii.

Core losses

The core losses are calculated on the basis of the core loss formulation. The calculation result for the static hysteresis losses is shown in Figure 4.21 for the alternating field according to the known loss coefficients [89] and for the resultant field of ellipsoidal rotation according to derived loss coefficients (Appendix A).

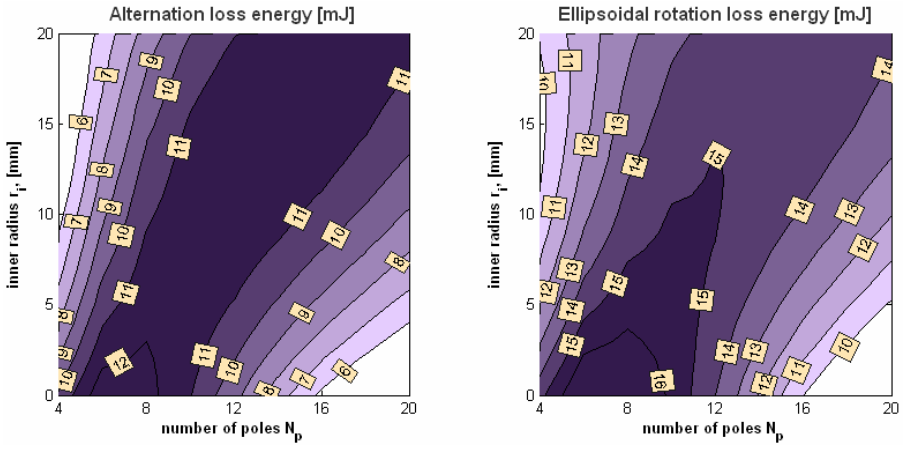

Figure 4.21: Static loss energy according to the hysteresis loss formulation per mechanic revolution. Figure on the right shows the loss if only the field alternation is considered. The complete hysteresis loss is presented on the left where the field rotation is taken into the consideration.

The comparison between the evaluations of the static core loss energy shows (Figure 4.21) that the uncounted effect of the field rotation leads to loss underestimation. The difference is from 1.4 or up to 2.0 times the alternating field loss. The specific hysteresis loss energy is dominating in the flanks and the claw-poles at the increased number of poles and inner radius (Figure 4.22).

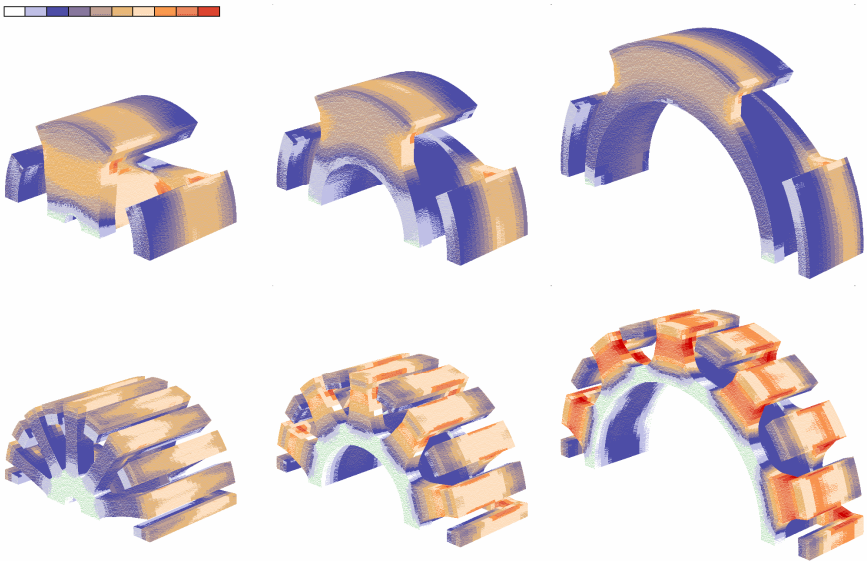

Figure 4.22: Hysteresis loss energy density between 0 and 2kJ/m³ of a single-phase claw pole structure with circumferential tapering of γ_1=0°. The geometric change is in the number of poles N_p of 4 and 20, and inner radii r_i of 2, 10 and 20 mm.

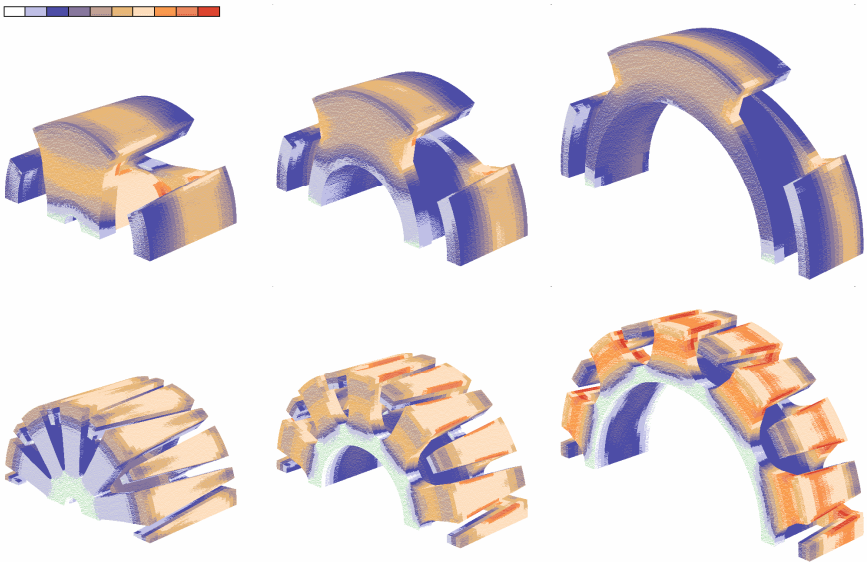

Figure 4.23: Hysteresis loss energy density between 0 and 2kJ/m³ of a single-phase claw pole structure with circumferential tapering of γ_1=5°.

The change of circumferential tapering from $\gamma_1=0^o$ (Figure 4.22) and $\gamma_1=5^o$ (Figure 4.23) increases the static losses in the domain of increased number of poles and small inner radius of the stator. This increase is as much as 5% compared to the initial core of 4 poles and inner radius of 2 mm.

Cogging torque

One qualitative criterion of the electromechanical energy conversion is low cogging torque. Similar to the coupling torque magnification, each pole contributes to the cogging torque. If there is no counteraction between the poles that is due to a different geometrical configuration of the other pole-pairs, then the cogging torque of a single phase is a multiple of poles.

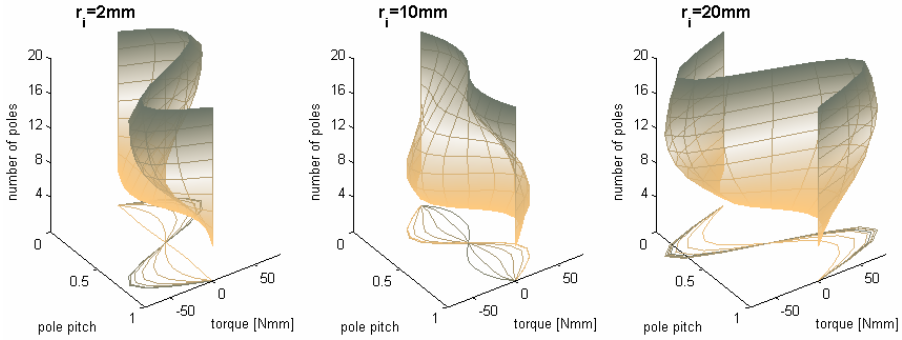

Figure 4.24: Cogging torque waveform depending on number of poles and on the air-gap radius. The air-gap radius is the result of a given inner radius and the constant volume of stator core. Depending on the coupling length through the core compared to the leakage via claw-poles the rotor has stabile equilibrium position where the coupling torque is the biggest for the symmetric poles.

The cogging torque as a function of number of poles and the air-gap radius has dominatingly sinusoidal waveform that is due to a magnet-ring which carries ideal circular-polar magnetization pattern (Figure 4.24). According to the relation between the transversal coupling flux path and circumferential leakage flux path the rotor of a claw-pole motor 'selects' resting position. The angular width of claw-pole is taken in proportions to the pole pitch ($K_p=0.35$). In consequence of increased number of poles, the leakage bath becomes shorter. As a result of the reduction of the air-gap radius, the transversal coupling flux path is longer. The latter is due to the increased cross-section area of the phase that is designed to keep the constant stator volume. The stabile equilibrium position of the rotor is the position where the magnet poles are between the claw-poles if the motor has small air-gap radius and more than 4 poles (Figure 4.24, leftmost figure).

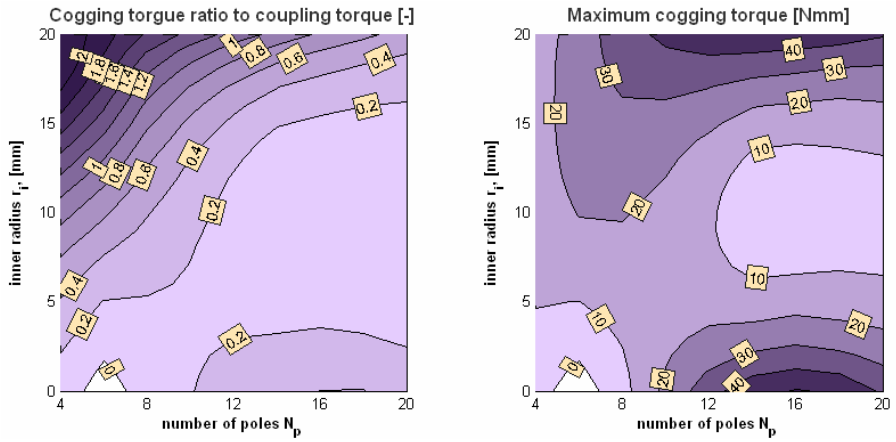

Figure 4.25: The maximum value of the cogging torque compared to the coupling torque (on the left) and the maximum value of the cogging torque for the different core construction.

Carefully selected angular width of the claw-pole for a certain number of poles gives advantage of the starting conditions of a single-phase core. Another important design issue is to get the cogging torque as low as possible or/and to maximize the ratio of coupling torque to the cogging torque (Figure 4.25).

Loaded core

One important output of the visibility study is the coupling torque (Figure 4.26) of the claw-pole motor as a function number of pole and air-gap radius. The air-gap radius is directly coupled to the inner radius of the stator core. The outer radius of phase its are *17.4 mm*, *22.0 mm*, and *29.6 mm* in respect of the increased inner radius of *2 mm*, *10 mm*, and *20 mm* at constant stator volume. The coil cross-section area is reduced about *79%* while the gap radius is increased and the bobbin wall thickness is kept constant. As the current density and the specific heat supply are remained unchanged, the total current in the coil is smaller in the motors with larger air-gap radius than the motor wit small gap-radius. The total heat source generated in the coil is 70% smaller at the final inner radius of *20 mm* compared to the initial radius at r_i*=2 mm*. Moreover, a cooling surface is *59.3%* larger at higher gap radius when only one side of the stator cylinder at circumferential/radial plane is considered as the cooling surface. Basically, the current density can be increased 2.3 times in order to get the same amount of copper losses per cooling surface for the motors, which inner radius of stator is r_i*=20 mm*. Consequently, the coupling torque, as a function of the air-gap radius and the number of poles, is less

dependent on the gap-radius. The results from the 3D FE visibility study show (Figure 4.26) that the increase of air-gap radius does not necessarily give benefit at higher radius and at increased poles.

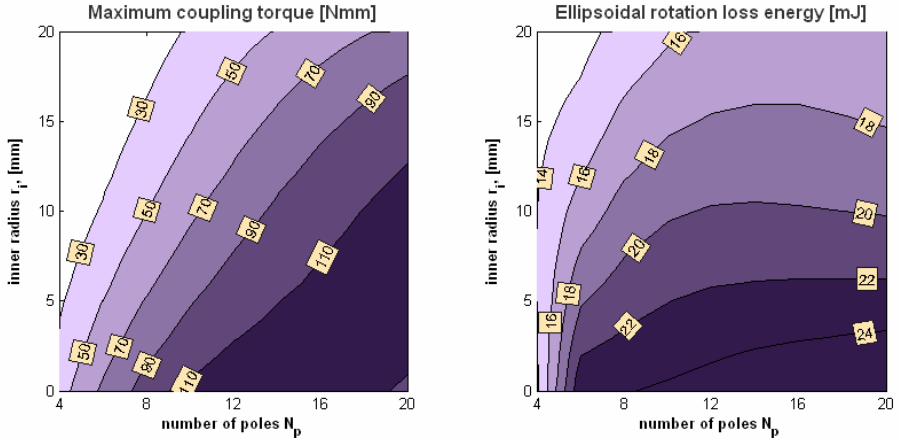

Figure 4.26: The coupling torque and core loss of the loaded claw-pole construction with rectangular pole shape at different pole numbers and inner radius of core.

The core loss formulation for magnetic hysteresis is not able to consider either the effect of the asymmetric hysteresis loop or the occurrence of the minor loops. The coil field influence on the excitation field rotation and rotational core loss is taken into consideration. The formulation that detects whether the field rotation or alternation takes place is not able to separate biased field alternation and pure rotation. As the number of steps over the magnetization cycle has been limited from 24 to 2, the positions of the pole alignment and the maximum coupling torque are not enough to determine whether the biased field alternation or rotation takes place. As a result, the magnetic core that is more loaded at the lower inner radius of the stator show excessive core loss.

Influence of plastic bounded NdFeB magnet-ring

Another important factor of the visibility study is the influence of the permanent magnet excitation. Similar to the previous study with the plastic bounded ferrite magnet-ring, the magnetic coupling, losses and the coupling torque is studied at the presence of the plastic bounded NdFeB magnet-ring.

The stronger magnet establishes stronger magnetic coupling and higher magnetic loading for the same stator core (Figure 4.27).

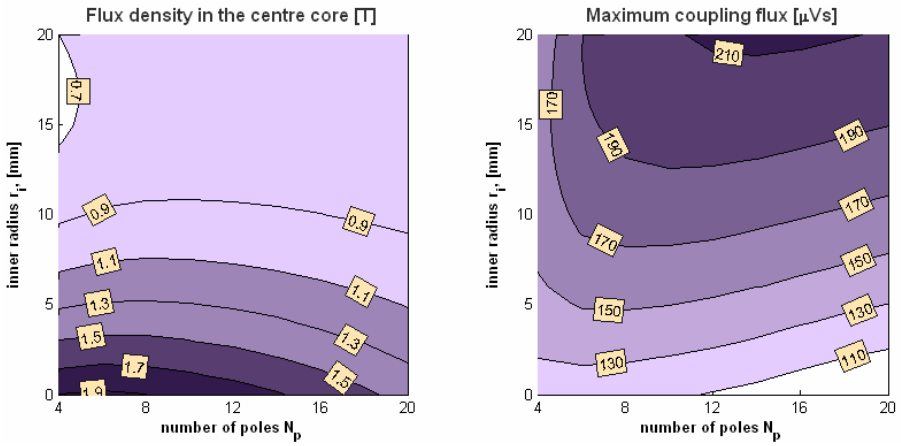

Figure 4.27: Flux density in the centre core and the coupling flux as a function of inner radius of the core and the number of poles. Plastic bonded Ferrite has been replaced with NdFeB magnet-ring.

Apart from the increase of the coupled flux around *40%*, the leakage is considerably higher for the new motor (Figure 4.28). This is partly due to magnetic saturation.

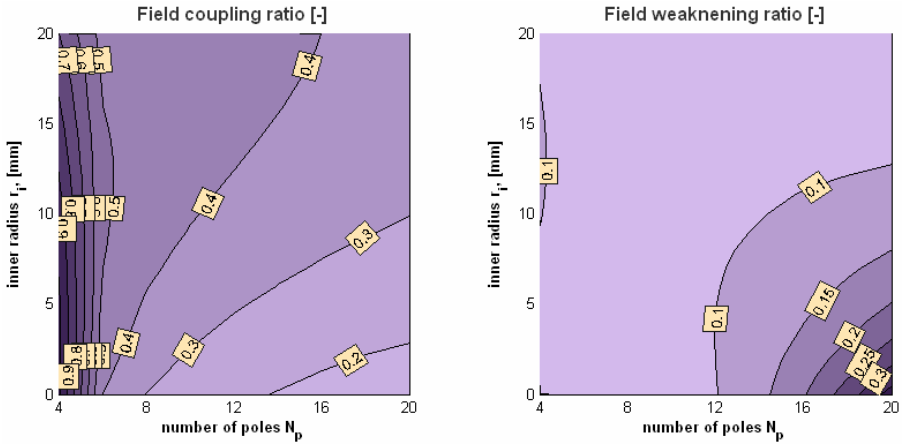

Figure 4.28: The amount of magnet flux seen in the centre core is defined as coupling ratio. The coil field ability to change the excitation field from magnets is noted as field weakening ratio.

As the magnetic coupling is stronger, the effect of the coil field to change it is smaller. As the stator core is nearly saturated, the hysteresis loss for the alternating field is about the same size as the hysteresis loss for the rotating

field (Figure 4.29). The hysteresis loss model for rotating fields is not adequate in order to predict the losses for highly saturated core parts.

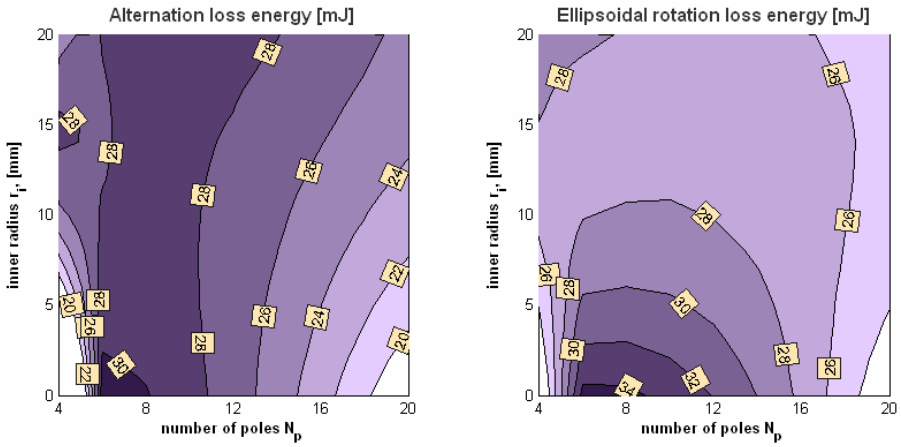

Figure 4.29: Hysteresis loss energy per mechanic revolution in the presence of NdFeB magnet-ring. Figure on the right shows the loss if only the field alternation is considered. The complete hysteresis loss is presented on the left where the field rotation is taken into the consideration.

The replacement of the magnet-ring doubles the maximum coupling torque of the core (Figure 4.30). The resultant core loss for the loaded core is determined according to two positions (Figure 4.30 on the right). The two position method, that is used to determine the major and the minor axis of the field rotation ellipse, is not enough in order to specify whether the field rotates or the field alternates and it is biased.

From this visibility study, it can be expected that the 20-pole two-phase motor is able to produce a coupling torque about *65 Nmm*. This estimation bases on the difference between active volumes of the claw-pole motors. The active volume is determined by the inner radius of the claw-pole core, the axial height of the claw-pole core and the outer radius of the magnet-ring. The hysteresis loss energy is expected to be around *10.4 mJ*. The predicted results are in the same range as the evaluated values for the initial design of two-phase claw-pole motor (Figure 4.5,Figure 4.6,Table 4.1). The overestimation is due to uncounted effect of an axial displacement of the phases.

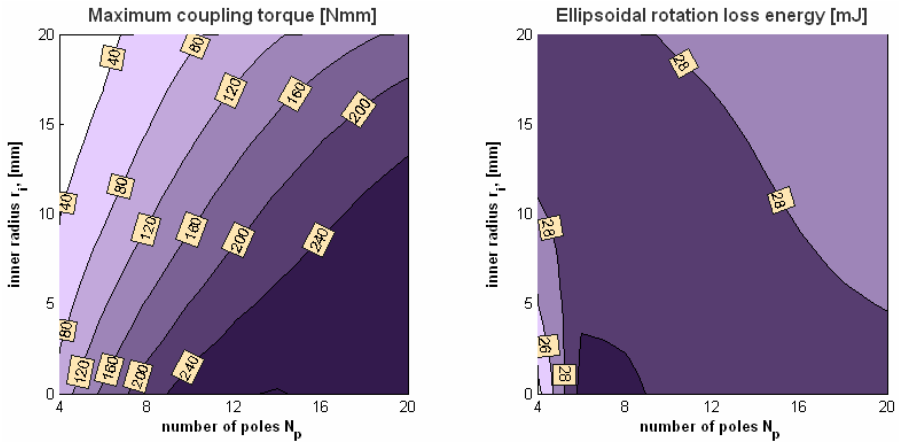

Figure 4.30: Maximum value of the coupling torque as a function of inner radius and number of poles. The corresponding hysteresis loss energy for the loaded core is shown on the left figure.

Summary

The visibility study of the claw-pole structure that is based on a series of 3D FE computations visualizes the qualitative and quantitative values of the electromagnetic energy conversion. The strength of the visibility study is to keep as many quantities unchanged as possible and to change 'key' parameters. The exhaustiveness of the problem formulation determines which quantities can be set unchanged in order that the comparability and readability of the result are obtained [93].

A better output of the motor can be reached at a higher pole number. A larger inner radius does not necessarily show improvements if the current loading is selected according to the thermal limit and the constant volume of the motor. An optimized motor construction with a ferrite magnet-ring is capable to produce an average torque about *60 Nmm* and this number increases for a stronger magnet. The magnetic coupling is limited by the leakage between the poles. The hysteresis loss, which depends on the trajectory of the flux density vector per magnetization cycle, reduces significantly for a magnetically unloaded core. The specific output of the maximum coupling torque from the single-phase claw-pole motor can be increased from the recent 0.1 Nm/kg to 0.6 Nm/kg at a temperature rise of 60 degrees.

The disadvantage of the simple EC circuits compared to the reduced 3D FEA is computational accuracy, that can handle correctly the complex problem.

Chapter 5

Sensitivity study and prototyping

In the sensitivity study one of the motor parameters is changed while the other parameters are kept constant. This refining is done for the further improvements of the proposed size of the claw-pole motors. A number of 3D FE calculations have been made in order to find out how the shape of the claw-pole structure influences the motor characteristics. The parameters, which are considered in this study, are the pole angles that influence the shape of the claw-pole and the circumferential width of the claw-pole. According to motor assembling, the factors such as the axial air-gap between the claw-pole rings and the axial displacement between the phases have been studied. The additional feature that is considered in the study of the geometrical tolerances and assembling is the radial length of the motor air-gap.

Apart from the changes which are introduced in stator geometry, the influence of material properties over the motor characteristics is analyzed. The importance of the magnetization of the magnet-ring is studied and it is compared with some other types of rotor constructions. Apart from the sensitivity study, the reliability of the obtained results has a great importance. The accuracy of the magnetic field representation in the middle of the air-gap is studied when a change in geometry, magnetization definition or material properties is introduced.

The FE model for the sensitivity study is made in Opera-3D Pre-processor where the hexahedral 3D FE mesh is created. Additionally, some cases are repeated in Opera-3D Modeller and Jmag-Studio that uses tetrahedral elements in order to discretize the model into a number of elements. The top view on the motor in the xy-plane and the respective initial conditions of the

magnetization vector, current flow direction in the coil and the direction of the motion from the initial position are specified (Figure 5.1).

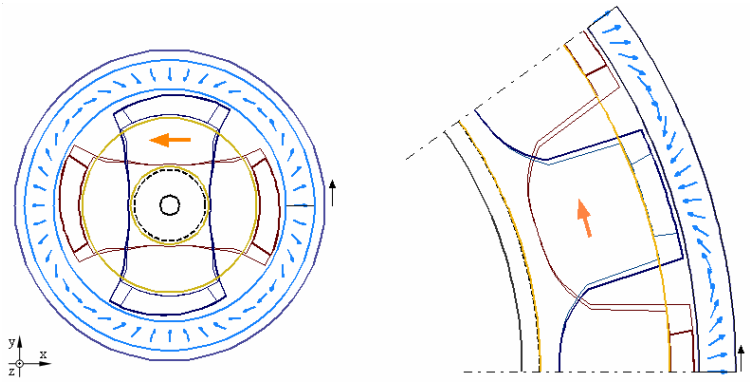

Figure 5.1: Specification of the negative current flow direction (big arrow on the winding domain), magnetization vectors (vectors in the magnet-ring region) and the direction of the motion (small dark arrow outside of the outer rotor) on the top view of the claw-pole motors in xy-plane. The rotor is turned from the initial alignment (0) to the next alignment position (1) of the same phase.

According to the initial condition the coil field is in opposition to the coupling transversal field of the permanent magnets. By neglecting the effect of the asymmetric air-gap to the static characteristics, this is an unstable equilibrium position for the motor with excited armature coil.

5.1 Variation in stator dimensions

It is considered that the 3D FEA is able to predict the magnetic field distribution more precisely than any 3D magnetic EC analysis. Moreover, the torque computation that bases on the predicted values of the field distribution is of great importance to the sensitivity study. The output of the study is to obtain the shape of the claw-pole ring that gives smallest cogging torque and largest coupling torque according to the proposed permanent magnet excitation. Apart from the possible improvements of the static characteristics of the motor, the influence of the manufacturing tolerances over the stator construction is predicted.

Optimal claw-pole shape

The width of the claw-pole as well as the angle of tangential tapering has been changed in order to find the optimal size and the shape of the claw-pole for

the single-phase claw-pole motor. If the tangential tapering angle is chosen to be large, then the magnitude of the reluctance torque is decreasing as much as 25%, while the angle is increased from $\gamma_1=0^o$ (Figure 5.2) to $\gamma_1=30^o$ (Figure 5.3). The influence of the tangential tappering on the cogging torque waveform is slightly smaller when the pole clearance factor K_p is small. A reduced angular distance between the adjacent poles decreases cogging torque. Neither the angular pole width nor the tangential tapering has any signifficant influence on the linking magnetic flux and electromagnetic coupling torque component. The difference of flux linkage is within 2-2.5% and the coupling torque within 2-5% having the maximum around $K_p=0.35\text{-}0.4$ and $\gamma_1=5\text{-}10^o$.

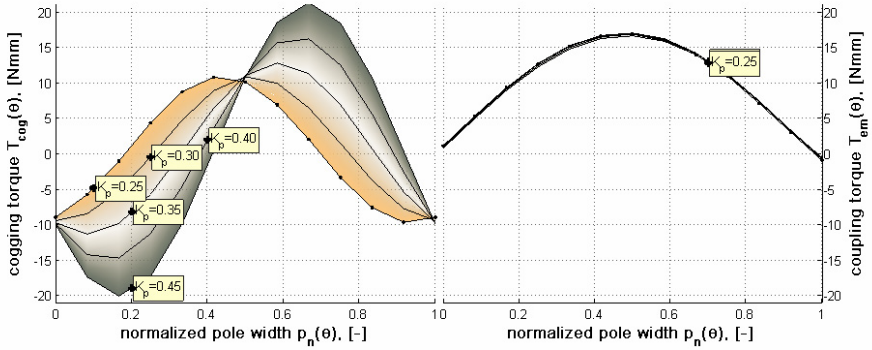

Figure 5.2: The angular pole width influence on the static torque characteristics of the single-phase claw-pole motor at a rectangular shape of the claw-pole ($\gamma_1=0^o$).

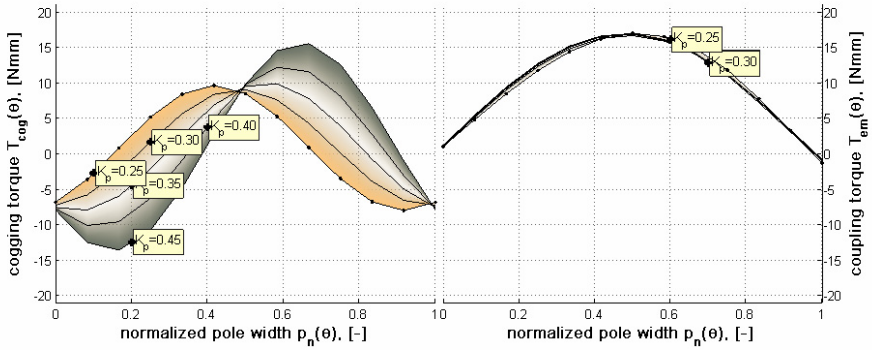

Figure 5.3: The angular pole width influence on the static torque characteristics of the single-phase claw-pole motor at a triangular shape of the claw-pole ($\gamma_1=30^o$).

A current loading of $2\ A/mm^2$ is applied to a coil with a cross-section area that is *64.5%* of the slot area. The wall thickness of a bobbin in considered about *1*

mm all around the coil. The coil has *77%* copper fill factor that specifies the pure conductor cross-section area to be *50%* of the slot cross-section area. This results in a conductor that is placed in the middle of slot having the distance from the core about *1.5 mm*. The total current of *109 A* is taken as a reference value in the FEA.

If the axial air-gap between the halves of the phases i.e. claw-pole rings is present then the linking magnetic flux and the electromagnetic torque component drop as much as *25%* when the axial gap width is *0.15 mm*. A difference between the circumferential tapering $\gamma_1=0^o$ (Figure 5.4) and $\gamma_1=30^o$ (Figure 5.5) gives slightly larger variation with the axial air-gap than without. The flux linkage and the coupling torque, respectively, variy within *5-6%* and *5-7%*. The optimum is in the range of parameters of $K_p=0.35\text{-}0.4$ and $\gamma_1=10\text{-}15^o$.

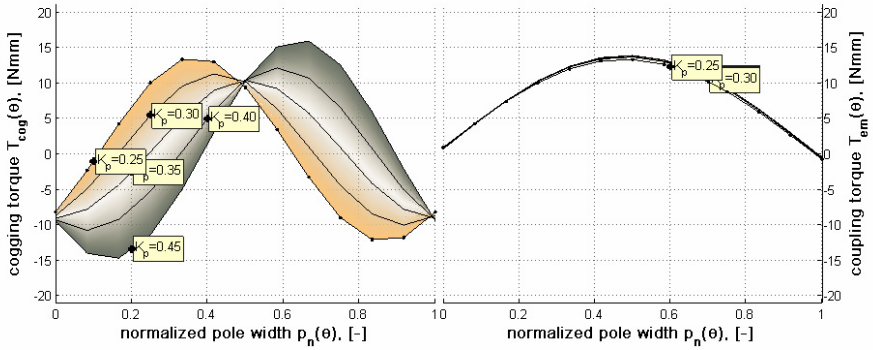

Figure 5.4: The angular pole width influence on the static characteristics of the single-phase claw-pole motor ($\gamma_1=0^o$) when the axial air-gap is present ($g_s=0.15mm$).

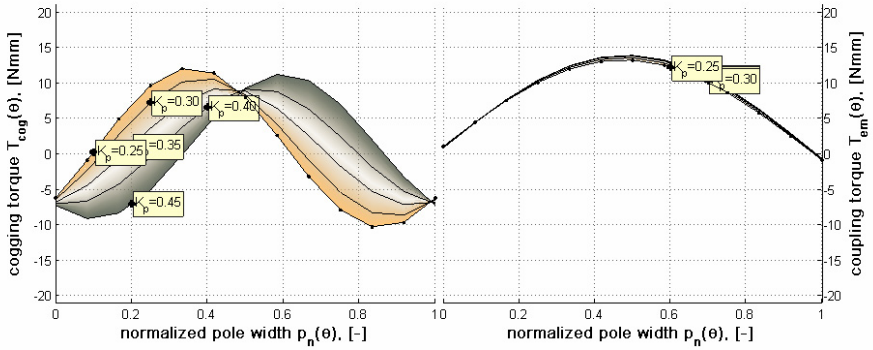

Figure 5.5: The angular pole width influence on the static characteristics of the single-phase claw-pole motor ($\gamma_1=30^o$) when the axial air-gap is present ($g_s=0.15mm$).

The claw-pole structure that is used in the pervious study has asymmetric poles in radial direction. The progressive radius of the claw-poles that gives a difference in the pole radius about *1 mm* in the pole edges is kept unchanged. A higher pole clearance factor K_p causes the angular width of the claw-pole to be smaller and the air-gap asymmetry larger. An axial air-gap between the claw-pole rings increases the dissymmetry angle between the resting position of the motor with non-excited and excited armature coil, and improves the starting conditions. The less favorable effect of the axial air-gap is the decreased transversal reluctance and electromagnetic coupling. The FEA shows that the optimal electromagnetical energy conversion occurs at the set of parameters of K_p*=0.35-0.4* and γ_1*=10-15º*.

The change of the shape of the claw-pole influences the shaping of finite elements. The magnetization vector can be defined as a continuous function and the magnet region does not need to be changed due to rotation. This allows all the 3D finite elements, which are above the claw poles, to have the same shape as defined by the claw-poles. This reduces the 'rapid' finite element deformation that could otherwise take place in the narrow air-gap in the radial/circumferential plane at the edges of the claw poles. The prevention of the rapid change of gap elements brings forth irregularly shaped elements on the upper half of the air-gap at the rotor side, which otherwise is forced to be regular. This smoother 3D FE mesh in the air-gap region gives almost no improvement in the field representation and it has insignificant influence on the torque computation from the field values in the air-gap (Appendix C).

Badly shaped hexahedral elements take place in the narrow air-gap of the two-phase claw-pole motor. This is mainly due to two criteria that the 3D hexahedral FE mesh or meshes have to fulfill. The mesh has to represent the shape of the motor parts and the whole mesh has to be continuous. The element quality control is based on the check whether an isoparametric finite element gives unique mapping from its global domain to its parent domain or not. The FE formulation is carried out in the parent domain where the brick element fulfills the requirement for a compatible shape of quadrilateral prism element, which has parallel sides to the coordinate axes. In order to achieve a one-to-one mapping between the element in the global and parent domain, the general requirement is that the determinant of the Jacobian matrix, related to mapping, supposes to be a positive definite. This requirement is fulfilled if all internal angles of hexa-elements are less than 180º. Furthermore, the additional mid-point, which represents the curvilinear sides of the isoparametric elements in the global domain where the motor geometry is represented, has to be in the middle half of the distance between adjacent corners [76].

It is important to estimate the reliability of the FEA results if the changes in geometry are introduced in order to minimize cogging torque of the two-phase claw-pole motor. The structural changes cause shape deformation of the hexahedral elements. There is no clear relationship between the element distortion and the torque computation accuracy. It is considered that a hexa element, where internal angles are no more than 135º, retains the expression quality. If the difference between the nodally averaged field and the differentiated field is small compared to the field values obtained from differentiation of the element approximation function, which is highest *2.5%*, then the obtained torque is within *5%* accuracy [16]. This accuracy shows only the quality of discretisation and not FE modeling errors [73]. The basic problem in this optimization of the cogging torque waveform is to specify the accuracy of the obtained results. The change in the motor structure supposes to alter the cogging waveform irrespective of the deformation of the 3D finite element.

The angular distance between the claw-poles and the tangential tapering of claw-poles are changed in order to study the influence on the cogging torque waveforms in the two-phase claw-pole motor. If the shape of the claw-pole of the 4-pole single-phase motor has relatively small influence on the tangential tapering then the 20-pole two-phase shows significant influence on the tangential tapering. The tangential tapering is changed from $\gamma_1=0^o$ to $\gamma_1=25^o$ that corresponds to a rectangular shape and nearly triangular shape of claw-pole, respectively. The latter has the angular length of the base of pole about twice as much as the top of pole. If the clearance between the adjacent poles is smaller ($K_p=0.2$, Figure 5.7) it can be assumed that the leakage is larger between the adjacent claw-poles compared to wider angular space between the claw-poles ($K_p=0.4$, Figure 5.6). The coupling torque increases when the angular distance between the claw-poles is smaller. This is for constantly rectangular shape of poles *6.6%* and trapezoidal poles *2.5%*, or the pole shape is changed from rectangular to trapezoidal. The stronger magnetic coupling is due to increased cross-section area of flanks and reduced magnetic loading of the powder core. The increase in the flanks' cross-section area is due to wider flanks at the same thickness of flanks.

As a result of increased flank surface the mutual magnetic coupling between the adjacent phases becomes stronger and it can be recognized from the unsymmetrical shape of the cogging waveform. The estimate of the torque calculation accuracy can be obtained from the relative discretization error over the torque integration surface. The smallest error of 5% is obtained for the rectangular shape of the claws-poles, which have air-space about $K_p=0.3$ of the

pole pitch between the claws. In this case the element distortion above the claw-poles in the gap is reduced to minimum. The elements have the same shape in circumferential/radial, circumferential/axial and radial/axial plane. The irregular shape of the elements appears in the region where the two phases need to be joined together. The relative error increases when the poles are made circumferentially wider (K_p=*0.2*, Figure 5.7) or narrower (K_p=*0.4*, Figure 5.6). This change causes irregular shapes of element sectors. The extra error increase can be seen when non-zero tangential tapering is introduced. This causes element skewing in the circumferential/axial plane. Additionally, the error depends on the position of the magnetization in the magnet-ring.

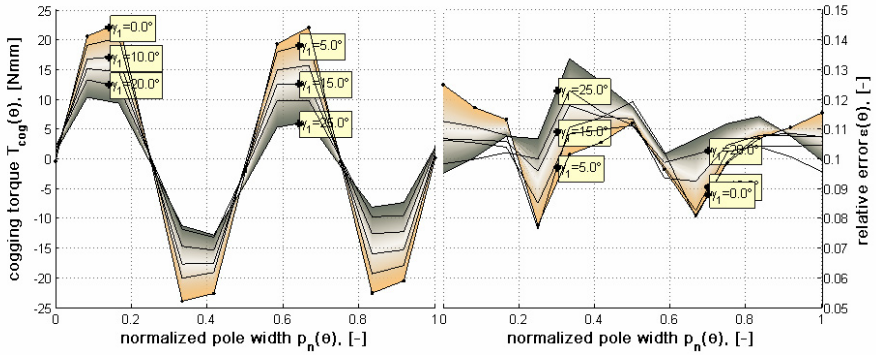

Figure 5.6: Tangential tapering (γ_1) influence on the cogging torque and relative field error of the two-phase claw-pole motor for a circumferentially 'narrow' claw-pole K_p=0.4.

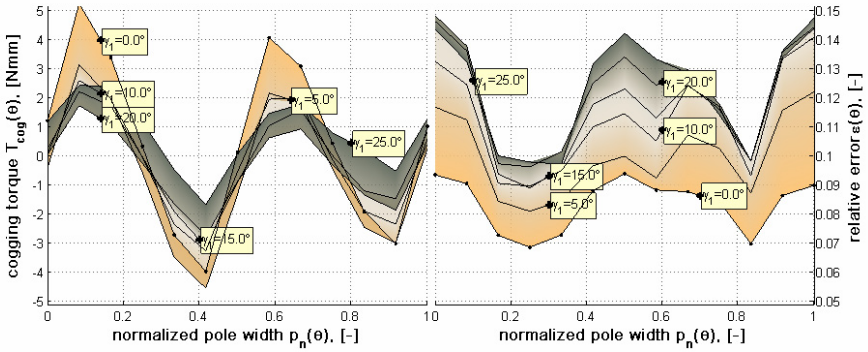

Figure 5.7: Tangential tapering (γ_1) influence on the cogging torque and relative field error of the two-phase claw-pole motor for a circumferentially 'wide' claw-pole K_p=0.2.

If the angular width of the claw-pole equals to the pole pitch then the shear forces at both ends of the claw-pole are balanced at any position of a magnet-ring that carries circular polar magnetization pattern. On the contrary, the transversal magnetic flux coupling is maximized when the direct circumferential leakage is reduced and the circuitous transversal linkage is increased. The ratio of leakage flux path length to linkage flux path length depends not only on the shape and distribution of claw-poles but also how the claw-rings are assembled.

Axial gap between the halves of a phase

The assembled phase of a claw-pole motor consists of two claw-pole rings. Joining these two SMC core halves together causes a small axial air-gap between them. Even the gap is small the additional reluctance in the magnet circuit reduces the flux linkage and the resultant interaction torque between the coil field and the excitation field. First, the waveforms of the torque components are calculated for the single-phase claw-pole motor (Figure 5.8).

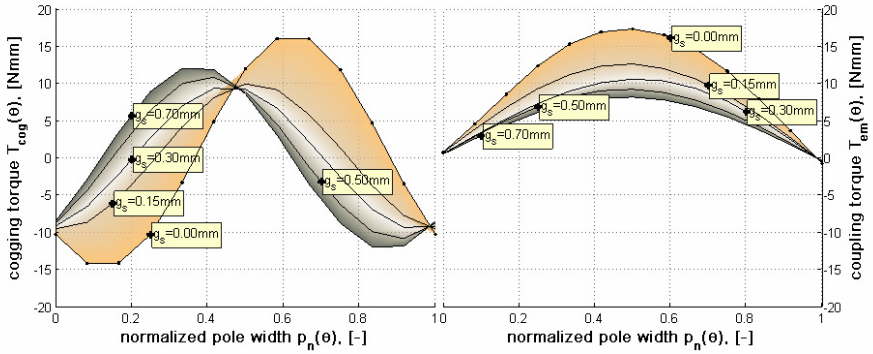

Figure 5.8: Cogging (left) and electromagnetic coupling torque (right) as a function of the axial air-gap (g_s) between claw-pole rings at K_p=*0.38 and* γ_1=*8°. The total current loading of the coil is 109A.*

The FE computations show that the additional axial air-gap about g_s=*0.1 mm* reduces the coupling flux *22%* and the air-gap about g_s=*0.5 mm* reduces the coupling flux more than *50%*. In order to reduce the additional reluctance in the magnetic coupling circuit either the distance between the coupling surfaces needs to be minimized or the cross-section area needs to be maximized. As an advantageous feature, the combination of the length of the axial air-gap, the resting position of the rotor and the reduced coupling torque give the optimal starting torque for the single-phase claw-pole motor (Figure 5.8).

The similar study is made for a single phase of the two-phase claw-pole motor. A plastic bounded *NdFeB* magnet-ring with circular polar magnetization is used in the rotor. The current loading is as high as *4 A/mm²* that gives a total current of *38.7 A*. In this case the copper filling factor is *80%*. This corresponds in FEA to a single turn conductor in the middle of slot that gives a spacing of *0.15 mm* from the core. The axial air-gap between the claw-pole rings are changed from g_s*=0.0 mm* to g_s*=0.4 mm*. The coupling flux reduces *42%* when the axial air-gap of g_s*=0.1 mm* occurs. At the same time the coupling torque decreases of *15%* and the cogging torque of the single phase decreases of *24%* (Figure 5.9).

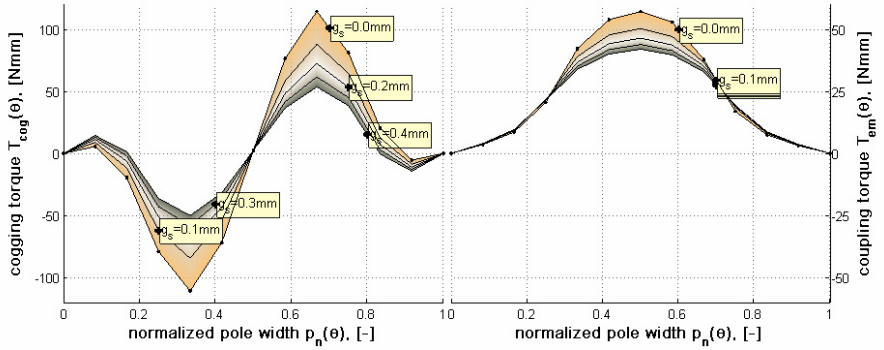

Figure 5.9: Static characteristics of the single claw-pole ring of the two-phase claw-pole motor as a function of the axial height (g_s) of the axial gap. The shape of the claw-pole is determined by tangential tapering γ_1=20° and pole clearance factor K_p=0.4.

The axial height of the magnet-ring plays important role on the shape of the static torque characteristics. If the axial height of magnet-ring is taken the same as the axial height of the claw-poles then the cogging waveform is almost symmetric over a half of pole pitch. The contribution of the neighbor phase, which is shifted angularly the half of a pole pitch, gives significant reduction to the resultant cogging waveform (Figure 3.5) of the two-phase motor. According to the series of 3D FE computation the cogging torque for an ideally coupled single phase has the same magnitude of cogging, which is independent of the axial height of the magnet-ring. A wider magnet-ring results in a larger peak value of the cogging torque waveforms when the axial air-gap between the claw-pole rings exists. The peak of the resultant cogging waveform of the two-phase motor is as high as *5 Nmm* when the height of the magnet-ring equals to the axial height of the claw-pole. This best case value is estimated from the single-phase counterpart and its value is considerably smaller than the computed values among the varied claw-pole tapering at the

same pole clearance for the complete assembled motor (Figure 5.6). If the projected magnet height is considered (Figure 5.9) then the peak of the resultant cogging torque is up to 20 higher times compared to the single phase counterpart with a narrow magnet-ring (Figure 5.10). The projected magnet height exceeds the height of phases and an axial shift between the phases. Even though the magnet core operates near to the magnetic saturation, the flux concentration effect enables stronger magnetic coupling. Compared to the magnetic coupling with the narrow magnet-ring, the wider magnet-ring gives increase in linking flux by 32% and coupling torque by 78%.

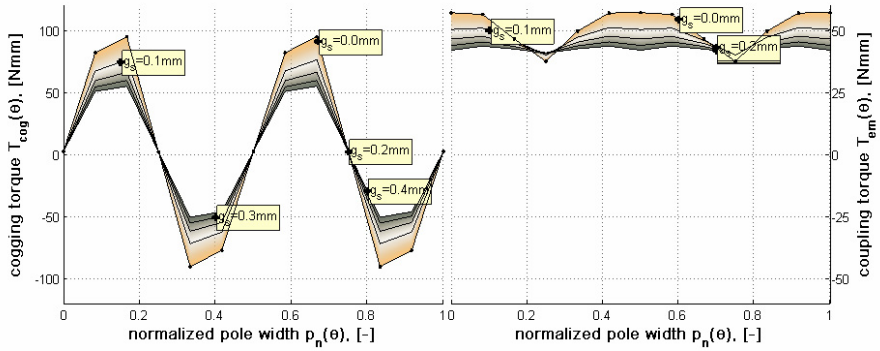

Figure 5.10: Static torque characteristics of the assembled two-phase claw-pole motor according to the characteristics of the single phase as a function of axial air-gap (g_s). The shape of the claw-pole is determined by γ_1=20° and K_p=0.4.

The study of the single phase of the two-phase claw-pole motor helps to understand the contribution of the single phase to the electromechanical energy conversion. Moreover, the values of interest are easily calculable and measurable. Less advantageous feature is that the reduced complexity of the computational model introduces the drawback of neglected mutual effects between the phases and the actual magnetic loading of the magnet-ring.

The resultant cogging and coupling torque waveforms of the whole two-phase claw-pole motor are calculated (Figure 5.11). It can be noticed that the coupling torque and the coupling flux is 10% smaller for a single phase in the two-phase motor compared to the single-phase study.

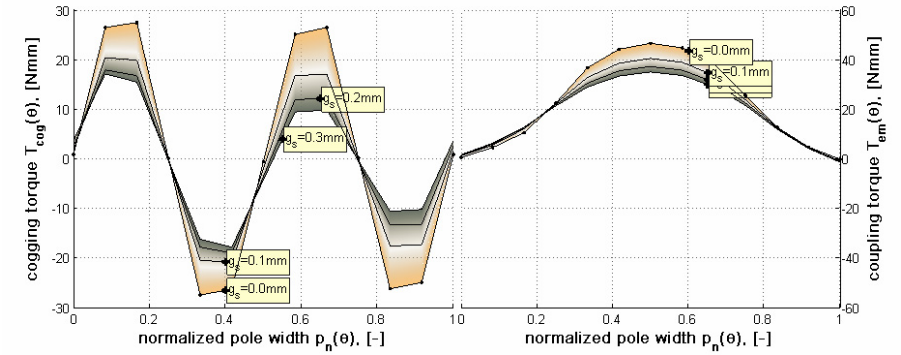

Figure 5.11: Cogging and coupling torque waveforms for the assembled two-phase claw-pole motor as a function of axial air-gap (g_s) between claw-rings. The projected height of the magnet-ring is used in the rotor.

Similar to the decreased magnetic coupling the magnitude of the cogging torque decreases in the complete motor model. Additionally, the enlarged axial distance g_s between the claw-pole rings increase the affect of the neighbor phase that is noticeable from the unsymmetrical shape of the cogging waveform over one pole pitch.

If the axial height of the magnet-ring is reduced to the axial height of the stator, then the magnitude of the cogging decreases of 30% (Figure 5.12). At the same time the strength of the magnetic coupling decreases of 8% that can be seen from the reduced magnetic linking flux and the coupling torque.

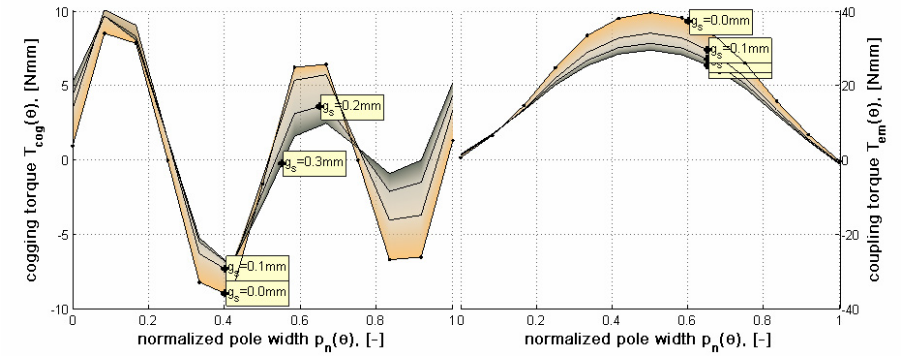

Figure 5.12: Cogging and coupling torque waveforms for the assembled two-phase claw-pole motor as a function of axial air-gap between claw-rings. The height of the magnet-ring is determined by the heights of phases and the axial distance between the phases.

One of the most important design issues for the two-phase claw-pole motor is to reduce cogging torque. Each pole gives its contribution to the resultant cogging waveform. The increased number of poles enlarges the coupling torque e.g. by increasing the number of poles from $N_p=20$ to $N_p=30$ the coupling torque increases by *62.5%* (Figure 5.13). At the same time the cogging torque increases by *166%* and the quality of electromechanical transmission becomes worse as the unwanted cogging torque is *35%* of the coupling torque compared to 20-pole motor of *21%*. The coupling flux is increased *5%* when the number of poles is increased from 20 to 30.

The cogging torque is influenced by the shape and distribution of the claw-poles, the magnetic coupling between the adjacent poles and neighbor phases, and the size of the permanent magnet and the magnetization pattern in the magnet. In order to smooth out the cogging torque waveform all these abovementioned conditions need to be considered simultaneously.

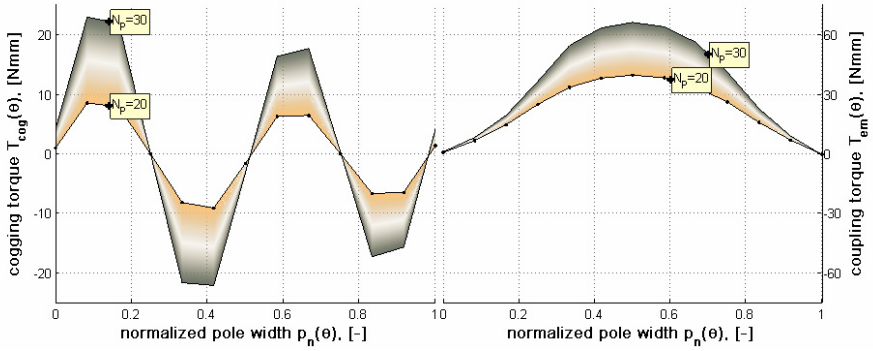

Figure 5.13: Cogging and coupling torque waveform as a function of position and pole numbers. The shape of the claw-pole is determined by tangential tapering $\gamma_t=20°$ and pole clearance factor $K_p=0.4$.

Next, the claw-pole arrangement in the circumferential/radial plane of the single-phase claw-pole motor is studied.

Progressive radius

The progressive radius of the claw-poles has been varied in order to determine the influence on the dissymmetry angle, starting torque and average torque of the single-phase claw-pole motor. The obtained results of cogging torque waveforms (Figure 5.14) does not show good correlation to the characteristics that are obtained from an energy method over the gap permeance (Figure 2.18). This is due to inaccurate modeling of the magnet and the air-gap.

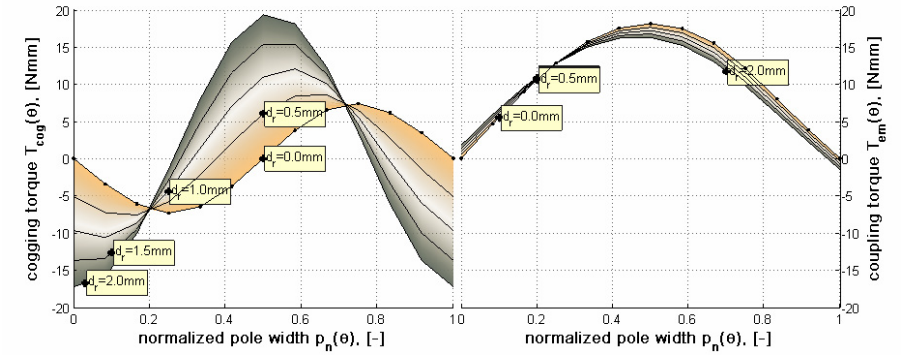

Figure 5.14: The progressive radius influence of the static characteristics of the single-phase claw-pole motor. The shape of the claw-pole is determined by tangential tapering γ_1=8° and pole clearance factor K_p=0.38.

The largest introduced reduction of pole radius that is d_r=*2.0 mm* decreases the coupling flux of *10%* and the electromagnetic coupling torque of *11%*. The largest progressive radius increases the cogging torque more than *200%* compared to the claw-pole motor with symmetric radial air-gap (Figure 5.14). The cogging waveform that is obtained from the Opera-3D magnetostatic solver shows that the stabile equilibrium points are at the positions of claw-pole alignment with the magnet poles. This in turn shows that the transversal reluctance is smaller compared to the circumferential reluctance. If the radius of the claw-pole is reduced in a lagging edge the stabile equilibrium point moves towards a leading edge. The leading and the lagging edge of a claw-pole is defined according to the counter clockwise motion of the magnet-ring. The largest achievable dissymmetry angle depends on the angular length of pole and on the claw pole regression depth for the ideal magnetically coupled claw-pole rings.

Axial shift between the phases

Apart from the shape of the claw-pole structure and the phase assembling tolerances, the static characteristics of the claw pole motor depends on the complete assembling of the stator. The axial displacement between the phases has been varied in order to find the influence on the magnetic coupling and the static characteristics for the two-phase claw-pole motor.

The two-phase claw-pole motor has a circular polar magnetized magnet-ring as an outer rotor.

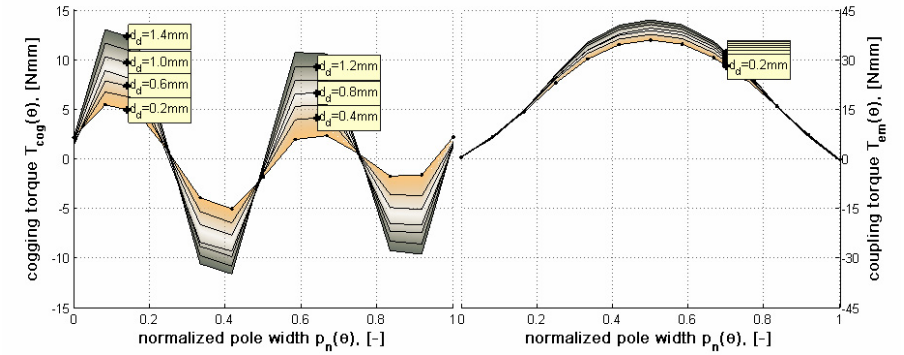

Figure 5.15: Cogging and coupling torque waveforms as a function of the axial space (d_d) between the adjacent phases. In this analysis the axial height of the magnet-ring is selected the same as the height of the complete stator. The coupling torque depends on the height of the magnet-ring, where the effect of the flux concentration increases the coupling torque.

The analysis can be carried out for the constant axial height of the motor, the constant height of the magnet-ring or to select the motor height according to the axial height of the completed stator. The latter (Figure 5.15) has the drawback of a variable magnet volume that has direct influence on the magnitude of the cogging torque. On the other hand, the asymmetric shape of the cogging torque waveform over one pole pitch shows the influence of the adjacent phase and the occurrence of the zigzag flux path between the flanks and poles of the adjacent claw-rings in the adjacent phases.

The influence of the radial air-gap

The strength of magnetic coupling between the stator and rotor depends on the radial length of the air-gap between the stator and the rotor, and it influences the electromechanical conversion and cogging torque. The influence of the air-gap length is studied for the two-phase claw-pole motor (Figure 5.16). The magnet-ring of the motor has circular-polar magnetization pattern. The axial height of the magnet-ring equals to the total height of the stator, that has the axial displacement disk about d_d=*0.8 mm* between the phases.

The increase of the radial air-gap is beneficial from motor assembling and the decreased cogging torque point of view.

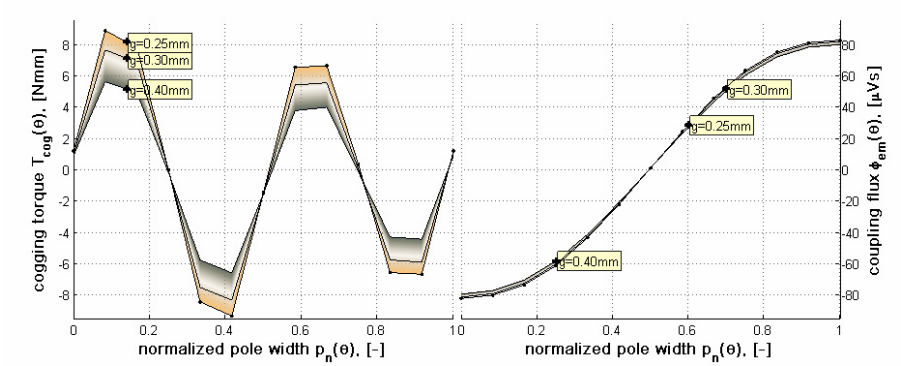

Figure 5.16: The influence of radial air-gap, g=0.25, 0.3 and 0.4 mm, over cogging torque waveform and linking magnetic flux waveform.

If the air-gap is larger *g=0.4 mm* compared to the initial *g=0.25 mm* then the cogging torque reduces *38.8%* and the maximum value of the linking flux decreases of *3.3%*.

Rotor eccentricity

A static eccentricity of the outer rotor of the single-phase claw-pole motor is studied (Figure 5.17).

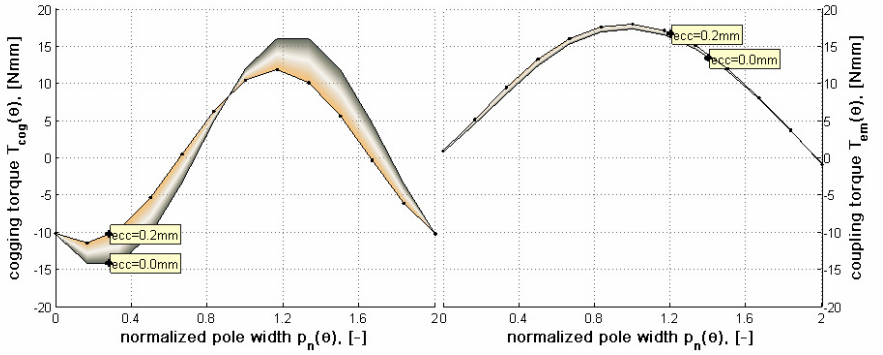

Figure 5.17: Influence of the static rotor eccentricity (ecc) on motor torque characteristics.

A whole motor is modeled in order to study the influence of the static rotor eccentricity. The outer rotor is displaced from the centre along the x-axis about *0.2 mm*. This causes a narrower air-gap on the one side of motor that is about *0.3 mm* compared to the opposite side about *0.7 mm*. The claw-pole cores are ideally connected and there is no axial air-gap considered. The analysis results

show that the cogging torque decreases due to the rotor eccentricity and the cogging torque waveform is shifted from the initial waveforms of the centered rotor.

5.2 Variation on material properties

Similarly, the geometrical changes, which are introduced in the claw-pole structure, changes of material properties in the stator is studied and the tolerance of small permeability changes in the core is analyzed. As the powder core has already low permeability and the complete assembled core may have additional air-gaps along the coupling path, then the motor construction chosen should tolerate or take even advantage of the low magnetic conductivity tolerance of the core material.

The permeability of the core material has been changed in order to determine its' sensitivity to the motor characteristics in respect of the core compaction. The mechanic output of the motor is relatively independent of the type of SMC premix and the compaction process chosen for the ferrous core. More than ten times higher permeability can increase the coupling torque by 7.5%. This is for the rotor without back iron. A better improvement can be reached if the back iron is used behind the magnet-ring. In this case the coupling torque could increase by 18.5%, while the cogging torque increases by 86.4% (Figure 5.18).

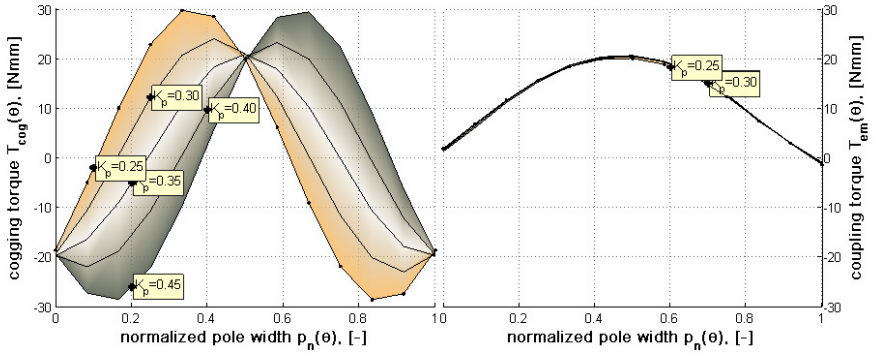

Figure 5.18: Back iron is present behind the lateral polar magnetized magnet-ring.

If the stator core is selected to be of solid iron then the iron core, which is subject to flux alternation, suffers from excessive core losses. Additionally, the amount of eddy currents, which act against the field that they are caused by,

needs to be restrained in order to promote rapid flux penetration and the full utilization of the iron core. The higher permeability of the solid iron core, which is used both in the stator and in the rotor, gives an increase in coupling torque as much as *68.8%* (Figure 5.19). On another way around, if in the stator core a poor magnetic conductor is used, e.g. a plastic bounded soft magnetic core, where relative permeability is taken ten times less than in SMC, then the coupling torque drops more than one third and the coupling flux is *1/5* compared to the initial design with SMC.

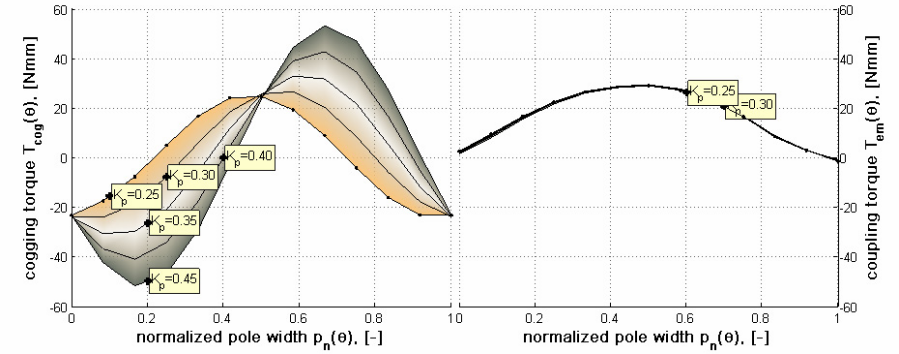

Figure 5.19: Stator core is replaced with iron and the magnet ring has back iron.

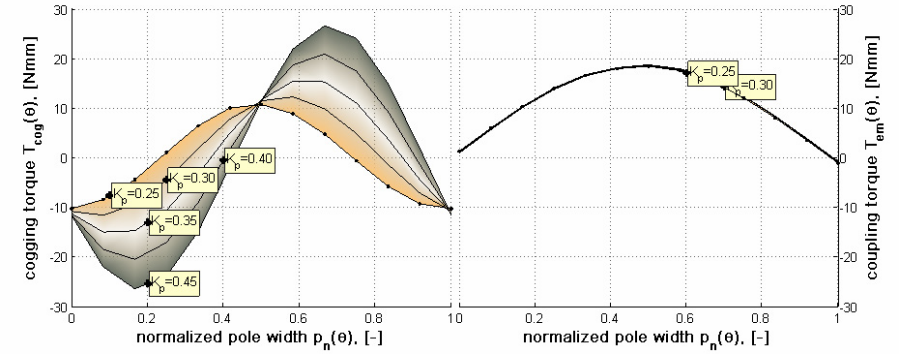

Figure 5.20: Stator core is replaced with iron while no back iron is added to the magnet-ring.

The sensitivity analysis is carried out for a magnet-ring, which is with or without solid back iron, respectively, for a stator core made of solid iron (Figure 5.19 and Figure 5.20) of SMC (Figure 5.2 and Figure 5.18). It can be noticed that the presence of a solid back core makes the magnetic coupling

stronger. This is due to the return path or the leakage that is present on the outer periphery of the magnet-ring. The effect of a better magnetic conductor in the stator core, compared to SMC, has low significance if back iron is not used behind the magnet-ring. The leakage path behind the magnetically unsupported magnet-ring becomes the dominant factor that influences the strength of magnetic coupling between stator and rotor.

Table 5.1: A mechanical output of the single-phase claw-pole motor in respect of the rotor core and the stator core material.

Quantity	symbol	unit	Motor type 1	Motor type 2	Motor type 3	Motor type 4	Motor type 5
Stator core	μ_{stator}	-	200	200	3700	3700	17
Rotor back core	μ_{rotor}	-	1	3700	1	3700	1
Coupling torque peak	T_{em}	Nmm	17.3	20.5	18.6	29.2	6.0
Cogging torque peak	T_{cog}	Nmm	12.5	23.3	15.0	33.3	15.6

The calculation results of the different soft magnetic materials used are summarized in Table 5.1. The peak value of the cogging torque is taken from the waveform where the pole clearance $K_p=0.35$.

5.3 Variation in magnetization patterns

Apart from the geometrical and material change in the claw-pole structure, the magnetization pattern and the hard magnetic material of the magnet-ring influence the static characteristics of the claw-pole motor. Next, the permanent magnet excitation ability to form a preferred cogging torque waveform is studied.

Optimal magnet span of radially magnetized magnets

First, an outer rotor with surface mounted radially magnetized magnets is analyzed. The angular width of the radially magnetized magnets has been changed in order to find the minimal cogging torque for the two-phase claw-pole motor. The angular width of the magnet is changed between $K_m=0.5$ and $K_m=0.7$ of pole pitch (Figure 5.21).

From analysis can be seen that the optimal angular width of the radially magnetized magnets are between $K_m=0.55$ and $K_m=0.6$. The relative field error is in the same range when the strain of the gap-elements in the circumferential /radial plane is introduced to represent the different angular width of magnets.

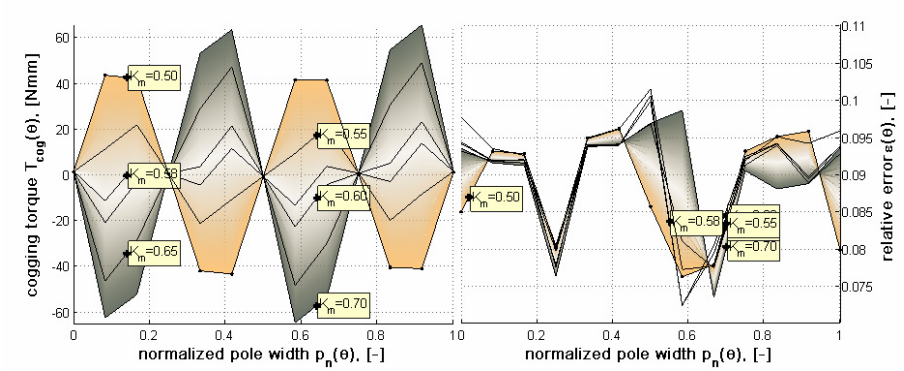

Figure 5.21: Selection of angular width of magnet for the two-phase claw-pole motor. The corresponding cogging waveform (left) and relative field error (right).

The static torque characteristics of the two-phase claw-pole motor with two different rotors are presented (Figure 5.22).

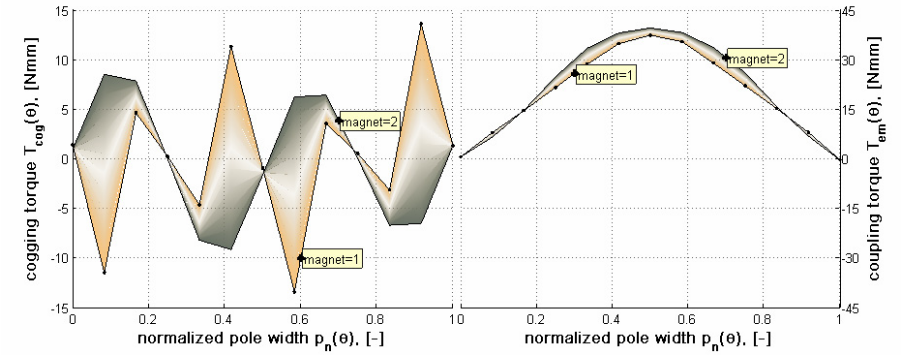

Figure 5.22: Cogging (left) and coupling torque waveforms (right) for radially magnetized magnets (1) and a magnet-ring with circular polar magnetization pattern (2).

The rotor that has circular polar magnetized magnet-ring shows smoother cogging torque. This phenomenon is mainly due to the sinusoidal mmf distribution in the air-gap. The maximum coupling torque, when one of the armature coils is excited, is around *40 Nmm* for both motors. The motor which has a rotor with radial magnets gives higher maximum resultant torque than the motor with circular polar magnet. This advantage is achieved at the expense of higher cogging torque, where maximum is *13.5 Nmm* or *8.5 Nmm* for the chosen type of magnets. This gives that the ratio of cogging torque to coupling torque is about *21.5%* to circular polar magnets and *36.4%* to radial magnets. The radial magnets produce slightly smaller amount of magnetic flux

through the bottom core of the claw-pole ring, which is 8.5% less, than the circular polar magnet ring. Reason for that is the reduced magnet material of the surface mounted and radially magnetized magnets compared to the solid magnet-ring with circular polar magnetization. The outer rotor with surface mounted magnets gives larger field weakening ratio that is *0.2* compared to circular polar magnetized magnet ring, which has the corresponding ratio about *0.15*. Surface mounted magnets inside an iron cylinder can give a mechanic output of the motor at the same range as the motor with solid magnet-ring. At the same time the surface mounted magnets give a significant reduction of the magnet material. The drawback of surface mounted magnets is more complicated assembling.

Similar study is made for the single-phase claw-pole motor where the angular width of the radially magnetized magnets are selected between $K_m=0.5$ and $K_m=0.7$ (Figure 5.23).

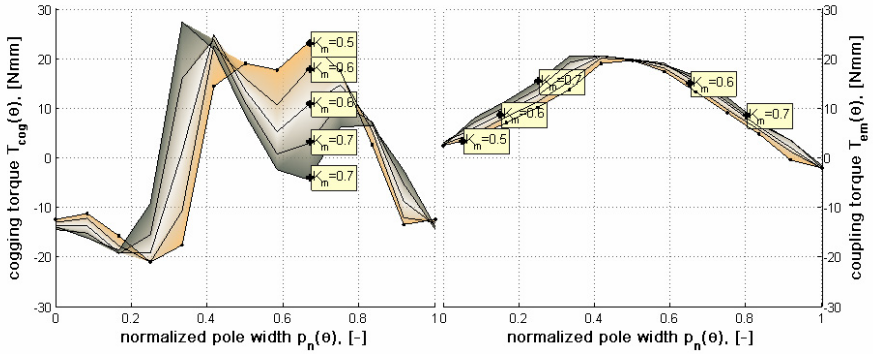

Figure 5.23: Selection of an angular width of the surface mounted radially magnetized magnets for a single-phase claw-pole motor (axial air-gap g_s=0 mm).

According to the optimal angular width of the surface mounted magnet, which has $K_m=0.65$, i.e. 65% of the pole pitch, the cogging can be reduced, compared to the wider magnet of $K_m=0.7$, about 18.5%, while the electromechanical coupling torque remains the same and the coupling flux decreases of 4%.

Surface mounted radial magnets together with back core use the same space as the magnet-ring with circular polar magnetization pattern would otherwise. The amount of magnet material used in the rotor is reduced by 57% if the angular width of the magnets is 2/3 of a pole pitch. The difference is between the solid magnet-ring that uses all the available space for the permanent magnet excitation and the radially magnetized magnets, which need to have back iron that outer diameter is the same as for the solid magnet-ring.

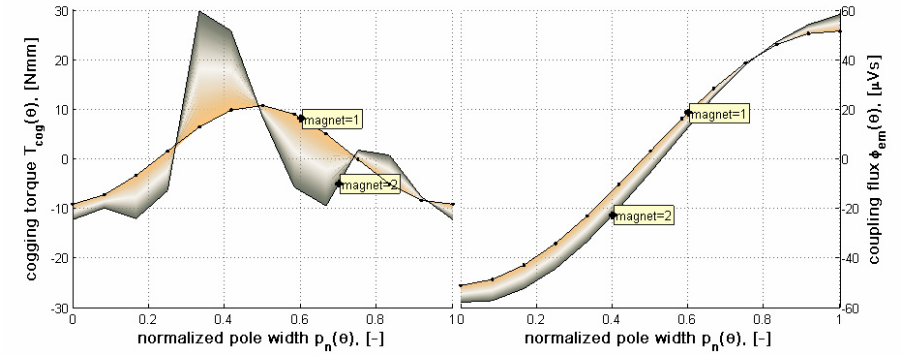

Figure 5.24: Cogging torque and coupling flux waveform of a magnet-ring with circular polar magnetization (1) and rotor with radially magnetized magnets (2) (g_s=0 mm).

The radially magnetized surface mounted magnets that is selected for comparison (Figure 5.24) have an angular width of magnet, K_m=*0.667* of the pole pitch. The radially magnetized magnets establish 13% stronger magnetic coupling between the stator and the rotor. The electromagnetic coupling torque of two different rotors (Figure 5.25) shows better mechanic output of the rotor with radially magnetized magnets. It can be noticed that the current loading has linear relationship to the coupling torque over the selected loading domain.

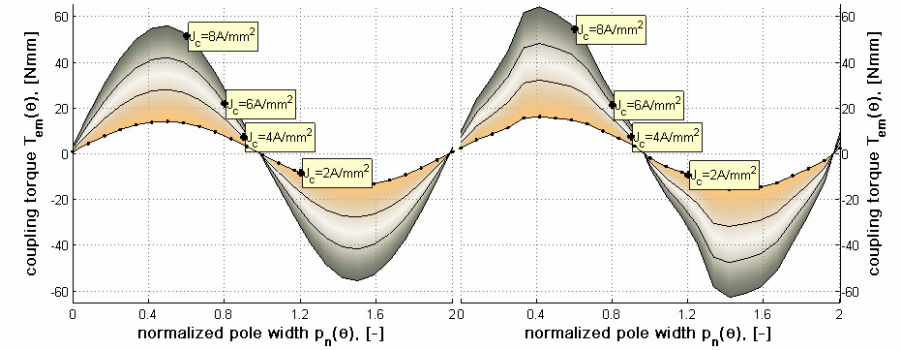

Figure 5.25: Coupling torque as a function of current loading (J_c). The magnet-ring with circular polar magnetization is shown in the left and the rotor with surface mounted magnets in the right. The bobbin has wall thickness about 1mm and the filling factor of the winding region is 0.76. The axial air-gap is present and this influences the torque/current characteristic to be linear.

A stronger magnetic coupling increases cogging torque. Cogging impedes fine speed control and high accuracy in the position control, which is particularly important for the two-phase claw-pole motor. Since the cogging torque is greatly affected by the geometric configuration of the stator and the magnetization in the rotor, it is preferable to minimize the cogging torque by the geometric shape optimization, in particular, the claw-pole shape of the stator and the magnetization distribution of the permanent magnet material. One possible way to reduce cogging torque is to reduce the strength of the magnetic coupling and to use plastic bounded ferrite instead of plastic bounded *NdFeB* magnet-ring. The replacement of the magnet-ring with ferrite instead of NdFeB reduces the coupling torque by 50%. The static characteristics of the complete two-phase motor are present in Figure 5.26.

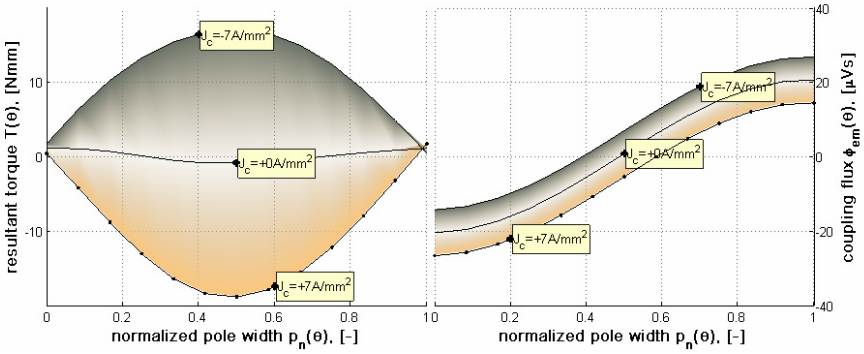

Figure 5.26: The static characteristics of the two-phase claw-pole motor that utilizes a ferrite magnet-ring with circular polar magnetization pattern. An axial air-gap between the claw-pole rings about 0.1 mm is present.

On the contrary, in the single-phase claw-pole motor the non-zero cogging is necessary in order to overcome static friction and to position the rotor at the unexcited rest position.

Table 5.2: A mechanical output of the single-phase claw-pole motor in respect of the rotor core and the stator core material.

Quantity	Symbol	unit	The single-phase claw-pole motor		The two-phase claw-pole motor	
Type of agnetization			polar	radial	polar	radial
Optimal magnet width	K_m	-	-	0.6	-	0.58
Coupling torque peak	T_{em}	Nmm	17.3	20	39.3	37.1
Cogging torque peak	T_{cog}	Nmm	12.5	23.5	8.5	13.5
Field weakening ratio		-	0.4	0.48	0.15	0.2

Optimal size of the magnet-ring

Previously, the affect of the axial length to the cogging torque waveform has been studied for the two-phase claw-pole motor. It was noticed that flux concentration lead to increased cogging torque. The study (section 5.2) that focuses on the need for a back iron behind the magnet-ring with circular polar magnetization pattern raises a question of the optimal thickness of the magnet-ring. The magnet-ring has to be able to carry the circular polar magnetization pattern for a certain radius and number of magnet poles to eliminate need for magnetic support behind the magnet-ring. The thickness of the magnet-ring with circular polar magnetization pattern was varied in steps l_{pm}*=4.4, 3.5* and *2.6 mm* for the single-phase claw-pole motor (Figure 5.27).

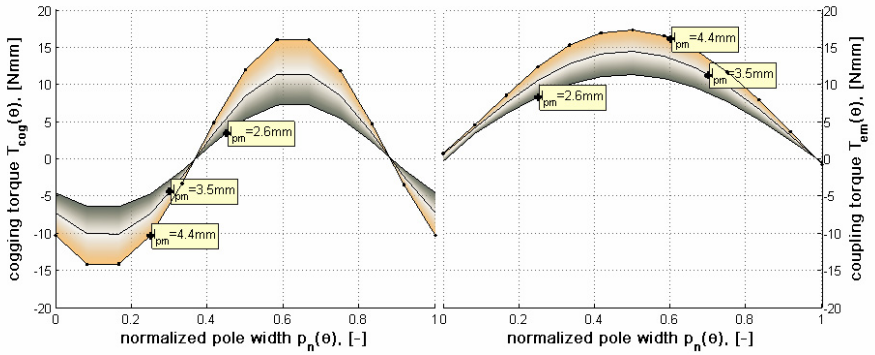

Figure 5.27: The thickness of the magnet-ring l_{pm} influences the static characteristics of the single-phase claw-pole motor. The shape of the claw-pole is determined by tangential tapering γ_1=8° and pole clearance factor K_p=0.38.

The maximum value of the coupling flux for the single-phase claw-pole motor with magnet-ring thicknesses of l_{pm}*=4.4, 3.5* and *2.6 mm*, respectively, is Φ_B*=75, 63* and *47 μVs*. The reduction of the magnetic coupling flux is due to decreased thickness of the magnet-ring. At the same time the fringing field due to the radial magnetization and the leakage field due to circumferential magnetization behind the magnet-ring are decreased (Table 5.3). The flux density value is taken from a patch that is placed *1 mm* from the outer surface of the magnet-ring. Two peak values of the leakage field can be noticed. These are near to the sides of the magnet-ring and in the middle of the magnet-ring, respectively, where the radial *(r)* or circumferential *(θ)* magnetization is dominating. The field evaluation is made at two rotor positions, which are alignment *(x)* and unalignment *(y)* position.

Table 5.3: Leakage field behind a ferrite magnet-ring of a single-phase claw-pole motor. Neither the value of the leakage flux from the total flux of the magnet or the coupling flux of the core is evaluated.

Quantity	symbol	unit	Thickness of magnet l_{pm}, mm		
			4.4	3.5	2.6
Radial fringing at alignment	δB_{rx}	mT	58	49	42
Circumferential leakage	δB_{0x}	mT	35	31	26
Radial fringing at unalignment	δB_{ry}	mT	52	43	38
Circumferential leakage	δB_{0y}	mT	40	36	30

The optimal magnet length in the direction of magnetization for a magnet-ring that carries circular polar magnetization pattern can be evaluated from the ratio of the coupling flux to the volume of the permanent magnet. According to these three calculations, the volume of magnet is reduced by 22% and 44% in respect of base value of the thickest magnet-ring l_{pm}*=4.4 mm*. At the same time the coupling flux decreases by 16% and 37.3%, respectively, according to the thickness of l_{pm}*=3.5 mm* and l_{pm}*=2.6 mm*.

The optimal overhang of a ferrite magnet can be obtained from the comparison between the additional coupling flux and the increase of magnet material. If the axial height of the magnet-ring is increased, then the magnetic coupling flux increases by 3.4%. It is due to axially higher magnet that is about *8 mm*, compared to the axial pole height of *20 mm*. This corresponds to 40% increase in the magnet material used. The magnetic flux coupling ratio compared to the source flux in this case is 0.77 (Figure 4.20).

The harmonic content in the excitation field

The magnetization pattern in the magnet-ring depends on the magnetization tool and magnetization process. The idealized sinusoidal magnetization vector rotation along the circumference specifies the fundamental distribution of magnet poles. In addition, the excitation space distribution may contain higher order distribution of magnet poles than the fundamental. The space harmonic content on the permanent magnet excitation field and its' influence on the static characteristics have been studied. A third harmonic is added to the fundamental (maximums aligned) so that the summation forms a magnetization pattern where the magnetization vectors are mainly oriented in the circumferential direction (Figure 5.28). The subtraction (maximums co-aligned) forms a resultant magnetization pattern that has the magnetization vectors mainly oriented in radial direction.

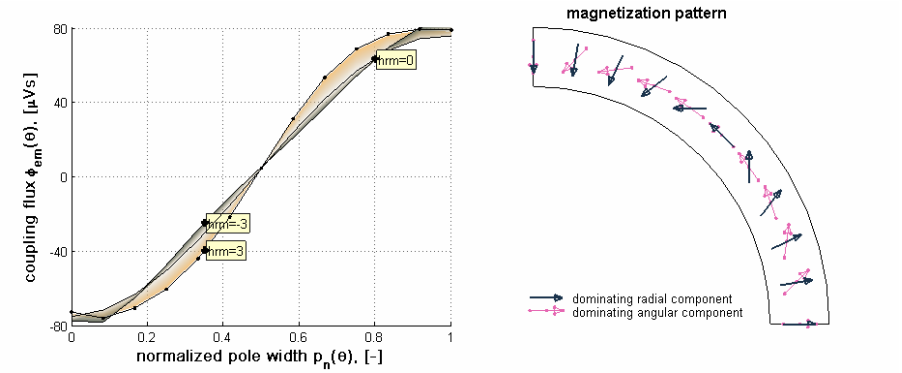

Figure 5.28: Third harmonic (hrm) introduced in the permanent magnet excitation field (right), and the corresponding coupling flux waveform in the centre core (left).

Due to the harmonic content in the excitation field, the coupling flux reflects the presence of the third harmonic in the coupling flux waveform.

The corresponding static torque waveforms show (Figure 5.29) that the magnetization pattern with dominating circumferential component increases the maximum value of cogging and the electromagnetic coupling torque. The starting conditions of the single-phase claw-pole motor are not improved when the excitation harmonics are introduced according to the static torque characteristics (Figure 5.29).

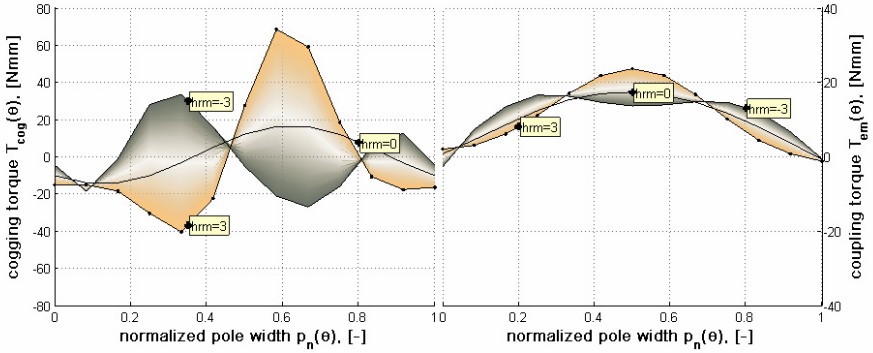

Figure 5.29: Cogging and coupling torque waveforms depending on the harmonic content on the permanent magnet excitation field of the single-phase motor.

The magnetization vector that describes the polar anisotropy along the inner surface of the cylinder can be described with a circle where centre is on a line that divides the magnet pole apart into symmetric halves. According to the

location of centre point either the radial or circumferential magnetization vector component is dominating in the magnet domain (Figure 5.30).

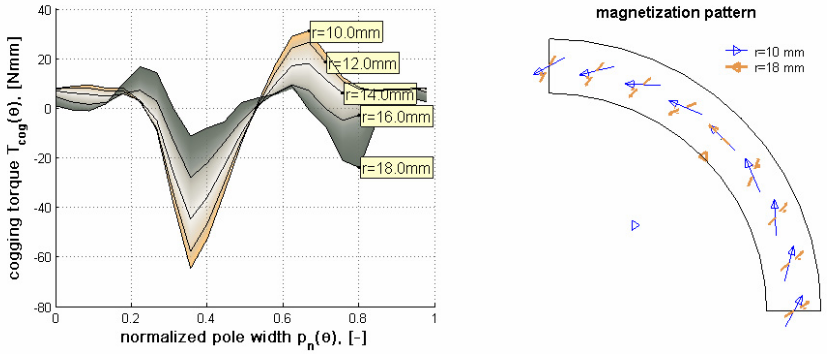

Figure 5.30: Cogging torque of the single-phase claw-pole motor according to the polar circular magnetization definition in Jmag-Studio.

The corresponding cogging torque waveforms are calculated with Jmag-Studio. The magnetic vector potential is calculated at each node point. The torque is calculated by using the nodal force method. Similar to the single-phase claw-pole motor, the cogging torque waveforms are calculated according to different magnetization pattern in the two-phase claw-pole motor (Figure 5.31).

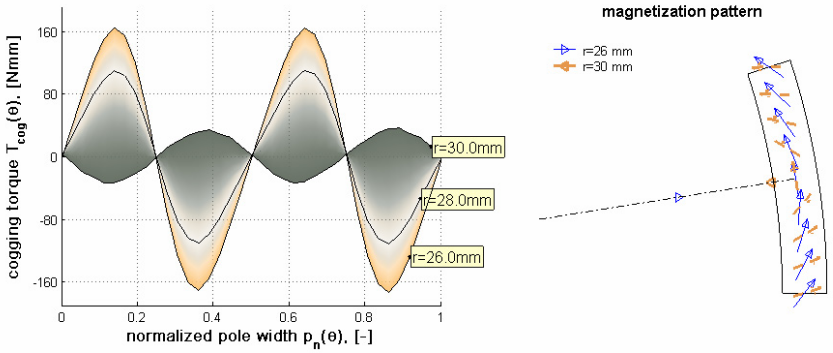

Figure 5.31: Cogging torque of the two-phase claw-pole motor according to the polar circular magnetization definition in Jmag-Studio where the centre of the magnetization circle is set at 26, 28 and 30 mm.

The torque computation results depend on the solution of the problem in electromagnetics and the torque computation method. An advantageous

feature in Jmag-Studio is a 3D permanent magnet magnetization analysis that is initial condition in the FE computation of the rotating machines. The resultant torque characteristics of the two-phase motor are obtained at low speed in order to reduce the effect of magnetodynamics [18]. The two-pole model has around 200000 tetrahedral elements. The current loading is *7 A/mm²* in a coil with filling factor *0.65*.

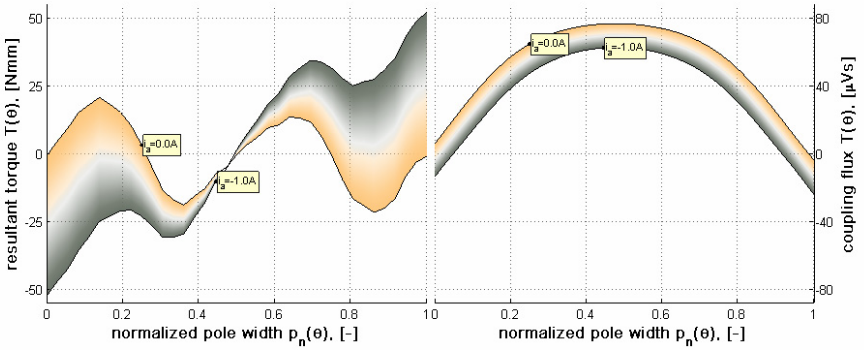

Figure 5.32: Static characteristics of the two-phase claw-pole motor obtained from the imported magnetization pattern, modeled in the magnetization tool in Jmag-Studio.

Similar to the two-phase claw-pole motor, the single-phase claw-pole motor is modeled with an imported magnetization pattern of a magnet-ring base on the analysis of the magnetization of magnet-ring. In both cases the magnetization tool is specified as a sintered *NdFeB* cylinder with lateral polar magnetization along outer periphery. The current loading of the single-phase motor is *4 A/mm²* in a coil where filling factor is *0.64*, which is specified by the slot opening of a bobbin.

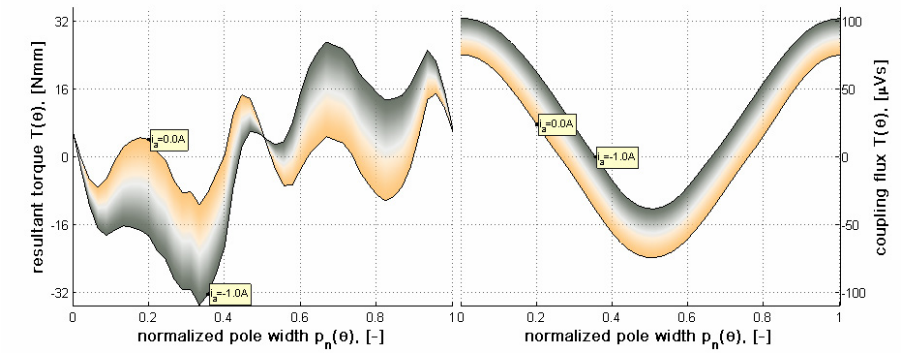

Figure 5.33: Static characteristics of the single-phase claw-pole motor obtained from pre-analyzed magnetization in Jmag-Studio.

The qualitative change in the motor dimensions is considered in the prototyping. Still, the analysis results and the determination of magnetization pattern of permanent magnets leave some uncertainties that an experimental work has to answer to.

5.4 The prototypes

The main dimensions of the motors, which are used to build the prototypes, are given in Table 3.1. Even though some of the dimensions have been changed from the values that were used in the beginning of the design process, the abovementioned table contains the final values that are considered in the prototyping. The geometrical changes have been made mainly because of the changed diameter of the magnet-rings, which have been selected according to standard measures or/and existing magnetization tool in order to facilitate fast prototyping.

The thickness of the plastic bounded ferrite magnet-ring that previously is analysed to be $l_{pm}=4.475\ mm$, is instead $l_{pm}=3.575\ mm$ in the prototype single-phase claw-pole motor. In the two-phase claw-pole motor the magnet-ring with circular polar magnetization has a ring radial thickness about $l_{pm}=2.7\ mm$ and axial height $h_{pm}=10.8\ mm$. The magnet-ring with radial magnetization and back-yoke has the corresponding values of radial thickness about $l_{pm}=2.5\ mm$ and $h_{pm}=10.6\ mm$ of the axial height. The inner diameter of the magnet-rings is slightly larger, which is $r_{pm}=60.2\ mm$. The slightly larger magnet-rings and air-gap of the two-phase claw-pole motor are presented compared to the values that are given before.

Compaction molded SMC

The SMC parts of the claw-pole motors (Figure 5.34) are manufactured from a compressed solid SMC part. The solid powder part is made from premix Somaloy500+0.6%LB1 that is warm-compacted under the pressure of 800 MPa and followed with heat treatment of 1 hour at 275ºC.

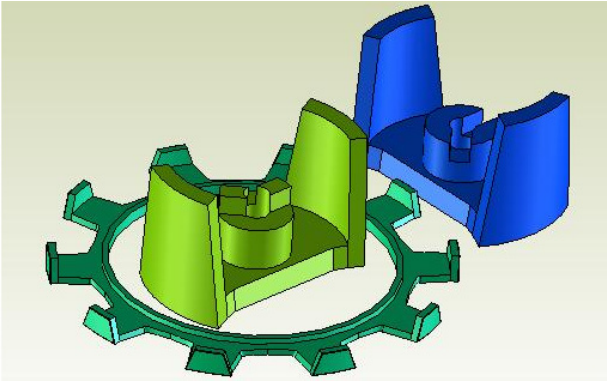

Figure 5.34: SMC parts of the designed claw-pole motors.

Winding

A wound coil of *180 turns* in a bobbin is used in the single-phase claw-pole motor. The diameter of the copper wire is *0.6 mm* and, considering coating thickness to be *5%* of the diameter, the total conductor area is *45.9 mm²*. The available cross-section area in the bobbin is *70.6 mm²* and this gives the copper fill factor about *0.64*. The bobbin with wall thickness about *1 mm* takes *35.5%* of the available slot cross-section area.

The coil in the two-phase claw-pole motor is wound without bobbin. Instead of foil tape conductor a thermo adhesive round-shaped wire is used. The diameter of the copper wire is *0.4 mm* and considering coating thickness to be *5%* of the diameter the total conductor area of *55 turns* is *6.24 mm²*. The available cross-section area in the slot is *12.2 mm²*. There is less space in actual use. A radial distance of *1.5 mm* between the claw-poles and the coil leaves space for connections. The coil is wrapped in cross-section area of *9.5 mm²* that gives the copper fill factor about *0.66*.

The single-phase claw-pole motor

The adjacent claw-pole rings are not identical and they are manufactured separately. The difference is due to the asymmetric pole structure with progressive air-gap radius, and the locking slots and teeth that are introduced

at the centre core (Figure 5.34). The latter is important to provide right angular displacements of the claw-pole rings. Joining these two SMC core halves together revealed a small axial air-gap between them, which is partly due to an expanded bobbin at its outer radius. The rotation shaft is made of electrically and magnetically conductive material that contributes to the losses in the machine. The inner radius of the stator is covered with a lubricating paint that gives mechanic support to the rotating system of the outer rotor. Additional ball-bearings are added to both ends of the shaft and the system incorporates a position sensor in the middle. A mechanic coupling to torque measurement system is constructed at one end of the shaft and the other end has a coupling to a reference electric machine.

Two-phase claw-pole motor

In the two-phase claw-pole motor the claw-pole rings are identical and interlock the simple hoop phase coils between them. Some assembling difficulties of the single claw-pole ring are due to the beginning and end strands of the thermally fastened coil. Namely, the attachment of the first and last turn is connected weakly to the rest of the strands. The complete wrapped coil needs to have fine tolerance, the same as the claw-pole rings, and the wire needs to be taken out from the slot. The wire from the inner radius of the coil requires special care when assembling the phase and taking the wire out so that the magnetic contact between the claw-pole rings at the inner radius is good.

The mechanic support system is made of a plastic holder that centers the stator parts and holds small ball-bearings of the shaft for the outer rotor cylinder. The motor parts with small dimensions and very fine tolerances need special care when assembled. The SMC claw-pole ring is glued on top of a thin plastic foil. This is done in order to prevent the claws from falling apart while assembling or reassembling. A narrow air-gap and relatively large gap radius require precision in motor assembling. Large attractive forces appear between the magnet ring and the thin details of the SMC core. An unfortunate assembling has shown that a mechanic failure of the SMC claw-pole ring occurs most likely at the thin core parts where the flanks are reduced to a minimum. It is less probable that the claw-pole falls apart from the flank. This can happen only if the adjacent claw-pole rings are improperly assembled so that the coil is not able to hold the broken pole with the flank and the saliency at the inner radius. In this case, the magnet drags the pole out from the phase. Still, the whole pole can be kept in one piece if care is taken while disassembling the motor.

The two-phase claw-pole motor has two rotors. One with multi-pole circular-polar magnetized magnet-ring and the other with a back yoke and a magnet-ring that carries radial magnetization pattern.

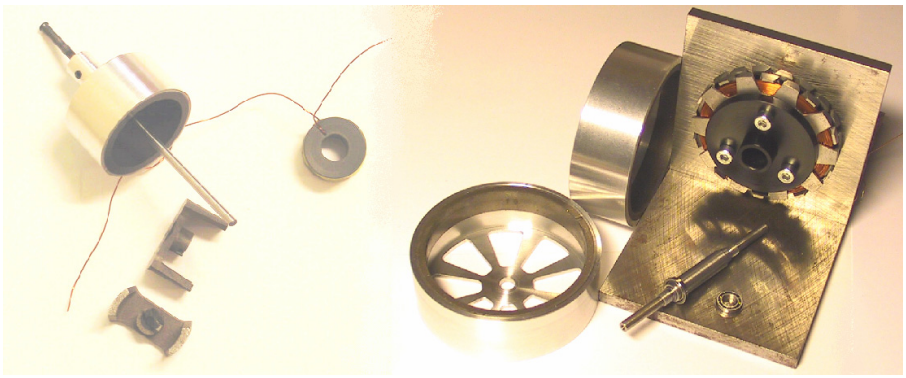

Figure 5.35: Prototype motors.

The prototype claw-pole motors are shown in Figure 5.35.

5.5 Static characteristics

The static characteristics of the claw-pole motor are evaluated from simple tests. In these tests the reluctance torque and the electromehanical coupling torque as a function of position and current loading is measured. The coupling flux is evaluated from induced voltage measurements. The speed introduces losses in the rotating system. Mechanic and magnetic losses are separated. Moreover, speed dependent and static losses are separated among them.

Static torque as a function of position

The electromechanical T/θ characteristics have been measured with a simple weighting-scale method. Either the load mass m or the position θ can be changed in order to detect the point of mechanic equilibrium (Figure 5.36). The mechanic coupling between the beam of the scales and the motor rotation axis is adjustable. The coupling adjustment helps to determine the motor torque even in unstable region by seeking the position of mechanic equilibrium. The beam is symmetric in respect of a pivot, and the load can be placed either to left or to right side in a weight-pan. The load weight is suspended in the beam of a distance l from the pivot point. The mechanic equilibrium is the balance between the motor torque applied to the rotation axis and the load applied to the arm of the scales. In case of unequal weights

the dislocation angle δ from the horizontal position of the arm l need to be considered.

$$T(\theta) = 9.81 \cdot l \cdot m \cdot \cos(\delta) \tag{5.1}$$

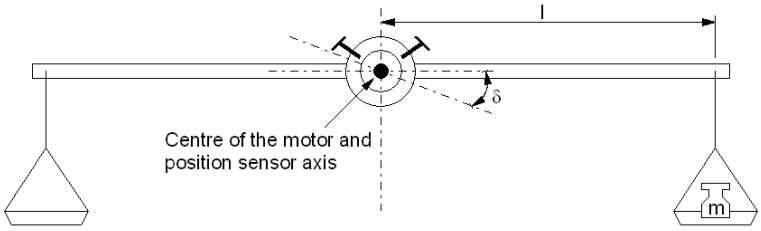

Figure 5.36: Weighting-scale measurement set-up. Two cylinders are mechanically fixed with a pair of screws at a certain position. The weight is changed in order to balance the resultant torque applied from the claw-pole motor.

Two types of errors are introduced in the measurement. One of them is the measurement accuracy of the position and the other is the estimation error of the load torque that causes the mechanical equilibrium. Alternatively, the motor torque characteristics are measured by the use of spring scales.

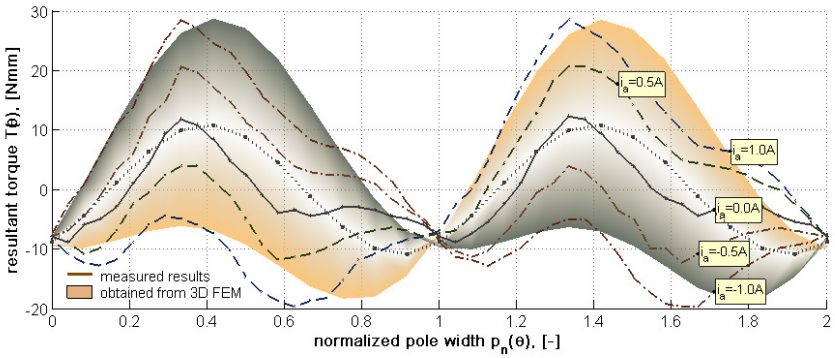

Figure 5.37: Static characteristic obtained from 3D FE adjusted model and the measured points.

The magnetic interaction (coupling) torque component coincides with the calculations having the maximum error about 9%. The shape of the magnetic attraction (cogging) torque differs from the one calculated from 3D FEM and only more exhaustive FEM calculation could give an answer whether the difference is due to an eccentricity, due to a different magnetization pattern of the plastic bounded ferrite magnet-ring or the 3D FE model formulation and solution itself.

The static torque measurement of the two-phase claw pole motor is made in two steps. First, the torque waveform is obtained for a single phase. Next, the static characteristics are obtained for the whole two-phase claw-pole motor. A series of measurements is done, which bases on the use of spring scales, in order to get the reliability of the measurements to admissible level. The complexity of the measurements increases due to relatively small radius and high number of poles. In addition, a study has been carried out where a single phase is placed in the middle of the magnet-ring. The dependence of the static characteristics on the axial air-gap *gs=0.0, 0.1, 0.2, 0.3* and *0.4 mm* between the claw-pole rings of the unexcited (Figure 5.38) and excited core (Figure 5.39), respectively, is shown.

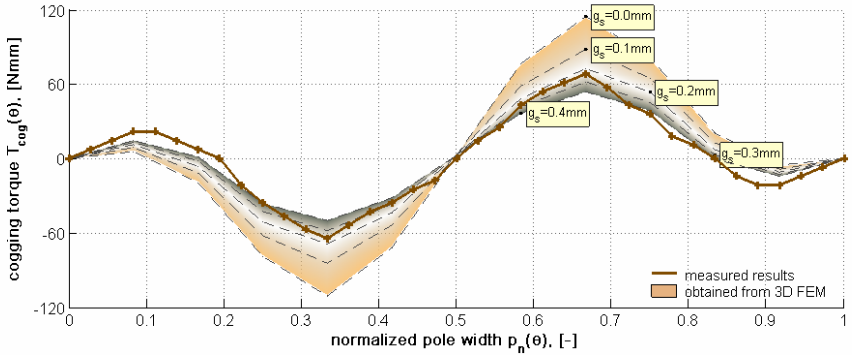

Figure 5.38: Cogging torque waveform of the single phase from the two-phase claw-pole motor. The filled zones in the background show the corresponding FEA result.

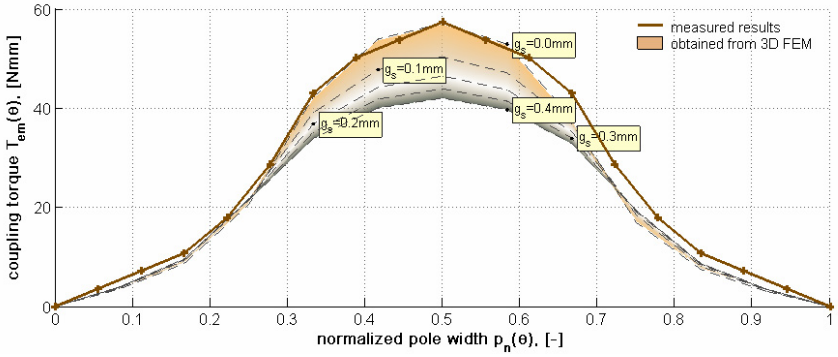

Figure 5.39: Coupling torque and flux waveform of the single phase from the two-phase claw-pole motor. The filled zones in the background show the corresponding FEA result at different length of the axial air-gap.

A series of experimental torque-position measurements are based on a simple spring scale test, where the equilibrium positions and the peaks on the torque waveform have been detected. The measurement points are increased between the stable and unstable equilibrium points, and the points where the maximum of the cogging torque occurs. The relative contribution of the coupling torque has been calculated from the torque change in the torque peak position.

The coupling torque measurement is based on the measured waveforms of the excited and the unexcited phase. A large measurement error is expected. The human error of determining the exact reference point for two series of measurements is presented. Moreover, an inaccuracy of the position and torque measurement around the unstable position of the rotor, where the peak of the coupling torque appears, causes difficulties in the measurement process to obtain accurate results.

According to the torque waveforms it can be expected that the height of the axial air-gap is between 0.0 and 0.3. This discrepancy between the two measurements indicates the measurement inaccuracy and this to be compared with an experimental work on coupling flux and core loss measurements.

The mechanic output of the assembled motor is presented in Table 5.4. The predicted values are obtained from 3D FEA (Figure 5.22).

Table 5.4: Main quantities of the assembled motor. The predicted values are based on 3D FEA.

Quantity	Circular-polar magnetization		Radial magnetization		Unit
	Predicted value	Measured value	Predicted value	Measured value	
Maximum phase current	1.0	1.0	1.0	1.0	A
Maximum coupling torque	40.0	50.0	38.0	50.0	Nmm
Maximum cogging torque	8.0	80.0	13.0	100.0	Nmm
Axial gap between core halves	0.0	0.2	0.0	0.2	mm
Axial distance between phases	0.8	0.4	0.8	0.4	mm

Regarding to the prediction of the torque components, the predicted coupling torque is underestimated as the torque is expected to be smaller due to the presence of the axial air-gap with respect to the cogging torque waveforms.

Similarly, FEA analysis the complete motor has 20% lower coupling torque compared to the measurement of the whole assembled motor. The simple torque measurement system allows estimating approximately the maximum values of the torque components while the measurement of torque position characteristic is too erroneous. From the measured and estimated torque components can be seen that the drive of the two-phase claw-pole motor is not possible without introducing over current. The predicted waveforms of the whole motor on the basis of the single-phase measurements are presented in Figure 5.40. This prediction compare well with the approximate measurements of the whole assembled motor.

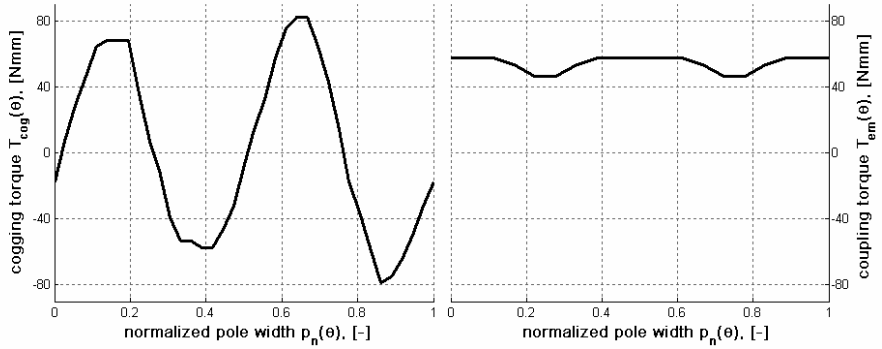

Figure 5.40: The torque components of the whole assembled claw-pole motor which are predicted from the measurements of the single-phase ring.

Coupling magnetic flux

The measured electromotive force is used to verify the calculated flux linkage and can be used to predict whether the lateral polar magnetization pattern of the plastic bounded ferrite magnet ring differs from the expectations. If the axial air-gap about 0.1-0.2 mm is considered then the predicted coupling magnetic flux of the single-phase claw-pole motor differs ±10% from the measurements (Figure 5.41).

The prediction of coupling flux in 3D FEA is based on the integration of the magnetic flux that couples through the base core. The measurements consider the flux that links with the coil. Therefore the leakage flux between the flanks is included in the measurements. Moreover the leakage flux component becomes more dominant if the magnetic core is magnetically saturated like in the two-phase claw-pole motor.

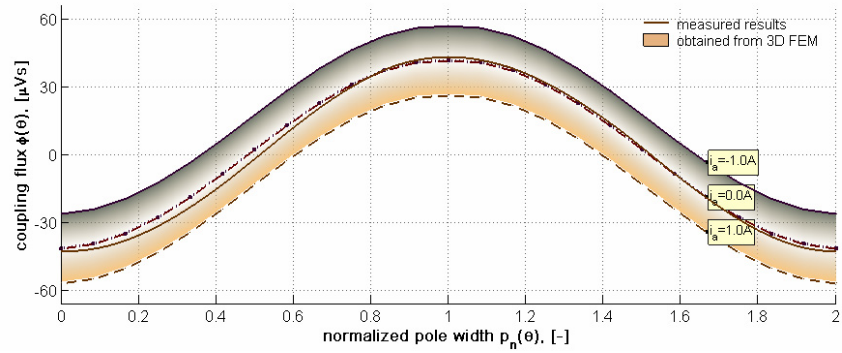

Figure 5.41: The coupling flux waveform obtained from 3D FE adjusted model and the measured points with no stator currents.

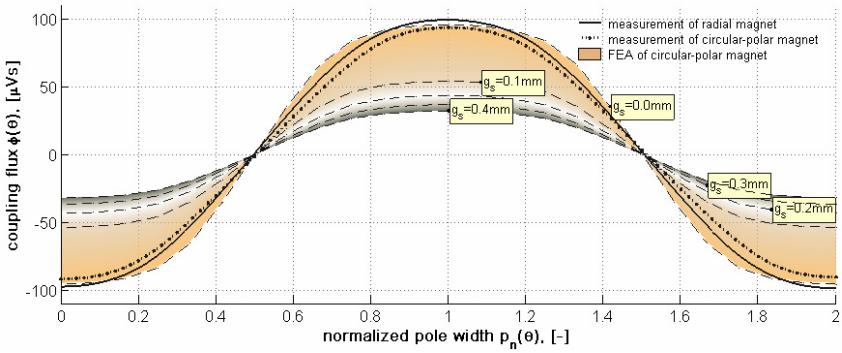

Figure 5.42: The coupling flux waveform obtained from induced voltage measurements for two different magnet-rings when the single phase is of the two-phase claw-pole motor is assembled. The filled zones in the background show the corresponding FEA result at different length of axial air-gap.

The coupling flux waveforms that are integrated from the induced voltage measurements of the two phase claw pole motor show a stronger magnetic coupling for the magnet-ring that carries radial magnetization pattern.

The estimated coupling flux waveforms are compared to FEA where the length of the axial air-gap is varied (Figure 5.42). The estimated coupling flux waveforms indicate that the magnetic connection between the claw-pole rings of a phase is near to ideal and the axial air-gap is practically less than 0.1 mm. According to visual observation the phase is well assembled compared to the neighbor phase that has improper magnetic and mechanic contact between the claw-pole rings due to coil assembling. The estimated coupling flux waveform

show 50% reduced induced voltage and flux linkage values for the improperly assembled phase. These values are realistic as an average of 0.1 mm axially displaced claw-pole rings are expected for this phase.

The harmonic content of the coupling flux waveform for the radially magnetized magnet-ring shows the third harmonic of -4.2% and the fifth harmonic 0.7% compared to fundamental. The same quantities for the circular-polar magnetized magnet-ring are respectively -2.0% and 0.6%. As the core is according to FEA is saturated, the harmonic content in the coupling flux waveform does not reflect the excitation harmonics that are present in the magnet-ring.

In respect to the discrepancy between the measurements and the FEA the difference between the estimated and the obtained results, the estimated coupling flux curve does not indicate the effect of the magnetic saturation. This is due to increased effect of magnetic leakage. The difference between the FEA calculation and the measurement depends also no the accurate formulation of 3D FE model. Therefore, it has been studied that the motor dimensions have been entered correctly 3D FE model, including any small gaps. The magnet excitation orientation has been set up according to ideal sinusoidal field distribution. Moreover, the permanent magnet excitation field has small difference between the radially magnetized and circular polar magnetized magnet-rings, if the comparison is based on induced voltage measurements Figure 5.41 vs. Figure 5.42 and Figure 2.14 vs. Figure 2.15. The BH data is slightly varied in order to investigate whether the data that has been used is correct for the actual material. This experimentation excluded the effect of material anisotropy. The calculation showed that 10% variation on magnetic conductivity influences the peak of magnetic coupling flux in the single-phase claw-pole motor about 6.8%. The accuracy of the FE model is studied, whether the obtained field values depend on the placement of the far field boundary, the FE mesh quality, an order and the number of elements. The experimentations of the 3D FE modeling have not shown any reasonable source of errors. Furthermore, the quality of the measured data is investigated and measurements are repeated in order to specify the difference between the estimation and the measurements. The measurement methods are based to the same technique and, therefore, no explanations have been found.

5.6 Core loss measurement

Two different methods are implemented in order to estimate the core losses in the claw-pole motors. The first method is based on current and voltage

measurement that is the estimate of the input power. The input power of an auxiliary dc motor is measured. The dc motor is loaded with mechanic system that includes a position sensor and a claw-pole motor without stator. The measurements are done at different speeds. Then, the SMC stator core is placed back to the claw-pole motor and the measurements are repeated at different speeds. By subtracting the resistive heat loss from the measurements the difference between the second and the first measurement, gives approximate estimate of the core losses in the claw-pole motor.

A second loss measurement method is based on a position controlled and a calibrated dc motor drive. Ideally, the current of the dc machine, which is driven at very low speed, builds the electromagnetic torque that is opposite to the cogging torque of the claw-pole motor and that overcomes the magnetic friction. Similar to previous method, the system is driven at different speeds in order to separate the mechanic and magnetic losses among the static and dynamic losses.

Loss measurement setup

A calibrated dc motor is used in order to estimate the energy needed to overcome friction losses. The friction losses are the static friction of the mechanic system and the physical work to magnetize the core (magnetic friction) over the magnetization period.

$$W = \psi_{dcm} \int_0^{2\pi} i_a(\theta) d\theta = \int_0^{2\pi} T_{frict}(\theta) d\theta + \oint HdB = 2\pi \overline{T}_{frict}(\theta) + A_{hyst} \tag{5.2}$$

The average static friction T_{frict} and the speed dependent mechanic losses are measured from the test bench without the claw-pole core. In order to estimate the dynamic losses the rotation speed is increased gradually,

$$P = 2\pi f \psi_{dcm} \overline{i}_a(\theta) = 2\pi f \overline{T}_{frict}(\theta) + fA_{hyst} + P_{dyn,core} + P_{dyn,mech} \tag{5.3}$$

where two unknowns appears: dynamic iron loss $P_{dyn,core}$ in the core and the total dynamic loss $P_{dyn,mech}$ in the mechanic system.

Losses in the single-phase claw-pole motor

The result of the calibrated dc motor drive is shown in Figure 5.43.

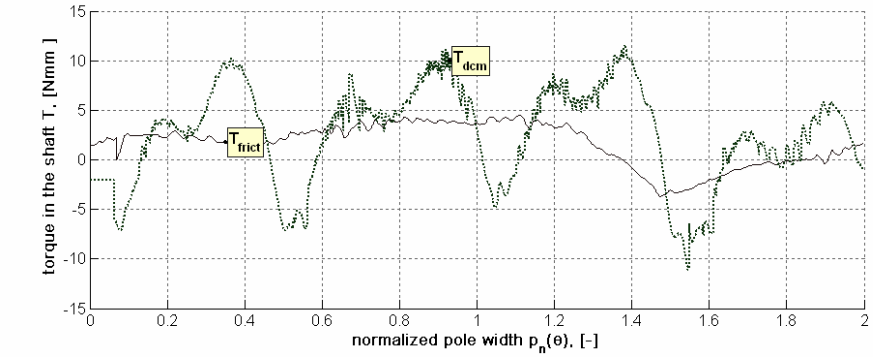

Figure 5.43: Static core loss measurement, torque characteristics over one mechanic revolution at low magnetization frequency of 0.07 Hz. The torque components, which are seen from the dc motor current, are the mechanic friction (dark solid line) and the sum of magnetization, mechanic friction and cogging torque (light dashed line).

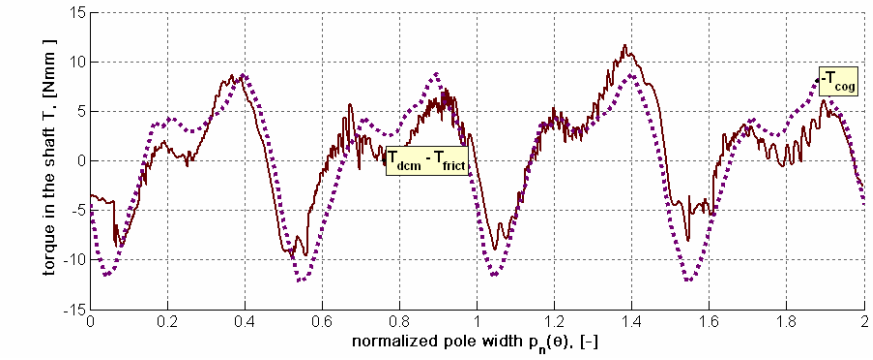

Figure 5.44 Static core loss measurement, torque characteristics over one mechanic revolution at low magnetization frequency of 0.07 Hz. The sum of magnetization friction and cogging torque (solid line) is compared to the inverted static torque measurement (dotted line) that is obtained from weighting-scale method.

The core loss measurements (Figure 5.45) show about 35% difference between the predicted and the measured static loss and 60% for the dynamic loss. The dynamic loss includes windage loss in the claw-pole generator. The mechanic loss does not include friction loss between the claw-pole stator and shaft.

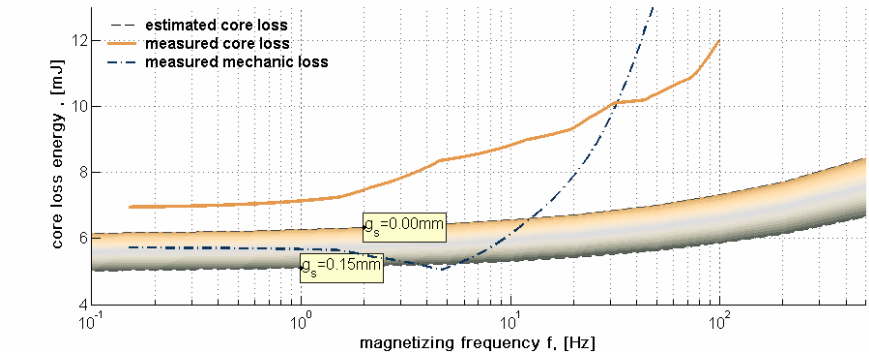

Figure 5.45: Dynamic loss energy per mechanic revolution as a function of electric rotation frequency.

Losses in the two-phase claw-pole motor

The resultant core loss, appearing in the SMC parts, depends on the trajectory and the rate of change of the flux density vector during a remagnetization cycle. The core loss that is due to the rotation of flux density vector is calculated for a single claw-pole ring. The length of the axial air-gap is varied. The loss energy prediction at different mechanic coupling of the claw-pole rings and the real measured loss per magnetization cycle is shown (Figure 5.46).

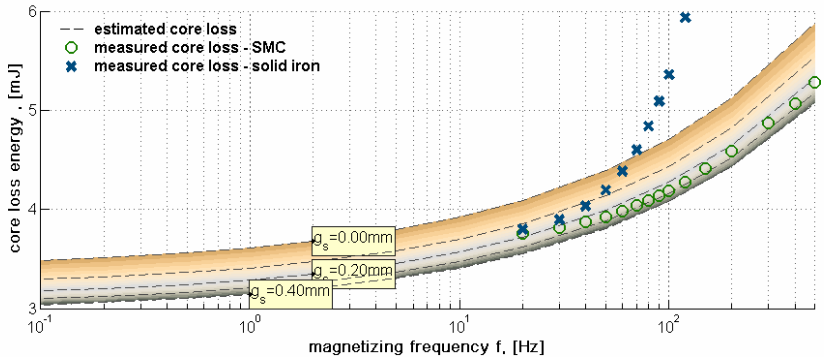

Figure 5.46: Core loss energy as a function of magnetization frequency of the single phase from the two-phase claw-pole motor. The filled zones in the background show the corresponding FEA result at different length of axial air-gap.

The hysteresis loss reduces in the flanks and in the bottom of the core, when the stator due to the increased distance between the core halves becomes magnetically less loaded (Figure 5.46). Even though a phase-core, which is made from solid iron, is better suited for a heavy magnetic and mechanic loading, the dynamic core losses become critical at high magnetization frequency. The magnetizing frequency of the motor that is higher than 20 Hz gives preference to SMC core (Figure 5.46).

Thermal loading

The thermal loading is studied for the standstill motors at the nominal and for the increased electric loading. First, the temperature rise in the two-phase claw-pole motor is measured. The temperature rise on the surface of the winding that is loaded as high as 7 A/mm^2 is 11K. As the thin and flat phase coil has a good thermal contact between the adjacent core-halves, the temperature rise is relatively small. This standstill situation is considered as the worst case for thermal loading because the active cooling is practically non-existent.

Similarly, the single-phase claw-pole motor, it is considered that the worst case for thermal loading is motor's deadlock at standstill, when the active cooling is practically non-existent. The copper loss that corresponds to the direct current density of *4* A/mm^2 causes temperature rise on the surface of winding by approximately 33 degrees. The resistive heat loss at nominal current is in the same range as the predicted value from the 3D FEA.

5.7 Conclusions

The static characteristics of the single-phase claw-pole motor has been modelled in 3D FEM and compared to the measurements. The characteristics compare well to the measurements, while the discrepancy with the cogging torque waveform needs further analyses and experiments to explain. The experimental results agree with prediction and show that the actual air-gap between the claw-pole ring halves is around 0.1-0.2 mm. A well-compacted winding with the ends at the outer radius will reduce the axial air-gap between the core halves.

The combination of the narrow radial air-gap, the high gap radius, the thin SMC parts and the strong magnet-ring makes the motor assembling of the two-phase claw-pole motor a challenge. The static characteristics of the single-phase ring of the two-phase claw-pole motor have been modelled in 3D FEM. The characteristics compare well to the measurements.

The reduction of cogging torque is important for high pole number claw-pole motors. If instead of plastic bounded NdFeB, the plastic bounded ferrite magnet-ring is used, then due to smaller magnetic attraction the cogging torque is decreased by 1/10 (Figure 5.26). The coupling torque reduces by 63%. According to the 3D FE magnetostatic calculations, a wider axial distance between the adjacent phase core- as well as a rectangular shape of claw-pole rings increases the cogging torque. The trapezoidal claw-pole with a distinguishable tapering in the axial/circumferential plane as well as the reduced space between the adjacent claw-poles will reduce the cogging torque. The coupling flux shows very small reduction when the pole angle of the poles is increased, unless the axial air-gap between the poles will improve the leakage in angular direction through the claw-poles.

The thermal loading shows good agreement with the prediction. The temperature measurement is done on the surface of the winding. Moreover, only a single-phase of the two-phase claw-pole motor contributes to the resistive heating. Therefore the temperature rise, which is obtained from the measurements, is relatively lower compared to the hot spot of the winding.

The sensitivity study indicates that the simple air-gap permeance vs. magnetization function method gives misleading results concerning to the best choice of the coupling and the cogging torque waveforms.

Chapter 6

Control of a claw-pole motor

A control strategy and drive circuit is proposed to the designed claw-pole motors. The chosen control strategy is simulated in Simulink. Thereafter the control circuits are used in real time control in dSpace for a prototype motor. The prototype motors are modeled according to the electromechanical characteristics, which are obtained from the 3D FE analysis and from the measurements. The goal of the control of a claw-pole motor is to obtain the dynamic characteristics of the claw-pole motors and to estimate the efficiency of the drive system. The dynamic characteristics of the single-phase claw-pole motor are simulated and tested for a proposed control system. The characteristics for the two-phase claw-pole motor are only simulated.

6.1 Control strategies

The control of the claw-pole motors is based on the use of a voltage source inverter (VSI). The VSI consist of a power electronic module of four MOSFET transistors that are connected to an H-bridge with the motor winding as load. The strategy of the commutation cycle of the transistors is determined by the action of a current controller.

The aim of the current controlled motor is to produce the required mechanic torque output or/and to keep the current loading of the machine within the secure limits. The drawback of the current and torque controlled motor is the cost of the complexity of the drive circuit that incorporates current and position transducers.

Control of the single-phase motor

The main requirements for an electric drive system that incorporates a single-phase motor are low cost, high efficiency, compactness, reliability and simplicity. Additional features are controllability of an output, i.e. a rotation speed, and adaptability of an input to a power supply, e.g. EMC and harmonic emission [26]. Depending on the power supply, the single-phase motor drive is usually connected into the mains or directly supplied by a DC voltage like a battery. Independent of the type of the power supply, the single-phase permanent magnet motors are usually VSI fed. Typically, a Hall Effect sensor is used to define the firing instant and the duration of duty cycle. Either ac brushless or dc brushless operation principle can be implemented where the loading compensation or the speed of the system is controlled [26]. Additionally, the phase commutation is adapted to the rotation speed to facilitate the high-speed torque capability. Otherwise, the current becomes delayed and the induced voltage falls out of phase at high operation speed and high winding inductance. As a consequence a negative torque component is generated and the overall torque is reduced [99].

In order to accelerate a rotor, a sequence of a driving field pulses has to interact with the permanent magnet excitation field. The monofilar winding, which is subject to bipolar excitation, is a relatively expensive control solution [23][26]. On the other hand, it is not evident whether the inexpensiveness of the unipolar inverter compensates the partly utilized excitation coils [26][99]. The advantageous feature of the bifilar coil is the good magnetic mutual coupling that facilitates the commutation process and the reduction of commutation losses in the MOSFETs [23]. The advantage of bipolar driver is chosen, even though the simple motor construction facilitates evaluation of different configurations. The H-bridge inverter (Appendix D), operated by a train of pulses, performs the control action. The control pulses are formed either from a hysteresis current controller or PWM modulated output of a sampled current controller. The control action of the current controller bases on the difference between measured current and a current reference. The latter is formed in a reference generator.

The reference current waveform should be chosen with respect to the maximized ratio of torque to current. The single-phase claw-pole motor is not able to produce electromechanical torque at rotor positions, where the excitation field in the air-gap is aligned with the applied armature field (Figure 6.1). The highest electromechanical torque is achievable at positions where the excitation field is orthogonal to the applied stator field.

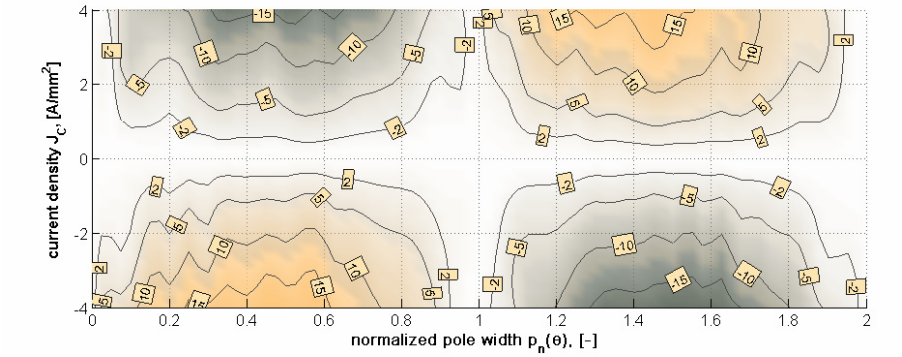

Figure 6.1: The current density needed to produce electromagnetic torque. The equi-torque contours (T_{em} in Nmm) show the corresponding electromagnetic torque as a function of rotor position and current. The initial zero position is at alignment position of the magnet pole and the claw-pole.

The resting position of the rotor is between 0.5 and 0.6 of the pole-pitch. Apart from the cogging torque, the electromagnetic torque needs to overcome the friction losses. The friction losses at low speed consist of mechanic and a magnetic loss, which according to measurements gives a mechanic load torque around *2 Nmm*. This is calculated from the energy that needs to be applied to the rotor in order to rotate it an angular distance that corresponds to a single remagnetization cycle. In dead zones, the motor is not able to produce enough torque to exceed the mechanical loading due to the friction.

The reference current waveform is formed to fit the best needs for a certain speed. The magnitude and the frequency of the reference waveform need to be carefully selected for sensorless control with a slightly varying load, so that the motor does not loose the synchronism.

Control of the two-phase motor

The additional phase, which is shifted about a half of pole pitch in the angular direction, contributes to the total electromagnetic torque production in the two-phase claw-pole motor. An optimal combination of the phase currents $i_a(t)$ and $i_b(t)$ has been selected in order to get a constant torque and least resistive losses at a known rotor position (Figure 6.2, right). Otherwise, unreasonably high current loading is needed to produce constant torque in a phase that is situated close to its dead-zone (Figure 6.2, left).

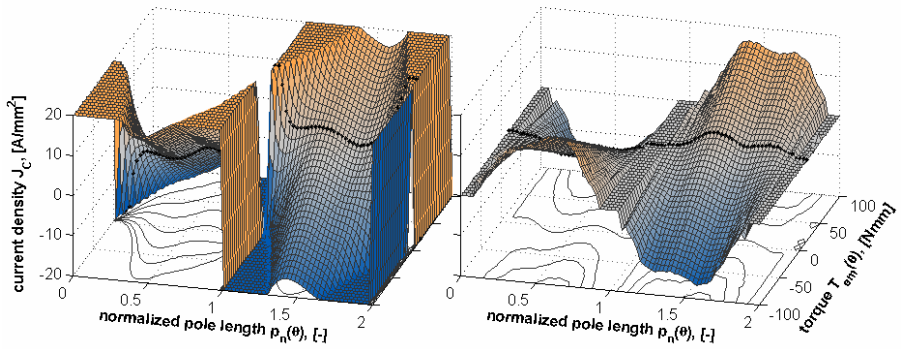

Figure 6.2: A current density reference of a single-phase in the two-phase claw-pole motor that gives constant torque (left). The optimal combination of phase currents that provides constant torque and gives the least resistive losses in the two-phase claw-pole motor (right).

Fast dynamic response and smooth movement are prioritized over a simple control strategy and an inexpensive control system. Therefore, the torque of the claw-pole motor has to be controlled and a closed loop control is applied to the drive system [53]. The torque control of an electric machine is done via a current control where the combination of phase currents that gives least copper losses is selected (Figure 6.3).

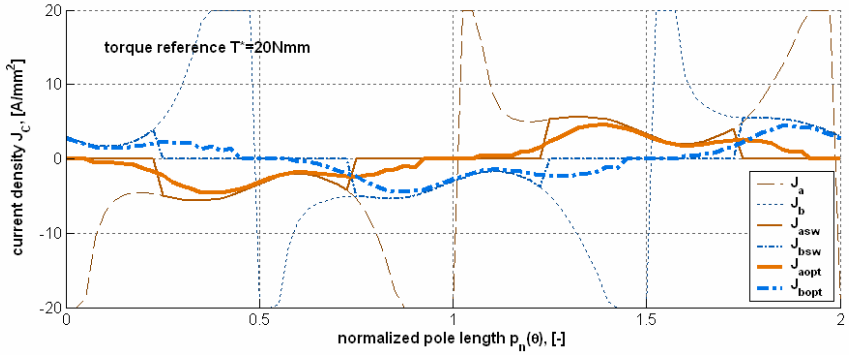

Figure 6.3: Selection of current density reference profile to produce a constant torque of 20 Nmm in the two-phase claw-pole motor. The thin lines (J_a,J_b) show the required current density if a single-phase has to provide the reference torque. Alternatively, the reference current can be selected according to minimized switching (J_{asw},J_{bsw}, normal lines) or copper losses (J_{aopt},J_{bopt}, bold lines).

The single-phase is not able to provide constant torque at all positions. Therefore, the combination of two phase currents is selected. The current density waveforms that are referred as J_{asw} and J_{bsw} require least switching while operated. The phases are activated only in the region of the highest ratio of torque to current. Alternatively, the references J_{aopt} and J_{bopt} can be chosen according to the least copper losses.

6.2 Drive system model

Simple control circuits have been designed for the single-phase (Figure 6.4) and two-phase claw-pole motors (Figure 6.5). The whole drive system has been built in a Simulink block diagram where later the control system is used to control the prototype via dSpace RT fast prototyping environment.

Two different current controllers are designed for the single-phase claw-pole motor (Figure 6.4). The direct current control (DCC) is based on a pair of hysteresis controllers that determine the switch states. The sampled current control (SCC) is based on a PE (Proportional + EMF feedforward) current controller action. The SCC controller output, which is a reference voltage, is pulse width modulated (PWM) in order to provide the same average voltage from the VSI.

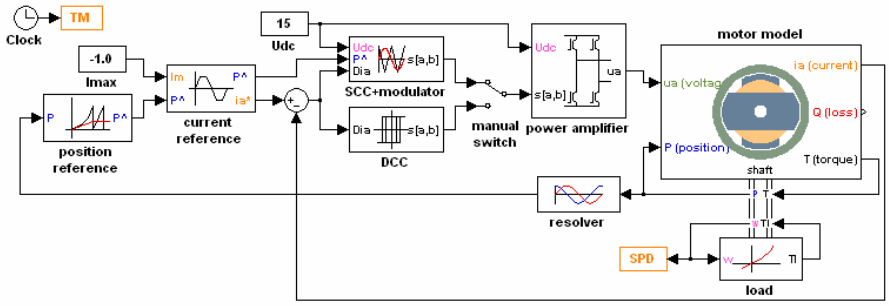

Figure 6.4: Model of drive system for the single-phase claw-pole motor developed in Simulink.

Different reference current waveforms can be evaluated for the single-phase claw-pole motor. The predefined types are a square wave, a trapezoidal, a sinusoidal and a pulse waveform. The waveform is generated according to the angular position of the magnet-ring and the magnitude of the current. The angular position reference can be formulated from the resolver signals or it can be generated according to a reference speed ramp. The later is done in order to study the sensorless control of the single-phase claw-pole motor. The torque

that the claw-pole motor is able to produce is loaded with the mechanical friction and load characteristic of an application drive.

The drive system for the two-phase claw-pole motor consists of a full servo-drive via cascaded speed and position control (Figure 6.5). The DCC is used to perform constant torque control of the two-phase claw-pole motor. Two look-up tables are used to specify the current references for the two phases, such that the output torque is constant at any rotor positions. The torque reference is formulated in the speed controller. The load is characterized as a rotary-to-linear transmission where the linear movement can be either on the horizontal or vertical axis.

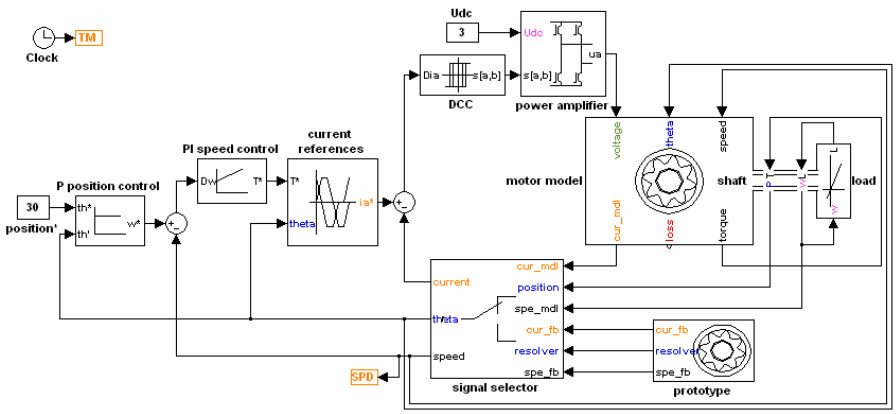

Figure 6.5: Functional block diagram of the control system for a two-phase claw-pole motor.

The control system is made in such a way that it is able to use a motor model or the real prototype motor. The selection of the feedback signal is made in a signal selector block.

The complete motor model for both claw-pole machines is based on the nonlinear characteristics, which are obtained from 3D FE modeling or/and from the measurements. The model of the electromechanical energy conversion includes the loss mechanisms and thermal heating. The temperature rise does however not influence the motor model parameters. Another less favorable feature of the loss formulation is that a simple core loss model is used. This is done in order to increase the speed of simulation. In addition, the effect of the core losses, which are obtained from the simple core loss model, has no influence on the torque production.

The generic formulations (Eq. 6.1-6.3) of the electromechanical energy conversion express the relations for the single phase rather than for the complete two-phase motor.

$$\psi(i,\theta) = \int \left(u(t) - R \cdot i(t)\right) dt - \psi_{PM}(\theta) \tag{6.1}$$

$$\omega = \frac{1}{J} \int \left(T(i,\theta) + T_{cog}(\theta) - T_{hyst} - T_{load}(\omega)\right) dt \tag{6.2}$$

$$\vartheta = \frac{\alpha \cdot A_{cool}}{c \cdot m} \int \left(\frac{R \cdot i^2(t) + P_{Fe}(i,\omega)}{\alpha \cdot A_{cool}} - \vartheta \right) dt \tag{6.3}$$

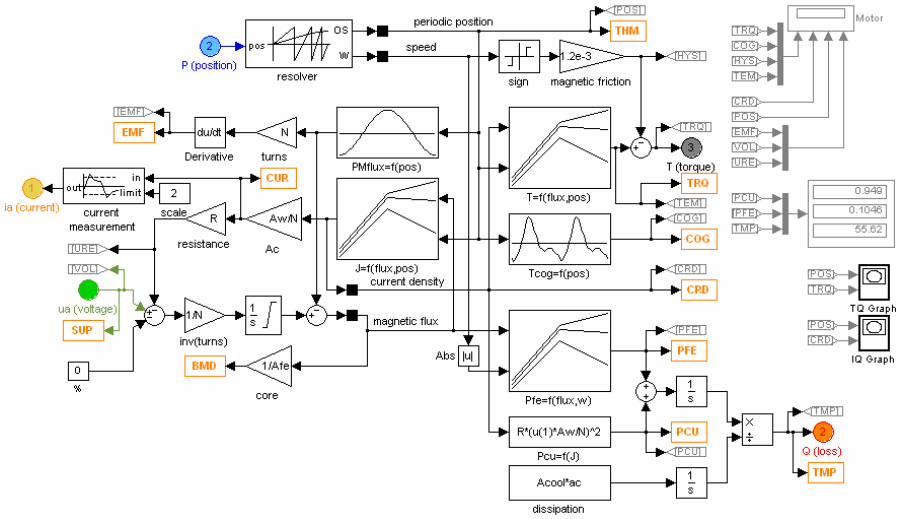

Figure 6.6: The model for electromechanical energy conversion.

The non-linear interaction between the electric input and the mechanic output, which is between the single phase and the magnet-ring, is the electromagnetic flux $\psi(i,\theta)$ and the coupling torque $T(i,\theta)$. The magnetic coupling between the winding magnetomotive force $i(t) \cdot N$ and the magnet flux $\psi_{pm}(\theta)$ is the actual transfer between electric and mechanic energy. Every phase has its' contribution to the applied torque. The resultant steady-state torque applied to the shaft depends on the no-load magnetic attraction (cogging) torque $T_{cog}(\theta)$, no-load magnetic friction (hysteresis) torque T_{hyst}, and a mechanic loading

applied to the shaft $T_{load}(\omega,\theta)$. The mechanic loading includes mechanic friction, windage and a fictive load. The resultant steady-state torque is a balance between the applied torque (Eq. 6.4) and the load torque (Eq. 6.5).

$$T = \frac{p}{2} \cdot i(t) \cdot N \cdot \phi_{PM}(\theta) + T_{cog}(\theta) \tag{6.4}$$

$$T_{load} = T_{hyst} + T_{frict}(\omega) + T_{eddy}(\omega) + T_{application}(\theta,\omega) \tag{6.5}$$

The rotational induced voltage depends on the magnet flux $\psi_{pm}(\theta)$ and the angular speed ω of the remagnetization cycle. The direct coupling between the electrical current and magnetic flux through the core $\psi(i,\theta)$ includes the effect of the permanent magnet excitation. Mutual effects are included in the complete two-phase motor model that has more than one phase.

The temperature rise $\Delta\vartheta$ in the stator is estimated according to a cooling capability, a cooling surface and the heat sources that are due to the known losses. The cooling capability is determined by the surface A_{cool} and heat transfer coefficient, which is the natural convection coefficient a. The materials ability to store heat can be taken into account as a heat capacity that is defined by the mass m and the specific heat constant c. In the Simulink model the heat balance between heat sources and cooling capability is simulated.

The core loss model is based on the loss separation technique for the known core loss mechanisms. The core loss estimation (Eq. 6.6) is approximate and it is assumed that the loss distribution is proportional to the flux density in the centre of the phase-core. The look-up table of the core losses considers the contribution of permanent magnet excitation field ϕ_{pm}, the armature field $\phi_A = 'Li'$ and the remagnetization speed ω.

$$P_{core}(\phi,\omega) = \sum_{i=1}^{core\ parts} V_i \cdot \left[k_h \left(\frac{|\phi_{pm} - \phi_A|}{A_i} \right)^n \frac{\omega}{2\pi} + k_{dyn} \left(\frac{|\phi_{pm} - \phi_A|}{A_i} \right)^{n_b} \left(\frac{\omega}{2\pi} \right)^{n_f} \right] \tag{6.6}$$

The losses are considered in three different parts of the stator core, which have different cross-section area A_i and volume V_i. The leakage is not taken into consideration. Alternating flux density variation is considered in the core and the loss coefficients for static and dynamic losses (Appendix A) are taken according to sinusoidal field variation. The drawback of the loss model is that this formulation does not take into consideration the core losses due to field rotation and the losses due to electrodynamics.

6.3 Simulations

The characteristics of the drive system are determined in two different ways for the single-phase and the two-phase claw-pole motor drives. Namely, the definition of the mathematical model of the single-phase claw-pole motor and the parameters of the drive system are based on measured values from the prototype motor. The idealized FEM-calculated motor characteristics are used in the motor model of the two-phase claw-pole motor. The reason for selecting the analytical results and not the experimental result is the large discrepancy between the predicted cogging waveform and the real cogging waveform. Moreover, the two-phase claw-pole motor has to be properly reassembled. It is necessary that the contribution of the coupling torque from the different phases is balanced and is able to overcome cogging torque. The experiment in order to get continuous movement costs 50-80% overcurrent compared to the nominal current.

The dc link voltage, the switching condition of the VSI and the controller parameters of the drive system for the two different claw-pole motors are presented in Table 6.1. The sampling time of the SCC is determined by the carrier of PWM. The sample time equals to the period of the carrier. This selection is made according to the signal synchronization conditions that are specified in dSpace.

Table 6.1: Specification of the drive system.

Quantity	symbol	unit	The single-phase claw-pole motor	The two-phase claw-pole motor
DC link voltage	U_{DC}	V	15	3
The first DCC tolerance band	Δi_1	mA	100	25
The second tolerance band	Δi_2	mA	$1.3 \cdot \Delta i_1$	$1.3 \cdot \Delta i_1$
Sampling time	T_S	ms	0.2	-
Proportional gain SCC	K_{PC}	-	18.2	-
Proportional gain SC	K_{PS}	-	-	0.001
Integral time constant SC	T_{IS}	ms	-	200
Proportional gain PC	K_{PS}	-	-	100

The simulation results are presented separately for the single-phase claw-pole motor and for the two-phase claw-pole motor.

Current control of the single-phase motor drive

The starting transient and steady-state operation are simulated for the single-phase claw-pole motor. The current reference is analyzed with respect to the different starting conditions and steady-state operation at high speeds. The objective is to find the best excitation waveforms, which gives least losses for a given speed. This study is carried out including the position sensor connected in the drive system.

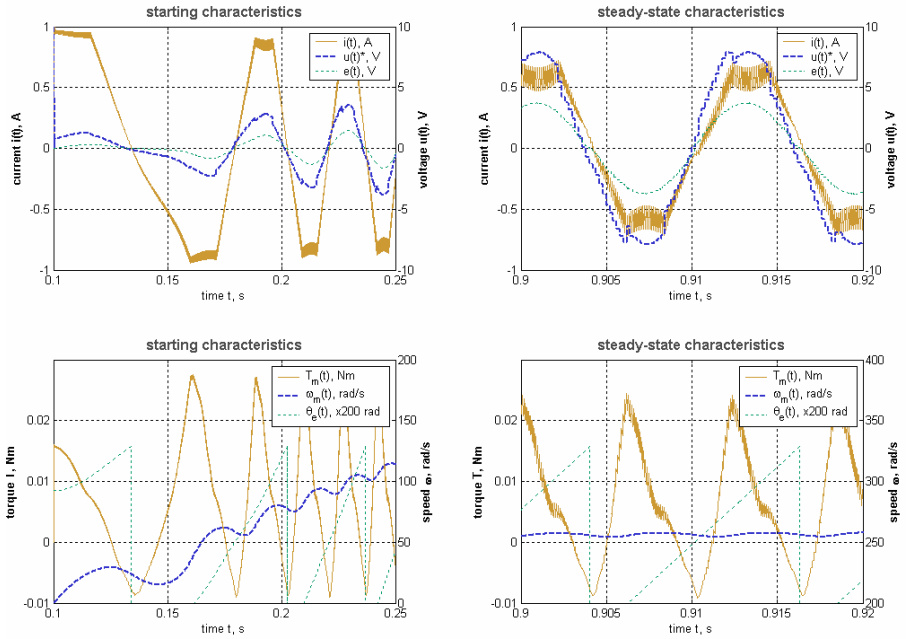

Figure 6.7: Trapezoidal current reference for the single-phase claw-pole motor that gains positive rotation speed. The reference voltage, the induced voltage and the motor current are shown in the upper figures. The lower figures show the electromechanical torque, the rotor speed and the resolver position.

Four different types of current reference waveforms are possible to apply. The simulated results are shown for three of them. The current control with respect to the trapezoidal current reference waveform is shown in Figure 6.7 and Figure 6.8, for a positive and negative speed reference. The corresponding figures for a sinusoidal current density waveform are, respectively, Figure 6.9 and Figure 6.10. The last pair, Figure 6.11 and Figure 6.12 visualizes the simulation results for a square wave current reference waveform. The electrical input and the mechanical output are shown at the starting conditions and at the steady state operation. In this simulation, the load torque is described as a

linear function of speed that gives loading of *10 Nmm* at the speed of *500 rad/s*. Therefore, a model inaccuracy is introduced that excludes all non-linear static loadings. It is assumed that the model inaccuracy helps to determine the acceleration ability of the idealized motor, which is fed from the VSI with different current reference waveforms.

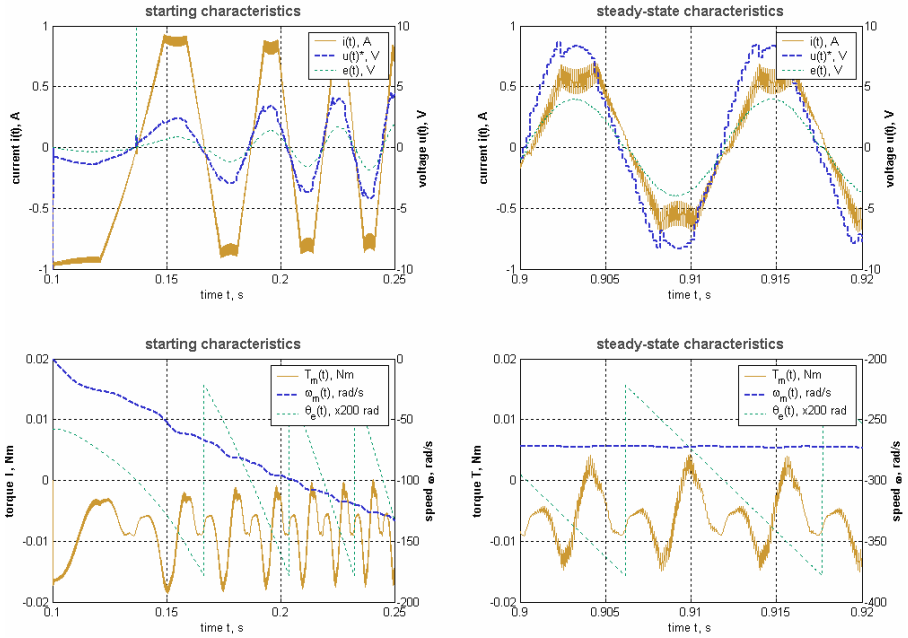

Figure 6.8: Trapezoidal current reference for the single-phase claw-pole motor that gains negative rotation speed. The reference voltage, the induced voltage and the motor current are shown in the upper figures. The lower figures show the electromechanical torque, the rotor speed and the resolver position.

The simulation results presented use the direct current control (DCC). Practically, the DCC give better response, when the tolerance band is selected to be narrow. The sampled current control (SCC) response depends on how the PE controller is tuned and how the control delay is taken into consideration. Generally, the current is intended to rise to the reference value within a certain angle of rotation. At the high speed, the time interval, which is available to build the current, decreases in inverse proportion to the speed (Eq. 6.7).

$$\frac{di}{d\theta} = \frac{U - E}{\omega L} = \frac{U - N\phi_{pm}\omega}{\omega L} \tag{6.7}$$

The current derivative is limited by the induced voltage E and the inductance L, which limits the voltage U and the speed ω. This limitation is seen from the current waveforms that are not able to reach to the maximum reference value of *1 A*. Additionally, the inductive loading causes the current delay and a decrease in the average output torque. In reality, the average output torque is more reduced and that is due to delays in the control system.

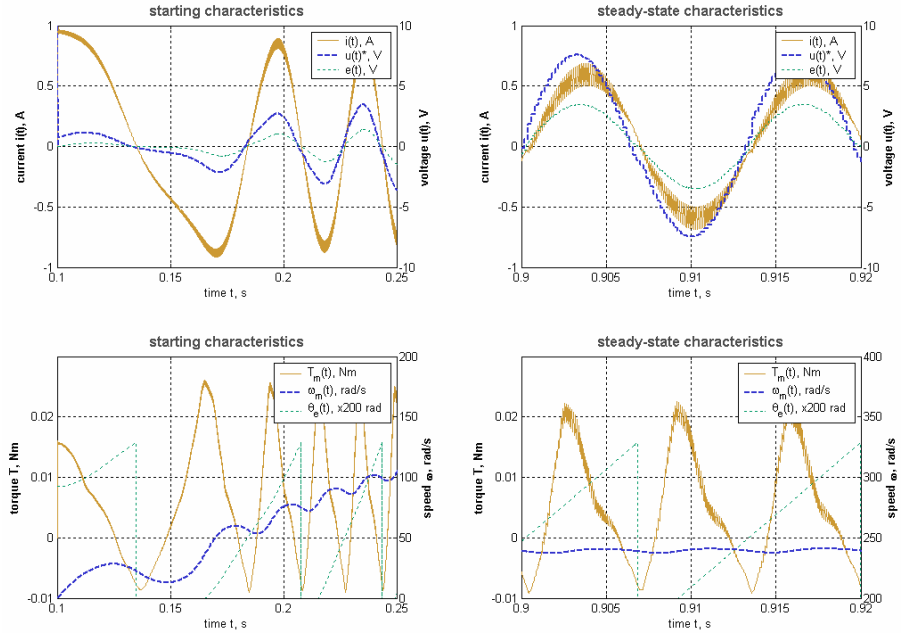

Figure 6.9: Sinusoidal current reference for the single-phase claw-pole motor that gains positive rotation speed. The reference voltage, the induced voltage and the motor current are shown in the upper figures. The lower figures show the electromechanical torque, the rotor speed and the resolver position.

The different current reference waveforms maintain different levels of average torque. At the same time the shape of the current density waveform determines the amount of the losses that are generated in the process of electromechanical energy conversion. There is a trade off between the quantitative and the qualitative output of the machine, interpreted as the output power and the efficiency. The evaluation process is based on the comparison, which is made between the ratio of the copper losses to the output power and the type of current reference waveform. The output power and the resistive loss are estimated from the clock-wise (CW) and counter clock-wise (CCW) rotation Table 6.2.

In this comparison is not included a pulse current waveform. The pulse can be seen as a square wave with reduced pulse width. The reduction of pulse with give advantages when the decelerating current has to be reduced.

Table 6.2: Selection of reference current waveform.

Quantity	symbol	unit	Trapeze waveform	Sinus waveform	Square waveform
Output power (CW)	P_{out}	W	0.90	0.87	01.2
Resistive loss (CW)	P_{Cu}	W	0.13	0.12	0.36
Output power (CCW)	P_{out}	W	1.6	1.4	2.1
Resistive loss (CCW)	P_{Cu}	W	0.12	0.11	0.33

According to copper loss and output power evaluation, which is made for the linear load characteristics, the best current density waveform is the trapezoidal wave.

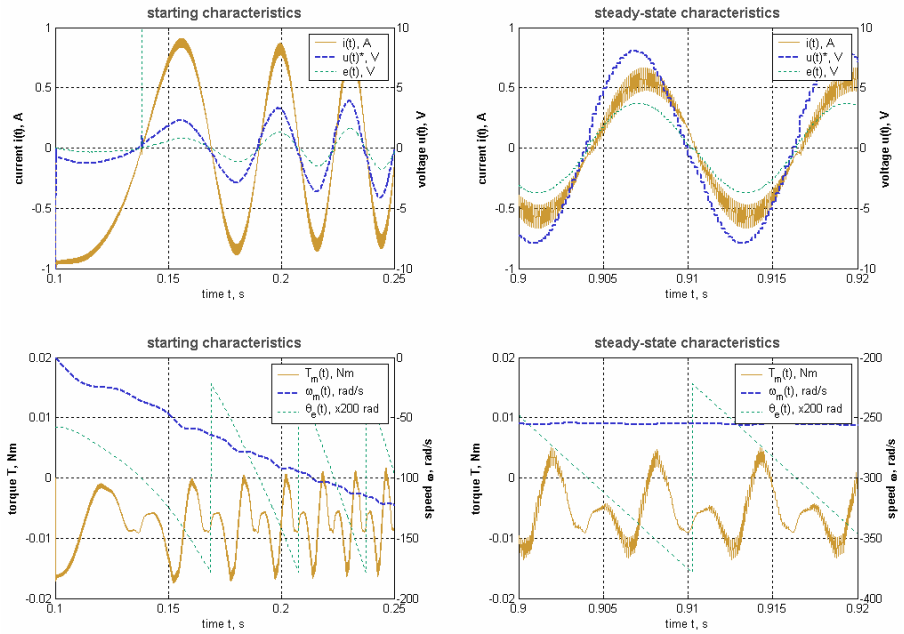

Figure 6.10: Sinusoidal current reference for the single-phase claw-pole motor at negative rotation speed. The reference voltage, the induced voltage and the motor current are shown in the upper figures. The lower figures show the electromechanical torque, the rotor speed and the resolver position.

It can be noticed that the motor reaches different speeds and output power, depending on the rotation direction. According to the asymmetric static torque characteristics of the motor (Figure 5.37), at a certain speed there is more time for the single-phase claw-pole motor to produce negative torque. This torque can be even constant as a combination of the cogging torque and the contribution of the electromechanical coupling torque.

It is assumed that the unbalance between the motors ability to produce the same average torque at CW and CCW is due to the delayed current action that produces deep negative torque response. This can be regulated with a position reference, which is used to form the current reference. The position reference can be set to give the value earlier than it otherwise is sensed from resolver (Appendix D).

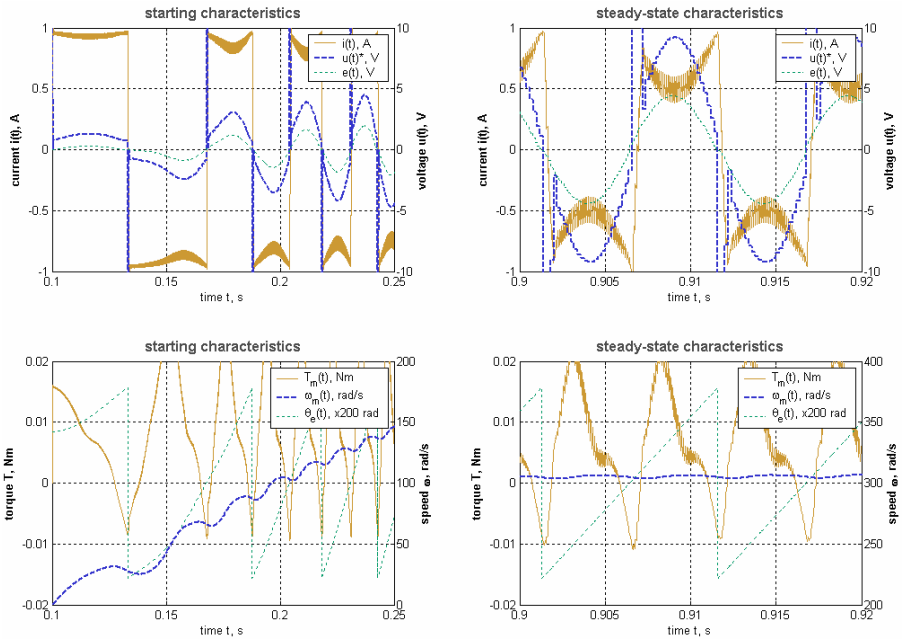

Figure 6.11: Square-wave current reference for the single-phase claw-pole motor that gains positive rotation speed. The reference voltage, the induced voltage and the motor current are shown in the upper figures. The lower figures show the electromechanical torque, the rotor speed and the resolver position.

The switching frequency of the transistors is around *2.5 kHz* to perform the control task. The loss model of VSI is not included in the model and the losses are evaluated in the experimental setup.

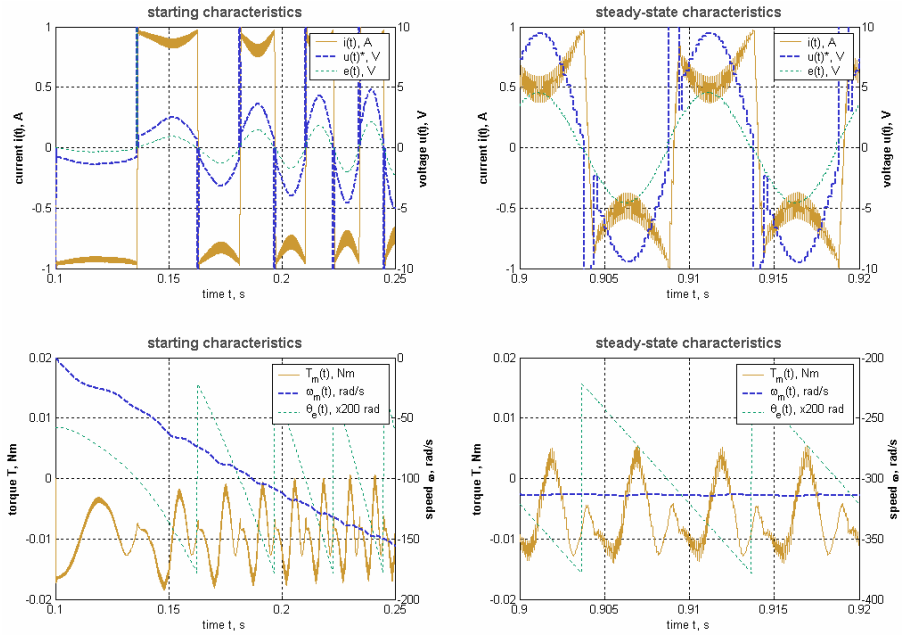

Figure 6.12: Square-wave current reference for the single-phase claw-pole motor that gains positive rotation speed. The reference voltage, the induced voltage and the motor current are shown in the upper figures. The lower figures show the electromechanical torque, the rotor speed and the resolver position.

Dynamic characteristics of the single-phase claw-pole motor

The dynamic characteristics are simulated for SCC (Figure 6.13) and DCC (Figure 6.14). The model of the drive system includes static core losses and speed dependent mechanical losses. The mechanic loading is formulated in order to make the results comparable with the experimental tests.

The VSI driven by control systems is able to provide constant torque up to 150-160 Hz. At the speeds above that the voltage is reached limitation. The efficiency of the DCC controlled VSI reaches to the maximum at the operation frequency of 110-170 Hz, while the SCC driven VSI is able to provide almost constant efficiency. The efficiency is calculated from the electromagnetical torque of the claw-pole motor at the rotation speed of the system. Basically, the motor is 'naturally' loaded by the losses. The loading due to magnetic

hysteresis at the maximum output power is 1.15 W. The rest of the losses from the maximum output of 4.6W are generated in the mechanic system. The dynamic core loss as a function of magnetization speed is not presented in this case in the motor model.

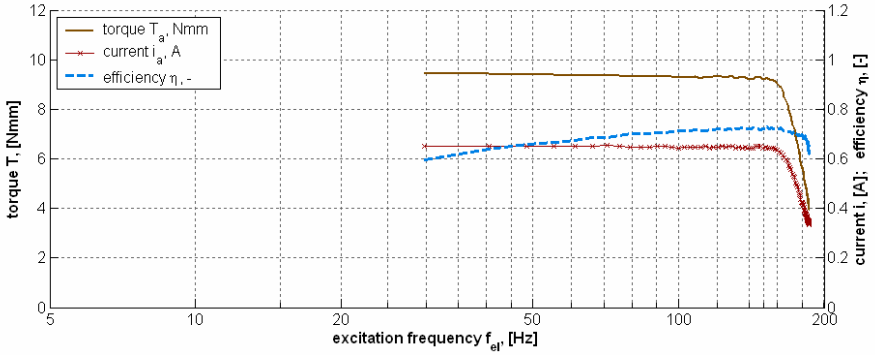

Figure 6.13: Dynamic characteristics of the single-phase claw-pole motor with sampled current control.

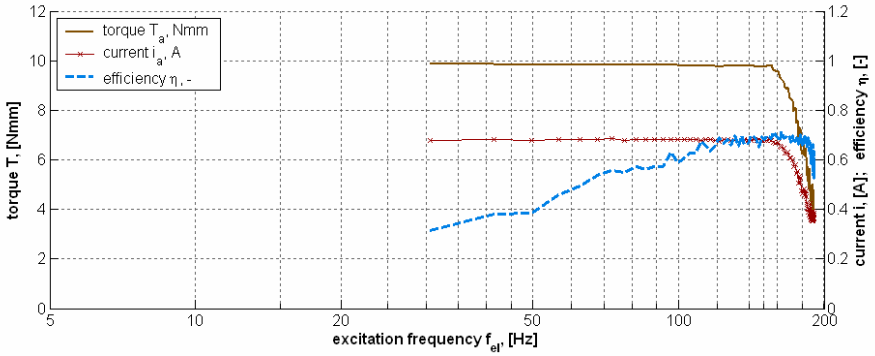

Figure 6.14: Dynamic characteristics of the single-phase claw-pole motor with direct current control.

The SCC that includes proportional gain (P) and feed forward part (E) gives lower output current than the reference of *1 A*. This is due to the reduced proportional part, which is used in the experimental set-up in order to avoid oscillatory behavior due to response delay in the control system.

Direct torque control of the two-phase claw-pole motor

The drive system that incorporates the two-phase claw-pole motor is expected to give smooth torque. On the contrary, the designed motor gives much larger cogging that has been expected. Therefore, the idealized motor characteristics are used to simulate the control system for the motor. The direct current controller with small tolerance band is used to implement direct torque control. The tolerance band is selected according to the power module ability to form the voltage pulses and the commutation losses in the power transistors. The magnitude of the reference current is increased in order to evaluate the electrical-to-mechanical conversion factors, copper losses and the temperature rise (Figure 6.15). The electromechanical coefficient of the idealized two-phase claw-pole motor is 0.04 Nm/A.

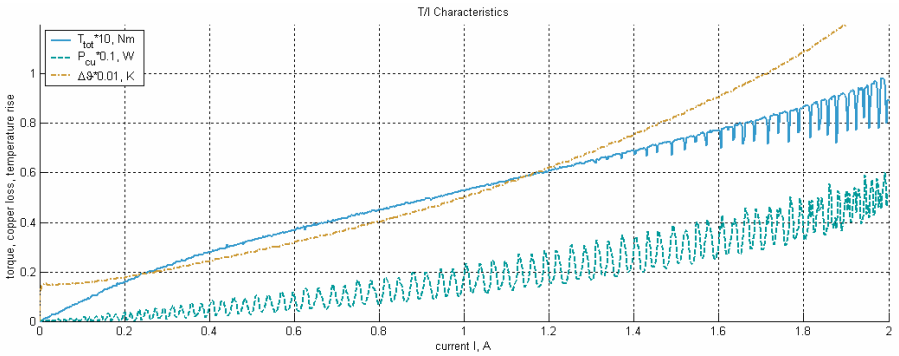

Figure 6.15: Electromechanical energy conversion in the direct current controlled two-phase claw-pole motor.

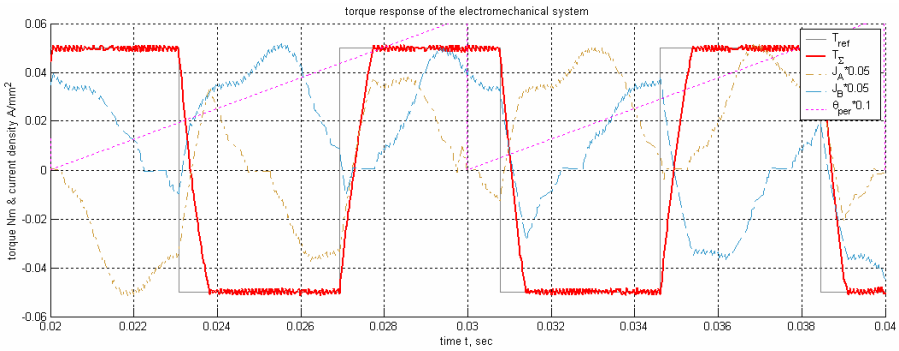

Figure 6.16: Torque response of the electromechanical system at the square wave reference of ±50Nmm and 130Hz.

The response time (Figure 6.16) shows the speed of the electromechanical system needed to reach to the reference value under the limitations, which are defined by the supply voltage and the electric inertia i.e. inductance (Eq. 6.7).

Dynamic characteristics of the two-phase claw-pole motor

The simulations (Figure 6.17) of the free rotor acceleration for different torque references show the voltage limit and the temperature rise in the core if the natural cooling condition, i.e. convective heat transfer, is specified about *5W/(K·m²)*.

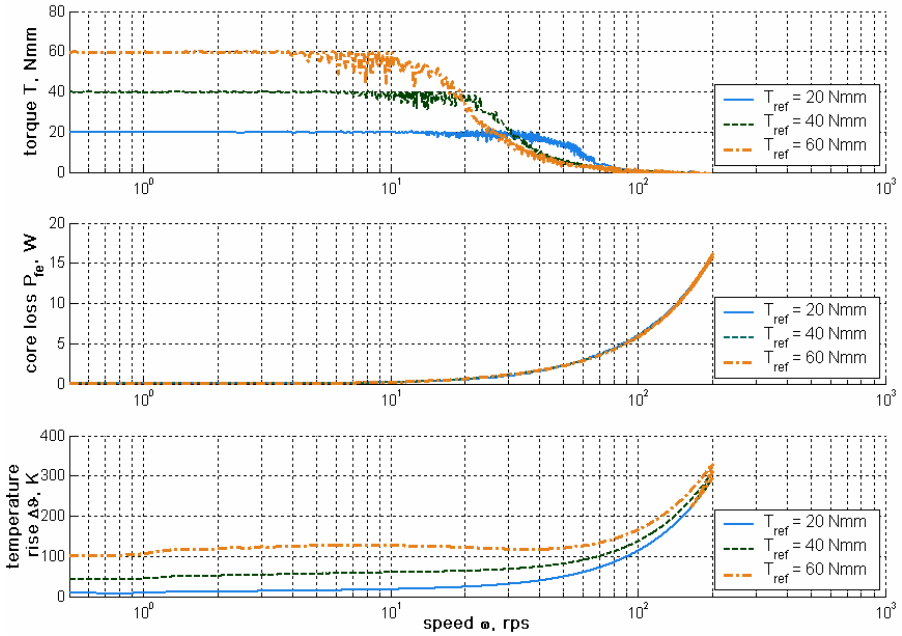

Figure 6.17: Dynamic characteristics of the two-phase claw-pole motor with direct current control.

The designed two-phase motor allows a rated power of *2.1 W* and rated torque of *31 Nmm*, which is referred to the total losses per cooling area about *1000 W/m2*. The efficiency is *47%*, force density *2.12 Nm/dm³*, specific torque *0.36 Nm/kg* and the force per air-gap area, which is *689.8 N/m²*. The output of the motor does not fulfill the requirements that specified (Table 2.1). The only way to increase the output of the designed motor is to increase the current loading. The motor has ability to operate on higher temperatures because the cooling

capability has a reserve. The allowed losses per surface area in normal conditions for a normal motor are around 1500 W/m2. Moreover, the cooling capability that represents the natural cooling condition can be bigger. Basically, the thermal design becomes more dominant in this case. Nevertheless, the temperature rise due to the resistive heating in the coils is smaller in reality than it was expected from the analysis. This indicates again the difficulties to specify the heat transfer coefficient properly for the small motors.

Position control

The motor application area is focused to servo drives. The position control of the drive system is simulated, where the position reference is set from 0º to 120º (Figure 6.18).

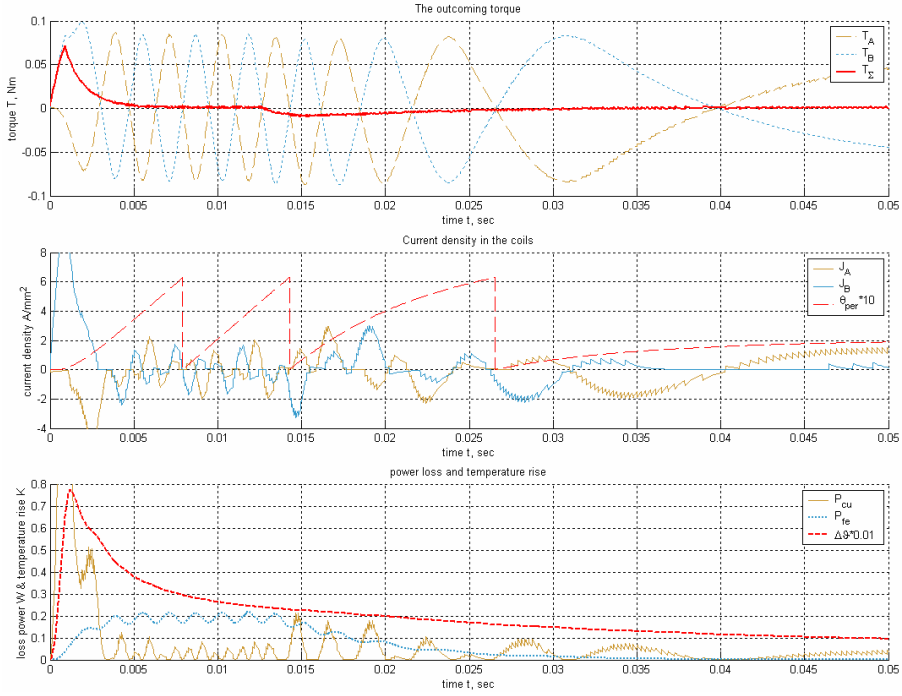

Figure 6.18: Position control of the drive system. The graph is lacking the response of the mechanical system. Nevertheless, the change of the resolver position indicates the 1/3 revolution of the 20-pole two-phase claw-pole motor.

The control task can be performed within 50 ms. The steady state temperature rise in the end of the operation cycle is 10ºC. The maximum temperature rise in the motor, which is less than 80ºC, indicates the instantaneous balance

between the heat production and dissipation. The influence of the heat capacity is not considered.

The other model of the drive system incorporates a rotary-to-linear transmission (Figure 6.19). The linearly moving load can be placed horizontally or vertically.

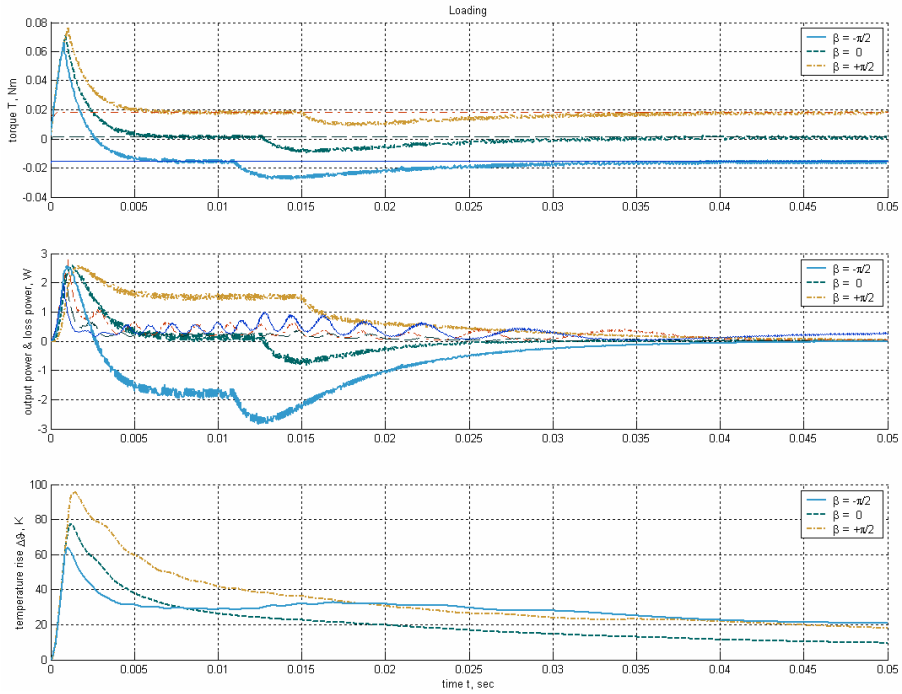

Figure 6.19: Position control of a weight from the rotary-to-linear drive system. The load of linear movement is placed horizontally (β=0°) and vertically (β≠0°). The latter is dividend into two cases when the load supposes to be lifted up (β=90°) or moved down (β=-90°). The upper graph shows the torque reference and the response of the motor torque. The diagram in the middle shows the out-put power and the loss power. The rotational core losses are not presented in the simple core loss model. The lower graph shows the intermediate temperature rise, which does not consider the thermal capacity.

6.4 Experimental results

The experimental work is finalized only with the drive system for the single-phase claw-pole motor. The mechanic assembling of the claw-pole motors into

a test bench and a reference dc motor are shown in Figure 6.20. The reference dc machine is not used as a load motor. The reason is the mechanical overloading that the single-phase claw-pole motor is not able to overcome.

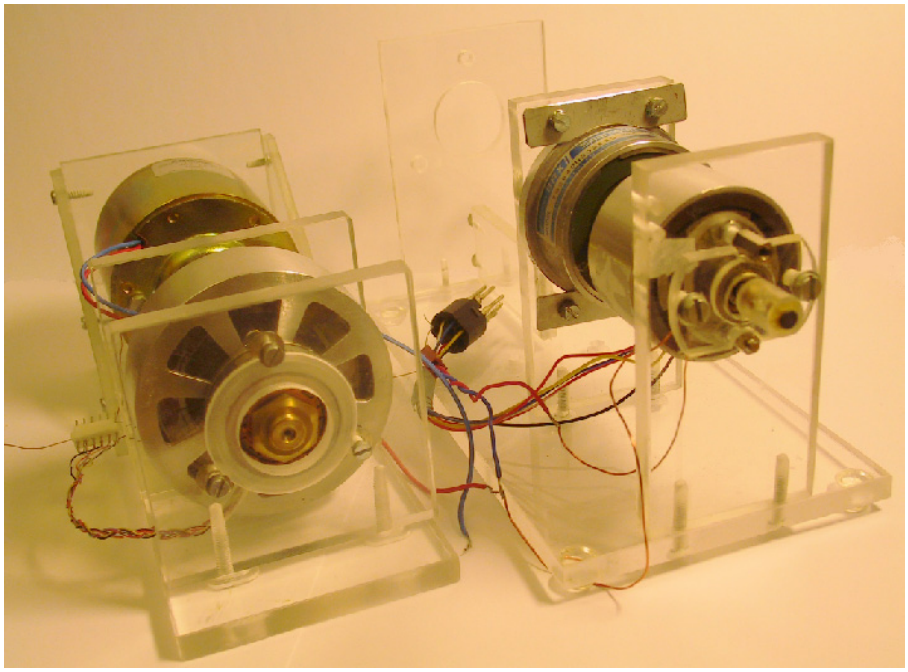

Figure 6.20: Claw-pole motors assembled to the test bench. The two-phase claw-pole motor is in the left and the single-phase claw-pole motor in the right. The same dc machine is used to gauge the motor characteristics of the claw-pole motors.

The experimental setup

The experimental set-up consists of the control system implemented in Simulink and executed in dSpace Real-Time hardware, a voltage source inverter to control the armature voltage, a position and current sensor, and a number of electronic circuits for signal conditioning. As the measurement set-up is lacking a dynamic torque measurement system, the static characteristics have been used in order to estimate the torque, output power and the operation efficiency of the drive system.

The experimental results of the single-phase claw-pole motor

The steady state characteristics are measured. Different current controllers are implemented. The experimental results are shown for sampled current control (SCC) (Figure 6.22) and direct current control (DCC) (Figure 6.23) for a free acceleration. The motor is loaded by the magnetic loading of the core, which is not subtracted from the average coupling torque curves, and by the mechanic loading of the test bench such as friction and windage.

The VSI is supplied by a dc-link voltage about 15V. The inverter has a fixed frequency for the SCC, that is 6kHz and for the DCC the maximum switching exceeds 10kHz. Different waveforms for the reference current have been studied. Instead of bidirectional direct current over the electric period, which corresponds to a quadratic waveform, the current conduction duration was reduced for a shorter interval. This helps to prevent the generation of the torque pulses with an opposite polarity when the current and emf are out of phase [99]. Next, the steep edges of the pulse waveform have been changed to a trapezoidal and a sinusoidal waveform. The best ratio of the electromagnetic power to the system input power is seen for the trapezoidal current reference.

Sensorless control

From the cost of the drive system point of view, it is unreasonable to have a resolver that has approximately the same size as the motor itself. In order to simplify the control system a few possibilities to implement sensorless control is studied for the single-phase claw-pole motor. Depending on the dynamics at the current controller for the sensorless operation, the corresponding shape of the speed-up ramp with sensor is used. An alignment pulse sequence is necessary in order to get the motor to accelerate in the desired direction. According to the static torque characteristics (Figure 5.37) the motor is always able to produce negative torque and the short positioning pulse will always bring the rotor to the determined position. On the contrary, as a high positive torque pulse is available only a short interval of positions, it is necessary to swing up the system's kinetic energy, so that the rotor can gain positive speed. It is easier to implement sensorless control for the DCC driven motor. The control action delay in the simple proportional (P) feed-forward (E) SCC causes oscillations and failures in order to follow the acceleration pulse train. Motor deadlock can occur when the speed ramp is too steep or too soft. The deadlock can occur also when the mechanic loading changes. It is difficult to detect from the current waveform whether the motor has lost synchronism as it is suppose to reflect a different action of the rotational induced voltage.

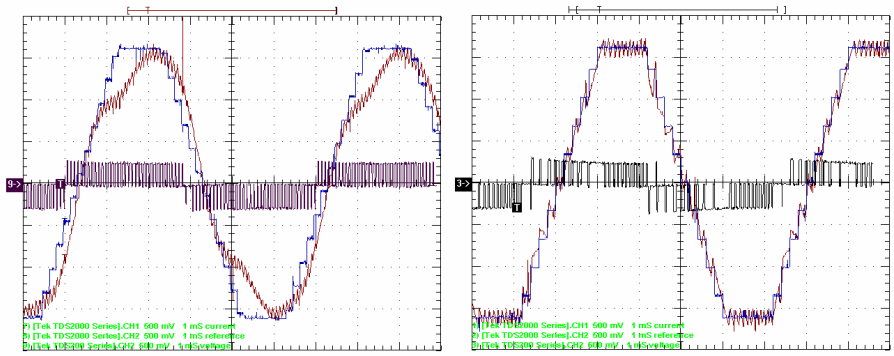

Figure 6.21: Voltage, reference current and measured current waveforms. The waveforms in the left belong to the SCC driven motor by the help of position sensor. Figure on the right shows the input of the sensorless DCC driven motor. The scaling for the measurement signals are 500mV and 1ms per unit.

The high-speed (166.7Hz) control action for these two different control strategies gives preference to DCC (Figure 6.21), as the delay in SCC causes malfunction in sensorless control. The delay is compensated by phase shift of the reference current former, where the support from the position sensor is included (Figure 6.21).

Dynamic characteristics

Motor T/ω characteristics is measured and simulated for two different current control methods. The efficiency curve shows a ratio between the input power of the driver and the electromagnetic output from the motor (Figure 6.22 and Figure 6.23). This ratio demonstrates the energy oscillations, which is due to resonances between the controller action and the mechanic system. The mechanic torque and the efficiency are lower as the hysteresis loss of the motor corresponds to re-magnetization friction about *2.2 Nmm*. The difference between the simulations and the measurements is the overestimated efficiency as the loss model of the VSI is not included in the model. Moreover, the electromechanic torque value does not represent the loading due to core and mechanical losses. As a matter of fact, the single-phase claw-pole motor is loaded 'naturally' by the losses in the core and mechanic system. The only way to increase loading is to increase current and this increases instability in the experimental drive system.

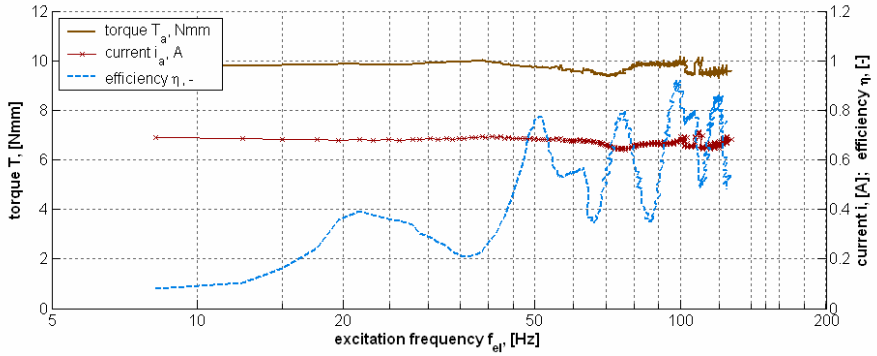

Figure 6.22: Free acceleration of the single-phase claw-pole motor involving the sampled current control.

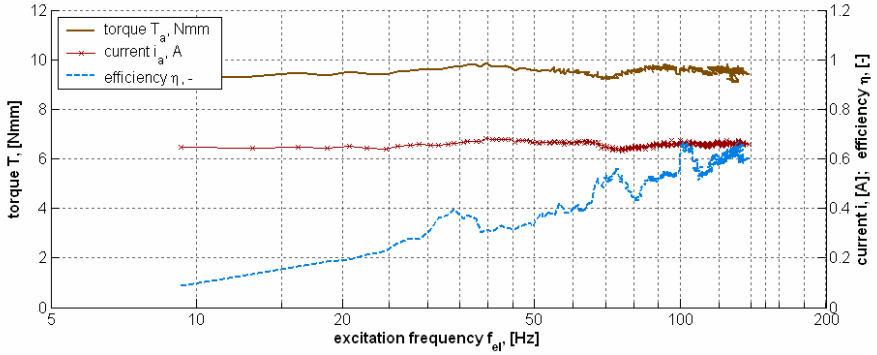

Figure 6.23: Free acceleration of the single-phase claw-pole motor involving the direct current control.

6.5 Conclusions and remarks

A control system is proposed for the single-phase claw-pole motor. The dynamic characteristics have been simulated on the basis of the mathematic model of the motor. The simulations show a good correlation with the experiments, where the same control system in Simulink is applied to the prototype via dSpace. Practically, it is easier to implement a simple control strategy for the direct current controlled voltage source inverter. More advantageous control system needs to be applied for the sampled current controller.

The large magnetic and mechanical friction complicates the starting conditions of the single-phase claw-pole motor in the positive rotation direction. This drawback can be solved either by selecting an advanced control system or by selecting the preferred rotation direction to be always in the negative direction.

The drawback in the two-phase claw-pole motor is large cogging, which makes the task of implementing the complete drive system difficult. Nevertheless, the electric drive system that incorporates the two-phase claw-pole motor is simulated with a fictive load.

Chapter 7

Conclusions

This thesis presents design methods and designs for small claw pole PM machines are created, analyzed and to some extent experimentally verified on two prototypes. This chapter summarizes the experience.

7.1 Summary of results

Calculation methods

3D equivalent circuits (EC) and 3D finite element (FE) analysis are the main tools, which are used to for field distribution and energy conversion process calculations. The following conclusions are drawn:

- The magnetic EC is able to correctly estimate the magnetic loading of the core when compared to FEM or experimental validation of the linking flux waveform.
- The discrepancy between the estimated core losses and the measured core losses is larger than the estimate of the magnetic loading. The difference is partly due to unspecified loss data and the errors gained from the loss measurement setup.
- The thermal loading estimated from a thermal EC leads to overestimation compared to the FE computation or experimental work on heat transfer. The inaccuracy is due to incorrectness in determining the cooling surface and the cooling conditions.

- The correctness of the cogging torque computation is prioritized. Nevertheless, the analytical results do not correlate closely with the experiments. The quality of meshing is studied, when the geometrical changes are introduced in the claw-pole core. The results do not indicate that the discrepancy between the estimated and the measured cogging is due to badly shaped hexahedral elements in the air-gap region.

- The torque computation method is not analyzed deeply enough, even though the results from different FE software give a good reason for that. A considerable difference between the results of the computation methods and measurements exist.

- The models of material elasticity do not adequately reflect the weakest part of the powder core. This is mainly due to unspecified loading in the analytical models that caused the powder core of the two-phase claw-pole motor to fail. The failure is due to bad manual handling, which is indirect to magnetic attraction.

According to the experience of analyzing the multiphysic process of the electromechanical energy conversion for a complex core and the source of magnetic excitation, it is realized that the magnetostatic analysis gives the necessary information. Several simpler models can be added to the magnetistatic solution in order to estimate the losses, the thermal and the mechanic limit for the motor structure.

Optimization methods and sensitivity study

It is not only the claw-pole motors but also the size of the models in the calculation methods that have to be optimized. The use of relatively simple EC gives, in particular for the magnetics, fast but rough calculation results. The stator dimensions, the best claw designs for minimized cogging and maximized starting torque, the size and the magnetization pattern of the magnet-ring, the material properties and the assembling conditions are analyzed in detail in 3d FEA. Different excitation possibilities for the PM outer rotors are compared. The following conclusions can be drawn:

- When used for geometrical optimization, the magnetic EC shows clearly that a high number of poles should be selected for the single-phase claw pole motor in order to increase the utilization factor.

- The analysis of an air gap between the phase core halves is supported by experimental results of the coupling flux and core losses.

- The study of the optimal claw-pole core of the two-phase motor shows the opportunity to reduce cogging torque if the claw-poles are chosen to be wider or a plastic bounded ferrite is used instead of NdFeB magnet-ring.
- For time saving, there must be a balance between the complexity and corresponding accuracy of the EC and the time used to set up the network. The experience from this project is that the "Broadsearch", which is referred also as a visibility study, is one of the most informative methods to visualize the results of a number of motor designs. The complexity of the magnetization of a magnet-ring and the powder core can be analyzed accurately. An advantageous feature of broadsearch is the systematical result, where a number of motors are analyzed without implementing any advanced objective function of multi-dimensional optimization search
- The core construction of the single-phase claw-pole motor can be simplified when the claw-poles are made wider. By doing that, there is no need for the progressive radius of the claw-poles. The parking position of the motor is at the position of the maximum coupling torque.

Prototypes

Two prototypes are built according to the proposed motor designs. . The coupling characteristics such as magnetic flux and coupling torque agree well with expectations. The utilization factors (Table 7.1) of the claw-pole motors are weaker than it is expected (Table 2.1).

Table 7.1: Qualitative values in design of powder core motors.

Quantity	symbol	unit	A single-phase claw-pole motor	A two-phase claw-pole motor
Specific torque	T_{mass}	Nm/kg	0.08	0.58
Torque density	T_{volume}	Nm/dm^3	0.327	2.47
Efficiency (designed/real)	η	%	60/50	47/0

The following conclusions can be drawn:

- The SMC core has superior properties. The experiences have shown that it is not that easy task to reach to the same tolerances with a simple wound coil. A bobbin coil simplifies the manufacturability and assembling of the coil. The advantageous feature of the bobbin is that it

gives mechanic support and facilitates stator core assembling. The drawback is that the slot cross-section area is not fully utilized for the winding.

- It is not an undemanding task to analyze properly the influence on material proprieties. The thin claw-pole structure made of SMC powder practically is possible even though the cost to manufacture a claw-pole ring to the two-phase claw-pole motor is increased due to high risk of constructional failure.
- The coupling torque measurement indicates that the measurement error converge rather due to 'known values' than due to exact weighted average of a varying reading.
- The drawback in the two-phase claw-pole motor is large cogging, which makes the task of implementing the complete drive system difficult.
- The utilization factors of the claw-pole motors are calculated according to the average of the coupling torque. This torque value does not represent the loading due to core losses. As a matter of fact, the single-phase claw-pole motor is loaded 'naturally' by the losses in the core and the mechanic system. The only way to increase loading is to increase current and this increases instability in the experimental drive system.

A large discrepancy exists in the cogging torque. The inaccuracies are believed to be due to:

1. The magnetization pattern not being exactly known
2. Not good enough precision in the assembling.
3. Errors in the numeric field computation add inaccuracy.
4. Low measurement precision, in particular in the single phase of the two-phase claw-pole motor around the unstable equilibrium position.

Experimentation on drive system

A power electronic drive was designed for both prototypes but results from only one of them are presented in this thesis. The hardware and software environment provided by dSpace simplified the control system development a lot. The main conclusions from the experimental work are:

- The current of the motor is controlled so that it is able to accelerate with and without position sensor.

- The best electromagnetic energy conversion is seen when trapezoidal current reference waveform and direct current controlled system determines the state of voltage source inverter.

The drawback of the test bench is the lack of good load measurements.

7.2 Future work

The motor design that incorporates the advantageous features of soft magnetic composite (SMC) and hard magnetic composite (HMC) can be improved. The further modifications and enhancements are summarized below.

Magnetic hysteresis

This work does not consider instantaneous value of hysteresis torque. Magnetic hysteresis can be formulated on the basis of physic based hysteresis model [4][72] that can be attached to a simple MEC model. More accurate modeling is possible on the table based analysis at post-processing level. This method can use the same structure that is used in this thesis while performing loss computation. From the energy variations it would be possible to obtain no load reluctance torque, i.e. cogging, and the hysteresis torque at the same time.

This work is lacking experimentally verified hysteresis losses that bases on a sample measurements and considers a different trajectory of external magnetizing field. The measurements for the used composite powder, namely Somaloy500+0.6% LB1, can be carried out in a 2D core loss tester [97].

Analysis and measurement of magnetization pattern

Theoretical improvement of analysis and modeling of a multi-pole permanent magnet magnetization process gives advantage to consider properly the influence on a real magnetization pattern. The motor design is not only to optimize a motor core but also to consider exactly the variation of permanent magnet excitation due to magnetization pattern. Therefore, a number of tests, which would analyze the real magnet and verify the magnet models, are necessary in order to improve the overall motor design.

Further improvements

The models of the transversal flux machine (TFM) with claw-pole structure can be improved in order to increase the computation speed and accuracy. The following improvements are suggested

1. The fast computation method, which bases on 2D FE and 2D EC analysis, evaluation and optimization of the no load reluctance torque, i.e. cogging torque waveforms.
2. Design optimization and motor performance analysis in terms of drive system efficiency.
3. The experimental activities in order to improve the motor model accuracy such as evaluation of material properties and magnetization pattern.

References

[1] Aguero, A.C., Actis, F.A., Silva, V.C., Cardoso, J.R., Nabeta, S.I., "Finite element analysis of a synchronous permanent magnet micromotor through axisymmetric and transverse planar simulations", *IEEE Trans Magn*, vol. 34, no. 5, Sept. 1998, pp. 3604-3607

[2] Allegre, J.M., Marchand, C., Ren, Z., "On the influence of mesh deformation to the force calculation when accounting for the movement", Computation in electromagnetics, *IEE Conf Publ* No. 420, Apr. 1996, pp. 253-258

[3] Arshad, W.M., Backstrom, T., Sadarangani, C., "Analytical design and analysis procedure for a transverse flux machine", *IEEE Int Electric Machines and Drives Conf, IEMDC'01,* June 2001, pp. 115-121

[4] Basso, V., Bertotti, G., "Hysteresis models for the description of domain wall motion", *IEEE Trans Magn*, vol. 32, no. 5, Sept. 1996, pp. 4210-4212

[5] Bentouati, S., Zhu, Z. Q., Howe, D., "Influence of design parameters on the starting torque of a single-phase PM brushless DC motor", *IEEE Trans Magn*, vol. 36, no. 5, Sept. 2000, pp. 3533-3536

[6] Blissenbach, R., Henneberger, G., Schäfer, U., Hackmann, W. (2000), "Development of a transverse flux motor in a direct drive system", *Int Conf on Electrical Machines, ICEM'00*, pp. 1457-1460

[7] Boglietti, A., Cavagnino, A., Lazzari, M., Pastorelli, M., "Two simplified methods for the iron losses prediction in soft magnetic materials supplied by PWM inverter" *IEEE Int Electric Machines and Drives Conf, IEMDC'01*, June 2001, pp. 391-395

[8] Bottauscio, O., Chiampi, M., Fiorillo, F., Repetto, M., "Dynamic hysteresis and voltage driven solution of a ferromagnetic laminated core", *IEEE Trans Magn*, vol. 36, no. 4, July 2000, pp. 1238-1241

[9] Bottauscio, O., Canova, A., Chiampi, M., Repetto, M., "Iron losses in electrical machines: influence of different material models", *IEEE Trans Magn*, vol. 38, no. 2, March 2002, pp. 805-808

[10] "CALFEM – A finite element toolbox to MATLAB version 3.3," Dept. of Structural Mechanics, Lund University, Sweden, 2002.

[11] Canova, A.; Ottella, M.; Rodger, D., "A coupled field-circuit approach to 3D FEM analysis of electromechanical devices", *9th Int Conf on Electrical Machines and Drives, EMD'99* Conf. Publ. No. 468, 1-3 Sept. 1999, pp. 71-75

[12] Cassat, A., Espanet, C., Wavre, N., "BLDC motor stator and rotor iron losses and thermal behavior based on lumped schemes and 3-D FEM analysis", *IEEE Trans Ind Appl*, vol. 39 no. 5, Sept.-Oct. 2003 pp. 1314-1322

[13] Colins, G.C., "Rotor assembly", *US patent No3,271,606*, filled Nov. 5, 1962

[14] Cros, J., Viarouge, P., Chalifour, Y., Figueroa, J., "A new structure of universal motor using soft magnetic composites", *IEEE Ind Appl IAS Annual Meeting*, Conf. Rec. vol. 1, 30 Sept - 4 Oct. 2001, pp. 75-82

[15] Cros, J., Viarouge, P., "New structures of polyphase claw-pole machines", *IEEE Ind Appl 37th IAS Annual Meeting*, Conf. Rec. vol. 4, 13-18 Oct. 2002, pp. 2267-2274

[16] Correspondence with Vector Fields user support

[17] Correspondence with FEMLAB user support

[18] Correspondence with Jmag-Studio user support

[19] Dickinson, P.G., Jack, A.G., Mecrow, B.C., "Improved permanent magnet machines with claw pole armatures", *Int Conf on Electrical Machines, ICEM'02*, Aug. 2002, 5 pp

[20] Ebihara, D., Nakata, Y., Watada, M., Watanabe, T., Nakano, H., "Flux distribution to inductor in claw pole linear pulse motor", *IEEE Trans Magn*, vol. 29, no. 6, Nov. 1993, pp. 2926-2928

[21] Engström, J. "On design of slotless permanent magnet machines", Licentiate thesis, Royal Institute of Technology, Stockholm 1999, ISSN-1102-0172

[22] Fakler, B., "Slipring-less caw-pole generator", *US patent No. 5,543,677*, filed Sep. 19, 1994

[23] Felicetti, R., Ramesohl, I., "Design of a mass-production low-cost claw-pole motor for an automotive application", *Int Conf on Electrical Machines, ICEM'02*, Aug. 2002, 6 pp.

[24] Fehrenbacher, W., "Mini-fan unit especially for use as a fun in printed circuit boards", *US patent No.6,013,966*, filed Oct. 9, 1998

[25] Frister, M. (1990), "Alternating-current generator with claw-pole rotor", US patent No.4,972,114, filed Nov. 20, 1990

[26] Gerlando, A.D., Vistoli, I., "Distortion problems and design solutions of converter fed single-phase permanent magnet motors for small power applications", *8th Int Conf on Harmonics and Quality on Power*, Proc. vol. 2, 14-16 Oct. 1998, pp. 712-719

[27] Godkin, M., "Axial air gap brushless alternator", *US patent No. 4,611,139*, filed Jul. 8, 1985

[28] Guo, Y.G., Zhu, J.G., Ramsden, V.S., "Design and construction of a single phase claw pole permanent magnet motor using composite magnetic material", *Renewable Energy*, vol. 22, Elsevier Science Ltd, 2001, pp. 185-195

[29] Guo, Y.G., Zhu, J.G., "Improved methods for force and torque calculation in electrical machines by 3D finite element analysis", *Conf. on Electrical Machines and Systems, ICEMS'01*, vol. 2, 2001, pp.1191-1194

[30] Guo, Y.G., Zhu, J.G., Watterson, P.A., Wu, W., "Comparative study of 3D flux electrical machines with soft magnetic composite cores", *IEEE Ind Appl Conf, 37th IAS Annual Meeting*, Conf. Rec., vol. 2, 2002, pp. 1147-1154

[31] Guo, Y.G., Zhu, J.G., Zhong, J.J., Wu, W., "Core losses in claw pole permanent magnet machines with soft magnetic composite

stators", *IEEE Trans Magn*, vol. 39, no. 5, Sept. 2003 pp. 3199-3201

[32] Guo, Y.G., Zhu, J.G., Watterson, P.A., Holiday, W.M., Wu, W., "Improved design and performance analysis of a claw pole permanent magnet SMC motor with sensorless brushless dc drive", *IEEE Int Conf on Power Electronics and Drive Systems, PEDS'03*, 2003, pp. 704-709

[33] Guo, Y.G., Zhu, J.G., Ramsden, V.S., "Calculation of cogging torque in claw pole permanent magnet machines", *Australasian Universities Power Engineering Conference*, The University of Queensland St. Lucia, Brisbane, Australia, 26-29 Sept. 2004, 5 pp.

[34] Hamdi, E.S., "Design of small electrical machines", Design and measurement in electronic engineering John Wiley & Sons 1994, 260 p.

[35] Hecquet, M., Brochet, P., "Modeling of a claw-pole alternator using permeance network coupled with electric circuits", *IEEE Trans Magn*, vol. 31, no. 3, May 1995, pp. 2131-2134

[36] Hecquet, M., Brochet, P., "Time variation of forces in a synchronous machine using electric coupled network model", *IEEE Trans Magn*, vol. 34, no. 5, Sept. 1998, pp. 3214-3217

[37] Henneberger, G., Kuppers, S., Ramesohl, I., "Numerical calculation, simulation and design optimisation of claw pole alternators for automotive application", *IEE Colloquium on Machines for Automotive Applications*, Digest No. 1996/166, pp. 3/1-3/5

[38] Huang, S., Luo, J., Leonardi, F., Lipo, T.A., "A general approach to sizing and power density equations for comparison of electrical machines", *IEEE Ind Appl Conf, 31st IAS Annual Meeting, IAS'96*, Conf. Rec., vol. 2 , 6-10 Oct. 1996, pp. 836-842

[39] Huang S., Luo, J., Lipo, T.A., "Analysis and evaluation of the transverse flux circumferential current machine", *IEEE Ind Appl Conf, 32nd IAS Annual Meeting, IAS'97*, Conf. Rec., vol. 1, 5-9 Oct. 1997, pp. 378-384

[40] Hultman, L.O., Jack, A.G., "Soft magnetic composites-materials and applications", *IEEE Int Electric Machines and Drives Conf, IEMDC'03*, vol. 1, June 2003, pp. 516-522

[41] Ichimura, H., "Stepping motor", *US patent No.5,331,237*, filed Apr. 23, 1993

[42] Ishikawa, T., Matsuda, M., Matsunami, M., "Finite element analysis of permanent magnet type stepping motors", *IEEE Trans Magn*, vol. 34, no. 5, Sept. 1998, pp. 3503-3506

[43] Ishikawa, T., Takakusagi, R., Matsunami, M., "Static torque characteristics of permanent magnet type stepping motor with claw poles", *IEEE Trans Magn*, vol. 36, no. 4, July 2000, pp. 1854-1857

[44] Jack, A.G., Mecrow, B.C., Maddison, C.P., Wahab, N.A., "Claw pole armature permanent magnet machines exploiting soft iron powder metallurgy", *IEEE Int Electric Machines and Drives Conf.* Rec. 1997, pp. MA1/5.1-MA1/5.3

[45] Jack, A., "Experience with using soft magnetic composites for electrical machines", *IEE Colloquium on New Magnetic Materials - Bonded Iron, Lamination Steels, Sintered Iron and Permanent Magnets* (Digest NMo. 1998/259), pp. 3/1-3/4

[46] Jack, A.G., Mecrow, B.C., Maddison, C.P., "Combined radial and axial permanent magnet motors using soft magnetic composites", Conf. on Electrical Machines and Drives, EMD'99, Conf. Publ. No. 468, 1999, pp. 25-29

[47] Jack, A.G., Mecrow, B.C., Dickinson, P.G., "Iron loss in machines with powdered iron stators", *Int Conf Electric Machines and Drives, IEMD'99*, 9-12 May 1999, pp. 48-50

[48] Jack, A., Dickinson, P., Mecrow, B., Jansson, P., Hultman, L., "A scoping study for universal motors with soft magnetic composite stators"; *Int Conf on Electrical Machines, ICEM'00*, vol. 2, Aug. 2000, pp.613-617

[49] Jack, A.G., Mecrow, B.C., Dickinson, P.G., Stephenson, D., Burdess, J.S., Fawcett, N., Evans, J.T., "Permanent magnet machines with powdered iron and prepressed windings", *IEEE Trans Ind Appl*, vol. 36, no. 4, Jul/Aug 2000, pp. 1077-1084

[50] Jansson, P., "Soft magnetic composites from dc to 1 MHz with iron powder", *Powder Metallurgy World Congress*, 1998

[51] Jung, I.-S., Chang, H.-S., Baek, S.-H., "Magnetic field analysis of polar anisotropic ferrite-bonded magnet for brushless DC motor application", *6th Int Conf Electrical Machines and Systems, ICEMS'03*. vol. 2, 9-11 Nov. 2003, pp. 774-777

[52] Kaehler, C., Henneberger, G., "Eddy-current computation in the claws of a synchronous claw-pole alternator in generator mode", *IEEE Trans Magn*, vol. 38 n.2, 2002, pp. 1201-1204

[53] Kenjo, T., Sugavara, A. (1994), Stepping Motors and Their Microprocessor Controls, second edition, New York, Oxford University Press, ISBN 0-19-859386-4

[54] Kliman, G.B., "Method for manufacturing a claw pole stator structure", *US patent No.5,890,277*, filed Nov. 4, 1996

[55] Kolb, R.P., Bennett, S.P. "Mechanics of materials", Ch. 7 at Rothbart H.A., Mechanical design and systems handbook, 2.ed. McGraw-Hill handbooks, New York, 1985

[56] Kurowski, P., "When good engineers deliver bad FEA", *Machine Design*, vol. 67, no. 20, 1995, pp. 61-65

[57] Kurowski, P., "Good solid modeling, bad FEA", *Machine Design*, vol. 68, no. 21, 1996, pp. 67-72

[58] Kurowski, P., "More errors that mar FEA results", *Machine Design*, vol. 74, no. 6, 2002, pp. 51-56

[59] Laansoo, A., Käerdi, H., "Powder materials and coatings", Transactions of Tallinn Technical University, No. 741, 1994, pp. 53-59

[60] Lagorce, L.K., Allen, M.G., "Magnetic and mechanical properties of micromachined strontium ferrite/polyimide composites", *Jour Microelectromechanical Systems*, vol. 6, no. 4, Dec. 1997, pp. 307-312

[61] Lee, J. H., "Design solutions to minimize iron core loss in synchronous reluctance motor using Preisach model and FEM", *IEEE Trans Magn*, vol. 38 no. 5, Sep 2002, pp. 3276-3278

[62] Li, L., Xiang, Y., "Finite element computation of 3-D nonlinear magnetic field in claw-pole electric machine using two scalar potentials, hybrid elements and automatic mesh generation", *IEEE Trans Magn*, vol. 26 n. 2, March 1990, pp. 371-374

[63] Lin, D., Zhou, P., Fu, W.N., Badics, Z., Cendes, Z.J., "A dynamic core loss model for soft ferromagnetic and power ferrite materials in transient finite element analysis", *IEEE Trans Magn*, vol. 40, no. 2, March 2004, pp. 1318-1321

[64] Liorzou, F., Phelps, B., Atherton, D.L., "Macroscopic models of magnetization", *IEEE Trans Magn*, vol. 36, no. 2, March 2000, pp. 418-428

[65] Lipo, T.A. "introduction to AC machine design", vol. 1, Wisconsin Power Electroncs Research Center, University of Wisconsn, 1996

[66] Lundell, R., "Improvements relating to dynamo electric machines", GB patent No. 190706847 Publication Mar. 12, 1908

[67] Lei Ma, Sanada, M., Morimoto, S., Takeda, Y., "Prediction of iron loss in rotating machines with rotational loss included", *IEEE Trans Magn*, vol. 39, no. 4, July 2003, pp. 2036-2041

[68] Marcotte, A., Hultman, L., Jack, A., "Invitation to SMC seminar tutorial: IEMDC, June 1st 2003", Int Conf Electric Machines and Drives, IEMD'03

[69] Mellor, P.H., Roberts, D., Turner, D.R., "Lumped parameter thermal model for electrical machines of TEFC design", *IEE Proc. B Electric Power Appl*, vol. 138 no. 5, 1991, pp. 205-218

[70] Mecrow, B.C., Jack, A.G., Atkinson, D.J., Dickinson, P.G., Swaddle, S., "High torque machines for power hand tool applications Power Electronics", *Int Conf Machines and Drives*, (Conf. Publ. No. 487) , 4-7 June 2002, pp. 644-649

[71] Mi, C, Slemon, G.R., Bonert, R., "Modeling of iron losses of permanent-magnet synchronous motors", *IEEE Trans Ind Appl*, vol. 39 no. 3, May-June 2003, pp. 734-742

[72] Nakmahachalasint, P., Ngo, K.D.T., Loc Vu-Quoc, "A static hysteresis model for power ferrites", *IEEE Trans Pow Electr*, vol. 17, no. 4, July 2002, pp. 453-460

[73] Opera-3D user quide, Vector Fields Ltd., Oxford, England, Feb. 2004

[74] Ostovic, V., Dynamics of Saturated Electric Machines, New York, Springer-Verlag, 1989, ISBN 0-387-97079-7

[75] Ostovic, V., Miller, J.M., Garg, V.K., Schultz, R.D., Swales, S.H., "A magnetic-equivalent-circuit-based performance computation of a Lundell alternator", *IEEE Trans Ind Appl*, vol. 35, no. 4, July/Aug. 1999, pp. 825-830

[76] Ottosen, N.S., Petersson, H., "Introduction to the finite element method", University of Lund, Sweden, Prentice Hall Europe 1992, ISBN 0-13-473877-2

[77] Panchanathan, V., "New high performance bonded Nd-Fe-B permanent magnets", Electrical Insulation Conference, and Electrical Manufacturing & Coil Winding Conference. Proceedings , 22-25 Sept. 1997, pp. 375-378

[78] Pawlak, A.M., "Claw pole rotary actuators", *Int Conf on Electrical Machines, ICEM '92*, 1992, pp. 122-126

[79] Pawlak, A.M. (1995), "Magnets in modern rotary actuators", *IEEE Ind Appl Conf, 30th IAS Annual Meeting*, Conf. Rec. vol. 1, 1995, pp. 498-504

[80] Pennander, L.O., Jack, A., "Development of iron powder SMC-materials and the application in electrical machines", Electrical machines symposium, Dept. of Electrical Engineering, KTH, Stockholm, 26th June 2001

[81] Perho, J., "Reluctance network for analyzing induction machines", *Ph.D Thesis*, Laboratory of Electromechanics, Helsinki University of Technology, 2002, Espoo, Finland

[82] Persson, M., Jansson, P., Jack, A.G., Mecrow, B.C., "Soft magnetic composite materials-use for electrical machines", *Conf. on Electrical Machines and Drives, EMD'95*, Conf. Publ. No. 412, 1995, pp. 242-246

[83] Poole, N.J., Sarvar, F., "Fundamentals of heat transfer", *IEE Col. Thermal Design of Electronic Systems*, 1989, pp.1/1-1/4

[84] Ramesohl, I., Henneberger, G., "Calculation and measurement of vibration and acoustic noise considering different pole geometries of a claw-pole alternator", *Int Conf on Electrical Machines, ICEM'98*, 1998

[85] Ramesohl, I., Henneberger, G., Kuppers, S., Hadrys, W., "Three dimensional calculation of magnetic forces and displacements of

a claw-pole generator", *IEEE Trans Magn*, vol. 32, no. 3, 1996, pp. 1685-1688

[86] Reinert, J., Brockmeyer, A., De Doncker, R.W.A.A., "Calculation of losses in ferro- and ferrimagnetic materials based on the modified Steinmetz equation", *IEEE Trans Ind Appl*, vol. 37, no. 4, Jul/Aug 2001 pp. 1055-1061

[87] Santander, E., Ben Ahmed, A., Gabsi, M., "Prediction and measurement of detent torque of a single-phase machine", *Conf on Electrical Machines and Drives, EMD'97*, Conf. Publ. No. 444, 1997, pp. 210-214

[88] Sivasubramaniam, K., Salon, S., Chari, M.V.K., "Numerical errors in the scalar potential formulations used in low-frequency field problems", *IEEE Trans Magn*, vol 36 n 5, Sept. 2000, pp. 3096-3098

[89] Skarrie, H., Design of Powder Core Inductors, *Licentiate Thesis*, Lund University, 2001, ISBN 91-88934-19-5

[90] SMC shool at Höganäs AB, 27-28 November, 2001

[91] Smith, A.C.; Edey, K., "Influence of manufacturing processes on iron losses" *7th Int Conf Electrical Machines and Drives*, (Conf. Publ. No. 412), 11-13 Sep 1995, pp. 77-81

[92] Suzuki, Y., "Claw pole type synchronous motor", US patent No.5,818,143, filed Mar. 11, 1997

[93] Takahashi, N., "Some useful techniques in analysis and design of electric machines", IEEE Int. Electric Machines and Drives Conf, 18-21 May 1997, pp. WC2/1.1 - WC2/1.6

[94] Trout, S.R.; Wooten, G.D., "Selection and specification of permanent magnet materials", *Electrical Insulation Conference and Electrical Manufacturing & Coil Winding Technology Conf*, Proc. , 23-25 Sept. 2003, pp. 59-63

[95] Wang, J.P., Lieu, D.K., Lorimer, W.L., Hartman, A., "Comparison of lumped parameter and finite element magnetic modeling in a brushless dc motor", *IEEE Trans Magn*, vol. 33, no. 5, Sep 1997, pp. 4092-4094

[96] Yamashita, F., Watanabe, A., Fukunaga, H., "New preparation method of anisotropic and isotropic Nd-Fe-B-bonded magnet for

small dc motors", IEEE Trans Magn, vol 39 n 5, Sept. 2003, pp. 2896-2898

[97] Zhu, J.G., Ramsden, V.S., "Improved formulations for rotational core losses in rotating electrical machines", *IEEE Trans Magn*, vol. 34, no. 4, July 1998, pp. 2234-2242

[98] Zhu, J.G., Zhong, J.J., Lin, Z.W., Sievert, J.D., "Measurement of core losses with 3d magnetic fluxes", *IEEE Int Magn Conf INTERMAG 2003*, March 28 - April 3, 2003, pp. EP-03-EP-03

[99] Zhu, Z.Q., Bentouati, S., Howe, D., "Control of single-phase permanent magnet brushless DC drives for high-speed applications", *Power Electronics and Variable Speed Drives,* IEE Conf Publ No. 475, Sept. 2000, pp. 327-332

Appendix A

Material data

Material data that have been used in the calculations are presented.

Nonlinear magnetic characteristics

In Figure A.1 are shown non-linear magnetic characteristics for the soft magnetic and hard magnetic materials.

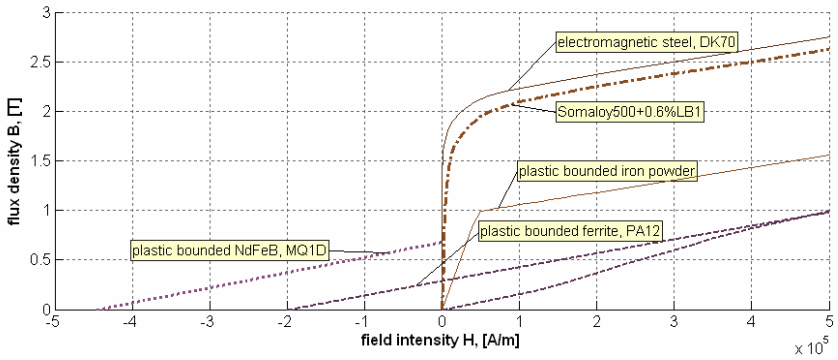

Figure A.1: Non-linear magnetization characteristics of compression molded SMC, electromagnetic steel and injection molded ferrite magnet. The magnetization characteristic of an injection molded iron powder is constructed according to the saturation level of 1T and maximum permeability of 17μ_0 (Premix OY, Finland). The demagnetization characteristics of the injection molded ferrite and compression molded NdFeB magnets are shown in the second and partly in the first quadrant.

The magnetic materials that have been considered are isotropic in the EC and FE analyses. The magnetic properties of non-oriented electromagnetical steel

DK70 (Surahammars Bruk AB, Sweden) and plastic bounded iron powder (Premix OY, Finland) is used in the comparative calculation of a claw-pole structure in the single-phase claw-pole motor. The back iron material that is used in the rotor is considered to have the same magnetic characteristics as DK70. SMC bases on a water atomized highly pure iron powder particle with an oxide surface coating, which is known as Somaloy 500 (Höganäs AB, Sweden). The iron powder is mixed with 0.6% lubricating binder (LB1) that makes the material more suitable for high frequency and high mechanical stress applications. Magnet materials are compression molded NdFeB powder and injection molded ferrite powder (Sura Magnets AB, Sweden).

Physical properties

Physical properties of the materials are summarized in table A.1

Table A.1: Physical properties of the materials used in the claw-pole motors.

Quantity	symbol	unit	Copper	SMC core Somaloy500	Plastic bounded ferrite (PA12)	Plastic bounded NdFeB (MQ1B)	Plastic bounded NdFeB (MQ1D)	Insulation (Polyethene)
Mass density	σ	g/cm^3	8.9	7.31	3.73	6	6	0.92
Resistivity[1]	ρ	Ω·m	1.75e-8	0.75		1.4	1.4	3e+15
Resistivity thermal coefficient[1]	α	1/K	4e-3					
Relative magnetic permeability	μ	-	1	200	1.16	1.22	1.22	
Remanence	B_R	T		0.13	0.292	0.69	0.68	
Coercivity	H_C	kA/m		0.4	200	414	446	
Intrisic coercivity	H_{ci}	kA/m			230	716	812	
Energy product	BH	kJ/m^3			16	80	80	
Compressive strength		MPa				38.8	38.8	
Tensile strength		MPa			46.1	37.3	37.3	
Young's Modulus	E	GPa	124	90		0.843	0.843	
Poisson Ratio	v	-				0.2	0.2	
Transverse Rupture Strength	TRS	MPa		100		31.4	31.4	
Hardness (Rockwell B)		-			115	30	30	
Green strength	GS	MPa		29.7				
Max operating temperature	T_{max}	˚C		150	128	110	110	
Thermal conductivity	λ	W/(m·K)	349	13	30	2	2	0.24
Special heat capacity	c	J/(kg·K)	385		400	420	420	2100
Temperature coefficient Br	B_rT	%/˚C				-0.105	-0.07	
Temperature coefficient Hci	$H_{ci}T$	%/˚C				-0.4	-0.4	
Curie temperature	T_{cur}	˚C				360	470	
Thermal expansion coefficient		1/K				4.8e-6	4.8e-6	100e-6

[1]Electric resistivity and thermal resistivity constant are given at temperature of 20ºC (Table A.1).

A plastic bounded ferrite magnet-ring is injection molded from ferrite powder of grade F 16/23 with nylon binder PA12. An aligning field is used in the molding kit to align the magnetic-particles in a preferred magnetization direction. A plastic bonded NdFeB magnet-ring is compression molded from MagneQuench powder (MQP) that is blended with an epoxy resin.

Loss coefficients

Rotational core loss coefficient for Somaloy500+0.6%LB1 is estimated according to the measurements of the pulsating core losses for Somaloy500+0.6%LB1 and Somaloy500+0.5%Kenolube [89] and according to the measurements of the rotational core losses in Somaloy500+0.5%Kenolube [98].

Table A.2: Core loss coefficients for Somaloy 500. Different loss coefficients (coef) and exponents (exp) are applied for different origin of losses and a locus of the flux density vector, which is alternation (alt) or rotation (rot). Complete loss coefficients for loss components at sinusoidal field are presented in brackets (Eq. 3.18)

Loss component, **B** locus	symbol	unit	Loss coefficient			
			0.5%Kenolube[1]	0.6%LB1[2]	0.5%Kenolube[3]	0.6%LB1[4]
Hysteresis, coef, alt **B**	k_h	W/m³	880	1160	1031	1213
Hysteresis, exp, alt **B**	n	-	1.7	1.6	1.548	1.88
Hysteresis, coef, rot **B**	a_1	W/m³	-	-	50000	64000
Hysteresis, coef, rot **B**	a_2	-	-	-	1.054	1.054
Hysteresis, coef, rot **B**	a_3	-	-	-	1.445	1.445
Saturation induction	B_S	T	-	-	2.134	2.134
Dynamic, coef, alt **B**	k_{dyn}	W/m³	2.8 (21)	7.0453 (57)	-	7.0453 (57)
Dynamic, exp, alt **B**	n	-	1.35	1.85	-	1.85
Dynamic, exp, alt **B**	n	-	1.45	1.40	-	1.40
Eddy current, coef, alt **B**	k_e	W/m³	0	0	0.0906 (1.79)	0
Anomalous, coef, alt **B**	k_a	W/m³	1.4 (12.3)	3.6 (31.5)	2.6791 (23.5)	3.6 (31.5)
Eddy current, coef, rot **B**	k_a	W/m³	-	-	1.6927 (33.4)	0
Anomalous, coef, rot **B**	k_a	W/m³	-	-	0	3.6 (31.5)

1. Core loss coefficients of compression molded core of Somaloy 500 + 0.5% Kenolube measured at pulsating field [89].
2. Core loss coefficients of compression molded core of Somaloy 500 + 0.6% LB1 measured at pulsating field [89].

3. Core loss coefficients of compression molded core of Somaloy 500 + 0.5% Kenolube measured at pulsating field and rotating field [98]. The mass density of 7350 kg/m^3 is considered when scaling the specific loss coefficient per unit of core mass to loss coefficient per unit of a core volume.
4. Core loss coefficients, which are used in this thesis, are estimated from the previous measuments by Skarrie [89] and Guo [98] for a compression molded core of Somaloy 500 + 0.6% LB1. The higher hysteresis loss for alternating magnetizing field is measured by Skarrie but not presented in his work [89].

Appendix B

Motor construction

The objective is to formulate the shape of the claw-pole structure for the outer rotor motor. That is necessary in order that the structure is easily parameterized and formulated in FE software.

B.1 Formulation of a claw-pole core

The shape of a claw-pole determines the ratio of transversal coupling flux to the direct leakage flux in TFM. The shape of the flank has smaller influence on the ratio. The effect of a base core to the ratio of coupling flux to leakage flux is minor unless the improper magnetic coupling reduces the magnetic coupling.

The shape of the claw-pole can be determined by the uniform magnetic loading in radial and axial direction (Eq. 2.1). The cross-section area of the claw-pole in the radial/circumferential plane can be expressed as

$$A_C = \frac{1}{2} \cdot (\theta + 2\Delta\theta) \cdot \left[R^2 - (R - \Delta R)^2 \right]. \tag{B.1}$$

The incremental decrease in a pole radius ΔR and an angular pole length $\Delta\theta$ determines the growth of the claw-pole in the axial direction. Pole surface area in the axial/circumferential plane, in respect of the incremental growth in axial direction ΔZ and along the circumference $\Delta\theta$, is at pole radius R expressed as

$$A_P = R \cdot (\theta + \Delta\theta) \cdot \Delta Z . \tag{B.2}$$

If the cross section-area in the half distance $\Delta Z/2$ is taken to be equal to the pole surface area, then the incremental growth of the pole dimensions are given by the following relation

$$\frac{\Delta R}{\Delta Z}\cdot\left(1-\frac{1}{2}\frac{\Delta R}{R}\right)=1\cdot \tag{B.3}$$

The geometrical representation of the formulation (Eq. B.3) is shown in Figure B.1.

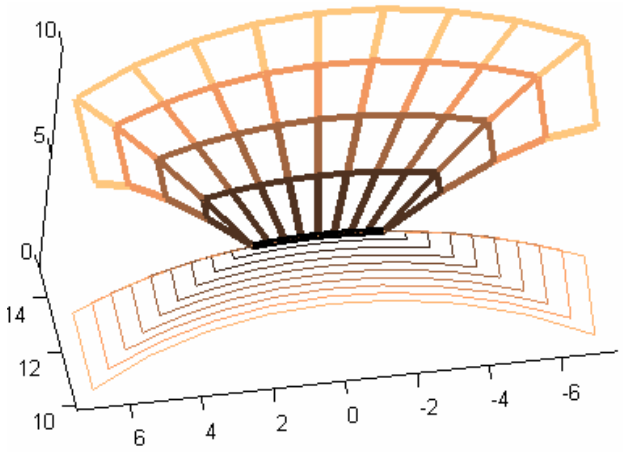

Figure B.1: Claw-pole formulation in respect of flux concentration, where the cross-section area is decreased by half compared to pole surface area. Pole radius is r_p=15 mm, circumferential tapering γ_1=30°, axial tapering γ_2=15°, the number of poles N_p=6 and the space between the poles is 40% of the pole pitch. The axial height of the claw-pole h_p=10 mm and the dimensions in the axis are shown in millimeter scale.

The geometric representation of the symmetric part of the claw-pole ring is shown in Figure B.2. The axial height of the phase-ring h_p determines the thickness of the flank that is *1/4* of h_p at the slotting ratio of *50%*. The radial thickness of the base l_b core is taken to be equal to the axial thickness h_f of the flank (Figure B.2). In reality the thickness of the base core is reasonable to choose according to the cross-section area of the flank. The radial thickness l_t of the claw-pole is determined either by the selected thickness of the pole and axial tapering γ_2 or one of the aforementioned dimensions. The claw-pole motors in this work have constant radial thickness of the claw-poles.

The geometry of the claw-pole has flux concentrating effect, while the magnetic coupling between the adjacent claw-poles is established via the flanks

and base-core. The flank is formed on the basis of the cross-section area of the claw-pole. The cross-section area of the flank along the radial direction can be either constant or become larger at the inner radius, where the flank is joined to the base core. The angle between the radial axis and the side of the flank is formulated according to the constant cross-section area of the flank (Eq. 2.6). The area of the flank is chosen to be constant or slightly changing, which is determined by concentration angle γ_3. The side of the flank from the radius r_{s2} to the radius r_{s1} is formed according to a cubic function, which is used to join smoothly the adjacent flanks of the claw-pole ring.

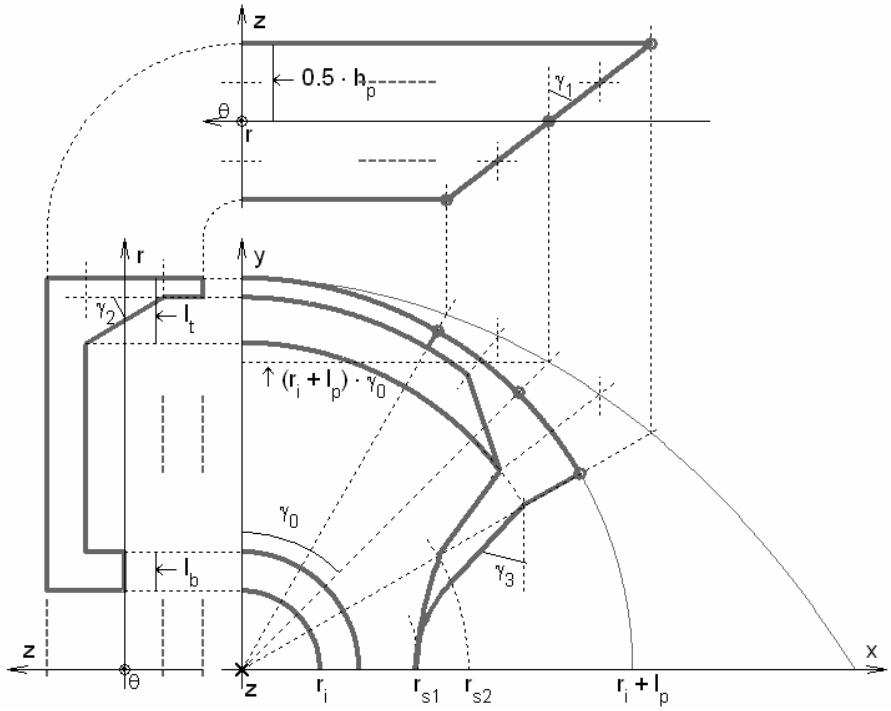

Figure B.2: Formulation of a claw-pole core for an outer rotor motor. The core geometry is shown in the θz, rz and θr-plane.

The progressive radius of the claw pole is formulated according to the radial increment of the pole radius to the increment of angle, which gives linear progressive radius of the claw-pole.

B.2 Core formulation in 3D FE software

The magnetically optimal core design is influenced by the successfulness of the 3D FE meshing. The Modeller uses geometric primitive volumes and Boolean operations in order to construct the model, while the core volume in the pre processor is extruded from a 2D cross-section in the base. The increased solution time associated with the larger problem must be weighed against the time to create the model that uses only hexahedral blocks. It has been noticed that the mathematic capability to formulate a block structure of any type of motor in MATLAB, where it is possible to create a readable file format for the Pre-Processor, gives advantage over a number of other tools (Appendix C). The most advantageous feature is successful and reliable meshing.

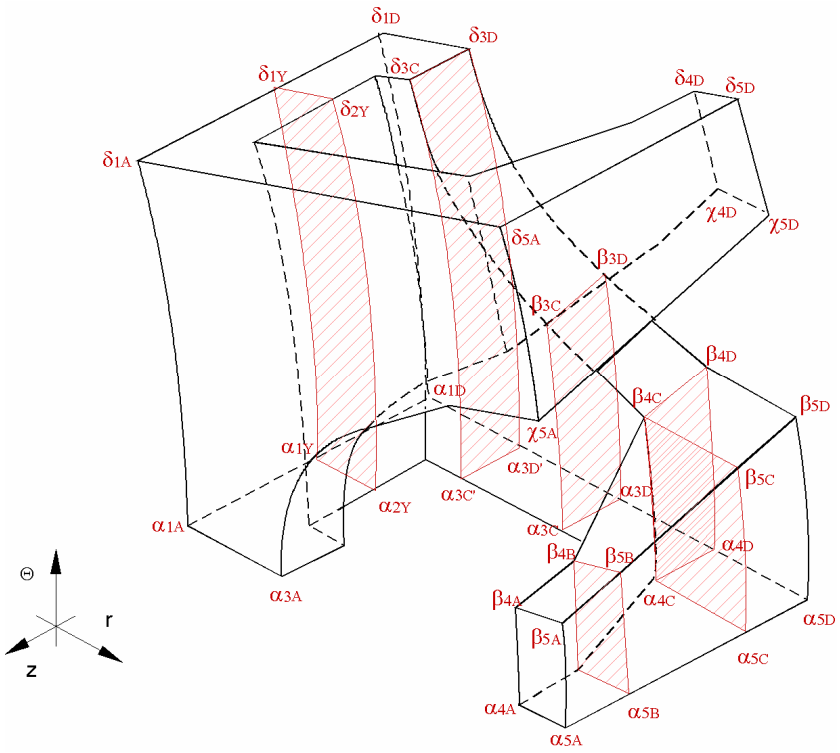

Figure B.3: Formulation of the claw-pole core.

The claw-pole core is formulated from a cube of node-points $N(\theta,r,z)$ that are shifted according to claw-pole core shape formulation (Figure B.3). The used

terminology of the claw-pole structure formulation is summarized in Table B.1.

Table B.1: Formation of claw-pole structure. The node point N(θ,r,z) of a volume is defined in respect of sectors α-β-χ-δ, levels 1-2-3-4-5 and layers A-B-C-D.

Formation of claw-pole structure	symbol	unit	Description
Tangential or circumferential tapering[1]	γ_1	deg	Trapezoidal shape of claw-pole δ5A-δ5D-χ5D-χ5A
Axial tapering[2]	γ_2	deg	Claw-pole sharpening in rz-plane β4C-β4B-β5B-β5C
Constant radial thickness of the claw-pole[3]	l_t	mm	α4A-α5A-β5B-β4B
Flank forming near to poles[4]			Constant cross section area along r-axis β4C-β4B-β5B-β5C
Flank forming in the centre[5]	γ_3	deg	Increased cross section area along r-axis β4D-β4C-β5C-β5D
Flank formation in order to join it to the adjacent flank[6]	r_{s1},r_{s2}	mm	Cubic function defined surface δ3C-δ3D-β3D-β3C
Base core formation[7]	r_i,l_b	mm	Cross-section area of the base core α1Y-α2Y-δ2Y-δ1Y

The formulation of the claw-pole structure (Table B.1) shows the variable, which defines the shape of the core.

1. The symmetric trapezoidal shaping in the θz-plane is preferred. Unsymmetrical shape of the claw-pole surface has not shown any advantages according to the sensitivity study.
2. The axial tapering formulates the claw-pole sharpening in the rz-plane. The axial tapering is not preferred in the designed motors. This is done in order to improve manufacturability. At the same time, the configuration does not to give any significant drawbacks in the magnetic core design.
3. The combination of constant radial thickness and the axial tapering can be preferred from structural mechanic design point of view. Moreover, the effect of flux concentration that is causing the magnetic overloading can be reduced by using extra magnetic material, where the poles are joined to the flanks. The motor design in this work is based on the constant radial thickness of the poles.

4. The bottom of the claw-pole and the upper part of the flank have constant cross-section area that is along the flux path. The side of the flank *β4D-β4D* is parallel to the centre-line of the flank *a4D-a5D*. On the FE models, the top of claw-pole has the sides *β4A-β4A* and *a4A-a5A* unparallel. This is done in order to increase the distance between the opposite flank and the claw-pole.
5. The centre part of the flank is formed according to constant cross section area or the increased cross-section area of the flank. The flank formation angle γ_3 is defined from the parallel line to the center-line of the flank.
6. A cubic function is used in order to form the radius of the lower part of the flank. The union between the adjacent flanks is defined between two radius r_{s1} and r_{s2}, which defines the lower part of the flank.
7. The base core includes an axial air-gap between claw-pole rings. The gap is defined as an extra layer of elements.

Appendix C

CAD incorporated with 3D FEA

Computer aided design (CAD) that can incorporate effectively the computational capability of 3D FE analysis (FEA) is indisputably a powerful tool for a product development and especially for electric machine design.

C.1 Controlled CAD and 3D FEA

The motor design is a process loop of different tasks that usually use different software's. It is important that this loop is able to operate without user interaction. The 3D FEA Opera-3D is used in conjunction with the MATLAB programming language in order to perform automated simulation and performance analysis of the claw-pole motors. The design tool is operated in MATLAB that specifies the input data to 3D FE analysis, depending on the type of 3D FE mesh to be used, does the model administration, analyses results and creates animations. The latter is useful for a fast visual evaluation process. Depending on whether the Pre-processor or the Modeller is used to construct a 3D FE model, the input data is a complete model definition in an 'oppre' file or set of parameters in a 'comi' file that is used in a geometric Modeller module. The latter allows a complex 3D model to be constructed swiftly from formed and primitive solids using Boolean operations. These operations are specified in a comi file of the motor construction model. The structural mechanic and heat transfer problem are formulated in FEMLAB command language and executed in MATLAB.

Geometrical representation

Transfer of geometric data between CAD and analysis systems has a high priority. It saves time when the motor structure can be specified quickly according to set of parameters that are specified for a type of motor construction. The drawback of Opera-3D Pre-processor is that the 3D FE model can not be exported as easily as geometric data and the module is not able to read any of the common transferable geometric data formats. SolidWorks has powerful design environment to construct 3D models with great complexity. When the motor construction model is to be used together with construction data that is defined in Microsoft Excel, then these tools are difficult to be controlled in MATLAB without user interaction.

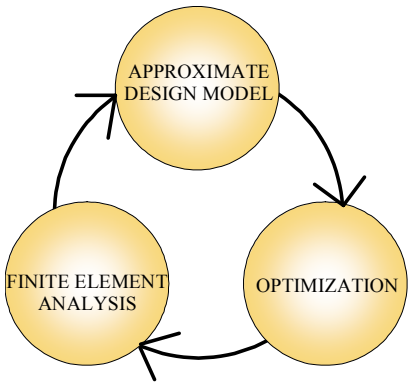

Figure C.1: Computation loop in the design process of electrical machines.

In this work, the completeness of the computation loop is mainly focused on the powder core design that bases on the magnetostatic field analysis. The output of the computation loop is not only an optimized motor design but also an improved design tool for the TFM with claw-pole structure. One of the aims of the design tool is the computation effectiveness, which especially are 3D FEA accuracy, a reduced need for calculation time and for computer memory usage. The important output from the magnetostatic field analysis is the static characteristics of the designed motor.

3D discretization of air-gap region

The work is focused more on the appropriate FE model discretization than on the torque computation method. The accuracy of force computation from the field values in the middle of air-gap depends on the 3D FE elements and meshing quality. This can be achieved only by having strong control over the shape and position of the elements, as is the case with the hexahedral mesh

generation strategy within OPERA-3D. Due to the complex geometry the hexahedral elements becomes badly shaped in crucial areas.

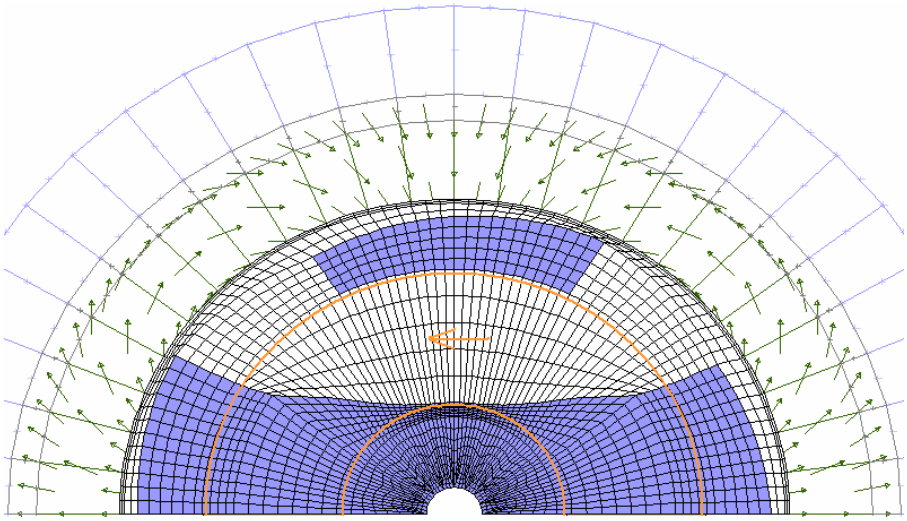

Figure C.2: 3D FE mesh in the radial/circumferential plane of the single-phase claw-pole motor.

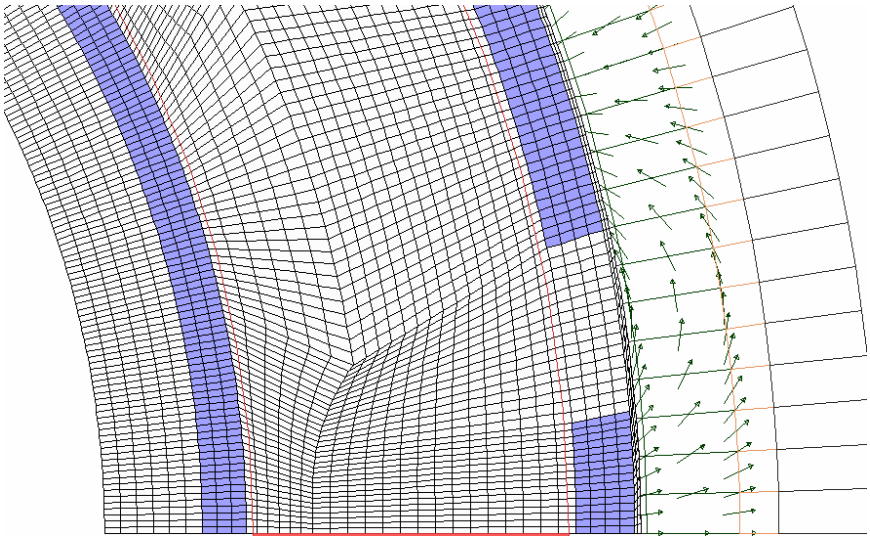

Figure C.3: 3D FE mesh in the radial/circumferential plane of the two-phase claw-pole motor.

C.2 Accuracy of 3D FE modeling

The stress computation in 2D FEA on electromagnetics and 3D FEA on structural mechanics are often considered as imperfect due to inadequate FE mesh in the crucial areas. The same problem appears in a 3D FE formulation on electromagnetics when the torque evaluation is carried out from Maxwell shear stress computation. The aim of the next lines is to visualize the efforts of 3D FE mesh improvements and its influence on the computation accuracy.

Field representation in the air-gap

The mesh in the space around the air-gap is refined to improve the accuracy of the field representation, while evaluating relatively coarse mesh density in the rest of the model to keep computational time at reasonable levels.

Field evaluation error

The field evaluation error is investigated on four different gap meshes with hexahedral elements and two gap meshes with tetrahedral elements that have different number of elements. A patch is placed in the middle of the air-gap and the previously described function ERRBMOD/BMOD is evaluated over the patch. From the results it is seen that the field error is rather related to the fringing field representation in the outer sides of poles and not to claw-pole tapering between the poles.

Shear stress evaluation error

Shear stress is evaluated over the same patch that has been used in order to determine the field estimation error. The magnitude of the stress reverse is increasing at the inner edges of claw-poles, while the circumferential tapering or asymmetric pole profile is introduced.

Tetrahedral mesh

The field and the shear stress values are compared with tetrahedral mesh. The tetrahedral elements may have more regular shape of the elements that are not distorted due to the shaping of claw-poles.

Visualization of the 3D FE analysis results

The field evaluation error is shown in Figure C.3, Figure C.4 and Figure C.7, The shear stress evaluation results are shown in Figure C.5, Figure C.6 and Figure C.8.

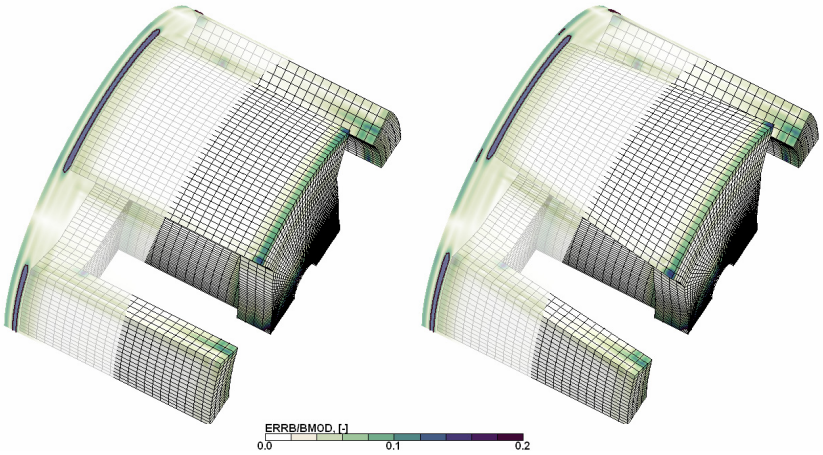

Figure C.4: Discretization error due to skewed hexahedral elements on circumferential/axial plane. Figure on the left shows the field differentiation error for a rectangular shape of the claw-poles. Figure on the right shows the same error for the trapezoidal shape of claw-pole. A dark line on the patch indicates the error of more than 10%. 112480 elements are used in the 3D FE models with hexahedral elements.

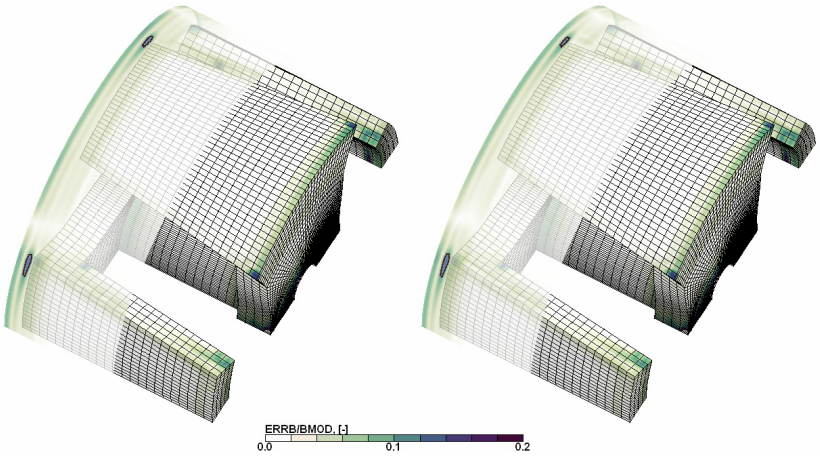

Figure C.5: Discretization error due to the deformed hexahedral elements. The field differentiation error is shown on the patch in the middle of the air-gap and on the surface of the claw-pole structure for the asymmetric air-gap. Figure on the left has a continuous skewing of the elements through the air-gap and a rotor structure. Uniform 3D elements with rectangular facets are defined in the middle of the air-gap (figure on the right).

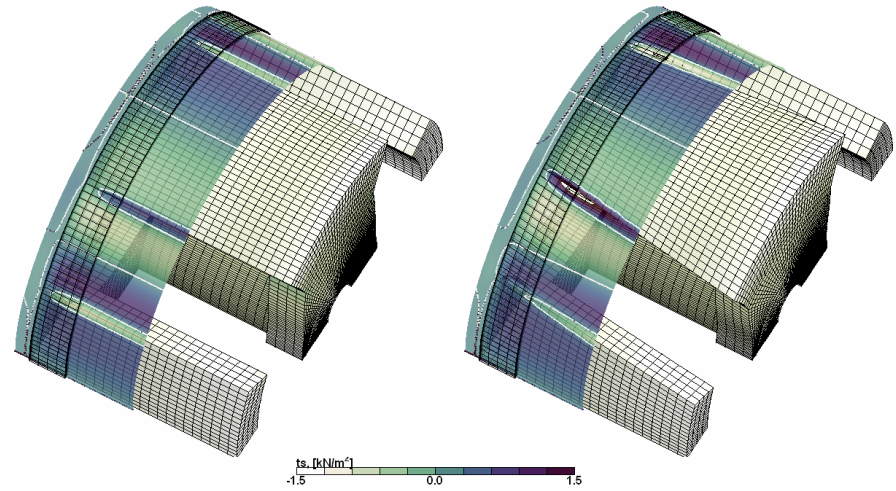

Figure C.6: Shear force in the middle of air-gap for rectangular (left) and trapezoidal (right) claw-pole. White lines indicate the region where the force changes sign.

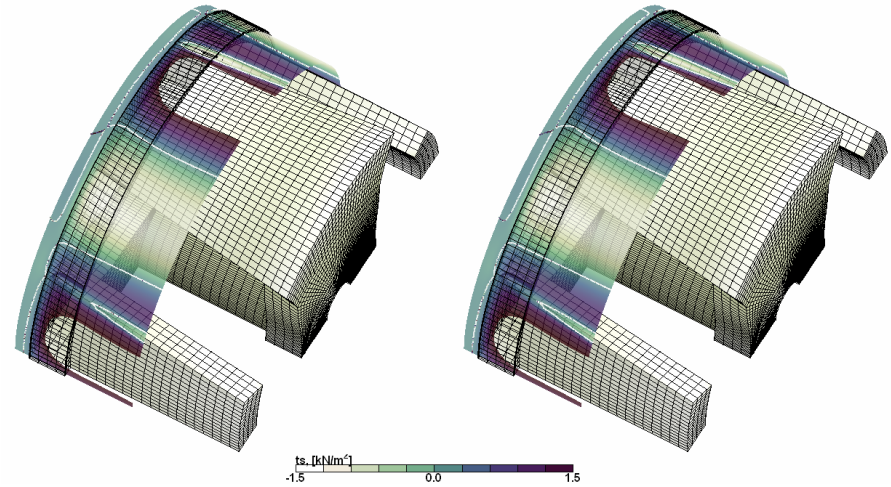

Figure C.7: Shear force distribution dependence on the element deformation in the middle of asymmetric air-gap. White lines indicate the region where the force changes sign.

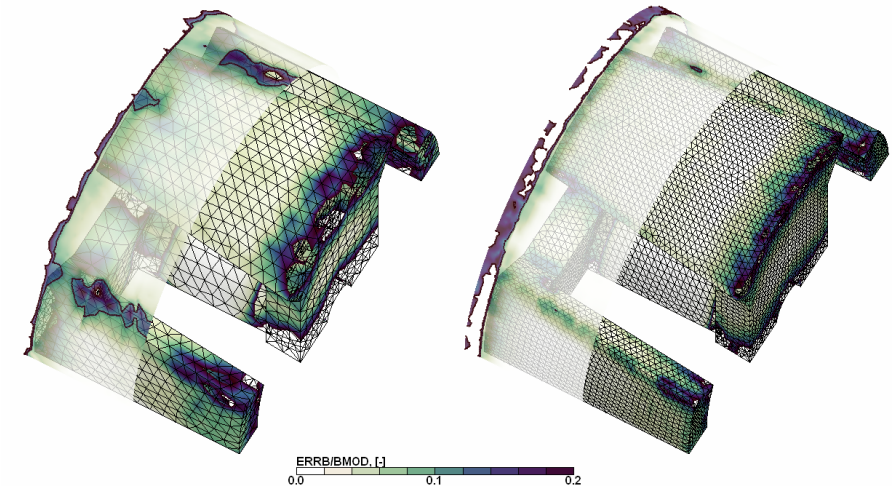

Figure C.8: Discretization error due to the tetrahedral elements. The field differentiation error is shown on the patch in the middle of air-gap and on the surface of the claw-pole structure for the asymmetric air-gap. Figure on the left has a continuous skewing of the elements through the air-gap and a rotor structure. Uniform 3D elements with rectangular facets are defined in the middle of the air-gap (figure on the right). 235628 and 921685 elements are used in the models. The estimated error in B field is, respectively, 12.05% and 4.96%.

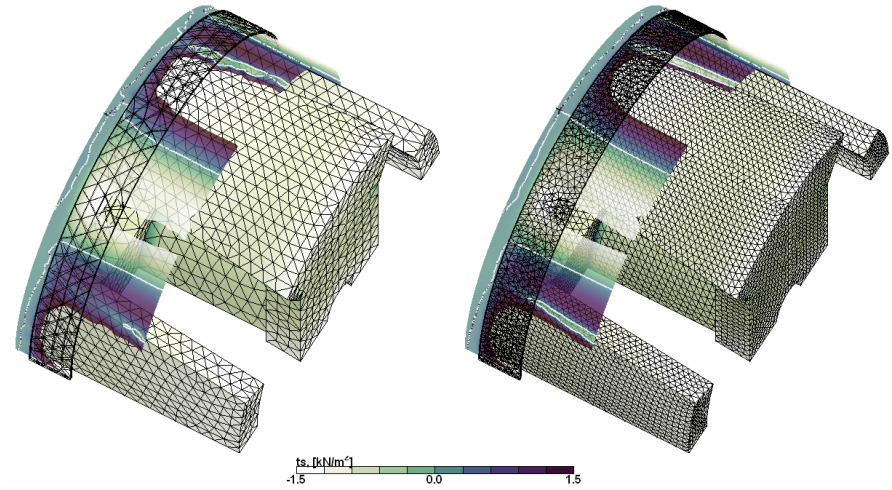

Figure C.9: Shear force distribution dependence on the tetrahedral elements. White lines indicate the region where the force changes sign.

There is no evident sign that the deformed hexahedral elements give inaccurate estimate of field or shear stress compared to the tetrahedral elements. It is however expected that tetrahedral elements fit better do discretize a motor core that have complex shape.

C.3 Analysis at post-processing level

The implementation of the empiric core loss formulation a posteriori to field evaluation is one of the tools to evaluate the motor performance. The other analysis that is introduced at post-processing level is the coupling and leakage flux evaluation.

Core loss computation

Using the FE method allows to discretize the machine in a larger number of 3D elements. This allows a more precise calculation of the magnetic loading and core losses in the machine over the excitation cycle that is compared to a MEC model.

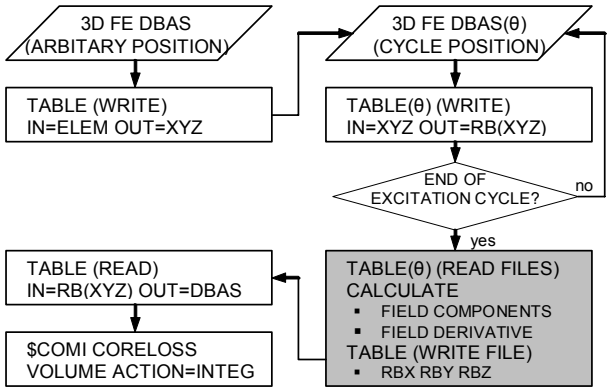

Figure C.10 Post-processing approach applied to the series of 3D FE magnetostatic solutions over the magnetization cycle. Opera-3D command language is used in order to describe the function blocks in the flowchart. The content of the gray block is processed outside the Opera-3D post-processor

The equation describing the magnetization pattern in the permanent magnet is redefined in order to simulate the rotation while keeping the same 3D mesh and element numeration. This is convenient in order to carry out the harmonic analysis directly at each element. Alternatively, if the 3D FE mesh is rotated then the elements are renumbered, and they only can be identified by using an

external table, where the original coordinates of the elements have been stored. The flow-chart of the loss calculation procedure is shown in Figure C.10.

The coordinates are calculated at the centre of the 3D FE elements (ELEM) in the database for the initial position (DBAS). The table of coordinates that belongs to the initial model is used to to obtain the field values of a rotated mesh. It should be noted that when calculating the fields in the rotor, the mesh will have to be rotated back, so that the rotor coordinates correspond to those at the initial position. A number of tables, which are generated, equals to the analysis steps. Each table consists of field components that are obtained from a FE solution according to the coordinate table. As the field values are picked according to the points that are defined in the reference model, then the 3D FE model, from where the field values are obtained, can have different mesh. It is not problem to read the field values from tetrahedral mesh according to reference hexahedral mesh. The field behavior is analyzed from the number of tables over the magnetization cycle. A few result tables are written and these tables contain the suitable input for core loss calculation. Finally, the result table, containing the calculated flux density values (RBX, RBY, RBZ), is loaded into the initial 3D FE reference database. The specific core loss is calculated according to the new values at each element. The result table, for static loss calculation contains the values of the minor and the major axis of the field rotation ellipse, and the values of dc component of field. The result table for dynamic losses includes the averaged field derivative at different dimensions. The total loss is computed by performing a volume integral over the FE model.

Appendix D

Power electronic control

The power electronic control is carried out in a driver circuit where action is determined by a control signal. The control signal is formulated in a Simulink model that is executed in dSpace RTI1104. A feedback from the drive system is the winding current and the angular position of the rotor.

D.1 Driver circuit

The driver circuit consists of DMOS full bridge driver (L6203), a pair of comparators that formulate the control impulses according to hysteresis control, and protective snubber network (Figure D.1).

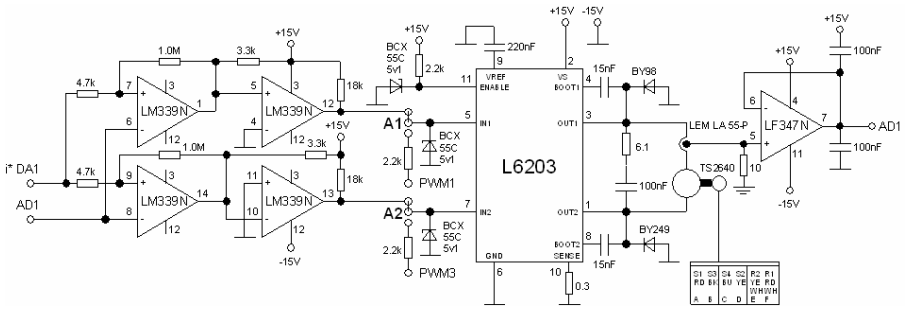

Figure D.1: Driver circuit that can be used either for sampled current control or direct current control. In the first case the control pulses are formed in dSpace card in digital side. The hysteresis loop is built on two operational amplifiers and the control signal is carried out in the analoque side. Alternatively, the output of PWM generator can be connected to the H-bridge by flipping the exciting connection at A1 and A2.

The soft switched VSI causes unbalanced loading to the transistors. This is due to a simple direct current control (DCC) circuit. Apart from DCC the control signal can be taken directly from dSpace interface card. A pair of PWM channels is used to form a control signal from the output of the sampled current controller (SCC). The same conditions are specified in the driver circuit, which are used in simulations (Table 6.1). Some of the characteristics of the full bridge driver L6203 by SGS-Thomson are presented in Table D.1.

Table D.1: DMOS full bridge driver L6203.

Quantity	symbol	unit	Value
Power supply	U_{dc}	V	12…48
Peak current	I_{peak}	A	5
RMS current	I_{rms}	A	4
Operating frequency	f_{sw}	kHz	100
Total power dissipation	P_{tot}	W	20

D.2 Feedback

Two feedback circuits are implemented in the drive system: angular position measurement and current measurement.

Angular position of motor poles

The angular position of rotor is necessary in order to form the reference current waveform. The angular position can be generated or measured, which is, respectively, sensorless or closed loop control. In the sensorless control the angular position is generated according to the speed ramp and maximum speed (Figure D.2).

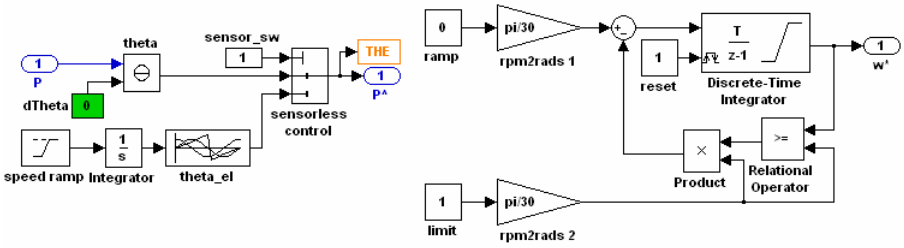

Figure D.2: Position reference selector for current reference generator (left). The subsystem of the speed ramp sets the suitable acceleration and maximum speed (right).

The speed ramp is selected according to an ability of the drive system to accelerate and to keep constant speed without loosing a synchronism. The closed loop control bases on the resolver output, which is coupled via resolver-to-digital conversion, digital-to-analogue and analogue-to-digital converter into dSpace RT processor. The conventional lab-setup is used in order to implement the position sensor circuitry to the drive system. The position of resolver can be adjusted in the Simulink model in order to form the correct reference current at certain position and to feed the current reference earlier in order to overcome the control delay.

Current measurement

Two LEM modules are used to measure the current in the motor coil and in the primary of the four quadrant dc/dc converter.